

جامعة الملك عبدالعزيز
KING ABDULAZIZ UNIVERSITY



In vivo studies of B cell differentiation during the extrafollicular and germinal centre responses to T-dependent antigens

by

Amani Taher Al-Zahrani

A thesis submitted to the University of Birmingham for the degree of

DOCTOR OF PHILOSOPHY

Department of Immunology and Immunotherapy
College of Medicine and Health
University of Birmingham
January 2026

UNIVERSITY OF
BIRMINGHAM

University of Birmingham Research Archive

e-theses repository

This unpublished thesis/dissertation is copyright of the author and/or third parties. The intellectual property rights of the author or third parties in respect of this work are as defined by The Copyright Designs and Patents Act 1988 or as modified by any successor legislation.

Any use made of information contained in this thesis/dissertation must be in accordance with that legislation and must be properly acknowledged. Further distribution or reproduction in any format is prohibited without the permission of the copyright holder.

Abstract

The connection between antibody affinity maturation and the quality of humoral immunity is critical for inducing a protective immune response. Considering that plasma cells (PCs) can be extrafollicular (EF) and germinal centre (GC)-dependent, the *S1pr2*^{CreERT2} *Rosa26*^{LSLtdTomato} *Prdm1*^{GFP} mouse model was used to distinguish EF-derived and GC-derived PCs. Using this mouse model, early GC-derived plasmablasts (PBs) peaked at day 5, whereas GC-matured PCs accumulated by day 6. Furthermore, EF-derived Blimp-1^{GFP+} plasmablasts-plasma cells (PBs-PCs) were detected within the GC cluster, representing an unexpected observation, the basis of which remains to be determined.

In the IgMg1AID^{Cre} mouse model, expansion of IgG1^{+} GC B cells was confirmed to drive the reduction of IgM^{+} GC B cells in the original IgMg1 model. Interestingly, the chimeric IgG1 tail controlled Tfh cells and GC B cell expansion in the IgMg1AID^{Cre} mouse model, unlike the marked expansion of Tfh cells in the IgMg1 model and GC B cells in the AID^{Cre} model.

In the recall immune response, we investigated how the location and nature of the initial priming event shaped the B cell response after a boost with the same antigen. The recruitment of memory B cells at local versus distal sites determines the magnitude of the recall response. Distal sites can act as secondary survival niches for PBs-PCs, thereby supporting sustained antibody production. In addition, the abundance of NP-binding naive B cells at both sites may further influence the effectiveness of the recall response.

These *in vivo* models should be useful to interrogate the biology of B cell differentiation that allows us to investigate multiple stages simultaneously.

Acknowledgements

One of the highest expressions of gratitude and appreciation is to say 'thank you'. Sincere thanks to the three supervisors, Kai-Michael Toellner, Adam Cunningham, and Michael Price, who provided valuable guidance in advancing the research project. My deepest appreciation to Yang Zhang for her support and patience with the scientific and technical aspects throughout my practical studies.

I also extend my sincere gratitude to the flow cytometry specialists and to colleagues—both within and outside the research group—who contribute with their own expertise and scientific background.

I would like to express my gratitude to King Abdulaziz University for the financial support it provided, which had a significant impact on the progress of my research. I also appreciate the University's commitment to supporting the research process and ensuring the quality and completion of its outcomes.

A very special thanks to my parents and children (Thamer, Meral, and Basem) for their eager anticipation of this achievement and their constant concern for me while I was abroad alone. Though abroad, I was surrounded by the Tuwaiq cubs—a reference to the emblematic Tuwaiq mountain that symbolises Saudi pride. I would like to tell them, in the Zahrani dialect, "Ana afdakum أنا أفداكم", meaning "I am here for you no matter what". Ultimately, throughout this research journey, I have gained actionable insights that have shaped my perspective on research and strengthened my commitment to continuous learning.

I used SciSummary and Grammarly for editorial support: proofreading grammar and refining academic tone.

Contents

Chapter 1. Introduction. 1

1.1. Adaptive immunity. 1

1.2. Participation of B cells in an immune response. 5

1.2.1. Immunisation-derived B cell response. 11

1.2.2. Extrafollicular response 16

1.2.3. Follicular response. 18

1.2.3.1. Formation and maturation of germinal centres. 19

1.2.3.2. Participation of T follicular helper cells in the follicular response. 24

1.2.3.3. B cell signalling and selection in the germinal centre. 28

1.2.3.4. Differentiation of germinal centre B cells into plasma cells and memory B cells. 30

1.3. Transcriptional program. 32

1.3.1. Transcriptional regulators in plasma cells. 34

1.3.2. Transcriptional regulators in memory B cells 36

1.4. The phenotype of plasma cells and memory B cells. 39

1.5. Aim of this thesis. 42

Chapter 2. Research Methodology 44

2.1 Reagents and materials 44

2.2 The experimental mice. 49

2.2.1 *S1pr2*^{ERT2Cre} *Rosa26*^{LSLtdTomato} mice. 49

2.2.2 *Prdm1*$^{eGFP/wt}$ *mice.* 50

2.2.3 *S1pr2*^{CreERT2} *Rosa26*^{LSLtdTomato} *Prdm1*$^{eGFP/wt}$ mice. 50

2.2.4 *Aicda*$^{Cre/Cre}$ mice. 51

2.2.5 IgM$^{g1/g1}$ mice. 51

2.2.6 IgM$^{g1/g1}$*Aicda*$^{Cre/Cre}$ mice. 51

2.3 Antigens....52

2.3.1 Sheep red blood cells (SRBCs). 52

2.3.2 NP-conjugation. 52

2.4 Adjuvants....53

2.4.1 Alum precipitation. 53

2.4.2 *Bordetella pertussis*. 53

2.5 Administrations and Immunisations. 53

2.5.1 Tamoxifen. 53

2.5.2 Primary immunisation. 54

2.5.3 Secondary immunisation. 55

2.6 Tissue preparation for flow cytometry. 55

2.6.1 Harvesting and processing tissues. 55

2.6.2 Staining panels. 56

2.6.2.1 Plasma cell staining panel. 56

2.6.2.2 Tfh cell staining panel. 57

2.7 Immunofluorescence histology. 57

2.7.1 Preparation of spleen samples. 57

2.7.1.1 Fixation and cryopreservation. 57

2.7.1.2 Tissue embedding. 58

2.7.1.3 Cryosectioning. 58

2.7.2 Immunofluorescence staining protocol. 59

2.7.2.1 Antigen retrieval and permeabilisation. 59

2.7.2.2 Immunofluorescence staining panel. 59

2.7.3 Immunofluorescence Imaging. 60

2.7.4 Quantification of GC-associated cells following imaging. 61

2.8 Enzyme-linked immunosorbent assay (ELISA). 63

2.9 Data analysis. 66

Chapter 3. A Study on Early Germinal Centre-Derived Plasma Cells in HALO Mice 67

3.1 Introduction. 67

3.2. Results. 72

3.2.1. The efficiency of GC-matured PB-PC labelling in HALO mice following primary SRBC immunisation. 72

3.2.1.1 HALO mice showed that EF- and GC-matured *S1pr2*$^{tdT+}$ Blimp-1^{GFP+} PB-PC responses dominate at day 5, and GC-derived *S1pr2*$^{tdT+}$ PB-PC dominate at day 6. 78

3.2.1.2 GC-matured *S1pr2*$^{tdT+}$ Blimp-1^{GFP+} PB-PC peaked at day 5, and the GC response peaked at day 6. 81

3.2.1.3 GC-derived CD38^{+} Blimp-1^{GFP+} *S1pr2*$^{tdT+}$ PC precursors peaked at day 5 and raised memory B cells at day 6. 83

3.2.1.4 GC-matured CD138^{+} TACI^{+} *S1pr2*$^{tdT+}$ Blimp-1^{GFP+} PB-PC accumulated at day 6. 86

3.2.1.5 The fully differentiated PC peaked at day 6 after the primary response with SRBC. 88

3.2.1.6 Dissemination pattern and quantification of PB-PCs in HALO mice using immunofluorescence analysis following SRBC primary immunisation. 94

3.2.2. Characterisation of the later response of NP-specific GC-matured *S1pr2*$^{tdT+}$ Blimp-1^{GFP+} PB-PC after primary NP_{27}-KLH challenge. 111

3.2.3. Characterisation of GC-matured *S1pr2*$^{tdT+}$ Blimp-1^{GFP+} PB-PC in HALO mice following secondary NP_{27}-KLH challenge. 125

3.2.3.1. GC-derived CD38^{+} PC precursors peaked at day 5, with a high proportion of GC-matured CD138^{+} PB-PC at day 8 following secondary challenge. 125

3.2.3.2. GC-matured CD19^{lo} B220^{lo} CD138^{+} TACI^{+} *S1pr2*$^{tdT+}$ Blimp-1^{GFP+} PB-PC occurs on day 8 post-boosting immunisation to NP_{27}-KLH. 138

3.2.3.3. NP_{2}-specific IgG1 antibody titre was enhanced at day 8 post-boosting. 144

3.2.4. Histology quantification of GC-matured *S1pr2*$^{tdT+}$ Blimp-1^{GFP+} PB-PC. 146

3.2.5. Histology identification and quantification of GC-associated IRF4^{+}PB-PC. 150

3.2.6. GC-resident Tfh cells in HALO mice. 155

3.2.7. Investigation of *S1pr2*^{tdT} and Blimp-1^{GFP} expression in splenic CD4^{+} and CD3^{+} T cells. 157

1.3 Discussion. 164

1.4 Conclusion. 172

Chapter 4. Investigating the Impact of the Chimeric Tail of IgMg1 on Germinal Centre Response in the Context of AID Deletion. 174

4.1 Introduction 174

4.2. Results. 178

4.2.1. Experimental design for studying IgMg1AID^{Cre} mice. 178

4.2.2. CD138^{+} PB-PC are impaired in the IgMg1AID^{Cre} mouse model. 178

4.2.3. IgMg1AID^{Cre} impairs IgM^{+} GC B cell recruitment. 185

4.2.4. IgMg1 BCR in the IgMg1AID^{Cre} model contributes to the regulation of IgM^{+} CD38^{+} B cells. ... 194

4.2.5. Tfh cells are reduced in the IgMg1AID^{Cre} model. 198

4.3 Discussion. 202

4.4. Conclusion. 208

Chapter 5. The Impact of Antigen Localisation on the Induction and Persistence of Memory B Cells. 210

5.1 Introduction 210

5.2 Results 215

5.2.1. The number of memory B cells declines at distal sites 6 days after boosting. 215

5.2.2. Sustained distal GC activity may require adjuvant-driven inflammation during rechallenge. 220

5.2.3. Early increase in GC-matured PB-PCs response in the distal site after boosting. 228

5.2.4. Booster immunisation leads to a notable rise in NP_2-specific IgG1 titre by day 6. 234

5.3 Discussion. 239

5.4. Conclusion. 249

Chapter 6. General Discussion and Future Direction. 250

Chapter 7. References.....258

List of figures

Figure 1.1. Overview of the origins of ASC in the immune response through various precursors. 4

Figure 1.2. The four framework regions within the variable domains. 7

Figure 1.3. Overview of antigen-activated B cell participation in the immune response. 10

Figure 1.4. Schematic of BCR microcluster formation. 15

Figure 1.5. B cells are retained in the centre of the primary follicle. 22

Figure 1.6. Schematic participation of Tfh cells in the follicular response. 25

Figure 1.7. Schematic representation of relationship between Bcl6 and Blimp-1 to induce PC. 37

Figure 2.1. Immunofluorescent analysis of GC-matured *S1pr2*^{tdT} Blimp-1^{eGFP} PB-PCs in HALO mice. 62

Figure 2.2. Immunofluorescent analysis of GC-derived IRF4^{+} *S1pr2*^{tdT} Blimp-1^{GFP} PB-PCs in HALO mice. 63

Figure 3.1 Schematic illustrating the principle underlying the generation of PB-PC responses in HALO mice. 69

Figure 3.2. Schematic of the experimental procedure for primary immunisation in HALO mice with SRBCs. 73

Figure 3.3. Gating strategy for the analysis of splenic GC-matured *S1pr2*$^{tdT+}$ Blimp-1^{GFP+} PC in HALO mice. 74

Figure 3.4. Predicted output of GC-matured *S1pr2*$^{tdT+}$Blimp-1^{GFP+} PC in HALO mice. 76

Figure 3.5. Baseline of *S1pr2*^{tdT} and Blimp-1^{GFP} expression in a HALO mouse. 77

Figure 3.6. CD138^{+} PB-PC response analysis in HALO mice following primary SRBCs immunisation. 79

Figure 3.7. Fas^{hi} GC B cell response analysis in HALO mice following primary SRBCs immunisation. 82

Figure 3.8. Blimp-1^{GFP+} PB-PC phenotype observed within CD38^{hi} *S1pr2*$^{tdT+}$ memory B cells. 84

Figure 3.9. CD138^{+} TACI^{+} PB-PC response analysis in HALO mice following primary SRBCs immunisation. 87

Figure 3.10. CD138^{+} TACI^{+} PB-PC fractions in HALO mice following primary SRBCs immunisation. 89

Figure 3.11. Analysis of CD138^{+} TACI^{+} PB-PC fractions in HALO mice following primary SRBCs immunisation. 91

Figure 3.12. The presence of GC-matured *S1pr2*$^{tdT+}$ Blimp-1^{GFP+} PB-PC within CD138^{+} TACI^{+} PB-PC fractions. 93

Figure 3.13. Validation of anti-GFP antibody specificity in single reporter mice. 96

Figure 3.14. GC-matured *S1pr2*$^{tdT+}$ Blimp-1^{GFP+} PB-PCs in a non-treated HALO mouse. 98

Figure 3.15. Migration pattern of EF-derived Blimp-1^{GFP+} PB-PCs and GC-matured *S1pr2*$^{tdT+}$ Blimp-1^{GFP+} PB-PCs into splenic compartments. 100

Figure 3.16. Localisation of GC-matured *S1pr2*$^{tdT+}$ Blimp-1^{GFP+} PB-PCs within GC B cell clusters. 102

Figure 3.17. GC-matured *S1pr2*$^{tdT+}$ Blimp-1^{GFP+} PB-PCs emerging from the GCLZ side without GFP amplification. 103

Figure 3.18. GC-matured *S1pr2*$^{tdT+}$ Blimp-1^{GFP+} PB-PCs emerging from the GCLZ side with GFP amplification. 106

Figure 3.19. Migration pattern of EF-derived and GC-derived CD138^{+} PB-PC. 107

Figure 3.20. EF-derived Blimp-1^{GFP+} PB-PCs inside the GC B cells cluster. 109

Figure 3.21. Example image of IgG1^{+} response in HALO mice. 111

Figure 3.22. Schematic of the experimental procedure for primary immunisation with NP$_{27}$-KLH in HALO mice. 113

Figure 3.23. Analysis of CD138^{+} PB-PC in a later response to NP$_{27}$-KLH. 114

Figure 3.24. Percentage of Fas^{hi} GC B cells at day 10 and day 14 post-NP$_{27}$-KLH immunisation. 116

Figure 3.25. GC-matured *S1pr2*$^{tdT+}$ Blimp-1^{GFP+} PB-PC and GC-derived *S1pr2*$^{tdT+}$ Fas^{hi} B cells on day 10 and day 14 post-NP$_{27}$-KLH immunisation..... 117

Figure 3.26. NP-specific GC-derived Fas^{hi} B220^{hi} B cells response on days 10 and 14 post-NP$_{27}$-KLH immunisation. 118

Figure 3.27. GC B cells remain enriched in the GCDZ after 10 and 14 days post-NP$_{27}$-KLH immunisation. 119

Figure 3.28. Analysis of CD38^{hi} non-GC B cells at days 10 and 14 post-NP$_{27}$-KLH immunisation. 121

Figure 3.29. MFI of membrane-bound IgG1 and IgM antibodies in a later stage of the CD138^{hi} and Fas^{hi} GC B cells response. 123

Figure 3.30. NP$_{2}$-specific antibody response in a later response to NP$_{27}$-KLH immunisation. 124

Figure 3.31. Schematic of the experimental procedure for secondary immunisation in HALO mice. 127

Figure 3.32. Analysis of splenic B cell populations in HALO mice. 129

Figure 3.33. Analysis of the maturation of CD138^{+} PB-PC. 130

Figure 3.34. GC-derived CD138^{+} *S1pr2*$^{tdT+}$ NP^{+} PB-PC. 133

Figure 3.35. Analysis of GC B cell reaction during recall responses to NP_{27}-KLH immunisation. 134

Figure 3.36. Analysis of NP-specific GC-derived B cells during recall responses to NP_{27}-KLH immunisation. 136

Figure 3.37. Analysis of non-GC B cell reaction during recall responses to NP_{27}-KLH immunisation. 137

Figure 3.38. Analysis of GC-matured CD138^{hi} TACI^{hi} *S1pr2*$^{tdT+}$ Blimp-1^{GFP+} PB-PC during recall responses to NP_{27}-KLH immunisation. 139

Figure 3.39. Analysis of CD138^{hi} TACI^{hi} PB-PC fractions during recall responses to NP_{27}-KLH immunisation. 141

Figure 3.40. Number of CD138^{hi} TACI^{hi} PB-PC fractions during recall responses to NP_{27}-KLH immunisation. 142

Figure 3.41. Analysis and number of GC-matured CD138^{hi} TACI^{hi} *S1pr2*$^{tdT+}$ Blimp-1^{GFP+} PB-PC during recall responses to NP_{27}-KLH immunisation. . 143

Figure 3.42. NP_{2}-specific antibody response after recall responses to NP_{27}-KLH immunisation. 145

Figure 3.43. An example image of NP-specific B cells in a recall response on day 5 post-boosting. 147

Figure 3.44. An example image of NP-specific B cells in a recall response on day 8 post-boosting. 148

Figure 3.45. Histology quantification of GC-matured *S1pr2*$^{tdT+}$ Blimp-1^{GFP+} PB-PC in HALO mice in response to SRBCs. 149

Figure 3.46. Identification of GC-matured *S1pr2*$^{tdT+}$ Blimp-1^{GFP+} IRF4^{hi} PB-PCs in a small GC cluster. 151

Figure 3.47. Identification of GC-matured *S1pr2*$^{tdT+}$ Blimp-1^{GFP+} IRF4^{hi} PB-PCs in the bridging channel. 152

Figure 3.48. Identification of GC-matured *S1pr2*$^{tdT+}$ Blimp-1^{GFP+} IRF4^{hi} PB-PCs at the GTI of matured GC. 153

Figure 3.49. GC-resident Tfh cells in HALO mice. 156

Figure 3.50. Typical image of *S1pr2*$^{tdT+}$ and Blimp-1^{GFP+} expression in CD4^{+} T cells. 159

Figure 3.51. Analysis of *S1pr2*^{tdT} and Blimp-1^{GFP} expression in CD4^{+} CD3^{-} T cells in HALO mice. 160

Figure 3.52. Analysis of *S1pr2*^{tdT} and Blimp-1^{GFP} expression in CD3^{+} CD4^{-} T cells in HALO mice. 161

Figure 3.53. Analysis of *S1pr2*^{tdT} and Blimp-1^{GFP} expression in CD3^{+} CD4^{-} and CD4^{+} T cells in HALO mice. 162

Figure 4.1. Schematic overview of the IgMgAID^{Cre} mouse models. 177

Figure 4.2. Schematic of the experimental mouse models and the protocol... 179

Figure 4.3. Analysis of the CD138^{+} PB-PC response. 180

Figure 4.4. Analysis of the NP^{+}-specific CD138^{+} PB-PC response. 182

Figure 4.5. Analysis of the NP^{+}-specific IgG1^{+} CD138^{+} PB-PC response. 183

Figure 4.6. Analysis of IgG1^{+} and IgM^{+} CD138^{+} PB-PC response. 184

Figure 4.7. Analysis of the Fas^{+} GC B cell response. 187

Figure 4.8. Analysis of IgG1$^+$ and IgM$^+$ B220$^+$ Fas$^+$ GC B cell response. 188

Figure 4.9. Analysis of the NP$^+$-specific B220$^+$ GC B cell response. 190

Figure 4.10. Analysis of the NP$^+$-specific IgG1$^+$ GC B cells response. 192

Figure 4.11. Analysis of the GC zones' response. 193

Figure 4.12. Analysis of IgG1$^+$ and IgM$^+$ CD38$^+$ non-GC B cell response. 195

Figure 4.13. Analysis of NP$^+$-specific CD38$^+$ non-GC B cell response. 197

Figure 4.14. Analysis of CD44$^+$ T cell response. 199

Figure 4.15. Analysis of CXCR5$^+$ PD-1$^+$ Tfh cells response. 201

Figure 5.1. Schematic of the experimental procedure for studying recall memory B cell responses. 213

Figure 5.2. Analysis of CD38$^+$ *S1pr2*$^{tdT+}$ memory B cells after recall responses. 216

Figure 5.3. Analysis of NP$^+$-Specific *S1pr2*$^{tdT+}$ CD38$^+$ B cells after recall responses. 219

Figure 5.4. Analysis of Fas$^+$ GC B cells after recall responses. 221

Figure 5.5. Analysis of B220$^+$ *S1pr2*$^{tdT+}$ GC B cells after recall responses. 223

Figure 5.6. Analysis of TACI$^+$ *S1pr2*$^{tdT+}$ GC B cells after recall responses..... 225

Figure 5.7. Analysis of NP$^+$-Specific *S1pr2*$^{tdT+}$ GC B cells after recall responses. 227

Figure 5.8. CD138$^+$ PB-PC after recalling responses..... 229

Figure 5.9. GC-matured *S1pr2*$^{tdT+}$ TACI$^+$ CD138$^+$ PB-PC after recalling responses. 231

Figure 5.10. NP$^+$-specific GC-matured *S1pr2*$^{tdT+}$ CD138$^+$ PB-PC at day 6 after recalling responses. 235

Figure 5.11. Affinity of IgG1 and IgM antibody response after recall responses to NP_{27}-KLH immunisation. 237

List of tables

Table 2.1. Reagents and kits that were used throughout the study. 44

Table 2.2. Materials were used throughout the study. 45

Table 2.3. Antibodies used for ELISA assays. 46

Table 2.4. Antibodies and Reagents Used for Flow Cytometry Analysis. 46

Table 2.5. Antibodies and Reagents Used for Immunofluorescent Staining. 48

Table 2.6. Two-step process for spleen tissue fixation from mice expressing fluorescent reporters..... 58

Table 2.7. Preparation of reagents and buffers used in immunofluorescent staining. 59

Table 2.8. Preparation of reagents and buffers used in immunofluorescent staining. 60

Table 2.9. Preparation of buffers and reagents for the ELISA assay. 64

Table 3.1. Definition of B cell populations in the triple transgenic mice. 70

Table 3.2. Quantification of GC-matured IRF4^{+} *S1pr2*$^{tdT+}$ Blimp-1^{GFP+} PB-PC at GTI. 154

Table 3.3. Summary of the main findings from the HALO mice experiments. . 163

Table 5.1. Description of lymph nodes abbreviations used in this study. 214

Abbreviations

ABF-1	Activated B cell factor 1
ads-AP	Alkaline phosphatase-conjugated antibodies
AID	Activation-induced cytidine deaminase
AIRR-seq	Adaptive Immune Receptor Repertoire sequencing
Alum	Aluminium potassium sulphate
αβ T cells	alpha-beta T cells
APRIL	A proliferation-inducing ligand
ASC	Antibody-secreting cell
BAC	Bacterial artificial chromosome
Bach2	BTB Domain And CNC Homolog 2
BAFF	B cell activating factor
BAFFR	B cell activating factor receptor
Bcl	B cell lymphoma
BCR	B cell receptor
BCMA	B cell maturation antigen
BER	Base excision repair
Blimp-1	B lymphocyte-induced maturation protein-1
BM	Bone marrow
BSA	Bovine serum albumin
C	Complement
CCL	Chemokine ligand
CCR	Chemokine receptor
CD	Cluster of differentiation
CDR	Complementarity-determining region
cDNA	Complementary DNA
CSR	Class switch recombination
CXCL	C-X-C motif chemokine ligand
CXCR	C-X-C motif chemokine receptor
CRCs	CXCL-12-expressing reticular cells
Cre	Cyclization recombinase
CreERT2	Cre protein fused with two components of the estrogen receptor containing a mutated ligand binding domain
D	Diversity
DC	Dendritic cell
dH_2O	Distilled water
DMSO	Dimethyl sulfoxide
DNA	Deoxyribonucleic acid
EBI2	Epstein-Barr virus-induced gene 2
EDTA	Ethylenediaminetetraacetic acid
EF	Extrafollicular
EGFP	Enhanced green fluorescent protein
ELISA	Enzyme-linked immunosorbent assay
FACS	Fluorescence-activated cell sorting

FcR	Fragment crystallizable receptor
FBS-HI	Fetal bovine serum heat inactivated
FDC	Follicular dendritic cell
FITC	Fluorescein isothiocyanate
FMO	Fluorescence minus one.
FO	Follicular
FRC	Follicular reticular cell
γδ T cells	Gamma-delta T cells
GC	Germinal centre
GCDZ	Germinal centre dark zone
GCLZ	Germinal centre light zone
GFP	Green fluorescent protein
GLTs	Germline transcripts
GMI	GCDZ: GC-medulla interface
GTI	GC:T cell zone interface
GTIRC	Fibroblastic reticular cells at the interface between the GC and T cell zone
HALO	High affinity Low affinity
HCl	Hydrochloric acid
i.p.	Intraperitoneal
Ig	Immunoglobulin
IFN-γ	Interferon-gamma
IGH	Immunoglobulin heavy chain
IL	Interleukin
IRES	Internal ribosome entry site
IRF	Interferon regulatory factor
J	Joining
KLH	keyhole limpet hemocyanin
LPS	Lipopolysaccharide
MHC	Major histocompatibility complex
MMR	Mismatch repair
mRNA	Messenger Ribonucleic acid
MZ	Marginal zone
$NaHCO_3$	Sodium hydrogen carbonate and sodium bicarbonate
NaOH	Sodium hydroxide
NP	4-hydroxy-3-nitrophenyl-acetyl
NP-APC	4-hydroxy-3-nitrophenyl-acetyl-allophycocyanin
NP-OSu	4-Hydroxy-3-nitrophenylacetic acid Succinimide Ester.
XBP-1	X-box binding protein 1.
PAMPs	Pathogen-associated molecular patterns.
PAX5	Paired box protein 5
PB	Plasmablast.
PBS	Phosphate-buffered saline.
PC	Plasma cell.
PDL1	Programmed death ligand 1
PFA	Paraformaldehyde.
pNPP	p-Nitrophenyl Phosphate.

PNI	Pronuclear injection.
PRRs	Pattern recognition receptors.
RNA	Ribonucleic acid.
RPMI	Roswell Park memorial institute
S1pr	Sphingosine-1-phosphate receptor
SARS-CoV-2	Severe acute respiratory syndrome coronavirus 2
SHM	Somatic hypermutation
SRBCs	Sheep red blood cells
TACI	Transmembrane activator of and CAML interactor
TCR	T cell receptor
TD	T cell-dependent
tdT	tdTomato
Tfh	Follicular helper T cells
TGF-β	Transforming growth factor-beta
Th	T helper
TI	T cell-independent
TI type I	T cell-independent type I
TI type II	T cell-independent type II
TLR	Toll-like receptor
UNG	Uracil-DNA glycosylase

Chapter 1. Introduction.

1.1. Adaptive immunity.

Adaptive immunity is an orchestrated process initiated by signals from the innate immune system [1]. Innate immune cells, particularly dendritic cells (DCs), sense pathogens through pattern recognition receptors (PRRs), initiating a cascade of responses that shape the nature and strength of the adaptive immunity [2].

DCs are extensively distributed throughout the body—at sites where antigen entry occurs—and play a role in linking the innate and adaptive immune systems. After antigen contact, recognition, and uptake, DCs mature and upregulate major histocompatibility complex (MHC) and costimulatory molecules, enhancing their ability to activate T cells. DCs shift their cytokine profile towards a pro-inflammatory state that supports the activation of both Th and cytotoxic T cells. Moreover, DCs form networks with other immune cells and adapt their responses based on local signals to be potent activators of T cells [3].

Macrophages—which also can function as antigen-presenting cells—present peptide-MHC complexes and can produce complement (C) components, such as C1q and C3. These complement components can contribute to local complement activation and shape the adaptive immune response through their interaction with both B and T cells [4].

Cytokines play a role in modulating the development, differentiation, and activation of immune cell types [5]. For example, T helper (Th)1 cells produce interferon-gamma

(IFN-γ), which activates macrophages to enhance their pathogen-fighting capabilities [4, 6]. Th2 cells produce interleukin (IL)-4 to stimulate B cell activity and boost antibody production [4]. T follicular helper (Tfh) cells secrete cytokines, such as IL-4, IL-6 and IL-21, stimulating B cell activation and differentiation into plasma cells (PCs) [4, 7, 8]. The final balance of cytokine production is essential in modulating immune response, ensuring that they are proportional to the threats encountered.

A subset of lymphocytes shares a common origin with T cells and B cells, but it is characterised by minimal diversity in its antigen receptors [4]. These lymphocytes are innate-like in speed and can contribute to adaptive humoral immunity; examples are natural killer T cells, Gamma-delta (γδ) T cells, and marginal zone (MZ) B cells [4]. Natural killer T cells exhibit reduced T cell receptor (TCR) diversity and narrow antigen specificity, but upon activation, they rapidly secrete large quantities of cytokines, including Th1 and Th2 cytokines [4, 9]. γδT cells are a small fraction of the overall T cell population and recognise unprocessed peptide antigens and some non-peptide antigens presented by CD1 [4, 10]. This contrasts with alpha-beta (αβ) T cells, which primarily recognise processed antigens presented via the MHC molecules [4, 10].

Within the B cell lineage, there are two recognised classes of B cells: B1 and B2. B1 cells are generated from foetal liver progenitors during embryonic development, maintaining themselves by self-renewal in the body cavities and the intestinal lamina propria. B1 cells respond primarily to polysaccharide antigens, producing low-affinity IgM without class switching and long-term memory. They recognise a limited range of antigens. B2 cells are derived from haematopoietic stem cells and continuously produced in the bone marrow (BM). These B2 cells leave the BM as immature

transitional B2 cells and complete their maturation into MZ B cells and follicular (FO) B cells [11-14]. Whether a B cell becomes FO or MZ is determined by the signals it receives through the BCR [13, 14]. MZ B cells are found in the splenic red pulp, making up 5-10% of the mature B cells [15]. While FO B cells are found in the splenic white pulp positioned next to the T cell zone, making up 80-90% of the mature B cells [15]. MZ B cells can influence T cell and DC function through cytokine production, highlighting their importance in bridging innate and adaptive immune responses [12, 16]. MZ B cells can also stimulate Tfh cells within the T cell zone [17]. The dual activation of MZ B cells through BCR and toll-like receptor (TLR) engagement allows them to rapidly produce low-affinity antibodies, bridging the temporal gap until FO B cells have undergone germinal centre (GC) reactions [16]. Antibodies produced by antibody-secreting cells (ASCs), including both plasmablasts (PBs) and plasma cells (PCs), mediate humoral immunity. Figure 1.1 illustrates the precursors that give rise to ASCs, providing both immediate and long-term protection.

B cells possess a set of surface immunoglobulin (Ig) receptors (known as B cell receptors, BCR) [18, 19]. These BCRs, which include IgD, IgM, IgA, IgE, and IgG, differ structurally from each other in their constant region. BCRs enable B cells to recognise antigens that can be freely circulating or more typically be displayed as an immune complex on the surface of antigen-presenting cells, such as macrophages [18, 20]. In mice, IgG is sub-classed into IgG1, IgG2a, IgG2b, IgG2c, and IgG3, while in humans, the sub-classes include IgG1, IgG2, IgG3, and IgG4 [21]. Recent studies using long-read sequencing have revealed that genetic variation within the Ig heavy chain (IGH) locus, including allelic polymorphisms, copy number variation, and structural variation in immunoglobulin gene segments, significantly influences the composition and

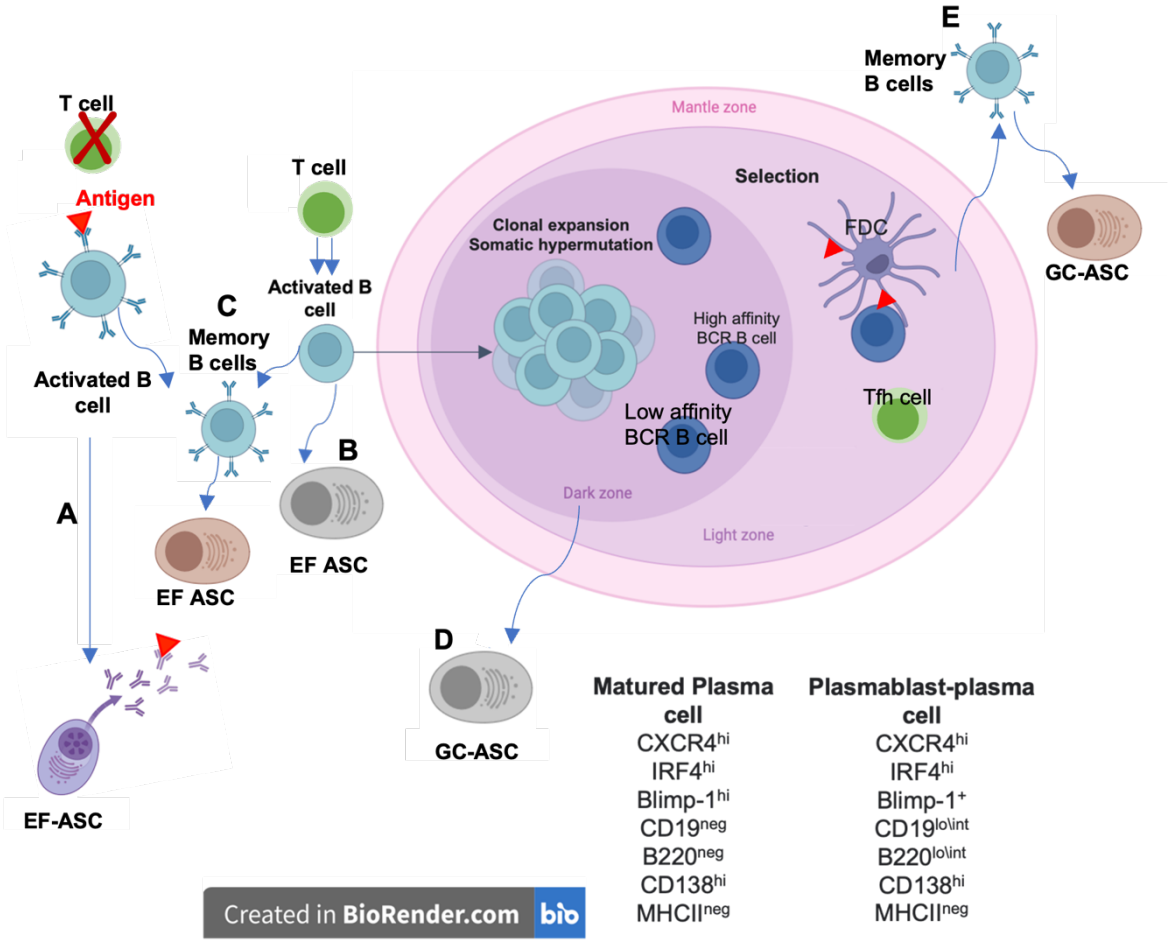


Figure 1.1. Overview of the origins of ASC in the immune response through various precursors.
ASCs can arise from (A) activated B cells independent of T cell help (purple EF ASC), (B) activated B cells dependent on T cell help (grey EF ASC), (C) memory B cells with or without T cell help (brown EF ASC), (D) a selected clone within the GC reaction (grey ASC), and (E) memory B cells that generated from the GC (brown ASC). EF-ASC indicates that ASC generates independently of the GC reaction. GC-ASC indicates that ASC generation was dependent on the GC reaction.

diversity of the antibody repertoire, shaping an individual's outcome of adaptive immune response. These genetic differences may help explain why some individuals respond better or worse to infection, vaccination, or autoimmune triggers. Therefore, the authors proposed that personal IGH genetic variation should be considered when

studying immune responses, vaccines, and antibody-based therapies [22]. Evidence from COVID-19 research further supports this concept, where individuals exhibit substantial variability in their humoral responses to SARS-CoV-2 infection [23]. Studies showed that patients differed in their ability to generate neutralising antibodies, antibody affinity, and clonal antibody expansion, despite exposure to the same virus. Some individuals developed potent neutralising antibody responses associated with effective viral clearance, whereas others produced weaker or dysregulated antibody responses linked to severe disease and immunopathology. These differences have been associated with variation in immunoglobulin gene usage and antibody repertoire diversity, supporting the idea that host genetic variation within the IGH locus can influence the quality and effectiveness of adaptive immune responses [23].

In summary, adaptive immunity provides a highly specific response to diverse pathogens over time. Understanding these processes is essential for advancements in immunotherapy, vaccine development, and the treatment of immune-related diseases.

1.2. Participation of B cells in an immune response.

B cells participate in the immune response through a series of coordinated steps, beginning with the generation of a diverse antigen receptor repertoire. This diversity is established during development in the BM by V(D)J recombination – a process that occurs in the variable domain of Ig [20, 24]. This mechanism establishes the initial antigen-binding site of the Ig by recombining variable (V), diversity (D) and joining (J) gene segments. The recombination process is especially crucial for shaping the third

complementarity-determining region 3 (CDR3), which constitutes a central component of the antigen-binding site and contributes to determining antigen specificity. Additionally, the variable domain comprises four framework regions, which are relatively constant sequences alternating with the three CDRs (Figure 1.2). Somatic hypermutation (SHM) is a critical mechanism used by B cells to enhance their affinity for antigen. The process primarily targets the V segments of immunoglobulin genes, particularly within the CDR1 and CDR2, and sometimes in CDR3, to improve the affinity of antigen binding. Downstream of the V(D)J segments are the constant regions, which serve as the targets for class switch recombination (CSR). Both CSR and SHM are hallmark processes that characterise the participation of B cells in the adaptive immune response. CSR is a process that allows B cells to switch from expressing IgM and IgD to another Ig class (as described in Section 1.1) and occurs when activated B cells have received T cell help [20, 25, 26]. This process is regulated by the transcription of germline transcripts (GLTs), which precede isotype switching [18, 25, 26].

B cells participate in humoral immunity through a multifaceted approach. The antibodies produced can effectively neutralise and crosslink pathogens, they can opsonise them for enhanced phagocytosis, and activate the complement system [18, 27, 28]. The affinity and isotype of an antibody are key aspects in combating infections. Research on Neisseria meningitidis illustrates that effective protection against nasal colonisation involves not only the presence of antibody-mediated opsonisation but also the functionality of B cells capable of undergoing SHM and class switching [27]. The research further demonstrated that the distribution of ASCs is shaped by the route of immunisation. Mucosal immunisation led to the generation of Neisseria meningitidis-

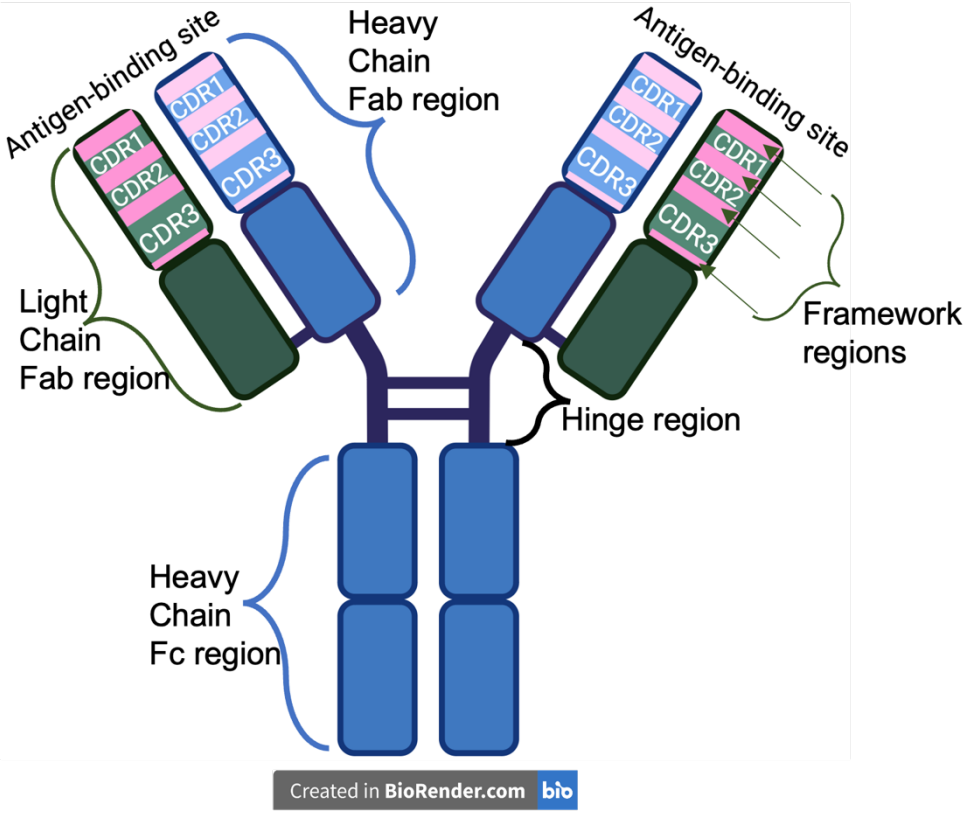


Figure 1.2. The four framework regions within the variable domains.
The four framework regions (shown as pink loops) alternate with the three CDRs (green loops in the light chains and blue loops in the heavy chains) within the antibody variable domain. They provide structural stability and position the CDR loops in the correct orientation.

specific IgA in the nasal-associated lymphoid tissue, whereas systemic immunisation primarily induced IgG production in the BM. Interestingly, the study also showed that complement was not required for protection against colonisation, highlighting the importance of antibody-driven phagocytosis and neutrophil recruitment at mucosal sites [27]. Another study highlights the critical role of spike-specific antibodies in shaping immune responses to COVID-19 [28]. Spike-neutralising antibodies contribute to mitigating viral entry, while spike-opsonising antibodies enhance phagocytosis by

monocytes. Notably, the study reveals a dose-dependent effect, where the concentration of these antibodies can either promote or impair phagocytosis [28].

In contrast, naive B cells co-express IgM and IgD BCRs, both of which recognise the same antigen. However, the IgM BCR is more sensitive to regulation by endogenous (self) antigen than is IgD [29]. IgD contributes to immune tolerance by remaining expressed in autoreactive B cells, while IgM is often downregulated to prevent inappropriate activation and autoimmunity. Following a CSR, IgM and IgD expression are lost because their constant region genes are deleted. Transient detection of IgM/IgD may still occur due to the persistence of pre-existing mRNA or protein, but actual co-expression with a switched isotype, such as IgG1, does not occur. It has been demonstrated that IgD-only B cells can enter the GC and undergo mutation and selection. However, these IgD-only B cells do not effectively generate $IgG1^+$ PCs, particularly the short-lived PCs that arise early in the T cell-dependent (TD) immune response [29]. Moreover, recent studies have identified specific B cell subtypes with an IgM^- IgD^+ phenotype involved in mucosal immunity—mucosal-associated lymphoid tissues— and their generation involves TD and T cell-independent (TI) [25]. Therefore, understanding the diverse responses of B cells is crucial for designing tailored immunisation strategies and therapeutic interventions that promote the desired type of immune response, rather than applying a one-size-fits-all approach.

SHM introduces DNA point mutations within the genes coding for the variable regions of Ig genes, allowing B cells to enhance their antibody affinity to generate high-affinity antibodies [20, 24, 25, 30]. In addition to the introduction of point mutations, SHM can also introduce rare insertions and deletions into the variable regions of Ig genes,

particularly in the CDRs [31, 32]. While CDR3 length is primarily established during V(D)J recombination, SHM-induced insertions and deletions may further modify and extend this region. Elongated CDR3 regions are a structural feature commonly seen in broadly neutralising and autoreactive antibodies, contributing to enhanced antigen binding and diversifying the antibody repertoire [32].

Activation-induced cytidine deaminase (AID) is responsible for initiating CSR and SHM for generating Ig diversity in activated B cells [20, 24, 25, 32, 33]. AID targets the DNA sequences encoding the variable heavy and light chains of Ig. AID specifically targets the cytosine residue in DNA and converts it into uracil (this uracil is called deoxyuridine, dU) through a process known as deamination. This process creates a U:G mismatch, which is recognised and processed by DNA repair pathways—base excision repair (BER) pathway and mismatch repair (MMR)—leading to point mutations in SHM in the variable heavy and light chains (V regions) and double-strand breaks and recombination in CSR in the switch regions (S regions). The formation of dU by AID is a shared initiating step in both SHM and CSR. However, whether a B cell undergoes SHM and CSR depends on the genomic region targeted (V regions or S regions) and the DNA repair pathways involved. The BER pathway and the MMR pathway recognise the U:G mismatches, but are activated in different circumstances and serve distinct roles in maintaining genomic integrity. The BER pathway excises uracil by recruiting enzymes such as uracil-DNA glycosylase (UNG), which leaves behind an abasic site (apurinic/apyrimidinic sites). After excision of an abasic site, high-fidelity polymerases are used to restore the DNA sequence (no mutation), error-prone polymerases (point mutation to SHM), or a DNA strand break in CSR. On the other hand, the MMR pathway excises the U:G mismatch and extends to some nearby A:T base pairs by

recruiting enzymes such as MSH2 and MSH6. After excision, high-fidelity polymerases are used to restore the DNA sequence, or error-prone polymerases to introduce mutations during SHM or DNA recombination required for CSR.

Participation of B cells in an immune response paves the way for understanding how immunisation shapes B cell response through extrafollicular (EF) and FO pathways (Figure 1.3), discussed in greater detail in the following sections.

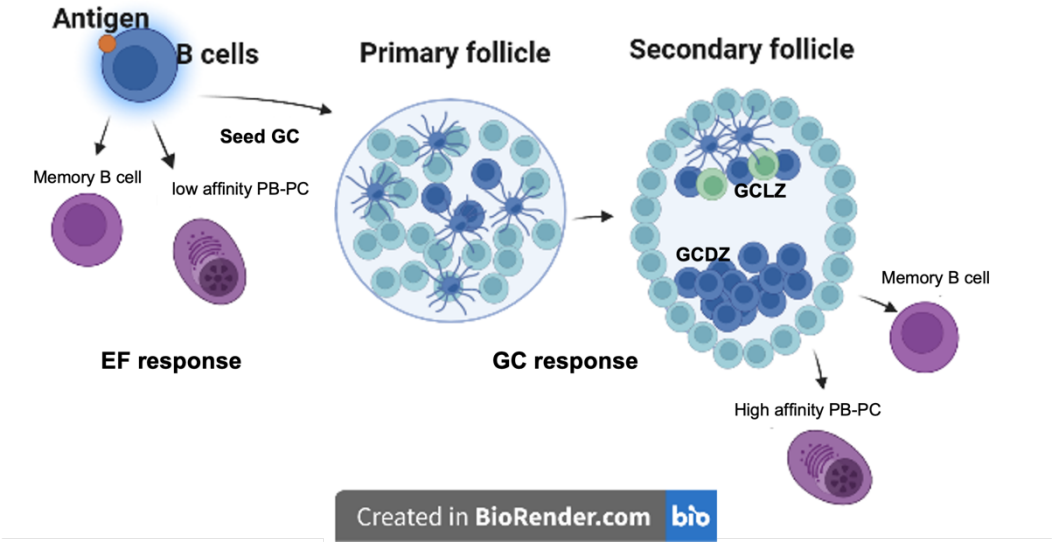


Figure 1.3. Overview of antigen-activated B cell participation in the immune response.
Activated B cells (for example, after binding an antigen, shown as an orange molecule) can develop into either EF or GC responses. The former is a GC-independent response. The latter is GC-dependent, in which activated B cells seed the primary follicle and rapidly expand, pushing naive B cells (shown as light blue cells) towards the edge of the primary follicle. The process results in the formation of a secondary follicle containing two zones: DZ B cells and LZ B cells.

1.2.1. Immunisation-derived B cell response.

B cells can respond to TD and TI antigens [16, 18, 34, 35]. TD antigens are proteins that require processing and presentation on MHC class II molecules, which lead to co-stimulatory signals from T helper cells. These can be contact-dependent, e.g., CD40 ligation, or soluble, e.g., T cell cytokines IL-4 and IL-21. In contrast, TI antigens are classified into two types: TI type I antigens, which function as mitogenic stimuli that activate B cells through TLRs acting as innate stimuli or adjuvants, enhancing weak BCR signals. TI type II antigens are polysaccharides that directly engage the B cell receptor and lead to strong BCR signalling through the generation of repetitive BCR clusters and can also lead to TI B cell activation. In the TD response, antibody isotype diversification is strongly shaped and capable of generating memory B cells [25]. Whilst TI responses are dominated by IgM^+ PB, class-switching in TI type II responses rises rapidly, with IgG3 becoming prevalent alongside exponential EF growth by day 7 [36]. TI type I memory responses show higher levels of IgG subclasses (IgG1, IgG2, IgG2a, IgG2b, IgG2c) [37]. TI type II antigens can also generate memory B cells that are class-switched, particularly to IgG1 and IgG3 [35].

TLRs with BCR can enhance or modify the signals received through the BCR to influence their activation and differentiation pathways, determining whether they will become PCs, memory B cells, or GC B cells [18, 38]. Signalling through PRRs, particularly TLRs, supports TI type I B cell responses by activating downstream pathways such as MyD88-dependent NF-κB and MAPK signalling [39], which promote B cell proliferation, survival, and AID expression that is required for antibody production and class-switch recombination [40]. TLR engagement by pathogen-associated

molecular patterns (PAMPs) activates intercellular signalling pathways, leading to the production of inflammatory cytokines and survival factors such as a B cell activating factor (BAFF) and proliferation-inducing ligand (APRIL). These factors promote B cell survival, proliferation, class-switch recombination, and differentiation into ASCs [41, 42]. Other PRRs, including NOD-like receptors and C-type lectin receptors, may also contribute to innate sensing and cytokine production that indirectly promotes B cell responses [18, 38, 39]. Consistent with this, experimental studies using LPS, a TLR4 ligand, showed that simultaneous activation of BCR and TLR pathways enhances switching to IgG1 [43, 44], indicating that innate receptor signalling can shape the magnitude and quality of TI B cell responses and influence subsequent antibody isotype outcomes.

Antigen valency plays a role in influencing the type of immune response, with multivalent antigens inducing stronger TD EF responses compared to low-valency antigens [45]. A recent review emphasised the variation of the B cell response to the antigen format [46]. Membrane-bound antigens stimulate a stronger response than soluble antigens. Anergic B cells demonstrate differential responses based on the type of antigen: excessive signalling from membrane-bound antigens results in clonal deletion, whereas soluble self-antigens lead to anergy [46]. A study suggests that IgD plays a significant role in responding to multivalent antigens and membrane-bound antigens [47]. While another study suggests that IgD is less suited for robust responses to multivalent and membrane-bound antigens [29].

In addition, different antigens are associated with specific isotype class switches, implicating the involvement of T helper cell subsets in guiding this process. For

instance, responses to certain antigens, such as aluminium (alum)-precipitated protein, typically lead to production of IgG1 and IgE isotype switch transcripts, reflecting Th2 activity. Conversely, responses to killed *Bordetella (B.) pertussis* result in the production of IgG2 switch transcript, indicative of Th1 activity, likely due to the production of pro-inflammatory cytokines such as IL-12 that promote Th1 differentiation and IFN-γ production [48]. These distinct switching patterns indicate the importance of T cell cytokines in determining the isotype of Ig produced during immune responses, where Th1-associated cytokines, such as IFN-γ, favour IgG2a switching, whereas Th2-associated cytokines, such as IL-4, promote IgG1 and IgE production [48]. Four T cell-derived cytokines have been identified that can regulate Ig class and IgG subclass production: 1) IL-4 promotes IgE and IgG1 responses, 2) IFN-γ enhances IgG2a and IgG3 responses, 3) transforming growth factor beta (TGF-β) induces IgA and IgG2b responses, and 4) IL-5 selectively stimulates IgA response [49].

Sheep red blood cells (SRBCs) are commonly used in GC studies due to their ability to induce strong immune responses [50, 51], inducing TD and TI type II responses. A previous study showed that SRBCs can behave both as TD and TI type II antigens, depending on how they are prepared and presented to the immune system [52]. Whole, intact SRBCs require T cell help to induce an antibody response in vitro. When SRBCs were lysed, they behaved as TI type II antigens due to the repetitive nature of the epitopes.

B cell responses following immunisation or infection can be broadly classified into two main pathways: a canonical pathway, characterised by GC formation, and a non-canonical pathway, which occurs at EF sites [53]. Following immunisation with

haptenated antigens, the canonical response typically begins with a rapid EF phase that produces non-mutated plasma cells rapidly, while GC formation develops in parallel [53]. The relative contribution and kinetics of these pathways can differ during natural infections. For instance, *B. burgdorferi* [54, 55] and *Salmonella enterica* [56] may dominantly suppress GC formation, leading to a sustained EF response without the corresponding generation of high-affinity memory B cells and long-lived PCs [53]. Overall, there is an interplay between antigen type, T cell involvement, and the B cell differentiation into the EF response or GC formation. For example, protein antigens such as NP-KLH require T cell help, where antigen-specific B cells present peptide on MHC class II molecules to Tfh cells. This interaction provides co-stimulatory signals, including CD40L and cytokines such as IL-4 and IL-21, which direct B cell fate whether the B cell enters the GC or the EF pathway [57].

The formation of BCR microclusters during antigen interaction enhances B cell signalling, even in response to low concentrations of antigens (Figure 1.4). This phenomenon is essential for initiating robust B cell activation, promoting downstream signalling pathways, organising the immune synapse (cell-cell contact formed between a B cell and an antigen-presenting cell or a T helper cell), and optimising signal transduction [46]. In addition, mechanosensitive ion channels embedded within the cell membrane, such as Piezo1 and TRPV2, are integral to the B cell membrane, where they regulate signalling strength by facilitating BCR microclustering and the structural organisation of the immunological synapse [58, 59]. The initial affinity of the BCR for an antigen is a crucial factor in determining B cell interactions and dictates whether B cells differentiate into an EF or GC response [38]. In vitro, high-affinity BCR

engagement can induce programmed death ligand 1 (PDL1) expression on B cells [60], which has been shown to inhibit the differentiation of CD4 T cells into Tfh cells.

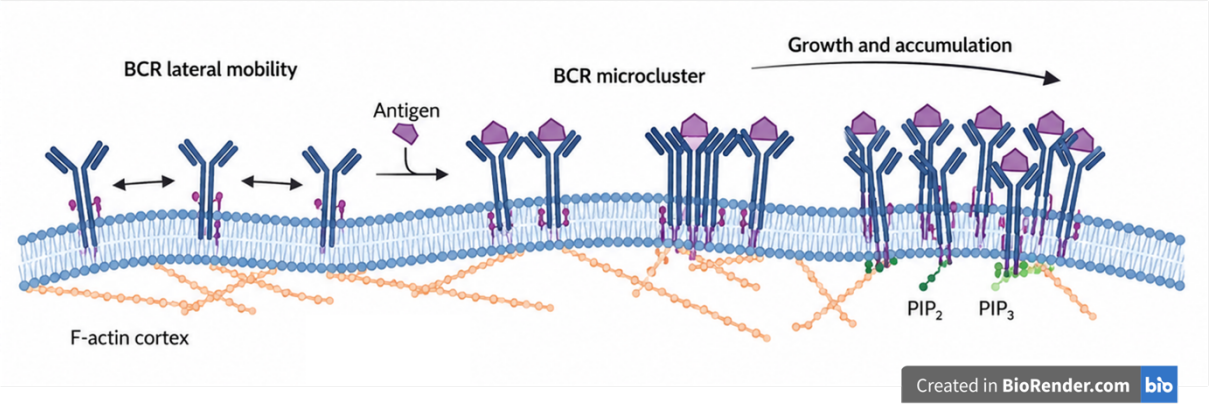


Figure 1.4. Schematic of BCR microcluster formation.

The schematic illustrates the lateral mobility of BCRs within the plasma membrane and their clustering following antigen engagement. In resting B cells, BCR movement is regulated by the underlying F-actin cortex. Upon antigen binding, BCRs aggregate to form microclusters that progressively grow and accumulate at the cell surface, promoting signal amplification and downstream B cell activation. The diagram also highlights the membrane-associated signalling lipids PIP_2 and PIP_3, which contribute to intercellular signalling during microcluster formation.

However, this effect was not observed in vivo [60], where low-affinity B cells instead promoted Tfh differentiation through inducible T cell co-stimulator ligand (ICOSL) signalling. High-affinity BCR engagement can also upregulate chemokine receptor (CCR) 7 to retain the B cells near the T cell zone and repress B cell lymphoma 6 (Bcl6) by promoting interferon regulatory factor 4 (IRF4) expression. These mechanisms promote progression into the EF response. Conversely, low-affinity BCRs promote Tfh differentiation through stronger ligation of ICOSL to ICOS, downregulate CCR7, upregulate Bcl6, and activate lower levels of IRF4 [60]. These mechanisms promote progression into the GC reaction.

Chemokine receptors and their ligands facilitate the antigen-induced migration of B cells toward the T cell zone, committing them to the EF pathway. B cells can be primed through BCR engagement and/or by acquiring antigen from DCIR2^{+} DCs, a murine MZ -associated CD8α-conventional DC subset that localises within splenic bridging channels, leading to upregulation of CCR7 and migration toward the T-B border [61]. At this interface, Bcl6^{+} CD4^{+} T cells (Th or pre-Tfh cells) provide additional activation signals to B cells—these T cells have been primed by the three signals from DCs [48, 62]. The importance of this interaction is supported by the observation that deletion of Bcl6 in T cells significantly reduces the EF PBs response. Following this priming, activated B cells migrate to the splenic red pulp and the lymph node medullary cord [33, 48, 62], where they can differentiate into plasmablast-plasma cells (PB-PCs) or GC B cells. Their migration is partly directed by C-X-C motif chemokine receptor (CXCR) 5 expression, which responds to C-X-C motif chemokine ligand (CXCL) 13 produced in these areas. Moreover, high expression of Epstein-Barr virus-induced gene 2 (EBI2) on naive or recently activated B cells promotes their localisation to the splenic MZ, bridging channels, and interfollicular regions—key sites that support early PB-PC responses [33]. As these B cells commit to the EF PB-PC fate, they upregulate CXCR4 and downregulate CXCR5, directing their migration toward effector sites such as splenic red pulp or lymph node medullary cords, where CD11c^{hi} DCs reside to extend activated B cell survival and terminal differentiation [33, 48, 63].

1.2.2. Extrafollicular response.

EF sites refer to regions outside follicles, where the initial rapid pathway of B cell differentiation into antibody-secreting cells occurs after TD or TI antigens [48]. EF

response predominantly occurs in the medullary cords of lymph nodes and red pulp regions of the spleen [48]. The EF responses generate IgM and IgG antibodies that can form immune complexes that may regulate GC responses through the inhibitory IgG Fc receptor FcγRIIB [45]. During the EF response, memory B cells are formed before GC development, with some memory B cells re-entering the GC after antigen re-stimulation [64].

Both naive and memory B cells have the potential to be recruited for EF responses [48]. There is a further difference in the roles of nonrecirculating and recirculating naive B cells in the EF antibody response [48]. Nonrecirculating naive B cells (identified as MZ B cells) prefer to recruit into an EF response and provide rapid IgM and IgG production in response to TI type II. The MZ B cells also serve as the route for B cells to exit the follicle, depending on the expression of S1pr1 [65].

In contrast, recirculating B cells with few MZ B cells show dual potential by contributing to both EF and FO responses to TD antigens. Unlike naive B cells, memory B cells exhibit enhanced sensitivity for the commitment to EF growth as plasmablasts (PBs). Importantly, despite lacking continuous contact with T cells, PBs require interaction with $CD11^{high}$ stromal cells to achieve full differentiation into ASCs [48].

EF reactions can lead to antibody production without the extensive SHM; however, SHM can occur extensively at the EF site under certain conditions. In lupus-prone mice, researchers found that B cells can undergo SHM at the T cell zone-red pulp border in the spleen [66, 67]. Monocytoid B cells localise to EF foci and participate in EF responses, especially in the perisinusoidal regions of lymph nodes during infection

[68]. Immunisation with NP-Ficoll (TI antigen) can induce low-level SHM in EF PBs compared to TD antigens [34].

CSR also occurs in EF response. Marshal et al. demonstrated that B blasts upregulate $CD138^+$ and B-lymphocyte-induced maturation protein 1 ($Blimp\text{-}1^+$) and no longer express AID as they differentiate into PB, suggesting CSR is lost upon differentiation [69]. Additionally, CSR was dependent on antigen dose, where a high dose of NP-Ficoll induces both PB and CSR to IgG3, and a low dose induces PB without CSR [69]. Toellner et al. demonstrated that in B blasts CSR to IgG1 is induced and underway within 12 hours, mainly in the outer T zone in response to SRBC or NP-CGG (TD antigen) [26]. Both studies show that CSR occurs early—in B cell blasts—after antigen stimulation and peaks within 3 days. Marshall et al. emphasise that CSR is lost once B cell blasts become $CD138^+$, while Toellner et al. show that some CSR continues at lower levels in GCs over time. A recent study by Liu et al., supports the earlier findings from the studies mentioned above. They expanded that CSR can be triggered by BCR engagement, CD40-CD40L interaction, and TLR signalling [25]. Notably, both switched and non-switched PCs were observed throughout the response, indicating that CSR does not affect all activated B cells equally [26].

1.2.3. Follicular response.

The FO response is characterised by the rapid clonal expansion and selection of B cells within the GC microenvironment. The decision for activated B cells—whether to follow the EF pathway or FO pathway—occurs early after antigen stimulation. For instance, the EF response is signalled by the rapid upregulation of Blimp-1 and abortive

GC development following TI type II antigen immunisation. In contrast, TD antigens, such as NP-conjugated proteins, can induce GC formation, which is marked by the upregulation of Bcl6 and sphingosine-1-phosphate receptor 2 (S1pr2), alongside the downregulation of EBI2. Therefore, the antigenic stimuli affect B cell fate early in the immune response [18, 34, 48, 70].

1.2.3.1. Formation and maturation of germinal centres.

Mature GCs are secondary follicles surrounded by primary follicular mantle B cells. GCs can be formed by TI and TD antigens. GCs that are induced by TI antigens have normal histological characteristics—GC zones express Bcl6 and bind peanut agglutinin; however, such GCs were thought to be functionally limited due to collapsing rapidly by apoptosis shortly after forming GC zones [34]. However, Lui et al., found that the functional limitation of TI-mediated GCs was due to producing memory B cells and long-lived PCs rather than collapsing by apoptosis [71]. Both studies found that TD-mediated GCs led to longer-lasting GCs with more extensive SHM.

Mature GCs are compartmentalised into two zones based on their histological characteristics: the dark zone (GCDZ) and the light zone (GCLZ). The GCDZ, located proximal to the T cell zone, is populated by actively proliferating B cells, called centroblasts, which exhibit a $CXCR4^{hi}$ $CD83^{lo}$ $CD86^{lo}$ phenotype. The GCLZ, located at the distal pole of the T cell zone, is populated by B cells called centrocytes, which express a $CXCR4^{lo}$ $CD83^{hi}$ $CD86^{hi}$ phenotype [18, 33, 63, 72, 73].

The spatial organisation of GC B cells is regulated by the chemokine gradients, particularly CXCL12 and CXCL13, produced by stromal cells within each zone. CXCL-

12-expressing reticular cells (CRCs) in the GCDZ and CXCL-13-expressing FDCs in the GCLZ establish these gradients. The resulting stromal cell chemokines enable CXCR4^{hi} centroblasts to be retained in the GCDZ and CXCR5^{hi} centrocytes to be retained in the GCLZ. Moreover, FDCs and CRCs play a role in the bidirectional migration of BCs between GC zones [63, 73, 74].

Functionally, the GCDZ is the primary site of rapid B cell proliferation and changes in the affinity during SHM, whereas the GCLZ acts as the secondary site for the selection of B cell clones through interaction with FDCs and Tfh cells. Bidirectional migration between these zones is essential for driving the iterative rounds of SHM and selection, ultimately enhancing the antigen affinity of GC B cells [18, 33, 63, 72-75].

FDCs are specialised stromal cells in the GCLZ that form extensive networks for structuring and regulating the GC response. Beyond providing signals that direct B cell movement, FDCs can capture the drained antigen and present it in the form of immune complexes that have a prolonged retention on their surfaces through receptors such as CD35, CD21, and FcγRII [63, 73, 74]. By sampling FDC-bound antigen, GC B cells test their newly mutated BCRs and present processed antigens to Tfh cells for affinity-based positive selection. Notably, pre-existing high-affinity antibodies can form immune complexes that mask antigens on FDCs, thereby limiting antigen availability within the GC. Earlier work by Song et al. (1998) proposed that immune complexes containing IgG antibodies on FDCs provide a feedback mechanism that limits antigen availability and regulates SHM [76]. This concept was later confirmed by Zhang and colleagues (2013), who demonstrated *in vivo* that high-affinity antibodies mask antigens on FDCs, thereby increasing selection pressure and promoting the survival

and output of higher-affinity B cell clones while reducing overall GC size [77]. Therefore, the interplay between FDCs and B cells influences the fate of cells within the GC. The next section delineates the participation of Tfh in follicular response due to the role of Tfh cells in the dynamics of GC B cell selection.

Following immune activation, fibroblastic reticular cells (FRCs) in the T cell zone secrete the chemokine ligands (CCL) 19, CCL21, and CXCL12, which help localise DCs, T cells, and B cells, respectively, through their expression of CCR7 [63]. Additionally, FRCs secrete BAFF to maintain primary follicle structure [63]. Recruitment of activated B cells at the T-B border is attributed to upregulation of EBI2 and CXCR5. The downregulation of EBI2, CCR7, and Blimp-1 and the upregulation of S1pr2 (Figure 1.4) alongside the maintenance of CXCR5 on B cells cause their accumulation in the centre of the follicle to form GC B cells [18, 33, 63]. The organisation of B cell responses to form the GC is regulated by Bcl6. Without Bcl6, B cells participate in the EF response and do not generate the GC response [48, 63, 78].

GCs begin to emerge between 4 and 8 days post-immunisation, typically initiated by a small population of approximately 50-200 B cells that enter a follicle and activate the response [79]. These founder B cells give rise to the majority of clonal progeny within the GC, which tends to be dominated by their descendants [79, 80]. Additional B cells activated at later stages of the immune response retain the capacity to enter ongoing GCs and participate in the reaction [73]. Moreover, naive B cells can enter the GCLZ, even though they are not initially part of the clonal GC reaction, carrying antigen to follicular dendritic cells (FDCs) through BCR-independent antigen transport, a process supported by BAFF-BAFFR signalling [73]. The interplay among antigen availability,

Tfh cell numbers, and founder B cell affinity collectively determines the maintenance of clonal diversity in GCs [80].

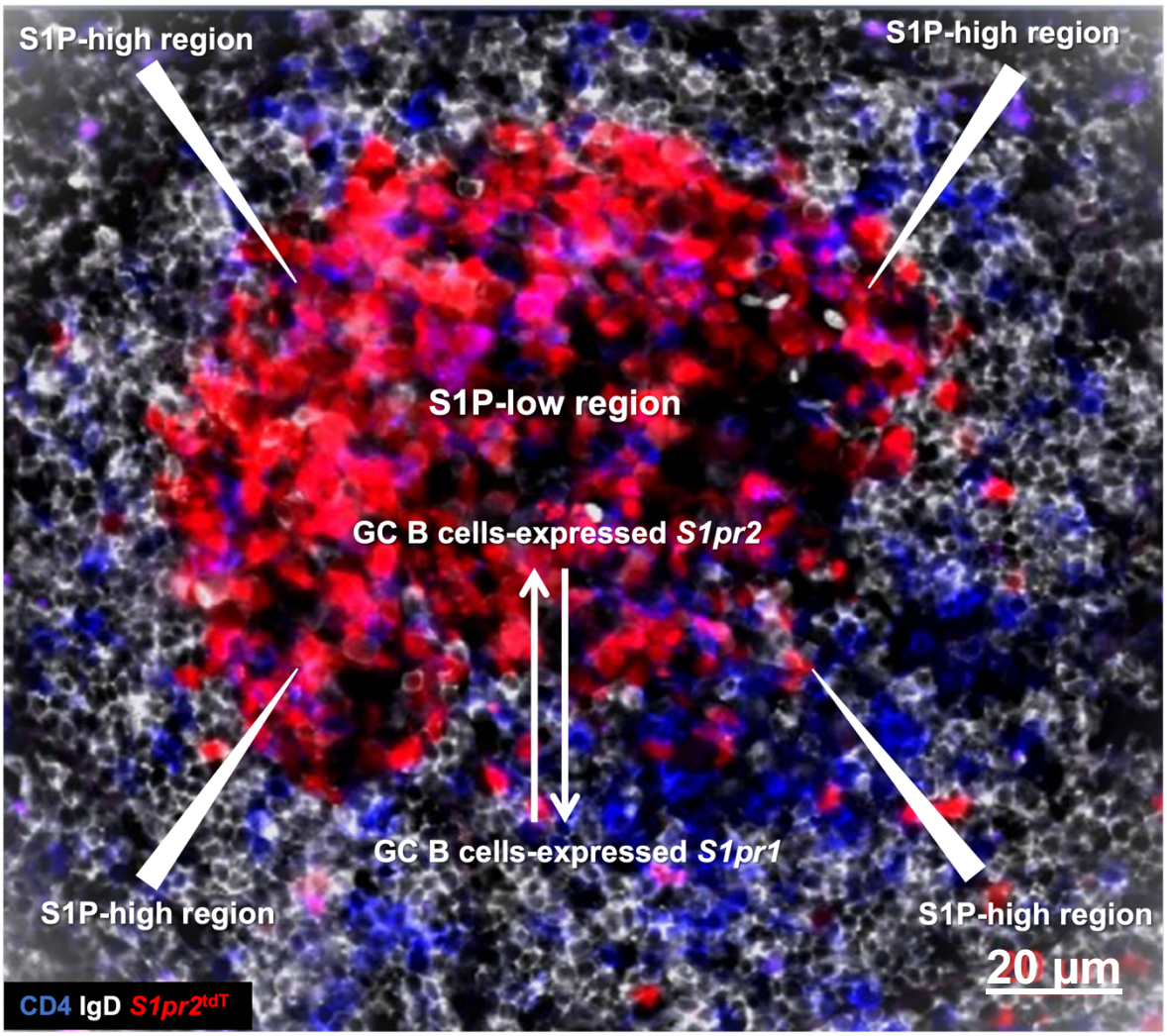


Figure 1.5. B cells are retained in the centre of the primary follicle.
Upregulation of *S1pr2* promotes B cell migration toward the S1P-low region in the centre of the primary follicle, while upregulation of *S1pr1* directs B cell migration toward the S1P-high region outside the primary follicle. This image was captured from the spleen of an experimental study mouse immunised with SRBCs, 6 days post-immunisation, following 48 hours of tamoxifen treatment before harvesting. The section was acquired at 20 µm using a Zeiss AxioScan.Z1 Slide Scanner and processed with Zen v3.1 (Blue Edition).

The quantity of FDC-bound antigens is critical, as it influences B cell competition and selection dynamics. In a theoretical study, three scenarios of antigen availability were

evaluated: low (100 units), intermediate (3000 units), and high (5000 units) antigen loaded on FDC [80]. The findings show that GCs with a low initial amount of antigen experience early collapse, causing a significant drop in B cell diversity.

Conversely, higher antigen levels enhance the longevity and size of GCs, allowing for sustained clonal diversity and a broader range of B cell responses [80]. The initial affinity of founder B cell clones entering the GC influences their diversity and output. High-affinity founders support broader clonal diversity and efficient affinity maturation.

In contrast, GCs seeded by low-affinity B cells undergo early loss of weaker clones, reduced diversity, and delayed or weaker high-affinity antibody responses. Furthermore, Tfh cells are essential for supporting B cell selection in the GC. Fewer Tfh cells reduce both GC size and affinity maturation, while a higher number supports diversity and optimal antibody responses [80].

AID is crucial for the maturation and refinement of B cell responses, and its absence has been shown to lead to significant abnormalities in GC behaviour [81]. Further, apoptosis is a highly regulated process that influences GC size and selection mechanisms. Survival of GC B cells is dependent on antigen-BCR signalling together with CD40-CD40L-mediated T cell help. This antigen-driven rescue from apoptosis drives the selection of higher-affinity B cells [82]. AID- or caspase 8-deficient mouse models show the abnormal accumulation of B cells within the GCs, indicating disruption of the balance of B cell proliferation and apoptosis [81, 83]. Apoptosis within GCs can occur via Fas receptors that activate caspase 8, and defects in either AID or apoptosis signalling can disrupt normal GC dynamics [81, 83]. Deletion of either AID or caspase 8 in GC B cells led to the accumulation of $CXCR4^{lo}$ centrocytes and failed

to mature efficiently into PCs [83]. By day 18 post-immunisation, the loss in affinity maturation in caspase 8-deficient B cells was less pronounced, suggesting some compensatory mechanisms may come into play as the immune response progresses [83].

1.2.3.2. Participation of T follicular helper cells in the follicular response.

Tfh cells are required for both EF response and GC formation [84, 85]. The behaviour and fate of Tfh cells are influenced by Bcl6 expression [73, 86, 87]. Bcl6 expression begins during the interaction of naive $CD4^+$ T cells with DC-bound antigen in the T cell zone (**Figure 1.6**) [88]. During this T:DC interaction, TCR:peptide-MHC class II and CD28:CD80/86 ligations are two signals required for naive $CD4^+$ T cells, alongside multiple cytokines that determine naive $CD4^+$ T cells' fate [63]. Subsequently, the interplay between $CD4^+$ T cells and activated B cells at the T-B border is critical for the differentiation of Tfh cells [60]. Strong BCR signalling negatively impacts Tfh cell differentiation in vitro, linked to reduced expression of the co-stimulatory molecule ICOS-L in activated B cells [60, 89]. In vivo immunisation approach revealed a diminished Tfh cell development when high-affinity antigens were administered compared to low-affinity options [60, 89]. To participate in the GC response, $Bcl6^+$ $CXCR5^+$ $IL\text{-}21^+$ Tfh cells need to undergo a selection process based on how well T cell receptors recognise peptide-MHC class II complexes that are presented by $Bcl6^+$ $CXCR5^+$ GC B cells at the T-B border [75, 90, 91]. $Bcl6^+$ $CXCR5^+$ $IL\text{-}21^+$ Tfh cells that bind with sufficient affinity to the antigen presented by $Bcl6^+$ $CXCR5^+$ GC B cells are preferentially selected to proliferate and continue participating in the GC and develop into IL-4 Tfh cells [75, 91, 92].

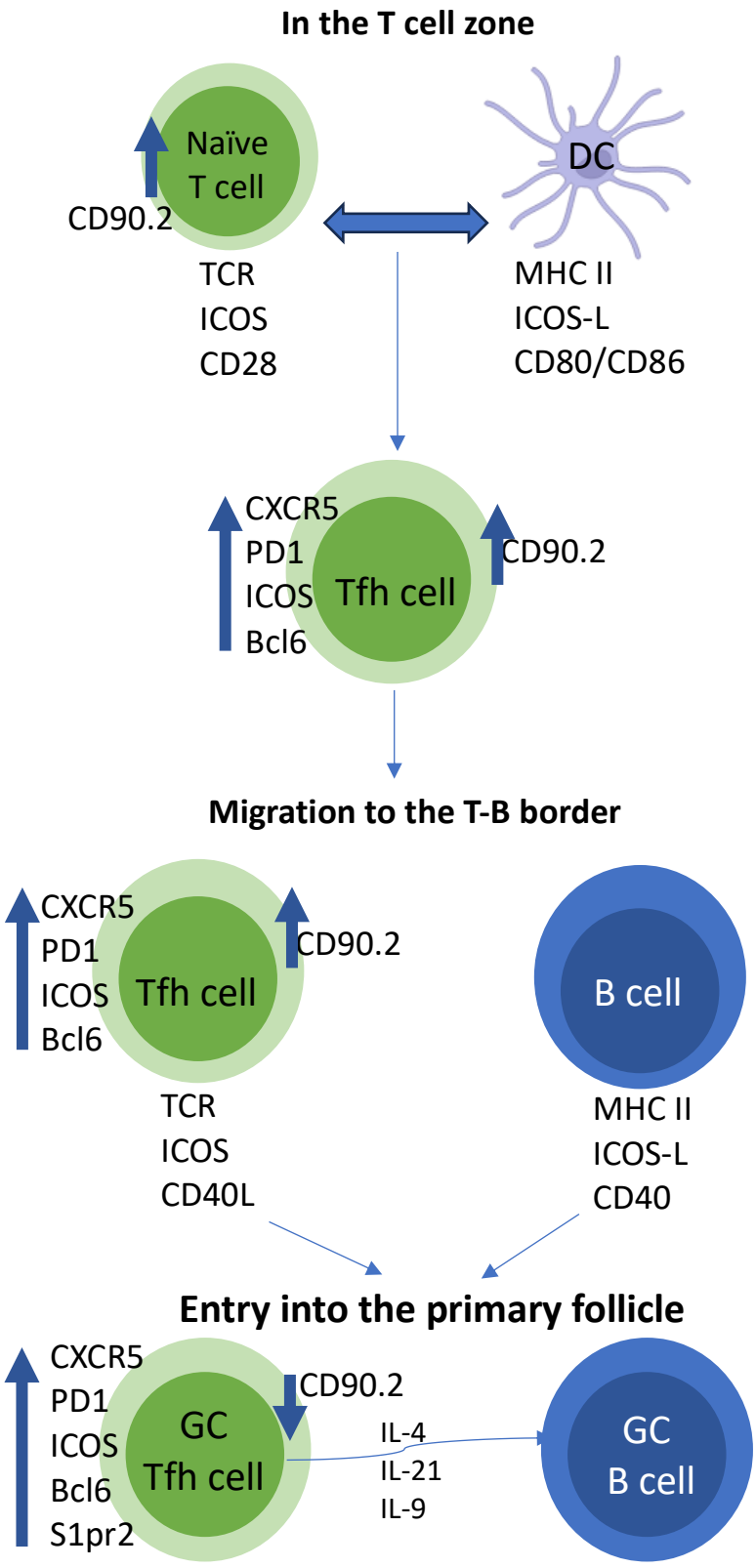


Figure 1.6. Schematic participation of Tfh cells in the follicular response.

Naive $CD4^+$ T cells are initially activated by DCs, leading to upregulation of CXCR5 and differentiation into pre-Tfh cells. These cells migrate towards the B cell follicle and interact with activated B cells at the T-B border. These interactions support GC formation and maintenance of the follicular response.

IL-21 produced by Tfh cells plays a critical role in regulating GC B cell responses, including the magnitude and duration of the GC responses, maintaining Bcl6 expression in GC B cells, promoting B cell proliferation, and influencing B cell selection and fate decisions [93, 94]. Mice deficient in IL-21, or its receptor, exhibit impaired GC maintenance and lower production of high-affinity antibodies [8, 94]. N-deacetylase and N-sulfotransferase 1 are specifically expressed in B cells, where they modify cell surface heparan sulphate. This modification enhances the binding affinity of IL-21 to its receptor on B cells, thereby increasing B cell responsiveness to IL-21 [95].

The role of Tfh cells in supporting GC B cells became evident when Tfh cells were ablated by anti-CD40L antibody, which led to subsequent GC collapse [75]. Tfh cells contribute to the positive selection and mediate affinity-driven competition of GC B cells (see section 1.2.3.3), even in the absence of BCR-mediated antigen recognition [75]. The strength and duration of Tfh cell-GC B cell interaction are critical in regulating the fate of GC B cells. For instance, the stable $CD40L^+$ Tfh-$CD40^+$ GCLZ B cell interaction is required for the induction of IRF4 expression in the $Bcl6^{lo}$ $CD69^{hi}$ GCLZ B cells, which helps drive their differentiation towards the PC fate [7]. The stability of this interaction is facilitated by higher expression of adhesion molecules, such as ICAM-1 and SLAM, in the $Bcl6^{lo}$ $CD69^{hi}$ GCLZ cells. Disrupting this interaction by blocking ICAM-1 reduces the development of the $Bcl6^{lo}$ $CD69^{hi}$ PC precursor population [7].

Conversely, intermediate $CD40L^+$ Tfh-$CD40^+$ GCLZ B cell signalling favours the growth of $Bcl6^{hi}$ $CD69^{hi}$ GCLZ B cells that are destined for re-entering the GCDZ [7].

S1pr2 is crucial for the localisation of Tfh cells within the GC [87, 92]. Using a reporter mouse strain, it was found that Tfh cells express varying levels of S1pr2, with a subset of Tfh cells expressing S1pr2 at levels comparable to those of GC B cells. The $S1pr2^{hi}$ Tfh cell subset is preferentially localised within the GC. S1pr2-deficient Tfh cells failed to be retained within the GC. However, S1pr2 deficiency alone in Tfh cells did not significantly impact overall GC responses, but the combined deficiency of S1pr2 and CXCR5 severely impaired Tfh cell localisation within the GC [87].

Due to the essential role of Tfh cells within GC, Yeh et al. characterised the GC-resident Tfh cell population compared to non-resident Tfh cells (GC-like Tfh cells) [92]. The GC-resident Tfh cells express high levels of Bcl6, CXCR5, PD-1, S1pr2 and low levels of CD90.2. Unlike GC-like Tfh cells, GC-resident Tfh cells are non-dividing cells, and need peptide-MHC class II complex-expressing B cells for their development [92]. This suggests that GC-resident and non-resident Tfh cells are comprised of different TCRβ repertoires and gene expression profiles, emphasising their functional differences.

In T cell differentiation, the balance between Bcl6 and Blimp-1 expression is crucial in determining effector and memory cell fate decisions in both $CD4^+$ and $CD8^+$ T cells [96]. While Bcl6 encourages a programme that favours memory differentiation, Blimp-1 encourages a programme that favours terminal effector differentiation. However, high expression of Bcl6 in GC-resident Tfh cells does not classify them as memory cells at that stage but allows them to retain memory characteristics after the GC reaction, such

as long-term survival capacity and the ability to rapidly re-differentiate into effector Tfh cells [96]. It suggests that almost all antigen-specific Tfh cells become Bcl6-low after weeks of immunisation [86]. The expression of Blimp-1 is low in GC-resident Tfh cells, as it is downregulated by Bcl6 expression [96, 97].

1.2.3.3. B cell signalling and selection in the germinal centre.

As discussed earlier (see section 1.2.3.1), B cell entry into the GC is determined by the initial BCR signalling and affinity for antigen. CSR and SHM are also initiated prior to GC entry, indicating some aspects of effector commitment begin early in the activation process. The potential outcomes of signalling and selection processes in the GC include apoptosis, positive selection, or differentiation into PCs and memory B cells [98]. Because B cells undergo multiple rounds of cycling within the GC, measuring the dynamics of positive selection can be complex [98]. BCR signalling has a critical role in the positive selection of GC B cells. After clonal expansion and antibody gene diversification of B cells in the GCDZ, B cells migrate to the GCLZ, where they undergo a selection process [99, 100]. Here, the GC B cells test their newly mutated BCR by capturing and processing FDC-bound antigen and presenting it to Tfh cells, enabling high-affinity-dependent selection [101]. BCR signalling serves dual functions: it acts as a signal transducer and an endocytic receptor, allowing B cells to capture and present antigens to Tfh cells (as described in section 1.2.3.2) [100, 102]. BCR-mediated positive selection involves at least three checkpoints to ensure efficiency [75, 103]. First, some B cells have mutations that damage their BCR after SHM in the GCDZ; therefore, these B cells cannot provide tonic signals and are eliminated before entering the GCLZ. The second checkpoint occurs in the GCLZ and represents the dual role of

BCRs, where the interplay with Tfh cells after recognising FDC-bound antigen will determine their fate, apoptosis or survival. The survival support is dependent on the coordinated engagement of CD40 on B cells with CD40L on T cells, and not just on BCR affinity. The third checkpoint ensures balanced BCR signalling; otherwise, excessive BCR signalling from T cells can negatively affect the survival of GC B cells and trigger apoptosis. This is to prevent the survival of autoreactive or hyperactive B cells, which could lead to autoimmunity [75, 104]. Myc (a regulatory transcription factor) expression is upregulated in GC B cells that receive sufficient BCR and Tfh cell help signals. Myc is associated with cell cycle entry [73, 75]; therefore, B cells that express Myc re-enter the GCDZ for further proliferation and affinity maturation [103, 105]. The understanding of the GC reaction suggests that B cells with higher Myc levels can undergo more rounds of division, leading to the selective expansion of high-affinity clones. However, this understanding does not account for the observed generation of memory B cells with lower affinity [106] or the continued differentiation of PC independently of affinity [107, 108]. These studies agreed that positive selection in the GCLZ is initially permissive, allowing a diverse range of BCR affinities to be retained in the GC, including lower-affinity clones. The subsequent selection steps, particularly involving proliferation and differentiation, are affinity-biased [106]. MacLean et al. expand on this by demonstrating that clonal dominance in PCs emerges primarily through the proliferation of high-affinity PC clones in the later stages of PC development following the permissive phase [109].

Moreover, the positive selection of GC B cells is also influenced by their constant region isotype [74, 75]. Studies have shown that IgG^+ GC B cells are preferentially selected over IgM^+ counterparts during the course of the GC reaction [110]. This

preference is not due to class switching of existing IgM GC B cells but rather reflects the differences in BCR signalling or antigen presentation capabilities between the two isotypes, although this requires further investigation.

Inappropriate BCR signalling can lead to unexpected cellular outcomes. For instance, a high level of IL-4 Tfh cell signalling in GC B cells can downregulate Bcl6, reducing the GC reaction [111]. The Src homology 2 (SH2) domain-containing protein-tyrosine phosphatase (PTP)-1 (SHP-1), encoded by the *Ptpn6* gene, helps maintain B cell survival by preventing excessive BCR signalling. Loss of SHP-1 leads to stronger BCR signalling, resulting in increased early apoptosis of PB and GC B cells, reduced GC size, and impaired antibody responses [112]. To conclude, positive selection ensures that B cells expressing the most effective BCR for binding antigen are preferentially expanded and retained for effective humoral immunity.

1.2.3.4. Differentiation of germinal centre B cells into plasma cells and memory B cells.

Tachó-Piñot et al. and Sutton et al. suggest that BCR affinity is not the sole determinant of B cell fate [107, 108]. Both low- and high-affinity GC B cells can give rise to PCs, reflecting the diversity of affinities present in the GC regardless of selection pressure. Moreover, lower-affinity and some high-affinity GC B cells favour differentiation into memory B cells [107, 108]. However, based on the affinity selection concept discussed in Section 1.2.3.3), studies by Nakagawa et al. and MacLean et al. agreed that cell fate decisions (PC vs. memory B cell) are influenced by affinity, but not exclusively dictated by it, at early selection stages [106, 109].

Myc positively correlates with GC B cell fate decision. The level of Myc expression in GCLZ B cells depends on the strength of the Tfh signal [109]. Then, Myc^{+} GCLZ B cells migrate back to the GCDZ to proliferate, undergoing divisions proportional to the level of Myc, called inertial proliferation [109, 113]. Nakagawa et al. identified three distinct subpopulations of positively selected c-Myc^{+} GCLZ B cells: pre-PB-PC, pre-memory B cells, and GCDZ B cell entrants [106]. The pre-PB-PC population has higher c-Myc levels, indicating these cells have received strong signals from Tfh cells. The pre-memory B cells are characterised by lower c-Myc expression, reflecting their more quiescent nature. While GCDZ B cell entrants will continue their proliferation and undergo SHM processes to improve their BCR affinity. The study also emphasised that the dynamic nature of positive selection allows for the retention of a significant proportion of low-affinity B cell clones [106].

Another characterisation of the GCLZ B cell fate was found in the study by Ise et al. [7]. They identified two precursor cells in the GCLZ B cells: a small population of $Bcl6^{lo}$ $CD69^{hi}$ GCLZ B cells express IRF4, downregulate S1pr2, and upregulate Gpr183, favouring PC fate compared to $Bcl6^{hi}$ $CD69^{lo}$ counterparts, which favour recycling. PB-PC transition from a precursor state in the GC to the maturation state at the GCDZ: GC-medulla interface (GMI) in the lymph node [113] and GC: T cell zone interface (GTI) in the spleen [8]. GMI and GTI serve as a niche for the local maturation of GC-derived PC, where stromal cells provide essential support for PC differentiation and survival, such as $Lyve1^{+}$ and $PDGFR1^{+}$ cells in the GMI [113] and $CD157^{+}$ $podoplanin^{+}$ cells in the GTI [8]. In both studies, a fate-mapping mouse model was used to track GC-derived PC, specifically looking for $IRF4^{hi}$ cells, which are indicative of recently differentiated PC. The identity of $IRF4^{hi}$ cells, at GMI and GTI, as PCs has been

confirmed by characterising the expression of markers associated with GC and PC phenotypes.

Various models for GC output have been proposed, indicating the complexity of the decision-making process within GC B cells [114]. Asymmetric fate model, where GC B cells undergo polarisation after interacting with Tfh cells, resulting in unequal distribution of fate-altering molecules in daughter cells. Depending on which molecules they inherit, they may either continue to differentiate into PCs (inheriting IRF4 and Myc), maintain their GC identity, or differentiate into memory B cells (inheriting Bcl6, PAX5, and IL-21R). The instructive fate model relies on the strength of Tfh cells, in which weak signals would favour the differentiation towards memory B cells or induce apoptosis. The decreasing-potential fate model implies the cumulative strength of Tfh cell-BCR signalling. As B cells spend more time in the GC and undergo multiple cycles of re-entry, their ability to differentiate into memory B cells diminishes, resulting in a shift towards PC differentiation. Lastly, the integrative fate model combines aspects of the previous models. GC B cells that have received less cumulative signalling require a stronger signal to differentiate into PCs, while those that have received more cumulative signals require much weaker prompts.

1.3. Transcriptional program.

Transcription factors coordinate the suppression of B cell-associated transcripts and the induction of ASC-associated transcripts, contributing to the terminal differentiation of B cells into ASCs. The antagonistic interaction between BC genes and PC genes is modulated by the signalling received, such as antigens and cytokines [115]. B cell-

promoting transcription factors include paired box protein 5 (Pax5) [116, 117], Bcl6 [118], and Bach2 [119]. In contrast, ASC-promoting transcription factors are distinct from those found in other subsets of B cells. Wei Shi et al. investigated mature B cell types, including FO, MZ, B1 cells, and PCs, and revealed transcriptomic variations associated with cell maturation. They identified 301 genes that distinguish ASCs (splenic PBs, splenic PCs, and BM PCs) from B cell subsets in RNA-seq data [117].

The different stages of B cell development and activation require distinct transcriptional programmes. Pax5 is a master regulator that maintains B cell identity at the pro-pre-B cell stage. The regulatory effect of Pax5 involves BCR components, immune receptors (CD19, CD21, and CD23), and transcription factors (Bach2, IRF4, and IRF8) [115, 120]. Pax5 serves as a gatekeeper to sustain the differentiation state of GC B cells as they undergo SHM and CSR and prevents premature expression of PB-PC-related genes until appropriate signals trigger a shift in the regulatory network [115, 120].

Bach2 is another transcription factor that delays the transition to ASC, allowing sufficient time for CSR to occur in activated B cells [115, 121]. Its expression is partially mediated by Pax5 and is amplified by Bcl6 in GCs [120]. Its action occurs by repressing Blimp-1 and promoting AID expression. Bach2-deficient mice showed that GC cannot form properly, SHM and CSR are impaired, and Blimp-1 is expressed too early [115, 120]. Removing Blimp-1 in Bach2-deficient B cells can rescue CSR, demonstrating that Bach2 functions by delaying Blimp-1 expression, thereby allowing CSR and SHM to occur first [115, 121].

Bcl6 is a transcription factor that has a role in B cell development in the BM and is particularly important for the function of GC B cells [120, 122]. Bcl6 controls B cell

positioning by inducing the expression of genes such as *S1pr2*, which encodes the S1pr2 protein, which promotes the confinement of GC B cells, while repressing the expression of genes encoding migratory receptors, such as EBI2 and S1pr1 [114, 120]. Additionally, Bcl6 regulates the expression of genes associated with cell cycle inhibitors, as well as Myc and B cell lymphoma 2 (Bcl2), which are involved in the proliferation and survival of GC B cells [122, 123]. The expression of Bcl6 in GC B cells is enhanced by the action of IL-21, and IRF8, which has been shown to support GC homeostasis by regulating Bcl6 indirectly and maintaining the proper balance of B cell populations within the GC [115]. Bcl6 expression antagonises Blimp-1 expression, thereby determining the fate of B cells towards GC reaction or PC differentiation [96, 124].

IRF4 has a role in determining whether activated B cells become either GC B cells or PCs [125, 126]. Transient expression of IRF4 leads to the generation of GC B cells by upregulating genes such as *Bcl6* and *Aicda* [115, 126]. IRF4-deficient mice showed a complete absence of GC B cells, although the interaction between B and T cells remained intact [115, 120, 125].

1.3.1. Transcriptional regulators in plasma cells.

PC-promoting transcription factors include IRF4, Blimp-1, and X-box binding protein 1 (XBP-1) [115]. Notably, the differentiation of PB-PCs under TD and TI antigens revealed transcriptional differences between *in vitro*- and *in vivo*-derived PB-PCs [117]. Wei Shi et al. found that while ASC populations share a common transcriptional program indicative of their antibody-secreting function, distinct differences arise

between intermediate PBs and fully differentiated PCs regarding genes governing migration, survival, and cell cycle control [117].

IRF4 exhibits different DNA binding modes and cooperates with other transcription factors to control the expression of genes essential for PC and GC B cell function [126, 127]. While transient IRF4 expression leads to GC B cell formation, sustained high levels of IRF4 activate Blimp-1, thereby initiating PC differentiation and downregulating genes associated with the GC program, such as *Bcl6* and *Aicda* [115, 126, 128]. Experiments demonstrated that high-affinity antigen interactions led to increased IRF4 expression, differentiating B cells towards PCs, thereby indicating how antigen affinity can impact differentiation outcomes. IRF4-deficient mice exhibit an inability to generate mature PCs [120]. This failure can be attributed to an insufficient induction of the Blimp-1 [128, 129] or result from a defect in XBP1 expression [128]. However, IRF4 is not required to maintain Blimp-1 expression in PCs [130]. IRF4-deficient mice that are stimulated with CD40 and IL-4 also exhibit impaired expression of AID and a failure to undergo CSR [128]. Despite the CSR defect, an initial production of switched memory B cells was observed in IRF4-deficient mice, suggesting that IRF4 may not be required for memory B cell generation; however, it is critical for the differentiation of memory B cells into PCs.

In the B cell lineage, Blimp-1, encoded by *Prdm1*, is expressed across all ASC, and its levels can be used to distinguish proliferating PBs from long-lived PCs in both mice and humans. Blimp-1 expression is induced in the light zone of the GC when Tfh secreted IL-21 signals through the IL-21R of the GC B cell, synergising with BCR and CD40 signalling pathways [93, 113]. However, only IL-21R-CD40 signalling drives PC

differentiation, while simultaneous BCR signalling drives memory-like fate [93]. Long-lived PCs differentiate through the activation of STAT3 in response to IL-21, reducing Bcl6 and increasing IRF4 [93]. Although Blimp-1 expression is not strictly required to initiate the ASC differentiation program [115, 131]—since the intermediate stage of PBs can emerge without it—it is essential for the progression into fully functional ASC, evidenced in both *in vitro* and in vivo settings [115, 132]. For instance, Blimp-1 is important for full XBP-1 activation—required for the immense Ig production—but XBP-1 expression can still be initiated and perform some limited functions in the absence of Blimp-1 [120, 132]. Blimp-1 suppresses genes that maintain the B cell identity, such as Pax5, and induces the expression of XBP-1. XBP-1 is a transcriptional factor required for the unfolded protein response, which prepares the cell to function as an antibody-secreting factory. In the absence of XBP-1, PCs fail to secrete high levels of Ig properly, despite appearing structurally intact [115, 120, 132]. In B cell differentiation, Bcl6 and Blimp-1 act as antagonistic transcription factors that control cell-fate decisions towards GC reaction or PC differentiation, respectively (Figure 1.7) [86, 96].

1.3.2. Transcriptional regulators in memory B cells.

Transcription factors such as Bach2 and activated B cell factor 1 (ABF-1) are important for memory B cell differentiation while blocking PC fate [127]. Bach2 supports memory B cell commitment in GCLZ B cells in a dosage-dependent manner [133]. ABF-1 is expressed predominantly in memory B cells and suppresses the PC differentiation pathway [134]. Wang et al. identified a population of GC memory precursor B cells that have exited the cell cycle and entered the G0 phase while still within the GC [135].

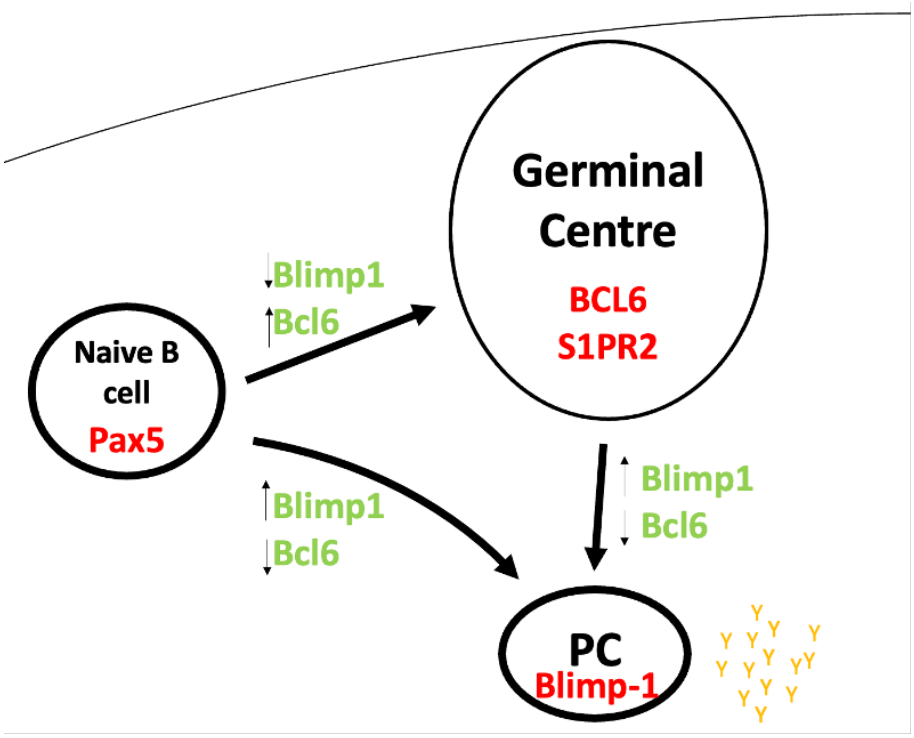


Figure 1.7. Schematic representation of relationship between Bcl6 and Blimp-1 to induce PC.
When a naive B cell encounters its cognate antigen, the naive B cell can upregulate either Bcl6, committing to the GC pathway, or Blimp-1, driving differentiation into a PC. The expression of Bcl6 in GC B cell is downregulated as they transition into Blimp-1-expressing PC.

By examining this population, researchers can explore the transitional programmes that facilitate the commitment to memory. Wang et al. demonstrate that signalling from IL-9-producing Tfh cells activates the STAT1 pathway, promoting transcriptional programs that drive the GC to memory transition [135]. Moreover, Zinc finger and BTB-containing 32 (ZBTB32) and Krüppel-like factor 2 (KLF2) have been reported to play roles as transcriptional factors in the development of memory B cells [114, 135]. Elevated levels of ZBTB32 are implicated in promoting the survival and persistence of memory B cells by repressing genes that are associated with differentiation toward

PCs [135, 136]. KLF2 is essential for maintaining their quiescence and retaining them in lymphoid tissues [114, 135].

A decrease in Bcl6 expression—lower than the level of GC B cells—is associated with the differentiation of GC B cells into memory B cells [114]. Bcl6 cooperates with other transcription factors, such as Bach2, which also promotes memory B cell differentiation. The regulatory interactions between Bcl6 and Bach2 impact the balance between memory B cells and other B cell subsets [114, 137]. For instance, ablation of Bach2 leads to an increase in Bcl6 expression, suppressing the differentiation of GC B cells into memory B cells. Furthermore, when T cell help is low, Bach2 levels remain elevated, reinforcing the memory B cell pathway by repressing genes that drive cell growth and division, such as *Cdkn1a* and *Cdkn2a*, while simultaneously enhancing the expression of anti-apoptotic genes, such as *Bcl2l1* [114, 138].

A decrease in Bcl6 expression can be attributed to sufficient BCR-driven KRAS signalling or weak exposure to T cell-derived IL-4 and IL-21. The weak signalling from T cells induces genes, such as haematopoietically expressed homeobox (*Hhex*), that interact with transducin-like enhancer 3 (TLE3) to further repress Bcl6 expression through upregulation of Bcl2 and Sloan-Kettering Institute (SKI) transcription factors. Ultimately, an understanding of the transcriptional regulators that govern the development of memory B cells will enhance the knowledge of adaptive immunity and the development of therapeutics.

1.4. The phenotype of plasma cells and memory B cells.

Transcriptional regulation significantly impacts the expression of surface markers on PCs and memory B cells, which dictates their identity, function, and ability to respond to external stimuli. APRIL and BAFF are survival factors for PCs, acting through shared receptors B cell maturation antigen (BCMA) and transmembrane activator of and CAML interactor (TACI) [139]. BCMA and TACI are induced upon B cell activation, with only TACI in GC B cells and memory B cells [139]. During their differentiation into ASCs (PBs and PCs), PBs and some PCs exhibit expression patterns of the BCMA and TACI: downregulation of TACI and the upregulation of BCMA [139]. BAFF also interacts with BAFF-R, which is expressed during the earlier stages of B cell development and is found at low levels in some PCs [139]. Recently, Eslami et al. revealed that BCMA and/or TACI are required for the survival of PCs, while BAFF-R is not crucial in this context [140]. Additionally, their findings indicate that BAFF-TACI, APRIL-TACI, and APRIL-BCMA represent self-sufficient ligand-receptor pairs for PC maintenance. This clarifies the functional redundancy and specificity of BAFF and APRIL beyond what was previously understood [140].

CD44 and CXCR4 are two important molecules involved in the trafficking of PCs, playing roles in their migration, localisation and survival within specific niches in the body [139]. CD44 is an adhesion molecule [141], and CXCR4 is a receptor for the ligand CXCL12 [142], both of which play a role in the homing and retention of PCs, particularly in the BM.

The CD138 marker, also known as syndecan-1, is a well-validated marker for identifying ASCs [130, 143, 144]. B cells at an earlier stage of terminal differentiation

and PBs typically exhibit low or absent levels of CD138 [130]. CD138 has an adhesive role that may contribute to homing to another tissue, such as the BM [145]. The expression of CD138 promotes the accumulation of ASC, facilitating a sustained humoral immune response by mediating their interaction with EF signalling molecules that support cell survival and proliferation [146]. $CD138^{hi}$ cells were found concentrated at the T-B border, which is located between the GCDZ and the T zone, supporting the idea that PBs may exit the GC through the DZ [147].

The expression of IRF4 is increased during the late stages of B cell differentiation to ASC; consequently, it directly induces the expression of the Blimp-1 gene. As PBs differentiate into PCs, Blimp-1 levels increase until levels peak within the fully matured PC [146]. Blimp-1 is used to confirm the identity of GC-derived PC at GMI and GTI. Blimp-1-expressing ASCs were found in large numbers at the GTI, in the medulla of the lymph nodes, and in smaller numbers within the GC and GMI. Zhang et al., used B220 as a reference marker to identify the $IRF4^{hi}$ ASCs in the GTI, highlighting that most of the $IRF4^{hi}$ ASCs lacked B220 but expressed high levels of CD138 [8]. The outer light zone of the GC showed lower quantities of Blimp-1-expressing ASCs [8, 113]. However, these cells were identified as $IRF4^{hi}$ and $CD138^{lo}$, indicating an earlier maturation stage compared to those in the GTI [8].

Although Blimp-1 is used for identifying ASCs, a significant fraction of $CD138^{hi}$ $B220^{lo}$ ASCs in the BM were reported to be Blimp-1 negative [148]. This likely reflects a limitation of the IRES-GFP reporter rather than a true absence of Blimp-1 expression. Therefore, Pracht et al. emphasise the importance of the four-marker staining protocol using CD138, TACI, B220, and CD19, which enables a more accurate identification of

PCs without relying on the Blimp-1 expression. Analysis of the CD138^{hi} TACI^{hi} population revealed four subsets, with a minor B220^{hi} CD19^{hi} fraction, proliferating PBs likely representing early activated B cells, and two non-proliferating PCs based on CD138^{hi} TACI^{hi} B220 CD19 expression levels. Binet et al. characterised that the CD138^{lo} B220^{int} ASC located at the GMI are in a transitional state of the differentiation process of B cells, suggesting they are actively engaged in the initial phases of maturation towards PC [113]. Conversely, CD138^{int} B220^{+} cells are characterised as being at a more advanced stage of becoming fully differentiated PC. Finally, CD93 has a role as a marker that varies in expression during B cell activation and differentiation, which is diminished in mature PCs compared to earlier differentiation stages [130].

Memory B cells express higher levels of costimulatory molecules of CD80, CD86, CD95, CD21, and CD24 compared to naive B cells [149]. Memory B cells consistently express CD27, indicating prior antigen exposure or activation [149, 150]. Moreover, memory B cells can be classified into subsets based on the expression of CD80 and PDL2: CD80^{+} PDL2^{+} exhibit either EF or GC B cell origins, and CD80^{-} PDL2^{-} form independently of GC, potentially from early memory precursor [151, 152]. After re-exposure to the antigen, CD80^{-} PDL2^{-} memory B cells differentiate into GC B cells [152]. EF-derived CD80^{+} PDL2^{+} memory B cells are more proliferative, while GC-derived CD80^{+} PDL2^{+} memory B cells differentiate into IgG1^{+} PBs [152].

Further, memory B cells can be divided based on the triple expression of CD80, PDL2, and CD73 [153]. The subsets expressing these markers also demonstrate varying levels of bone morphogenetic protein receptor 1a (Bmpr1a) [154]. Some Bmpr1a upregulation occurs in GC B cells and subsets of PCs that are differentiated from

$CD80^+$ $PDL2^+$ memory B cells. Given that elevated levels of ZBTB32 are known to promote the survival and persistence of memory B cells (section 1.3.2.), ZBTB32 is highly expressed in $CD80^+$ $PDL2^+$ memory B cells that are also positive for Bcl6 [151, 155]. High levels of Bcl6 are associated with a memory B cell phenotype, which is characterised by enhanced longevity and the ability to rapidly respond to antigen re-exposure. However, the deficiency of Bcl6 is not correlated with memory B cell differentiation. Bcl6-deficient mice produce memory B cells independent of GCs.

CCR6 is a specific marker for memory B cell precursors [156]. These cells are highly enriched in the GCLZ with low affinity, undergoing cell cycle exit, and showing a distinct gene expression profile. CCR6 low-affinity GCLZ and some CCR6 high-affinity GCLZ memory B cell precursors transition into memory B cells.

The transcription factor KLF2 affects the surface expression of homing receptors on memory B cells, such as CCR7 and CD62L, which are essential for their migration to lymphoid tissues [135]. Takatsuka et al. suggested a regulatory mechanism involving IL-9:IL-9R signalling in memory B cells during humoral recall responses [157]. IL-9 is produced by both memory B cells and Tfh cells [124, 157], suggesting it may play an autocrine and paracrine role in directing the proliferation and differentiation of memory B cells into PCs.

1.5. Aim of this thesis.

This thesis presents three research projects that investigate the immune responses of B cells induced in three different mouse models.

Chapter 3 presents the High-Affinity LOw-affinity (HALO) mouse model, *S1pr2*^{CreERT2} *Rosa26*^{LSLtdTomato} *Prdm1*$^{GFP/wt}$, which is an advanced experimental system for the simultaneous fluorescent labelling of both EF- and GC-derived PB-PCs. To further distinguish between the two populations of PCs, specific cell-surface marker antibodies conjugated with fluorophores were employed. This dual labelling technique not only enhances the resolution of cellular tracking but also enables precise identification of PC differentiation pathways and their stages.

Chapter 4 presents the IgMg1AID^{cre} mouse model. The GC B cells in the IgMg1 mouse model are predominantly IgG1^{+} B cells with a reduced frequency of IgM^{+} B cells. Crossing the IgMg1 mouse model with AID^{Cre} mice stems from the need to investigate how the IgMg1 B cells respond to the antigen and the resulting antibody production when they are restricted from undergoing CSR.

Chapter 5 presents the *S1pr2*^{CreERT2} *Rosa26*^{LSLtdTomato} mouse model, which is utilised to investigate recall GC B cell responses following booster immunisation. This investigation compares the responses stimulated by boost immunisations delivered either at the same site as the primary immunisation versus those delivered distally.

Chapter 2. Research Methodology.

2.1 Reagents and materials

Table 2.1. Reagents and kits that were used throughout the study.

Reagent	Supplier	Product number
Paraformaldehyde (PFA) 4% (v/v)	Thermo-Fisher Scientific	30525-89-4
AccuCount Blank Particles 10^6/mL	Spherotech	ACBP-100-10
Aluminium potassium sulphate (alum)	Fisher Chemical	A/2400/53
Bovine serum albumin (BSA) 100G Pcode 1003593040	Sigma Aldrich	A7906
Carbonate-Bicarbonate buffer capsule PCode 1002934517-50CAP	Sigma Aldrich	C3041
Cryomold Epredia™ disposable base moulds	Thermo-Fisher Scientific	58950
dimethyl sulfoxide (DMSO)-50mL	Sigma Aldrich	D4818
Epredia Neg-50™ Water Soluble Colourless	Thermo-Fisher Scientific	6502
Hydrochloric acid (HCl)-100ML	Sigma Aldrich	H9892
Heat-inactivated Bordetella pertussis stock 10^{11}/mL	LEE laboratories, BC, USA	-
Keyhole limpet haemocyanin (KLH) -250MG	Merck Millipore	374805
MicroAmp™ Clear Adhesive Film	Thermo-Fisher Scientific	4311971
Sodium hydrogen carbonate and sodium bicarbonate ($NaHCO_3$)	Sigma Aldrich	55761-1KG
Sodium hydroxide (NaOH)	Sigma Aldrich	S5881-1KG
Normal Horse Serum	Sigma Aldrich	H0146-5ML
Normal Mouse Serum	Merck	M5905-5ML
Normal Rat Serum	Merck	R9759-10ML
4-Hydroxy-3-nitrophenylacetyl N-hydroxysuccinimide ester (NP-OSu)	Biosearch	N-1010
4-hydroxy-3-nitrophenylacetyl-bovine serum albumin (NP-BSA)	Prepared in-house	N/A

4-hydroxy-3-nitrophenylacetyl-keyhole limpet hemocyanin (NP-KLH)	Prepared in-house	N/A
p-Nitrophenyl Phosphate (pNPP) SLCK1332	Sigma Fast™	N2765
Phosphate-Buffered Saline (PBS) 1X 500mL	Gibco	14190-094
PBS tablets	Gibco	18912-014
ProLong™ Diamond Antifade Mountant	Invitrogen	P36970
Saponin-100G Pcode 102205697	Sigma Aldrich	84510
Sheep red blood cells (SRBCs)	ThermoScience	SR053B
Sucrose-1KG Pcode 102164072	Sigma Aldrich	S0389
Tamoxifen-1G Pcode 102526690	Sigma Aldrich	T5648
Tris buffer SLCK1334	Sigma Fast™	T8790
Tween®20-50 mL	Sigma Aldrich	P9416
Tween®20-500ML	Sigma-Aldrich	P1379
LIVE/DEAD™ Fixable Near-IR Dead Cell Stain Kit	Invitrogen	2284645
Roswell Park Memorial Institute (RPMI) 1640 medium	Gibco	21875-034
Ethylenediaminetetraacetic acid (EDTA) 0.5 M	Sigma-Aldrich	E7889
Fetal Bovine Serum Heat Inactivated (FBS-HI)	Sigma-Aldrich	F9665
Triton®X-100 solution	Sigma-Aldrich	T9284-500ML
Molecular Probes ProLong Gold Antifade Mountant 10 mL	Invitrogen	P36930

Table 2.2. Materials were used throughout the study.

Material	Supplier	Product number
Cell strainer 70 µm	Greiner	542070
Flat-bottom Maxisorp 96-well plates	Thermofisher	442404
pH-indicator strip	MQuant® Merck	1.09533.0001
Superfrost™ Plus Adhesion Microscope Slides 25x75x1mm	epredia	J1800AMNZ
V-bottom 96-well plate	Thermo Scientific	611V96

Table 2.3. Antibodies used for ELISA assays.

Specificity and Conjugation	Supplier	Stock concentration	Product #	Final dilution	Clone
Goat anti-mouse IgG1, human ads-AP	Southern Biotech	1 mL	107004	1:1000	Polyclonal
Goat anti-mouse IgM human ads-AP	Southern Biotech	1 mL	102004	1:4000	Polyclonal

Table 2.4. Antibodies and Reagents Used for Flow Cytometry Analysis.

Specificity and Conjugation	Supplier	Stock concentration	Final dilution	Clone	Application
Anti-Rat Alexa Fluor647	Jackson Immunoresearch	0.3 mg	1:400	Anti-rat IgG	Tfh cells
B220 BV421	BioLegend	0.2 mg/mL	1:100	RA3-6B2	B cell lineage
B220 (CD45R) BUV395	BD Horizon™	0.2 mg/mL	1:800	RA3-6B2	B cell lineage
CD86 BV421	BD Biosciences	0.2 mg/mL	1:200	GL1	GCLZ B cells
CD86 AF700	BioLegend	0.2 mg/mL	1:300	GL1	GCLZ B cells
CD138 (syndecan-1) BV711	BioLegend	0.2 mg/mL	1:300	281-2	Plasma cell
CD19 BUV737	BD Biosciences	0.2 mg/mL	1:800	1D3	Total B cells
CD19 PE-Cy5	BioLegend	0.2 mg/mL	1:300	6D5	Total B cells
CD3 BUV395	BD Biosciences	0.2 mg/mL	1:300	17A2	Total T cells
CD38 BUV737	BD Biosciences	0.2 mg/mL	1:1000	90	Naïve and activated B cell

CD38 PerCP-Cy5.5	BioLegend	0.2 mg/mL	1:300	90	Naïve and activated B cell
CD4 BV510	BioLegend	0.2 mg/mL	1:300	GK1.5	Helper T cells
CD4 FITC	eBioscience	0.5 mg/mL	1;200	GK1.5	Helper T cells
CD44 PerCp-Cy5.5	eBioscience	0.2 mg/mL	1:300	IM7	Activated Tfh cells
CD62L BV510	BioLegend	0.2 mg/mL	1:300	MEL-14	Naïve T cell
CD90.2 AF700	BioLegend	0.2 mg/mL	1:800	30-H12	GC-resident Tfh cells
CXCR4 (CD184) Biotin	eBioscience	0.5 mg/mL	1:300	2B11	GCDZ B cells
CXCR5 Purified	BD Biosciences	0.1 mg/mL	1:25	2G8	Tfh cells
Fas (CD95) BV605	BD Biosciences	0.2 mg/mL	1:300	Jo2	GC B cells
Fc block anti-CD16/32	Invitrogen	0.25 µg/mL	1:200	93	Fc-receptor blocking antibody
IgD BV510	BioLegend	0.2 mg/mL	1:300	11-26c.2a	B cell Isotype
IgG1 PerCP-Cy5.5	BioLegend	0.2 mg/mL	1:300	RMG1-1	B cell Isotype
IgM PE-Cy7	BioLegend	0.2 mg/mL	1:600	RMM-1	B cell Isotype
Near-IR dead cell stain	Invitrogen (Cat # L10119)	kit	1:1000	n/a	Exclude dead cells
NP_2-APC	Made in-house	9.6 mg/mL	1:800	n/a	Antigen-binding B cell
PD1 (CD279) PE	eBioscience	0.5 mg/mL	1:200	J43	Tfh cells
PD1 (CD279) PE-Cy7	BioLegend	0.2 mg/mL	1:200	29F.1A12	Tfh cells

Streptavidin BV510	BioLegend (Cat # 405233)	0.1 mg/mL	1:400	n/a	Protein bind to biotin
TACI (CD269) BV421	BD Biosciences	0.2 mg/mL	1:300	8F10	Plasma cell differentiation
TACI (CD269) APC	BD Pharmingen	0.2 mg/mL	1/100	8F10	Plasma cell differentiation

Table 2.5. Antibodies and Reagents Used for Immunofluorescent Staining.

Specificity and Conjugation	Supplier	Stock concentration	Product #	Final dilution	Clone
affiniPureF(ab)2 fragment Donkey anti-rat Alexa Fluor647	Jackson Immunoresearch	0.3 mg	712-606-150	1:400	Anti-rat IgG
affiniPureF(ab)2 fragment Donkey anti-goat Alexa Fluor647	Jackson Immunoresearch	0.3 mg	705-606-147	1:400	Polyclonal IgG
Donkey anti-rat Biotinated	Jackson Immunoresearch	0.3 mL	712-066-150	1:400	IgG polyclonal
Goat anti-CD138 purified	R&D systems	100 µg	AF3190	1:400	Polyclonal Goat IgG
Goat anti-GFP FITC	Abcam	100 µg	1034170-1	1:600	Polyclonal AB6662
IgG1 purified	BIO-RAD	0.25 mg	MCA336	1:100	Rat anti-mouse IgG1 H chain
IgM purified	BIO-RAD	0.25 mg	MCA199	1:100	Rat anti-mouse IgM H chain
NP_2-APC	Made in-house	9.6 mg/mL	n/a	1:800	n/a
Rat anti-CD4 APC	eBioscience	100 µg	17-0041-82	1:100	GK1.5
Rat anti-IgD purified	BD Bioscience	0.5 mg	553438	1:800	11-26C.2a
Rat anti-IRF4 purified	BioLegend	100 µg	646402	1:100	IRF4.3E4 RatIgG1,k
Streptavidin Dylight™405	Invitrogen	1 mL	21831	1:50	SC244210

2.2 The experimental mice.

Mice were maintained under pathogen-free conditions at the Biomedical Service Unit (BMSU), University of Birmingham, Birmingham. All mouse experiments were conducted with procedural approval from the Home Office Project License PP8702596. Overall, mice 6 to 23 weeks old were used at the time of immunisation and were culled under the Schedule 1 method for harvesting spleens and lymph nodes.

2.2.1 *S1pr2*^{ERT2Cre} *Rosa26*^{LSLtdTomato} mice.

S1pr2^{ERT2Cre} mice were previously generated by Tomohiro Kurosaki (RIKEN Centre for Integrative Medical Science, Yokohama, Kanagawa, Japan) by inserting the coding sequence of the ERT2Cre fusion protein into exon 2 of the *S1pr2* gene expressed on a Bacterial Artificial Chromosome (BAC) clone (RPCI23.C-168D6). The BAC targeting *S1pr2*^{ERT2Cre} was injected into C57BL/6 zygotes using pronuclear injection (PNI) to generate transgenic mice [133]. The genomic integration of *S1pr2*^{ERT2Cre} has not been reported to cause immune defects or disrupt the developing B cells [7, 133].

Rosa26^{LSLtdTomato} mice were obtained from Jackson Laboratory (Cat # 007914). These reporter mice possess Cre-inducible expression of the red fluorescent protein tandem dimer Tomato (tdTomato, hereafter referred to as tdT) under the control of the *Rosa26* promoter. Expression of tdT is driven when Cre excises the LoxP flanked STOP codon before the tdT sequence, facilitating a permanent constitutive tdT expression [158]. The transgenic allele *Rosa26*^{LSLtdTomato} has not been reported to cause immune defects, and the phenotype data is available on MGI: 3809524; URL:

http://www.informatics.jax.org. *S1pr2*^{ERT2Cre} *Rosa26*^{LSLtdTomato} mice were aged 8 to 15 weeks at the time of immunisation.

2.2.2 *Prdm1*$^{eGFP/wt}$ *mice.*

Prdm1$^{eGFP/wt}$ mice were previously generated by Stephen Nutt, WEHI, Melbourne, Australia. A splice site acceptor, internal ribosome entry site (IRES), and enhanced green fluorescent protein (eGFP) cDNA were inserted into the *Prdm1* locus between introns 6 and 7. The expression of eGFP is driven when the endogenous *Prdm1* is transcribed. This genetic modification is prenatal lethal if the embryo is homozygous for the transgenic *Prdm1* allele [159]. The transgenic allele *Prdm1*$^{eGFP/wt}$ has not been reported to cause immune defects, and the phenotype data are available on MGI: 3510704; URL: http://www.informatics.jax.org. *Prdm1*$^{eGFP/wt}$ mice were aged 8 to 18 weeks at the time of immunisation.

2.2.3 *S1pr2*^{CreERT2} *Rosa26*^{LSLtdTomato} *Prdm1*$^{eGFP/wt}$ mice.

The *S1pr2*^{CreERT2} *Rosa26*^{LSLtdTomato} *Prdm1*$^{eGFP/wt}$ mouse model is a novel combination of alleles developed by the Toellner lab. A combination of the three transgenic alleles was achieved by mating *S1pr2*^{CreERT2} *Rosa26*^{LSLtdTomato} mice [7, 133] to *Prdm1*$^{eGFP/wt}$ mice [159]. The B cell compartment of immunised triple transgenic mouse model (also called High-Affinity LOw-affinity (HALO) mice) was compared with those in two other immunised mouse lines: *S1pr2*^{CreERT2} *Rosa26*^{LSLtdTomato} mice and *Prdm1*$^{eGFP/wt}$ mice. All mice were from 6 to 23 weeks of age at the time of immunisation.

2.2.4 *Aicda*$^{Cre/Cre}$ mice.

The *Aicda*$^{Cre/Cre}$ mice (hereafter referred to as AID^{Cre} mice) were developed by Michel Nussenzweig at the Rockefeller University [160] (MGI:4437052: *Aicda*$^{tm1.1(cre/ERT2)Crey}$). These mice were generated by replacing the coding sequence for AID with the Cre fusion protein knocked into exon 2 of the *Aicda* gene. AID^{Cre} mice were aged 9 to 12 weeks at the time of immunisation.

2.2.5 IgM$^{g1/g1}$ mice.

IgM$^{g1/g1}$ mice (hereafter referred to as IgMg1 mice) were developed by collaborators at MedImmune (now AstraZeneca), with their construction described in detail by Zhang et al. [161]. In this study, the extracellular domain of the BCR in IgMg1 is still that of IgM, while the intracellular signalling domain has been replaced with that of IgG1. IgMg1 mice were aged 10 weeks at the time of immunisation.

2.2.6 IgM$^{g1/g1}$*Aicda*$^{Cre/Cre}$ mice.

IgM$^{g1/g1}$ mice were bred with *Aicda*$^{Cre/Cre}$ mice to generate IgM$^{g1/g1}$ *Aicda*$^{Cre/Cre}$ mice (hereafter referred to as IgMg1AID^{cre}). IgMg1AID^{cre} mice were aged 9 to 12 weeks at the time of immunisation.

2.3 Antigens.

2.3.1 Sheep red blood cells (SRBCs).

SRBCs are whole cells used to induce both TI and TD responses [52]. SRBCs were washed three times in sterile PBS by centrifugation at 2500 rpm (1,250 x g) for five minutes, then resuspended in PBS at 2 x 10^8 cells/mL for *in vivo* studies.

2.3.2 NP-conjugation.

NP_{27}-KLH and NP_2-BSA were made in-house. First, lyophilised KLH or BSA was dissolved in freshly prepared 0.2 M $NaHCO_3$ at a concentration of 2 mg/mL. Next, a solution of NP-OSu in DMSO was gradually added dropwise to the first mixture with continuous stirring, followed by room temperature incubation for two hours on a rotator, shielded from light. To remove unreacted reagents following incubation, the solution was extensively dialysed at 4°C using a Slide-A-Lyzer dialysis cassette with a 10K molecular weight cut-off (Thermo Scientific). The dialysis process included three buffer changes with 0.2 M $NaHCO_3$ and two with PBS (pH 7.45), all performed in a light-protected environment. After dialysis, the KLH or BSA protein concentrations were determined using the Pierce bicinchoninic acid assay (Thermo Scientific). By measuring the absorbance at 430 nm (using a Nanodrop 1000, Thermo Scientific), NP concentration was calculated based on the Beer-Lambert Law.

$$\text{Concentration (M)} = \frac{\text{absorbance at 430 nm}}{\varepsilon \times L} = \frac{\text{absorbance at 430 nm}}{4230\ \text{M}^{-1}\ \text{cm}^{-1} \times 1\ \text{cm}}$$

After determining the molar concentration of both NP and the protein (KLH or BSA), the conjugation ratio was calculated by dividing the two values.

2.4 Adjuvants.

2.4.1 Alum precipitation.

Alum was precipitated with NP-KLH to enhance antigen presentation. NP-KLH was mixed 1:1 with 9% alum (in dH_2O), before pH adjustment to ≥ 6.5 with 10 M NaOH and/or lower concentrated HCl (0.1M). In a light-protected environment, the mixture was rotated for 1 hour at room temperature to allow for maximum precipitation. Then, the precipitated protein was spun at 10,000 rpm (9,500 x g) for 5 minutes in a microcentrifuge, followed by washing the pellet twice with PBS. Finally, the antigen was resuspended in PBS at 50 µg/20 µL for intraperitoneal (i.p.) injections, or at 10 µg/20 µL for injection into the plantar surface of the foot.

2.4.2 *Bordetella pertussis*.

Heat-inactivated *Bordetella (B.) pertussis* bacteria were used as an adjuvant for both the plantar surface of the foot and i.p. immunisations. *B. pertussis* was added at $1x10^5$ cells per 20µL for plantar surface of the foot injections and $1x10^7$ cells per 200µL for i.p. injections.

2.5 Administrations and Immunisations.

2.5.1 Tamoxifen.

Tamoxifen (Table 2.1) was used when mice carried an inducible form of Cre recombinase (CreERT2 system), such as the *S1pr2*^{ERT2Cre} *Rosa26*^{LSLtdTomato} and HALO

mice (sections 2.2.1 and 2.2.3). Tamoxifen was administered as a 200 µL solution at 20 mg/mL in corn oil (4 mg dose per mouse) and was delivered orally by gavage to each mouse. Tamoxifen solution was prepared by dissolving 200 mg of tamoxifen in 200 µL of 100% ethanol, followed by the addition of 9.8 mL corn oil to yield a final concentration of 20 mg/mL. The solution was protected from light, thoroughly vortexed, and incubated at 42 °C for 3-4 days until it was fully dissolved. Fresh preparation is recommended; therefore, it can be stored at 4°C for short-term storage.

2.5.2 Primary immunisation.

Two strategies were employed to investigate the primary immune response in HALO mice (see section 2.2.3). In the first strategy, mice were immunised intravenously (i.v.) via the tail vein with 200 µL of SRBC per mouse (prepared as per section 2.3.1). The second strategy involved a TD immune response using NP_{27}-KLH precipitated in alum, which was conjugated and precipitated in the lab (see sections 2.32 and 2.4.1). NP_{27}-KLH was administered via i.p. immunisation, with each mouse receiving 50 µg in 200 µL of PBS containing $1x10^7$ cells *B. pertussis*.

Primary immunisation was studied in *Aicda*$^{CreERT2/+}$ mice, IgM$^{g1/g1}$ mice, and IgM$^{g1/g1}$ *Aicda*$^{CreERT2/+}$ mice (see the experimental mice, 2.2.4, 2.2.5, and 2.2.6 respectively). Mice were immunised by injecting into the plantar surface of the foot with precipitated NP_{27}-KLH, receiving 10 µg in 20 µL of PBS per mouse containing $1x10^5$ cells of *B. pertussis*.

2.5.3 Secondary immunisation.

The secondary immune response was studied in *S1pr2*^{ERT2Cre} *Rosa26*^{LSLtdTomato} and HALO mice (sections 2.2.1 and 2.2.3). Mice were primed with alum-precipitated NP_{27}-KLH administered i.p. at 50 µg in 200 µL of PBS containing $1x10^{57}$ cells of *Bordetella pertussis* per mouse, or via the plantar surface of the foot injection at 10 µg in 20 µL of PBS containing $1x10^{5}$ cells of *Bordetella pertussis* per mouse. Boost immunisations were performed 4 weeks later with soluble NP_{27}-KLH i.v. at 20µg or via the plantar surface of the foot at 10µg.

2.6 Tissue preparation for flow cytometry.

2.6.1 Harvesting and processing tissues.

Spleen and popliteal lymph nodes were used in the study. For spleens, one-third was processed for flow cytometry (described in the current section 2.6), while the remaining two-thirds were used for immunofluorescence histology (see section 2.7). For lymph nodes, the entire organ was processed for flow cytometry analysis. After each step of cell processing, the cells were centrifuged for 5 minutes at 1400 rpm (400 x g) at 4°C to remove any residual substances. Flow cytometry staining panels contained reagents for cell-surface markers only.

Tissues were mechanically disrupted using a syringe plunger, resuspended in RPMI 1640 medium, and filtered through a 70 µm cell strainer. After centrifugation, cells were resuspended in FACS buffer (PBS, 2% FBS, 2 mM EDTA) and aliquoted into a V-bottom 96-well plate. To block non-specific FcγRIII (CD16) and FcγRII (CD32) binding

of staining reagents, cells were resuspended in 100 µL of FcR blocking antibody (anti-CD16/32) diluted 1:200 in FACS buffer and incubated for 20 minutes at 4°C. Next, cells were resuspended in 50 µl/well of staining cocktail (see section 2.6.2) diluted in FACS buffer and incubated for 30 minutes at 4°C. The last step was incubation with fixable near-infrared viability dye diluted 1:1000 in 1X PBS, for 20 minutes at 4°C. Cells were washed twice, resuspended in a final volume of 200 µL of FACS buffer, and passed through a 70 µm cell strainer into FACS tubes for acquisition on the LSR Fortessa X-20. Countbeads (AccuCount Blank Particles) were added at 5 µL per tube of the sample before running. All flow cytometry samples were acquired on the same day as tissue harvest.

2.6.2 Staining panels.

Staining panels were optimised to target surface markers relevant to the cell type of interest. All antibodies used for flow cytometry are listed in Table 2.4.

2.6.2.1 Plasma cell staining panel.

This panel was used to analyse plasma cells, germinal centre B cells, and NP-specific cells. Following the FcR blocking step, the staining cocktail included antibodies specific for CD138, B220, TACI, IgG1, IgM, NP-APC reagent, CD19, Fas, CD38, CD86, and CXCR4. The anti-CXCR4 antibody was biotinylated; therefore, a streptavidin-fluorochrome conjugate reagent was used for detection.

2.6.2.2 Tfh cell staining panel.

This panel was used to analyse the activation status of Tfh cells and GC-resident Tfh cells. Following the FcR blocking step, cells were stained and incubated for 1 hour at 4°C with purified rat anti-CXCR5 antibody, diluted 1:25 in FACS buffer. Afterwards, cells were resuspended and incubated for 30 minutes at 4°C with anti-rat IgG1 AlexaFluor647 at a 1:400 dilution in FACS buffer. To block non-specific binding of further rat-derived antibodies to the anti-rat IgG1, cells were resuspended and incubated for 20 minutes at 4°C with 10% normal rat serum. The final staining cocktail included the antibodies specific for CD3, CD4, CD23, PD-1, CD62L, CD44, CD19 and CD90.2.

2.7 Immunofluorescence histology.

2.7.1 Preparation of spleen samples.

2.7.1.1 Fixation and cryopreservation.

Splenic tissue was fixed before cryopreservation (Table 2.6). PFA fixative was used to maintain the tissue morphology, cell membrane integrity [162], and immobilise fluorescent proteins, e.g., eGFP [163]. Spleens were initially immersed in freshly prepared 1% PFA (Table 2.1) for 7-8 hours at 4°C [164], before immersion in a 30% w/v sucrose solution (Table 2.1) overnight at 4℃. Fixed tissue was cryopreserved by embedding (see section 2.7.1.2) the next day [163].

Table 2.6. Two-step process for spleen tissue fixation from mice expressing fluorescent reporters.

Step 1. 1% PFA

Reagent	Final concentration	Amount	Condition
4% PFA	1% (v/v)	10 mL	Stored at 4°C or -20 °C and warmed before use. Avoid freeze/thaw cycles.
PBS	1X	Up to 30 mL	
Total	n/a	100 mL	

Sept 2. 30% Sucrose

Reagent	Final concentration	Amount	Condition
Sucrose	30% (w/v)	30 g	Stored at 4°C, and it is stable for 1-2 months.
PBS	1X	Up to 100 mL	
Total	n/a	100mL	

2.7.1.2 Tissue embedding.

Spleens were placed in a cryomold 15 x 15 mm, which contained Neg-50 Frozen Section Medium. Tissue was placed on dry ice until the embedding medium solidified. This embedding medium preserves spleen sections down to -80°C for long-term storage.

2.7.1.3 Cryosectioning.

A spleen block was cut into 7 µm-thick sections using a cryostat (Bright Company, OTF5000). The cryo-section chamber temperature was set between -15°C and -17°C. The spleen block was left in the cryo-section chamber for up to 30 minutes to reach chamber temperature; care was taken to ensure the tissue did not thaw. Three spleen sections—selected based on their structural integrity—were loaded separately onto Superfrost™ Plus Adhesion Microscope Slides.

2.7.2 Immunofluorescence staining protocol.

2.7.2.1 Antigen retrieval and permeabilisation.

Fixation and embedding processes cross-link proteins in the section, leading to the masking of the antigen epitopes, which can result in weak antibody staining. Therefore, unmasking or antigen retrieval serves to reveal the epitopes of the antigen and improve staining intensity [162, 165]. To this end, slides were left for 30 minutes in 0.5% w/v saponin in PBS solution as the first step of the retrieval procedure to permeabilise the tissue. Permeabilising the tissue is an essential step when the target antigen is intracellular, such as transcription factor IRF4. Next, tissues were immersed in a 0.2% v/v Triton solution (Table 2.7) for 20 minutes, before staining antibodies were added.

Table 2.7. Preparation of reagents and buffers used in immunofluorescent staining.

0.2% Triton x-100			
Reagent	Final concentration	Amount	Condition
Triton x-100	0.2% v/v	20 µL	Stored at room temperature.
PBS	1X	100 mL	

2.7.2.2 Immunofluorescence staining panel.

Spleen sections were allowed to reach room temperature for 20 minutes, followed by rehydration for about 30 minutes in a saponin buffer. Splenic sections were blocked with 75 µL of normal horse serum and then kept in an air-moistened, humidified dark chamber shaker at very low rocking speed. Next, sections were incubated with the primary antibody, followed by their corresponding fluorophore-conjugated secondary, each for 1-2 hours. After each step, slides were kept in a washing buffer for 10 minutes. In some staining conditions, a tertiary stain was required. Slides were allowed to air-

dry (to avoid trapping air bubbles) before a drop of mountant medium was added per tissue section, followed by the addition of the coverslip. Slides were stored in the dark at 4°C overnight, and images were acquired the next day. Staining reagents are listed in Table 2.1; buffers in Table 2.8; and antibodies in Table 2.5.

Table 2.8. Preparation of reagents and buffers used in immunofluorescent staining.

10% Antibody diluent			
Reagent	Final concentration	Amount	Condition
BSA	10% w/v	10 g	Stored at -20°C, and it is stable for 5-6 months. Avoid freeze/thaw cycle
PBS	1X	100 mL	

10% Blocking buffer			
Reagent	Final concentration	Amount	Condition
Normal horse serum	10% v/v	10 µl	Freshly prepared
Antibody diluent	10%	100 µL	

Washing buffer			
Reagent	Final concentration	Amount	Condition
Saponin	0.5% w/v	2.5 g	Freshly prepared
PBS	1X	500 mL	

2.7.3 Immunofluorescence Imaging.

Immunofluorescence images were acquired using four channels of the Zeiss AxioScan.Z1 Slide Scanner (Carl Zeiss Microscopy GmbH, Jena, Germany) and processed using Zen v3.1 (blue edition). The red fluorescence of tdT was excited using an excitation filter of 545/25 nm and acquired using the 635/70 nm emission filter. The eGFP was imaged using 470/40 nm excitation and 525/40 nm emission. BV421 staining was imaged using 356 nm excitation and a 445/50 nm emission filter. Alexa Fluor 674 was imaged using a 620/60 nm excitation and 700/75 nm emission filter.

2.7.4 Quantification of GC-associated cells following imaging.

Splenic sections from HALO mice were stained with antibodies against CD4 (helper T cells), IgD (FO B cells), and GFP. Images that were acquired on Zeiss AxioScan.Z1 Slide Scanner in CZI format were processed at 50 µm with QuPath software (the Centre for Cancer Research and Cell Biology, Queen's University Belfast, UK). Four-channel parameters were used to enhance the contrast between cell populations: blue for $CD4^+$ T cells, white for IgD^+ FO B cells, red for *S1pr2*$^{tdT+}$-expressing cells, and green for Blimp-1^{GFP+}-expressing cells. GC-matured *S1pr2*$^{tdT+}$ Blimp-1^{GFP+} PB-PCs were detected by double expression of red and green reporter proteins (yellow). To facilitate the annotation of GC-matured double-positive (DP) PB-PCs, the white channel for the IgD staining was removed to minimise non-specific fluorescence and ensure that only the original signal of DP PB-PCs was captured by the annotation software (Figure 2.1A). Regions of interest were manually selected using the polygon tool at a scale of 1mm, ensuring that only intact tissue sections were included and avoiding areas with poor tissue integrity. The same approach was applied to define the T zone and GC regions, using regions of interest scaled between 250-500µm (Figure 2.1B). GC-matured *S1pr2*$^{tdT+}$ Blimp-1^{GFP+} PB-PCs were identified at 20-50µm, counted manually (Figure 2.1C and D) and reported as the number per mm² for each defined area. Figure 2.1 shows an example of how GC-matured *S1pr2*$^{tdT+}$ Blimp-1^{GFP+} PB-PCs were identified and counted using QuPath software.

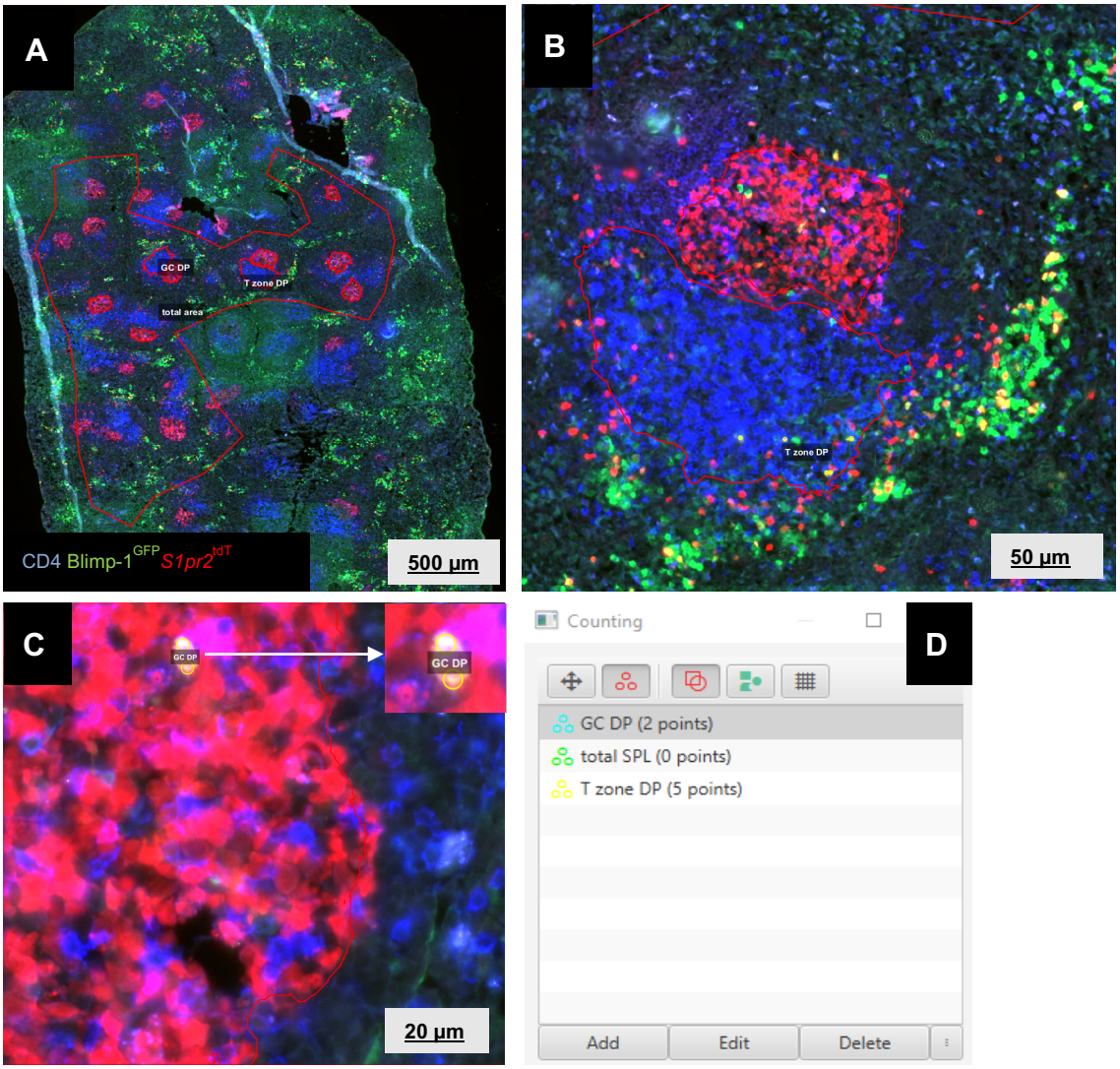


Figure 2.1. Immunofluorescent analysis of GC-matured *S1pr2*^{tdT} Blimp-1^{eGFP} PB-PCs in HALO mice.

An example image of a splenic section from a HALO mouse stained for T-cell zones (CD4), FO B cells (IgD), and Blimp-1^{GFP} PB-PCs (anti-GFP). (A) Region of interest and (B) GC and T-cell zones outlined in red. (C) An example image showing annotation of two GC-matured *S1pr2*^{tdT} Blimp-1^{GFP} PB-PCs within the GC region. (D) A QuPath counting table listing three annotated regions, where each GC-matured *S1pr2*$^{tdT+}$ Blimp-1^{GFP+} PB-PC is represented as a single point. GC DP refers to germinal centre double positive. The CZI-format image was processed at 50 µm, and GC-matured *S1pr2*$^{tdT+}$ Blimp-1^{GFP+} PB-PC were identified at 20 µm.

The GC-T cell zone interface (GTI) region was defined as the narrow band adjacent to the GC border facing the T cell zone (Figure 2.2), extending approximately 30-40 µm (corresponding to ~2-3 cell diameters) [8]. Using a fixed-width band of the GTI region ensures cells are counted spatially linked to the GC and in the earliest phase of GC exit. To identify GC-derived IRF4^{+} *S1pr2*$^{tdT+}$ Blimp-1^{GFP+} PB-PCs, splenic sections were stained using the same staining approach, except IRF4 staining replaced CD4.

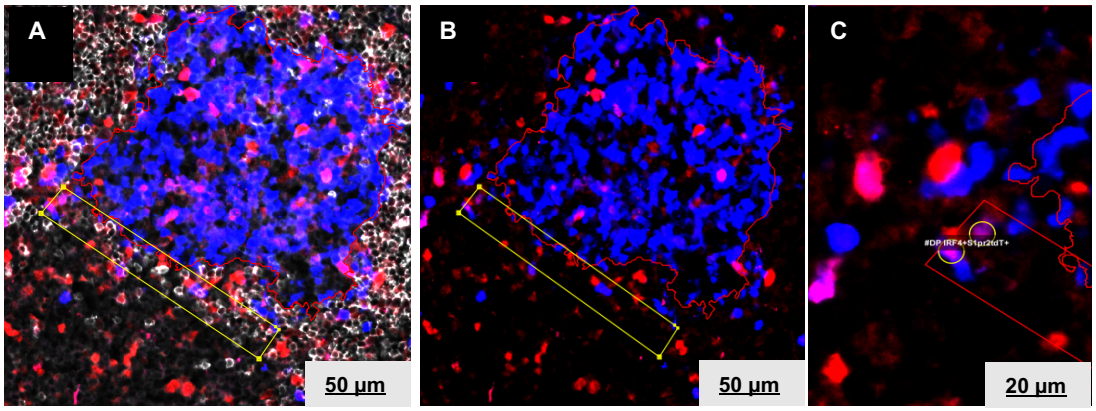


Figure 2.2. Immunofluorescent analysis of GC-derived IRF4^{+} *S1pr2*^{tdT} Blimp-1^{GFP} PB-PCs in HALO mice.
An example image of a splenic section from a HALO mouse stained for IgD^{+} FO B cells (white) and IRF4^{+}-expressing cells (blue). **(A)** The GC region is outlined in red, and the GTI is indicated with a yellow rectangular outline. **(B)** The same image as in (A) is shown after removal of the IgD white channel. **(C)** An example image shows annotation of two GC-derived IRF4^{+} *S1pr2*^{tdT} PB-PCs within the GTI region. The CZI-format image was processed at 50 µm with QuPath software, and GC-derived IRF4^{+} were identified at 20 µm.

2.8 Enzyme-linked immunosorbent assay (ELISA).

Whole blood from mice was obtained by cardiac puncture, incubated for 1 hour at 37°C to allow clotting, and then centrifuged at 2500 rpm (1,250 x g) for 5 minutes at room temperature. Serum was carefully aspirated from the red blood cell clot, aliquoted, and

stored at -20°C. Buffers used for the ELISA are listed in Table 2.9. Maxisorp plates were coated overnight at 4°C with NP_2-BSA at a concentration of 5 µg/mL in coating buffer. Following three washes with wash buffer, plates were blocked with 200 µL of blocking buffer for 1 hour at 37°C to prevent non-specific binding. After three washes, 5 µL of serum was added to the first well containing 145 µL of dilution buffer. For a 1:3 serial dilution, 50 µL was transferred from the first well to the next well containing 100 µL of dilution buffer. This process was repeated four more times, ensuring each well had a final volume of 100 µL. Diluted serum samples were incubated for 1 hour at 37°C before three washes.

Table 2.9. Preparation of buffers and reagents for the ELISA assay.

1x PBS			
Reagent	Final concentration	Amount	Condition
PBS	1x	2 tablets	Freshly prepared
dH_2O	n/a	1 L	
Coating buffer			
Reagent	Final concentration	Amount	Condition
Carbonate-Bicarbonate Buffer Capsule	0.05 M	One capsule	Stored at 4°C for short term.
dH_2O	n/a	100 mL	
NP_2-BSA in the coating buffer			
Reagent	Final concentration	Amount	Condition
4.9 mg / mL NP_2-BSA	5 µg/mL	11.2 µL	Freshly prepared
Coat buffer	0.05 M	11 mL	
Blocking buffer			
Reagent	Final concentration	Amount	Condition
BSA	1%	1.25 g	Stored at 4°C in a sterile condition.
PBS	1x	mL	
Wash buffer			
Reagent	Final concentration	Amount	Condition
PBS	1x	1L	Freshly prepared
Tween20	0.05%	500 µL	
Dilution buffer			

Reagent	Final concentration	Amount	Condition
BSA	1%	1.25 g	
PBS	1x	125 mL	Freshly prepared
Tween20	0.05%	62.5 µL	

AP-conjugated detection antibodies for one plate			
Reagent	Final concentration	Amount	Condition
AP Goat anti-IgM	1:4000	2.75 µL	
AP Goat anti-IgG1	1:1000	11 µL	Freshly prepared
Dilution buffer	1% BSA (w/v), 0.05% Tween 20 (v/v) in 1X PBS	11 mL	

Substrate buffer			
Reagent	Final concentration	Amount	Condition
Tris buffer	n/a	One tablet	
pNPP	n/a	One tablet	Freshly prepared.
dH_2O	n/a	20 mL	

Detection antibodies AP-IgG1 or AP-IgM (

Table 2.3) were added at 100 µL/well, followed by incubation at 37°C for 1 hour and three further washes. For detection, 100 µL/well of substrate buffer was added, and plates were incubated at 37°C for colour development. The optical density was measured at 405 nm using a microplate reader (SpectraMax® ABS Plus). Relative antibody titres were calculated by plotting the dilution against the optical density values. The antibody titre value for each sample was defined as the dilution at which the optical density intersected the threshold line, which was set above the background.

2.9 Data analysis.

Flow cytometry data were acquired on the LSR Fortessa X-20 and processed with FACS Diva v8 software. Single-colour antibody-stained samples were acquired to set voltages and perform compensations. Flow cytometry data were analysed using FlowJo™ v10.10.0 (BD Bioscience). Data was graphed using GraphPad Prism v10.4.1. A description of the statistical tests used is provided in the figure legends.

Chapter 3. A Study on Early Germinal Centre-Derived Plasma Cells in HALO Mice

3.1 Introduction.

Studying PC biology may help gain a better comprehension of multiple myeloma, a cancer of abnormal PCs, by providing insight into the mechanisms that regulate PC differentiation, survival, and antibody secretion, which are frequently dysregulated in malignant PCs. Additionally, dysregulated antibody production by PCs contributes to autoimmune diseases such as lupus and rheumatoid arthritis. Therefore, understanding PC biology may inform the development of therapeutic strategies for both PC malignancies and antibody-mediated autoimmune conditions.

Studies have proposed flow cytometry-based approaches for identifying PC subpopulations. The commonly used strategy to define mature PCs relies on detecting high levels of CD138 and reduced B220 and CD19 expression. However, analysis of cells from the spleen and bone marrow of Blimp-1^{GFP} reporter mice revealed a significant fraction of CD138^{hi} B220^{low} Blimp-1^{GFP}-negative cells, highlighting heterogeneity within the PC compartment [148]. A combination of markers, including CD138, TACI, B220, and CD19, enables discrimination between proliferating plasmablasts and two subsets of nonproliferating PCs.

Additionally, an alternative flow cytometry protocol has been established to distinguish immature and mature PC subsets in standard inbred mice without a Blimp-1^{GFP} reporter

[166]. This approach incorporates stem cell antigen-1 (Sca-1, also known as Ly6A/E) alongside other markers to enhance the separation of PC subpopulations across various tissues (bone marrow, spleen, and Peyer's patch).

Investigating the early output of PCs from GC provides insight into the initial stages of antibody production in response to an immune challenge. While much is known about the early stages of B cell development, genetically modified mice have helped clarify the molecules and processes involved in PC development and activity. Our lab has developed a novel model, *S1pr2*^{CreERT2} *Rosa26*^{LSLtdTomato} *Prdm1*^{GFP}, also known as triple mice, which enables the tracking and mapping of the growth and differentiation of GC B cells into PC (Figure 3.1). Breeding was done by crossing the offspring generated from *S1pr2*^{CreERT2} x *Rosa26*^{LSLtdTomato} mice with *Prdm1*$^{GFP/wt}$ mice. The decision to choose this breeding system is attributed to the efficiency of *S1pr2*^{CreERT2} in GC B cell fate mapping, the efficiency of Cre-mediated recombination of *Rosa26*^{LSLtdTomato}, and PC-specific *Prdm1*$^{GFP/wt}$. Triple transgenic mice carry three specific genetic modifications, which include: 1) a tamoxifen-inducible Cre allele, *S1pr2*^{CreERT2}, that allows for the inducible expression of Cre recombinase controlled by the expression of S1pr2; 2) a Cre-inducible fluorescent reporter, *Rosa26*^{LSLtdTomato}, which expresses tandem dimer tomato (tdT) upon Cre recombinase activity, enabling the visualisation and tracking of cells where Cre recombinase is active; 3) a *Prdm1*$^{GFP/wt}$ reporter allele that expresses green fluorescent protein (GFP) upon *Prdm1* expression. After immunisation, three types of cells will be identified simultaneously: (1) GC-derived *S1pr2*^{tdT} B cells, (2) Blimp-1^{GFP} PB-PCs, which include both EF-derived PB-PC and GC-derived PB-PC formed prior to tamoxifen administration, and (3) GC-

matured *S1pr2*^{tdT} Blimp-1^{GFP} PB-PCs labelled after tamoxifen administration (Table 3.1).

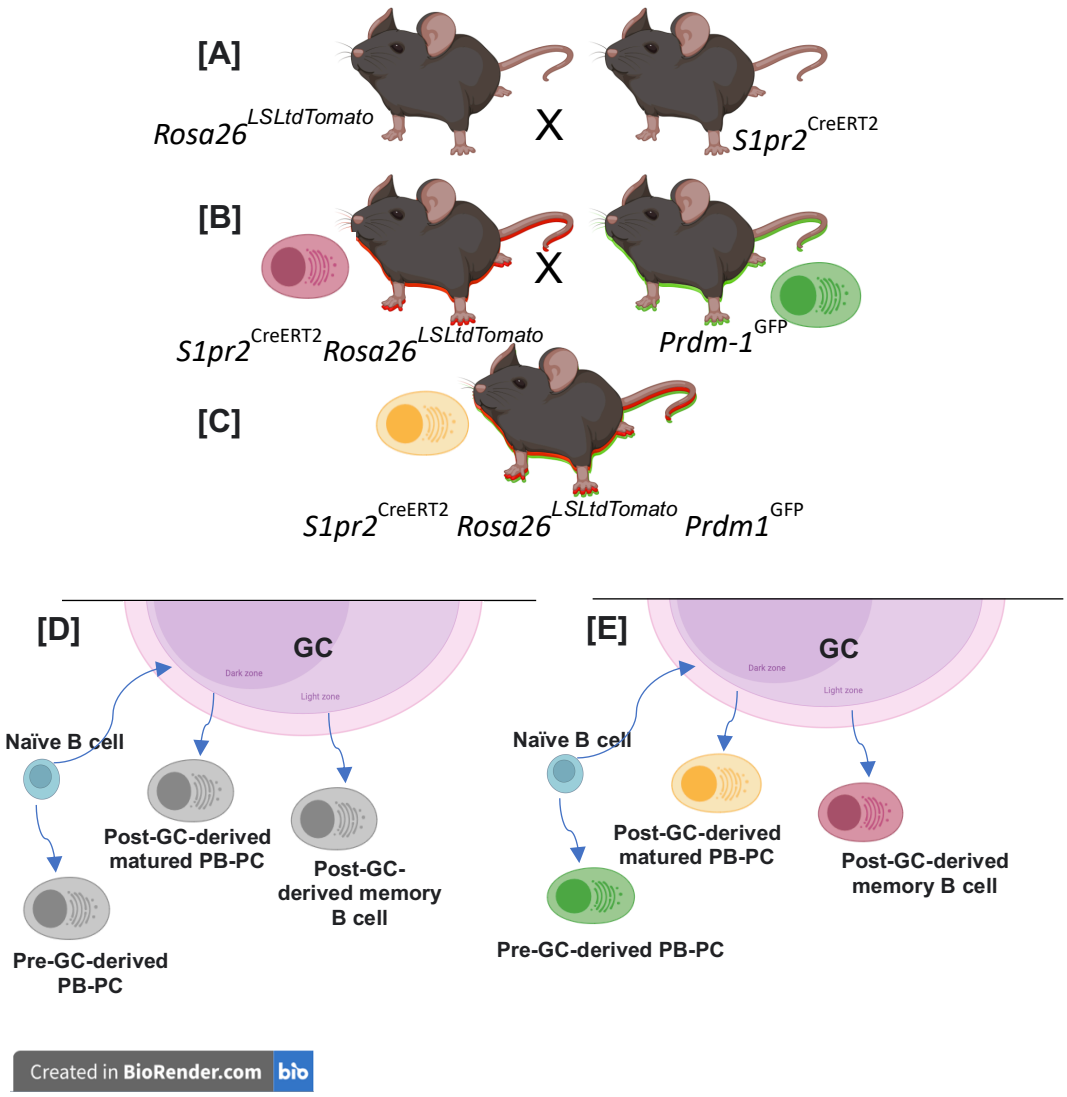


Figure 3.1 Schematic illustrating the principle underlying the generation of PB-PC responses in HALO mice.

This novel mouse model enables the simultaneous discrimination between EF-derived PB-PC and GC-derived PB-PC. A total of 54 HALO mice were used across three experimental protocols. Panels A - E schematically depict the following: **(A)** Mice with the fusion protein of Cre recombinase and estrogen receptor 2 (CreERT2) were crossed with *Rosa26*^{LSLtdTomato} mice. **(B)** The offspring were then crossed with mice encoding the *Prdm1*^{GFP} to generate triple alleles mice (HALO). **(C)** In HALO mice, the S1pr2 promoter-controlled ERT2Cre gene is activated following tamoxifen administration, leading to permanent expression of tdTomato (tdT), while the *Prdm1*

promoter drives expression of GFP^{+}. **(D)** and **(E)** Schematics illustrating how activated naïve B cells are simultaneously labelled in HALO mice.

Table 3.1. Definition of B cell populations in the triple transgenic mice.

Population	*S1pr2*^{tdT}	Blimp-1^{GFP}	Interpretation
GC B cells	+	–	GC B cells within the cluster are identified by expression of *S1pr2*^{tdT} (appearing red).
EF-derived PB-PC	–	+	GC-independent PB-PCs are identified by expression of Blimp-1^{GFP} (appearing green).
GC-derived PB-PC (pre-tamoxifen)	–	+	GC-derived PB-PCs are identified by expression of Blimp-1^{GFP} (appearing green).
GC-derived PB-PC (post-tamoxifen)	+	+	GC-derived PB-PCs are identified by co-expression of tdT and GFP (appearing yellow).
GC-derived B cells	+	–	Memory B cells are identified by expression of *S1pr2*^{tdT} (appearing red).

For simplicity, the mouse model expressing *S1pr2*^{CreERT2} *Rosa26*^{LSLtdTomato} *Prdm1*$^{GFP/wt}$ will hereafter be referred to as *S1pr2*^{tdT} Blimp-1^{GFP} throughout the text.

Breeding HALO mice to generate sufficient offspring carrying all three alleles takes several months and is associated with relatively low breeding efficiency. Initial development of the model showed that only 35 HALO mice were generated over approximately 16 months, with only 15 mice ultimately available for experimental use. In addition, interbreeding HALO mice resulted in poor pup survival, likely influenced by the embryonic lethality associated with homozygous *Prdm1*^{GFP} alleles. Consequently, these breeding limitations limit experimental throughput, reduce sample sizes, and

constrain the ability to conduct repeated or large-scale studies with this model. During the COVID-19 lockdown, the number of breeding pairs was minimised, which further restricted the expansion of the HALO colony before the commencement of this project in 2022. In the current study, 54 HALO mice were successfully validated to investigate PC induction through different immunisation routes. Despite these practical limitations, the HALO system provides a unique approach for simultaneously tracking GC-derived and extrafollicular PC responses in vivo.

The objective of this project was to investigate a fluorescent reporter mouse model that allows for the analysis of GC-matured PCs by flow cytometry and localisation in tissue, distinguishing them from those generated in the EF response. EF-derived Blimp-1^{GFP} PCs are associated with low affinity, whereas GC-matured *S1pr2*^{tdT} Blimp-1^{GFP} PCs are associated with high affinity. Accordingly, the triple transgenic mice have been named HALO mice and will be referred to as such throughout the text. Implementing this model facilitates the tracking and analysis of immune responses related to GC-matured PC differentiation. It can be used to study autoimmune diseases and immunodeficiencies, as well as to identify antibodies with high affinity and specificity. The aims of this study were as follows:

1. To evaluate the expression of Blimp-1^{GFP} using immunofluorescence staining in histological analysis.
2. Investigation of GC-matured CD138^{+} TACI^{+} PB-PCs during PC maturation phases.
3. Participation of GC B cells to mature into *S1pr2*^{tdT} Blimp-1^{GFP} PB-PC.

4. Exploring GC-matured PC differentiation during the different immunisation routes with model TD antigen NP-KLH.
5. Localisation of GC-matured PB-PC in histology.

3.2. Results.

3.2.1. The efficiency of GC-matured PB-PC labelling in HALO mice following primary SRBC immunisation.

The early stages of the B cell response in the HALO mouse model were studied by rapidly inducing a primary response in the spleen with SRBCs to elicit polyclonal B cell activation [167]. To provide context for the results described below, we first outline the experimental protocol used to generate the data. *S1pr2*^{tdT} Blimp-1^{GFP} mice were immunised intravenously (i.v.) with 2 × 10^8 SRBCs on day 0 (experimental protocol shown in Figure 3.2). The next step in the protocol is to introduce Cre recombinase activity. Therefore, a single dose of tamoxifen (200 µL of 20 mg / mL in corn oil) was administered orally by gavage on days 3, 4, or 6. Spleens were harvested after 48 hours from Cre induction – days 5, 6, and 8 – to capture different phases of the B cell responses for downstream analysis, including flow cytometry and immunofluorescence. Each spleen was bisected, with one-third processed for flow cytometry and the remaining tissue embedded in embedding media for immunofluorescence. However, the results from day 8 were based on only two mice, as two additional mice were later confirmed not to carry the required HALO genotype and were therefore excluded from the analysis. Mice were routinely genotyped by PCR by the animal facility to confirm the presence of the required transgenic alleles. During analysis, flow cytometry data revealed Blimp-1^{GFP} cells lacking tdT expression, which

was inconsistent with the expected reporter profile. This observation prompted retrospective verification, confirming that these two mice did not carry the complete HALO genotype.

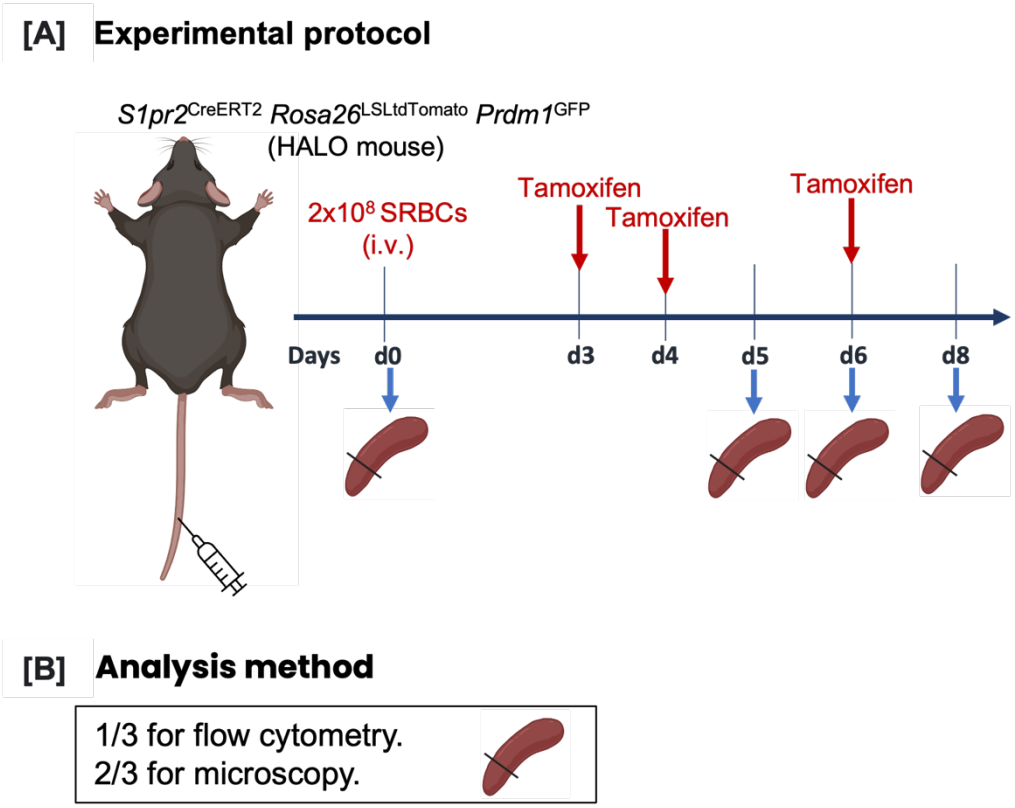


Figure 3.2. Schematic of the experimental procedure for primary immunisation in HALO mice with SRBCs.
(**A)** On day 0, 23 HALO mice were immunised i.v. with $2x10^8$ SRBCs. A single mouse was left unimmunised, treated with tamoxifen, and harvested on day 0. Mice received one dose of tamoxifen (200 µL of 20 mg/mL in corn oil) 48 hours before harvest on day 5 (n=10 mice), day 6 (n=11 mice), and day 8 (n=2 mice). **(B)** The chart shows the allocation of the spleen: one-third of the spleen was used for FACS analysis, and two-thirds was used for immunofluorescence staining.

We sought to characterise the GC-matured *S1pr2*$^{tdT+}$ Blimp-1^{GFP+} PB-PC response in HALO mice following primary immunisation with SRBCs by performing flow cytometry analyses of *S1pr2*^{tdT} and Blimp-1^{GFP} expression in splenic CD138$^+$ PB-PCs (Figure 3.3

A), Fas^{hi} GC B cells (Figure 3.3B), CD38^{hi} non-GC B cells (Figure 3.3C), and CD138^{+} TACI^{+} PB-PCs (Figure 3.3D) populations. Gates were defined using biological reference populations. Initial gates were set on forward and side scatter to identify

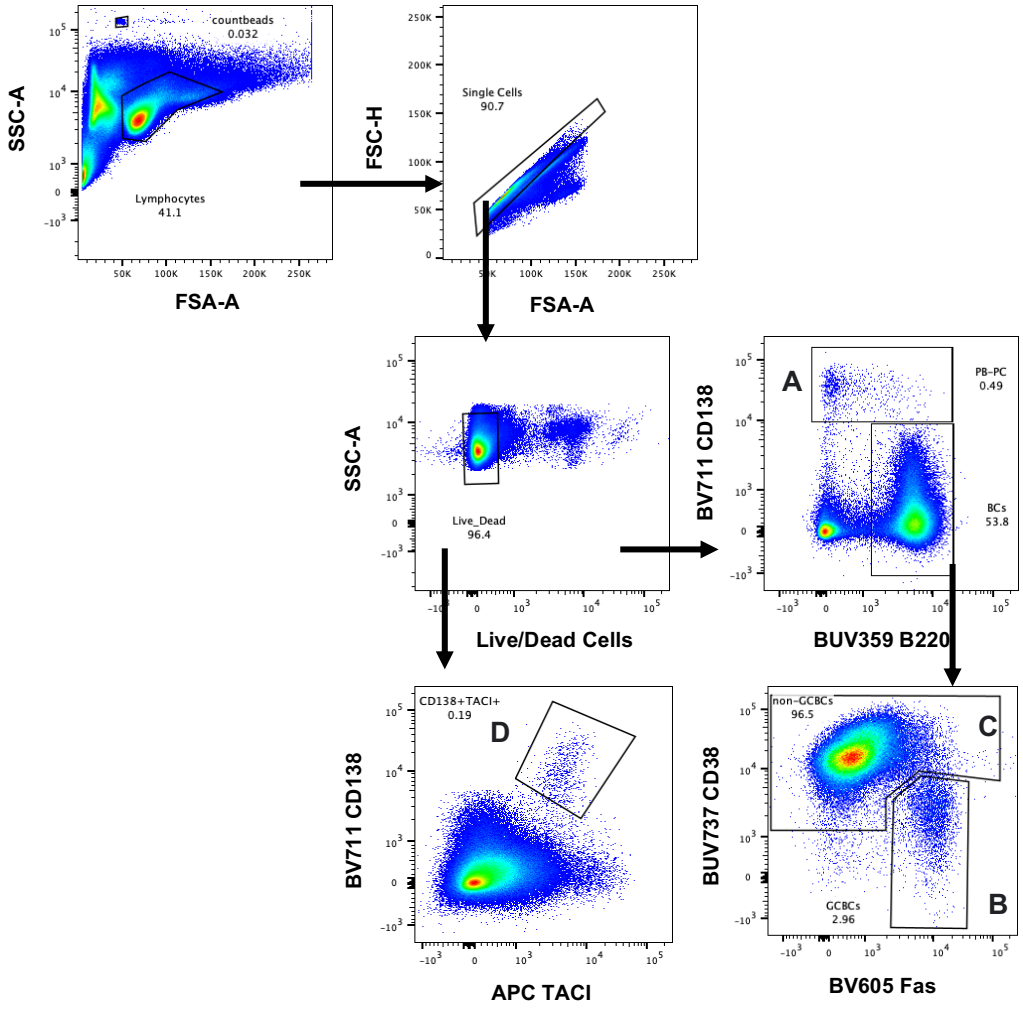


Figure 3.3. Gating strategy for the analysis of splenic GC-matured *S1pr2*$^{tdT+}$ Blimp-1^{GFP+} PC in HALO mice.

Representative flow cytometric gating strategy from *S1pr2*^{CreERT2} *Rosa26*^{LSLtdTomato} *Prdm1*^{GFP} mouse at day 6 of the primary SRBC response to quantify GC-matured *S1pr2*$^{tdT+}$ Blimp-1^{GFP+} PB-PC response from the experimental protocol outlined in Figure 3.1. GC-matured *S1pr2*$^{tdT+}$ Blimp-1^{GFP+} PC response was analysed within: **(A)** CD138^{+} PB-PC, **(B)** Fas^{hi} GC B cells, **(C)** CD38^{hi} non-GC B cells, and **(D)** TACI^{+} CD138^{+} PB-PC

lymphocytes, followed by doublet discrimination and live/dead gating. Subsequent gates for B cell subsets were established based on known marker expression patterns and validated using non-immunised control mice. live/dead exclusion was then applied in parallel gating strategies depending on the downstream population of interest: CD138 and TACI were used to define PB-PC, whereas CD138 and B220 were used to define B cell subsets. The $B220^{+}$ B cell fraction was subsequently subdivided using CD38 and Fas expression.

The predicted distribution of *S1pr2*^{tdT} and Blimp-1^{GFP} expression is shown in Figure 3.4, where the upper left quadrant is *S1pr2*$^{tdT-}$ Blimp-1^{GFP+} PB-PC (green quadrant), the upper right quadrant is GC-matured *S1pr2*$^{tdT+}$ Blimp-1^{GFP+} PB-PC (yellow quadrant), and the bottom right quadrant is GC-experienced *S1pr2*$^{tdT+}$ memory B cells (red quadrant). Before investigating the responses of *S1pr2*^{tdT} and Blimp-1^{GFP} in treated mice, we first established baseline expression levels in a HALO mouse that was neither immunised nor treated with tamoxifen (Figure 3.5). Flow cytometric analyses were performed on $CD138^{+}$ PB-PCs and Fas^{hi} GC B cells to assess the baseline fluorescence of *S1pr2*^{tdT} and Blimp-1^{GFP} expression. The values were compared with the expression patterns observed in immunised, tamoxifen-treated HALO mice (positive control) and in a non-immunised wild-type mouse (negative control). As shown in Figure 3.5, panel B, the untreated HALO mouse that was neither immunised nor tamoxifen-treated (HALO NI-NT) exhibited 66.9% $CD138^{+}$ Blimp-1^{GFP+} PB-PCs and only 1.8% GC-matured $CD138^{+}$ *S1pr2*$^{tdT+}$ Blimp-1^{GFP+} PB-PC. In panel D, the same HALO NI-T mouse displayed 2.58% Fas^{hi} Blimp-1^{GFP+} PB-PCs expression, 6.44% GC-matured Fas^{hi} *S1pr2*$^{tdT+}$ Blimp-1^{GFP+} PB-PC, and 76.4% GC-derived Fas^{hi} *S1pr2*$^{tdT+}$ B cells. To accurately define fluorescence thresholds for *S1pr2*$^{tdT+}$ and Blimp-

1^{GFP+}, mice expressing only a single reporter—either Blimp-1^{GFP+} or *S1pr2*$^{tdT+}$—were used as controls. These signal-reporter controls allowed independent determination of gating boundaries for each fluorophore. Thresholds were set above the background fluorescence detected in the wild-type control to ensure that only true positive populations were included in the analysis.

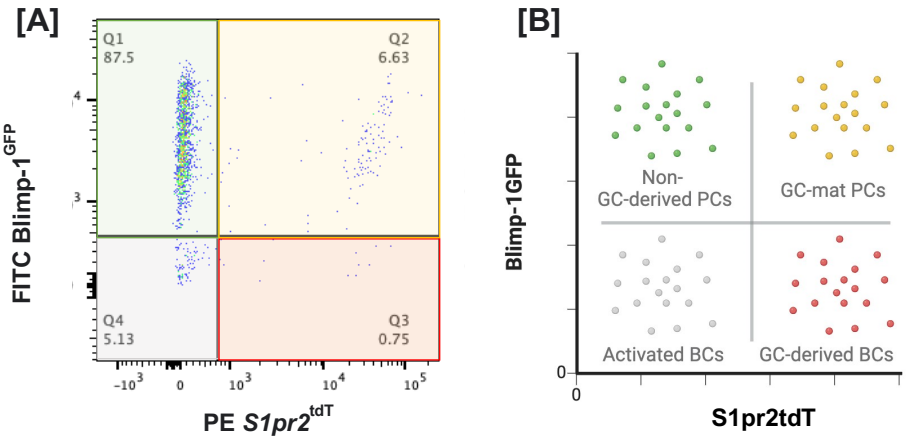


Figure 3.4. Predicted output of GC-matured *S1pr2*$^{tdT+}$Blimp-1^{GFP+} PC in HALO mice.
Representative data and schematic plots show results gated from CD138^{+} B220$^{+/-}$ PB-PC populations within lymphocytes (A), followed by further pairing with FITC-labelled Blimp-1^{GFP} and PE-labelled *S1pr2*^{tdT} (B). The upper left quadrant (green) contains Blimp-1^{GFP+} expressing PCs, the upper right quadrant (yellow) represents GC-derived *S1pr2*$^{tdT+}$Blimp-1^{GFP+} PCs, the bottom left quadrant shows activated B cells, and the bottom right quadrant (red) contains *S1pr2*$^{tdT+}$ expressing memory B cells.

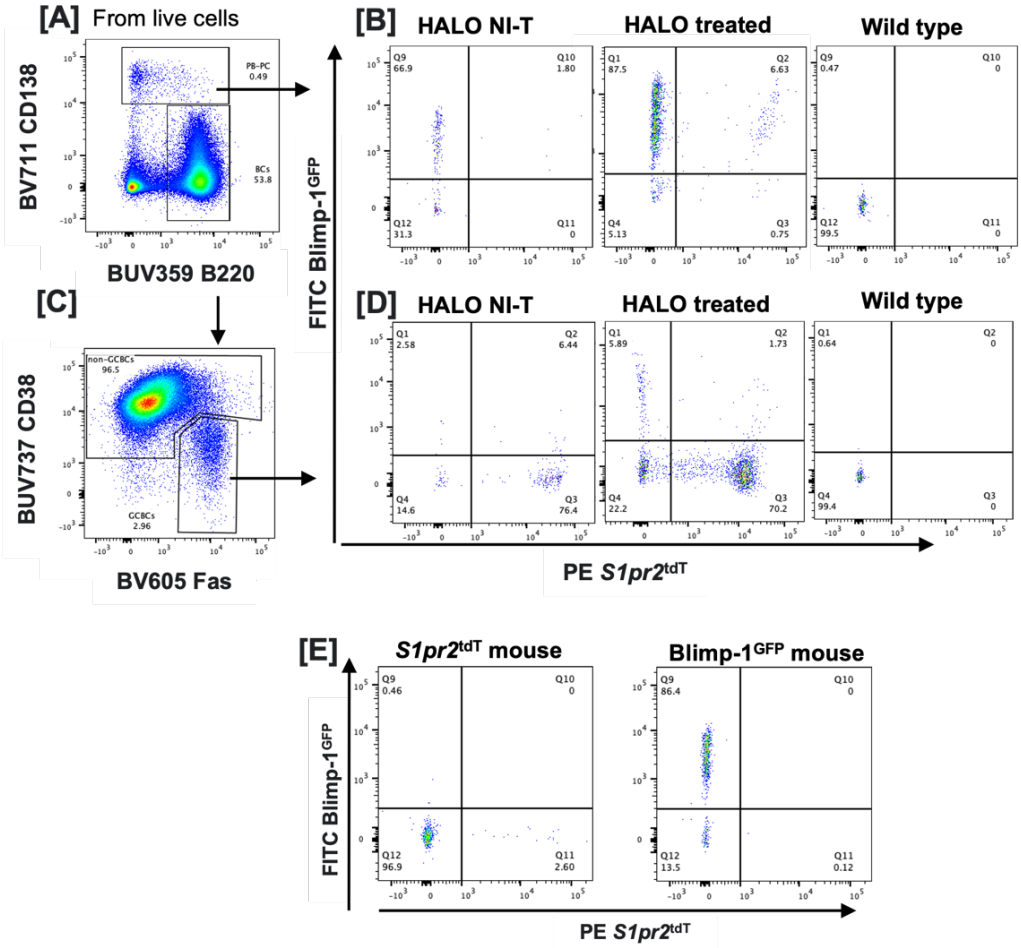


Figure 3.5. Baseline of *S1pr2*^{tdT} and Blimp-1^{GFP} expression in a HALO mouse. **(A)** CD138^{+} PB-PCs were gated and further analysed for the expression of *S1pr2*^{tdT} and Blimp-1^{GFP}. **(B)** Representative baseline fluorescence of *S1pr2*^{tdT} and Blimp-1^{GFP} (gated from CD138^{+} PB-P) showing HALO mouse not immunised but received tamoxifen (HALO NI NT) compared to treated-HALO mouse (positive control), and a non-immunised wild-type mouse (negative control). **(C)** Fas^{hi} GC B cells were gated from B220^{+} B cells and analysed for the expression of *S1pr2*^{tdT} and Blimp-1^{GFP}. **(D)** Representative baseline fluorescence of *S1pr2*^{tdT} and Blimp-1^{GFP} (gated from Fas^{hi} GC B cells) showing HALO mouse not immunised but received tamoxifen (HALO NI NT) compared to a treated-HALO mouse (positive control) and a non-immunised wild-type mouse (negative control). **(E)** Representative flow cytometry threshold plots of *S1pr2*^{tdT} (from *S1pr2*^{tdT} mouse), and Blimp-1^{GFP} (from Blimp-1^{GFP} mouse). HALO NI NT data were derived from a single experiment in which the mouse was not immunised but was treated with tamoxifen. Wild-type mice served as a baseline control to define red and green auto-fluorescence during flow cytometric analysis. The treated HALO mouse is a representative example illustrating *S1pr2*^{tdT} and Blimp-1^{GFP} flow cytometric plots.

3.2.1.1 HALO mice showed that EF- and GC-matured *S1pr2*$^{tdT+}$ Blimp-1^{GFP+} PB-PC responses dominate at day 5, and GC-derived *S1pr2*$^{tdT+}$ PB-PC dominate at day 6.

Based on the defined gating strategy, splenic B cells were identified by pairing with the CD138 PB-PC marker and the B220 B cell lineage marker (Figure 3.6A). CD138^{+} PB-PC have more mature phenotypic characteristics [166]. The number of CD138^{+} PB-PC did not change across all analysis days, although the distribution at day 6 appeared more clustered, suggesting consistent behaviour among those samples (Figure 3.6B).

CD138^{+} PB-PCs were then further analysed for GC-matured *S1pr2*$^{tdT+}$ Blimp-1^{GFP+} expression by gating on FITC for Blimp-1^{GFP+} and PE for *S1pr2*$^{tdT+}$ (Figure 3.6C). The number and frequency of CD138^{+} *S1pr2*$^{tdT-}$ Blimp-1^{GFP+} PB-PC (Figure 3.6D and G), which represent EF-derived PB-PCs, were the dominant CD138^{+} PB-PC population across all analysis days, compared to GC-matured CD138^{+} *S1pr2*$^{tdT+}$ Blimp-1^{GFP+} PB-PCs and GC-derived CD138^{+} *S1pr2*$^{tdT+}$ Blimp-1^{GFP-} PB-PC (Figure 3.6E, F, H, and I). The frequency of GC-matured *S1pr2*$^{tdT-}$ Blimp-1^{GFP+} PB-PC within the CD138^{+} population significantly increased at the earliest labelling time point (day 5) compared to day 6 (Figure 3.6G). The number of GC-matured *S1pr2*$^{tdT+}$ Blimp-1^{GFP+} PB-PC within the CD138^{+} population increased at day 5—with greater disparity—but declined two days later, although the change was not statistically significant (Figure 3.6E). The number and frequency of GC-derived CD138^{+} *S1pr2*$^{tdT+}$ Blimp-1^{GFP-} PB-PC (Figure 3.6F and I) rose at day 6, although this increase was not statistically significant compared to day 5 or day 8.

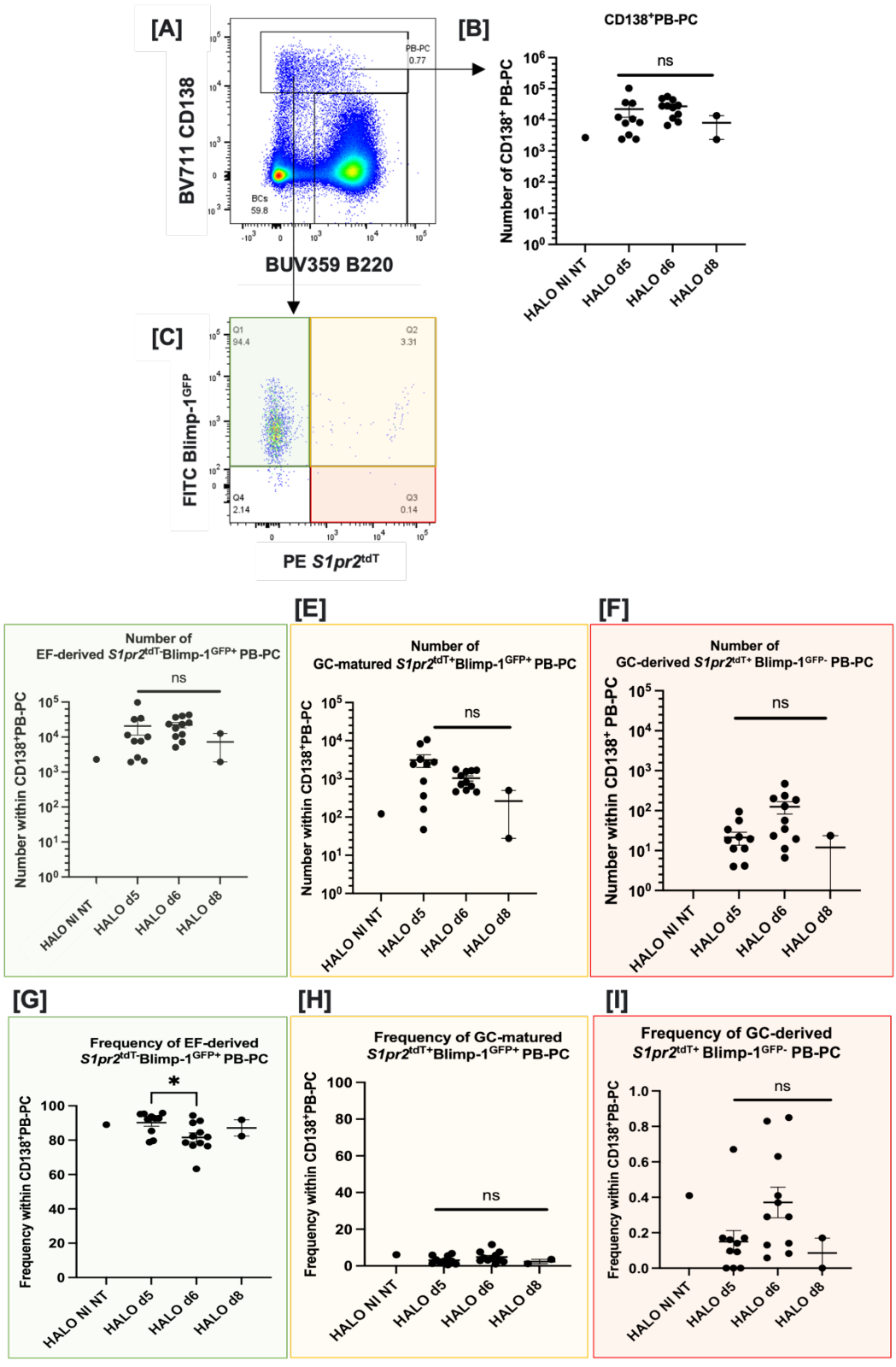


Figure 3.6. CD138⁺ PB-PC response analysis in HALO mice following primary SRBCs immunisation.
The experimental protocol is illustrated in Figure 3.2.

(A) Representative data plot of CD138^{+} PB-PCs was gated from live/dead cells. **(B)** The number of CD138^{+} PB-PCs (mean ± SEM). **(C)** CD138^{+} PB-PCs were further analysed for GC-matured *S1pr2*^{tdT} Blimp-1^{GFP} PB-PC expression. **(D)** The number of EF-derived *S1pr2*$^{tdT-}$ Blimp-1^{GFP+} PB-PC within the CD138^{+} PB-PCs (mean ± SEM). **(E)** The number of GC-derived *S1pr2*$^{tdT+}$ Blimp-1^{GFP+} PB-PC within the CD138^{+} PB-PCs (mean ± SEM). **(F)** The number of GC-derived *S1pr2*$^{tdT+}$ Blimp-1^{GFP-} PB-PCs within the CD138^{+} PB-PCs (mean ± SEM). **(G)** The frequency of EF-derived *S1pr2*$^{tdT-}$ Blimp-1^{GFP+} PB-PC within the CD138^{+} PB-PCs (mean ± SEM). **(I)** The frequency of GC-derived *S1pr2*$^{tdT+}$ Blimp-1^{GFP+} PB-PC within the CD138^{+} PB-PCs (mean ± SEM). **(J)** The frequency of GC-derived *S1pr2*$^{tdT+}$ Blimp-1^{GFP-} PB-PCs within the CD138^{+} PB-PCs (mean ± SEM). Each symbol represents one mouse. Data was obtained from three independent experiments where n = 10 at day 5, n = 11 at day 6, and n = 2 at day 8. Statistical tests were performed by a one-way ANOVA, a nonparametric test, and analysis with the Kruskal-Wallis test (ns $p > 0.05$). NI NT refers to a HALO mouse neither immunised nor treated with tamoxifen.

Notably, the absence of GFP signal in this GC-derived CD138^{+} *S1pr2*$^{tdT+}$ Blimp-1^{GFP-} PB-PC population does not indicate a lack of Blimp-1 expression. The endogenous *Prdm1* (Blimp-1) coding sequence is translated first by 5′ cap-dependent translation. After producing the functional Blimp-1 protein, the downstream IRES allows ribosomes to re-initiate translation to produce GFP from the same mRNA. However, IRES-mediated translation is less efficient than cap-dependent translation, resulting in GFP expression that can be weak or undetectable even though they are truly Blimp-1 positive due to limited IRES-driven translation efficiency [148].

Together, these data indicate that EF-derived PB-PCs and GC-matured *S1pr2*$^{tdT+}$ Blimp-1^{GFP+} PB-PCs dominate the early splenic CD138^{+} compartment at day 5 following SRBC immunisation. This is consistent with previous findings from our lab [8, 168]. While GC-derived CD138^{+} *S1pr2*$^{tdT+}$ Blimp-1^{GFP-} PB-PCs were dominant at day 6.

3.2.1.2 GC-matured *S1pr2*$^{tdT+}$ Blimp-1^{GFP+} PB-PC peaked at day 5, and the GC response peaked at day 6.

GC maturation is represented at day 5, characterised by an increase in centroblasts, apparent zonal segregation, and follicle swelling [169]. Therefore, we examined Fas^{hi} GC B cell responses at these indicated time points: day 5, day 6, and day 8. B220^{+} B cells were gated and further analysed based on CD38 and Fas expression (Figure 3.7A). The number of Fas^{hi} GC B cells within B220^{+} B cells (Figure 3.7B) did not differ significantly among the days, but the disparity of samples was clustered at day 6. However, the frequency of these cells significantly peaked at day 6 (**$p < 0.01$) compared to day 5 (Figure 3.7C).

The expression of Blimp-1^{GFP} and *S1pr2*^{tdT} was quantified within the Fas^{hi} GC B cells gate (Figure 3.7D), allowing the identification of three fractions: Blimp-1^{GFP+} PB-PC, which is interpreted as EF-derived Blimp-1^{GFP+} PB-PC; GC-derived *S1pr2*$^{tdT+}$ Blimp-1^{GFP+} PB-PC; and GC-derived memory B cells. The Blimp-1^{GFP+} PB-PC fraction represented a small fraction of the GC B cells, accounting for approximately 2% at day 5, 1.5% at day 6, and 2.9% at day 8 (Figure 3.7E and H). In contrast, GC-derived *S1pr2*$^{tdT+}$ Blimp-1^{GFP+} PB-PC constituted a large proportion, representing 5.5% of Fas^{hi} GC B cells at day 5 and decreasing to 2.8% at day 6. (Figure 3.7F). At day 8, the calculated proportion exceeded 100%, which is not biologically plausible and likely due to the small sample size, leading to overestimation. The mean frequency of GC-matured *S1pr2*$^{tdT+}$ Blimp-1^{GFP+} PB-PC showed variability at day 5, with three samples exceeding 10%, while the others remained comparable to levels observed at day 6 (Figure 3.7I).

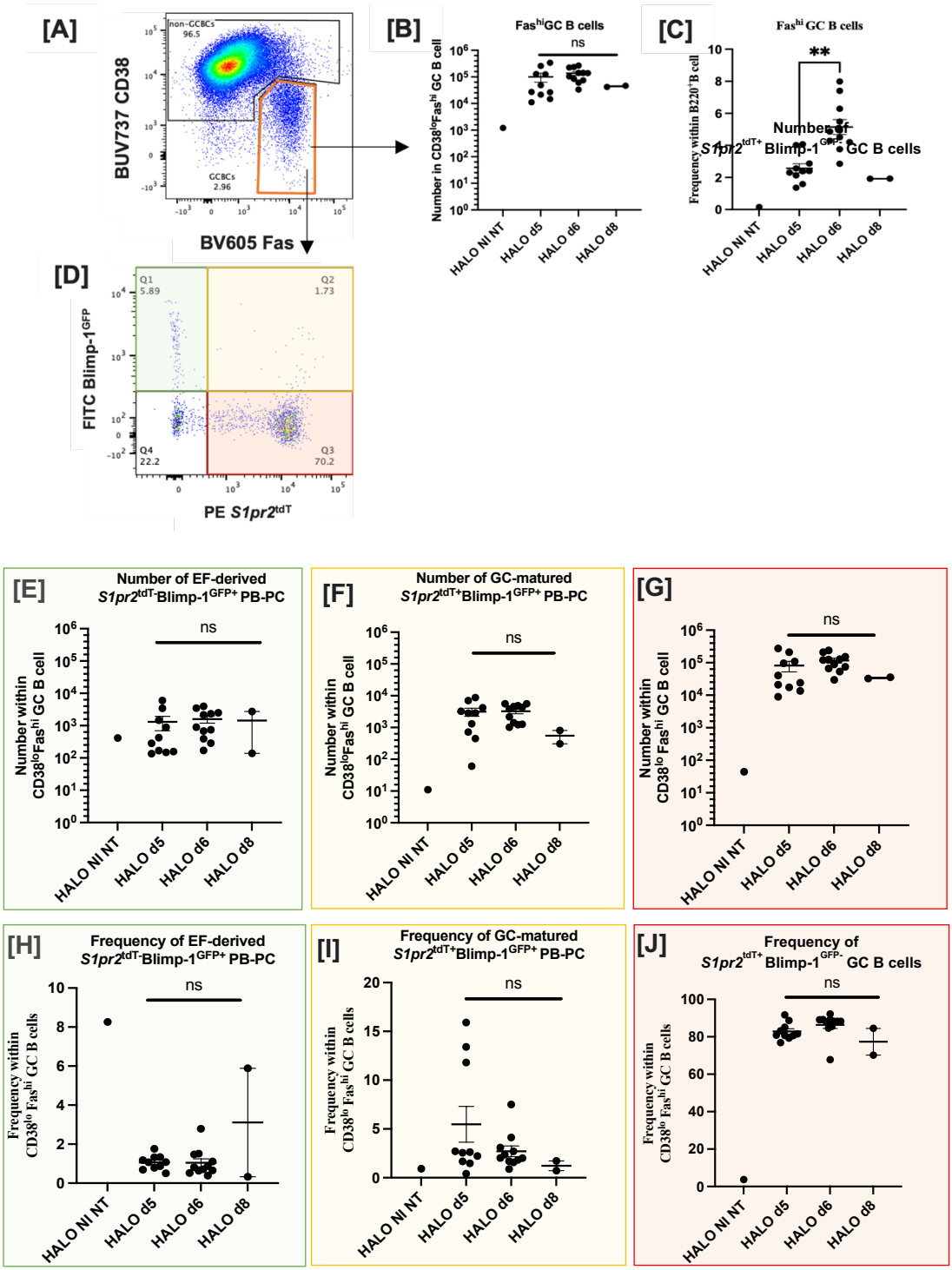


Figure 3.7. Fas^{hi} GC B cell response analysis in HALO mice following primary SRBCs immunisation.

The experimental protocol is illustrated in Figure 3.2. **(A)** Fas^{hi} GC B cells gated from B220^{+} B cells. **(B)** The number of Fas^{hi} GC B cells (mean ± SEM). **(C)** The frequency of Fas^{hi} GC B cells (mean ± SEM). **(D)** Fas^{hi} GC B cells were further analysed for GC-matured *S1pr2*^{tdT} Blimp-1^{GFP} PB-PC expression. **(E)** The number of GC-derived *S1pr2*$^{tdT-}$ Blimp-1^{GFP+} PB-PC within the Fas^{hi} GC B cells (mean ± SEM). **(F)** The number

of GC-derived *S1pr2*$^{tdT+}$ Blimp-1^{GFP+} PB-PC within the Fas^{hi} GC B cells (mean ± SEM). **(G)** The number of GC-derived *S1pr2*$^{tdT+}$ Blimp-1^{GFP-} GC B cells within the Fas^{hi} GC B cells (mean ± SEM). **(H)** The frequency of GC-derived *S1pr2*$^{tdT-}$ Blimp-1^{GFP+} PB-PC within the Fas^{hi} GC B cells (mean ± SEM). **(I)** The frequency of GC-derived *S1pr2*$^{tdT+}$ Blimp-1^{GFP+} PB-PC within the Fas^{hi} GC B cells (mean ± SEM). **(J)** The frequency of GC-derived *S1pr2*$^{tdT+}$ Blimp-1^{GFP-} GC B cells within the Fas^{hi} GC B cells (mean ± SEM). Each symbol represents one mouse. Data was obtained from three independent experiments where n = 10 at day 5, n = 11 at day 6, and n = 2 at day 8. Statistical tests were performed by a one-way ANOVA, a nonparametric test, and analysis with the Kruskal-Wallis test (ns $p > 0.05$). NI NT refers to a HALO mouse neither immunised nor treated with tamoxifen.

The number and frequency of GC-derived *S1pr2*$^{tdT+}$ Blimp-1^{GFP-} GC B cells (Figure 3.7G and J) were the highest populations compared to other GC-derived populations analysed in Figure 3.7E, F, H, and I. These GC-derived *S1pr2*$^{tdT+}$ Blimp-1^{GFP-} GC B cells showed an accumulation at day 6 compared to days 5 and 8, although this accumulation was not statistically significant. Overall, these findings indicate that GC-matured *S1pr2*$^{tdT+}$ Blimp-1^{GFP+} PB-PC peaked by day 5, and the GC response intensified and peaked on day 6.

3.2.1.3 GC-derived CD38^{+} Blimp-1^{GFP+} *S1pr2*$^{tdT+}$ PC precursors peaked at day 5 and raised memory B cells at day 6.

It has been suggested that a subset of PC precursors can exit the GC while retaining high levels of CD38 [170]. Therefore, we wanted to investigate PC precursors by identifying Fas^{lo} CD38^{+} non-GC B cell populations from B220 B cells, then further gated on CD38 and *S1pr2*^{tdT} (Figure 3.8A). CD38^{+} *S1pr2*^{tdT}-activated and/or naive B cells and CD38^{+} *S1pr2*$^{tdT+}$ memory B cells were then assessed for their expression of Blimp-1^{GFP} (Figure 3.8B-C).

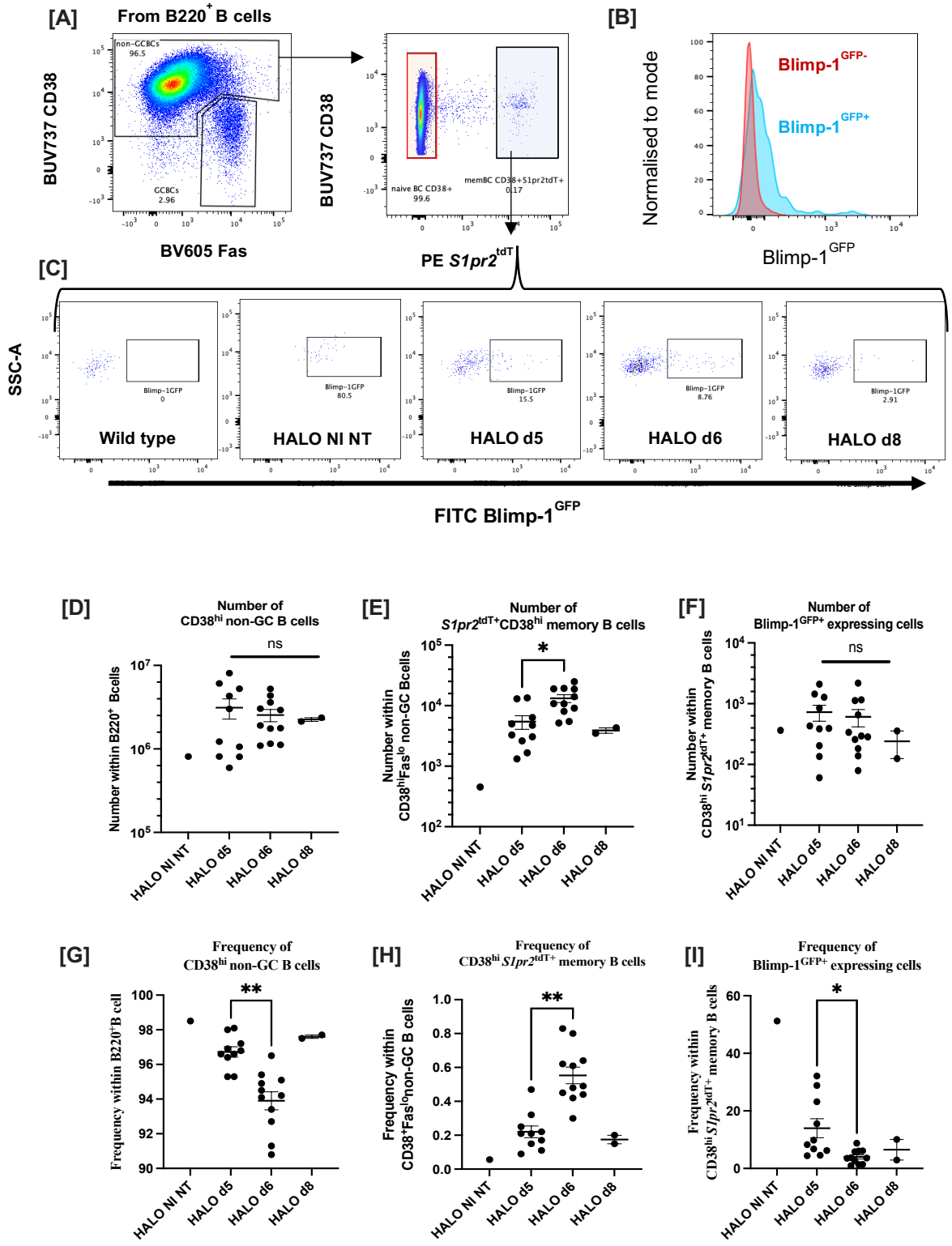


Figure 3.8. Blimp-1^{GFP+} PB-PC phenotype observed within CD38^{hi} *S1pr2*$^{tdT+}$ memory B cells.

The experimental protocol is illustrated in Figure 3.2. **(A)** Non-GC CD38^{hi} B cells (red lines) were gated from B220^{+} B cells and further analysed for *S1pr2*$^{tdT+}$ CD38^{hi} memory B cells (blue square). **(B)** Representative data histogram-based results show the

intensity of Blimp-1^{GFP+} within *S1pr2*$^{tdT+}$ CD38^{hi} memory B cells (blue histogram) compared to *S1pr2*$^{tdT-}$ CD38^{hi} naïve B cells (red histogram). **(C)** Representative data plot-based results show Blimp-1^{GFP+} expression gated from *S1pr2*$^{tdT+}$ CD38^{hi} memory B cells. **(D)** Number of CD38^{hi} non-GC B cells within B220^{+} B cells. **(E)** Number of *S1pr2*$^{tdT+}$CD38^{hi} memory B cells within CD38^{hi} Fas^{lo} non-GC B cells. **(F)** Number of Blimp-1^{GFP+} expressing cells within *S1pr2*$^{tdT+}$CD38^{hi} memory B cells. **(G)** Frequency of CD38^{hi} non-GC B cells within B220^{+} B cells. **(H)** Frequency of *S1pr2*$^{tdT+}$CD38^{hi} memory B cells within CD38^{hi} Fas^{lo} non-GC B cells. **(I)** Frequency of Blimp-1^{GFP+} expressing cells within *S1pr2*$^{tdT+}$CD38^{hi} memory B cells. The data were obtained from three independent experiments where n = 10 at day 5, n = 11 at day 6, and n = 2 at day 8. Statistical tests were performed using a one-way ANOVA, a nonparametric test, and analysis with the Kruskal-Wallis test (ns $p > 0.05$, * $p < 0.05$, ** $p < 0.01$). HALO NI NT refers to a HALO mouse neither immunised nor treated with tamoxifen.

The mean number of CD38^{+} non-GC B cells appeared slightly higher at day 5, although this difference was not statistically significant (Figure 3.8D). However, the frequency of CD38^{+} non-GC B cells (Figure 3.8G) increased significantly at day 5 compared to day 6. Within the CD38^{+} non-GC B cell population, both number (Figure 3.8E) and frequency (Figure 3.8H) of GC-derived CD38^{+} *S1pr2*$^{tdT+}$ memory B cells increased significantly at day 6, *$p < 0.05$ and ** $p < 0.01$, respectively. This is consistent with the output of GC-derived CD138^{+} *S1pr2*$^{tdT+}$ PB-PC (section 3.2.1.1, Figure 3.6F and I) and the GC response intensity (section 3.2.1.2, Figure 3.7C).

The proportion of Blimp-1^{GFP+} cells within GC-derived CD38^{+} *S1pr2*$^{tdT+}$ memory B cell subsets accounted for ~920 of 7,800 (11.8%) at day 5, ~790 of 15,000 (5.3%) at day 6, and ~390 of 6,000 (6.5%) at day 8 (Figure 3.8E and F). This indicates that PC precursors increase at day 5, consistent with the PB-PC output that was observed in Figure 3.6E, Figure 3.7F and Figure 3.7I.

Overall, HALO mice indicate that GC-derived CD38^{+} Blimp-1^{GFP+} *S1pr2*$^{tdT+}$ PC precursors peak at day 5, whereas GC-derived CD38^{+} *S1pr2*$^{tdT+}$ memory B cells increase markedly by day 6.

3.2.1.4 GC-matured CD138^{+} TACI^{+} *S1pr2*$^{tdT+}$ Blimp-1^{GFP+} PB-PC accumulated at day 6.

TACI signalling supports PB-PC differentiation from the GC, particularly at the GTI region [8]. Blocking TACI led to a reduction in PB-PC number in the GTI region. Accordingly, we analysed the splenic CD138^{+} TACI^{+} PB-PC for the proportions of EF and GC-derived PB-PC (Figure 3.9A). The number of CD138^{+} TACI^{+} PB-PC displayed similarly at day 5 and day 6 (Figure 3.9B). This peak is consistent with the total splenic CD138^{+} TACI^{+} PB-PC in the *S1pr2*^{ERT2Cre} *Rosa26*^{LSLtdTomato} model [171], which also confirmed the reduction of CD138^{+} TACI^{+} PB-PC to background by day 8. The frequency of CD138^{+} TACI^{+} PB-PC rose at day 6, although this was not significantly different from other time points (Figure 3.9C).

The splenic CD138^{+} TACI^{+} PB-PC response was further analysed for the GC-matured *S1pr2*$^{tdT+}$ Blimp-1^{GFP+} PB-PC (Figure 3.9D). The number and frequency of GC-matured *S1pr2*$^{tdT+}$ Blimp-1^{GFP+} PB-PC were accumulated at day 6, although this accumulation was not statistically significant (Figure 3.9E and F) compared to the early tamoxifen label (at day 5) and the late tamoxifen label (at day 8). This is consistent with the accumulation of splenic GC-matured PB-PC in the *S1pr2*^{ERT2Cre} *Rosa26*^{LSLtdTomato} model [171]. Together, the splenic GC-matured CD138^{+} TACI^{+} *S1pr2*$^{tdT+}$ Blimp-1^{GFP+} PB-PC response underwent accumulation at day 6 after primary immunisation with SRBCs.

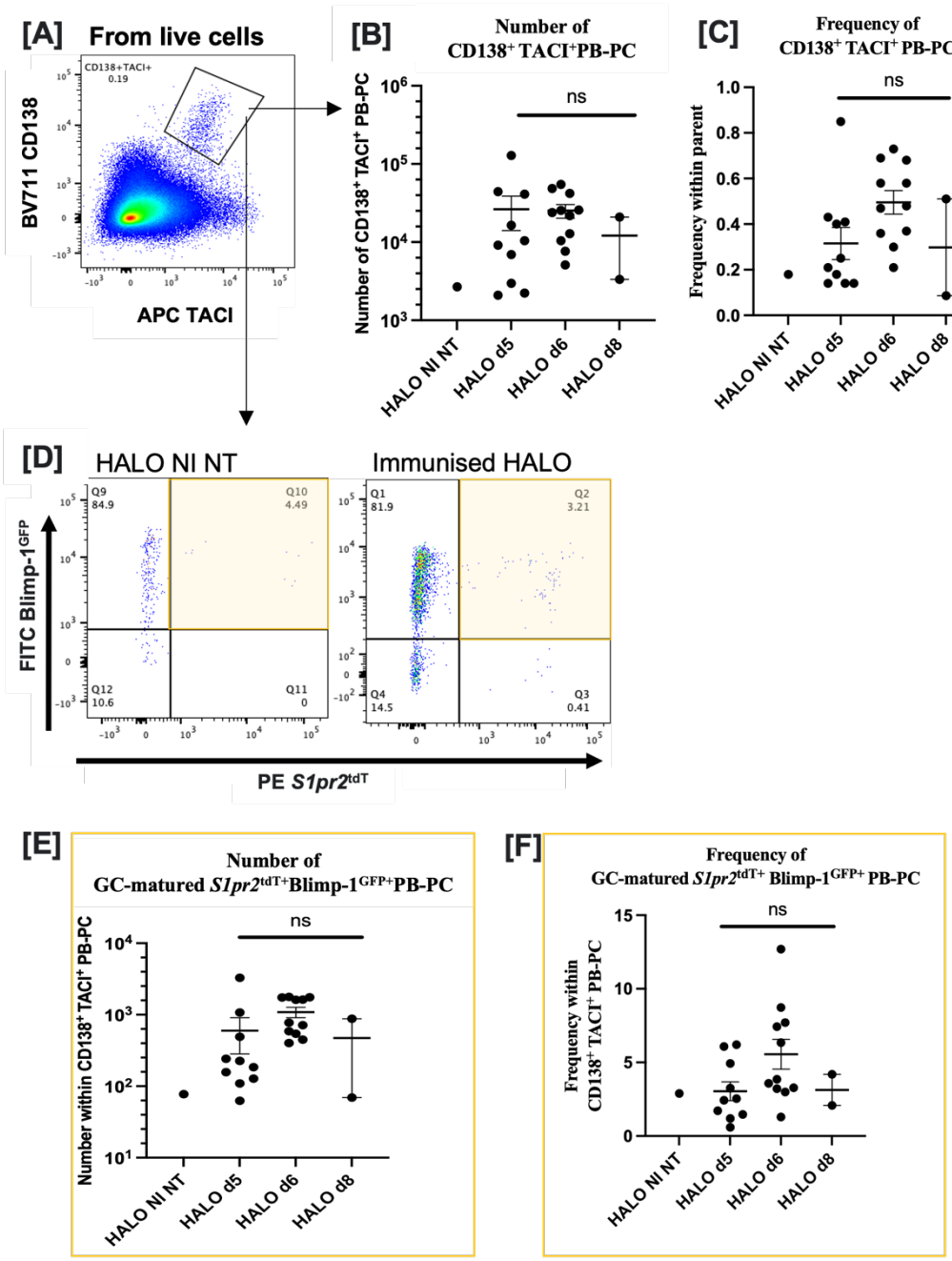


Figure 3.9. CD138⁺ TACI⁺ PB-PC response analysis in HALO mice following primary SRBCs immunisation.

The experimental protocol is illustrated in Figure 3.2. **(A)** Representative data plot-based results of CD138+ TACI+ PB-PC gated from live cells. **(B)** Number of CD138⁺ TACI⁺ PB-PC (mean ± SEM). **(C)** Frequency of CD138⁺ TACI⁺ PB-PC within parent (live cells) (mean ± SEM). **(D)** Representative data plot-based results of GC-matured *S1pr2*$^{tdT+}$ Blimp-1^{GFP+} PB-PC gated from CD138⁺ TACI⁺ PB-PC. **(E)** Number of GC-matured *S1pr2*$^{tdT+}$ Blimp-1^{GFP+} PB-PC (mean ± SEM). **(F)** Frequency of GC-matured *S1pr2*$^{tdT+}$ Blimp-1^{GFP+} PB-PC (mean ± SEM). Each symbol represents one mouse. Data was obtained from three independent experiments where n = 10 at day 5, n = 11 at

day 6, and n = 2 at day 8. Statistical tests were performed using a one-way ANOVA, a nonparametric test, and analysis with the Kruskal-Wallis test (ns $p > 0.05$). NI NT refers to a HALO mouse neither immunised nor treated with tamoxifen.

3.2.1.5 The fully differentiated PC peaked at day 6 after the primary response with SRBC.

Next, we investigated the maturation phase of $CD138^{+}$ $TACI^{+}$ PB-PCs using B220 and CD19 expression (Figure 3.10A and B). CD19 and B220 are B cell markers, and their downregulation is associated with the progression towards fully differentiated PCs. The gating strategy of PC maturation stages described by Pracht and colleagues was used as a reference [148]. Gate boundaries were positioned based on fluorescence intensity distribution and separation of populations, using non-immunised control mice to define the progressive downregulation of CD19 and B220. Early activated $B220^{hi}$ $CD19^{hi}$ B cells located in the upper-right region of the plot and represent cells entering the ASC compartment with low Blimp-1 expression. Early $B220^{int}$ $CD19^{int}$ PB occupied the adjacent upper-right region and represents the most immature, proliferating ASCs. Early non-proliferating PC $B220^{lo}$ $CD19^{int}$ PC were placed in the upper-left quadrant, reflecting downregulation of B220 while remaining CD19. Fully mature $B220^{lo}$ $CD19^{lo}$ PC were found in the lower-left quadrant, consistent with complete downregulation of both B lineage markers. Based on this distribution, four fractions were defined: a minor $B220^{hi}$ $CD19^{hi}$ population, $B220^{int}$ $CD19^{int}$ proliferating PB (P1), $B220^{lo}$ $CD19^{int}$ early non-proliferating PC (P2), and $B220^{lo}$ $CD19^{lo}$ late non-proliferating PC (P3) (Figure 3.10B). Figure 3.10C shows representative Blimp-1^{GFP} expression across the $CD138^{+}$ $TACI^{+}$ PB-PC fractions, illustrating the distribution of Blimp-1^{GFP} cells within the different PB-PC populations defined by CD19 and B220 expression.

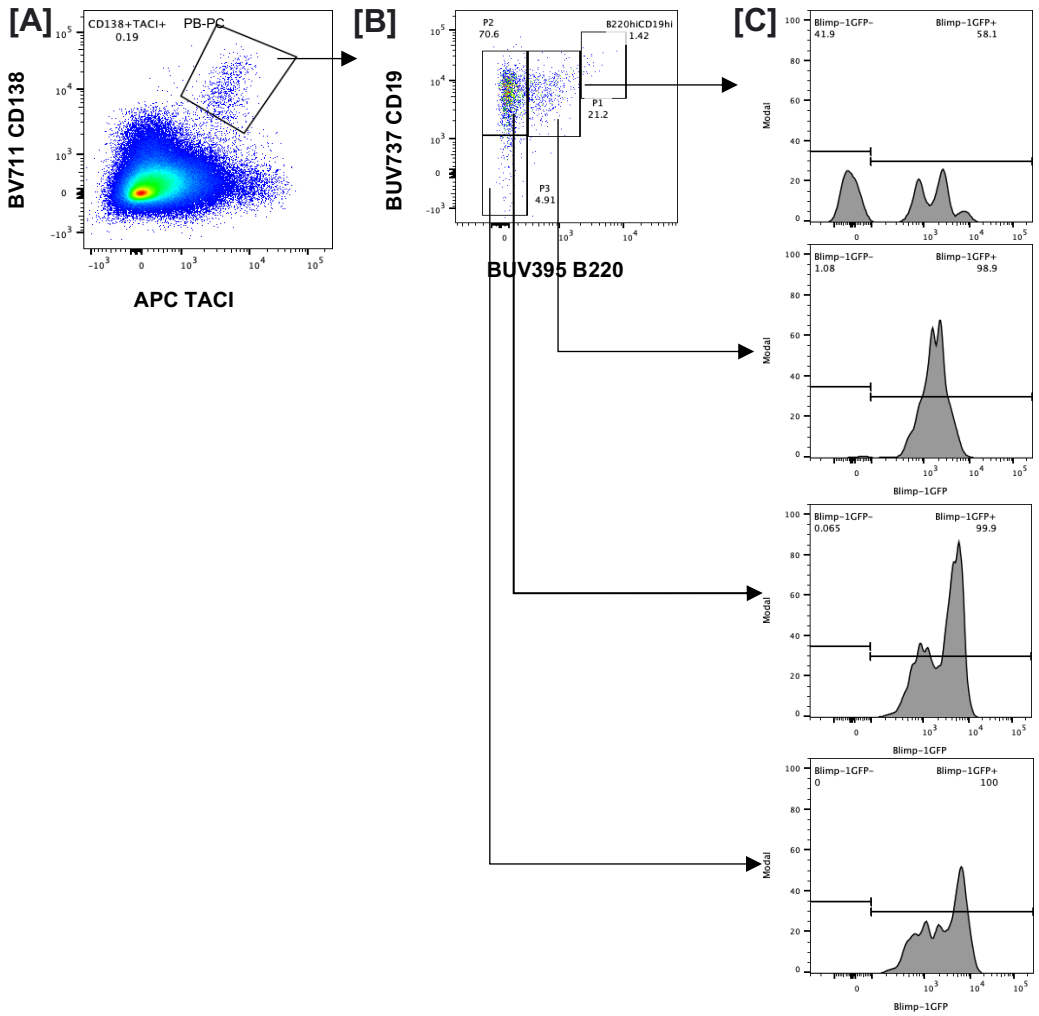


Figure 3.10. CD138^{+} TACI^{+} PB-PC fractions in HALO mice following primary SRBCs immunisation.

The experimental protocol is illustrated in Figure 3.2. **(A)** CD138^{+} TACI^{+} PB-PC were gated from live cells and further gated for the level of B220 CD19 expression, which was subdivided into fractions according to their expression of Blimp-1^{GFP} **(B)**. **(C)** Representative data histogram-based results of the fluorescence intensity of Blimp-1^{GFP} in each fraction of CD138^{+} TACI^{+} PB-PC. Data was obtained from three independent experiments where n = 10 at day 5, n = 11 at day 6, and n = 2 at day 8.

The number and frequency of B220^{hi} CD19^{hi} fractions within the CD138^{+} TACI^{+} PB-PC compartment were minor (Figure 3.11B and F). Because this subset is identified within the CD138^{+} TACI^{+} PB-PCs gate and displays dim Blimp-1^{GFP} expression, it likely represents an early PB-PC precursor population. Although the number of B220^{hi} CD19^{hi} B cell fraction (Figure 3.11B) showed a slight increase at day 6, the change was not statistically significant. In contrast, the B220^{lo} CD19^{int} P2 fraction (Figure 3.11D and H) was the most dominant subset, exceeding the B220^{int} CD19^{int} P1 and B220^{lo} CD19^{lo} P3 fractions (Figure 3.11C and G, E and I). Across all fractions, the distributions observed on day 5 and day 6 were similar, suggesting limited phenotypic changes within the PB-PC compartment during these early time points.

To further characterise the distribution of *S1pr2*$^{tdT+}$ and Blimp-1^{GFP+} expression within each fraction of CD138^{+} TACI^{+} PB-PC (Figure 3.12A-B), we quantified the proportion of GC-derived *S1pr2*$^{tdT+}$ Blimp-1^{GFP+} PB-PC (Figure 3.12C-F) across the four fractions (Figure 3.11B-E). Within the B220^{hi} CD19^{hi} fraction, GC-derived *S1pr2*$^{tdT+}$ Blimp-1^{GFP+} PB-PC accounted for approximately 17.7% at day 5, 10.7% at day 6, and 14.6% at day 8. This indicates that GC-derived PB-PC reached its peak at day 5. In the P1 fraction, 7.4% of cells were GC-derived *S1pr2*$^{tdT+}$ Blimp-1^{GFP+} PB-PC at day 5, 7.7% at day 6, and 6.7% at day 8. There was no significant difference across time points, although the value was slightly higher at day 6. For the P2 fraction, GC-derived *S1pr2*$^{tdT+}$ Blimp-1^{GFP+} PB-PC represented 0.7% at day 5, 2.9% at day 6, and 2.4% at day 8. Within the P3 fraction (fully differentiated), defined as B220^{lo} CD19^{lo} CD138^{+} TACI^{+} PB-PC, GC-derived *S1pr2*$^{tdT+}$ Blimp-1^{GFP+} PB-PC were 0.9% at day 5, 1.9% at day 6, and 0.1% at day 8. Day 6 displayed an increased output of the early non-proliferating PC (P2) and late non-proliferating PC.

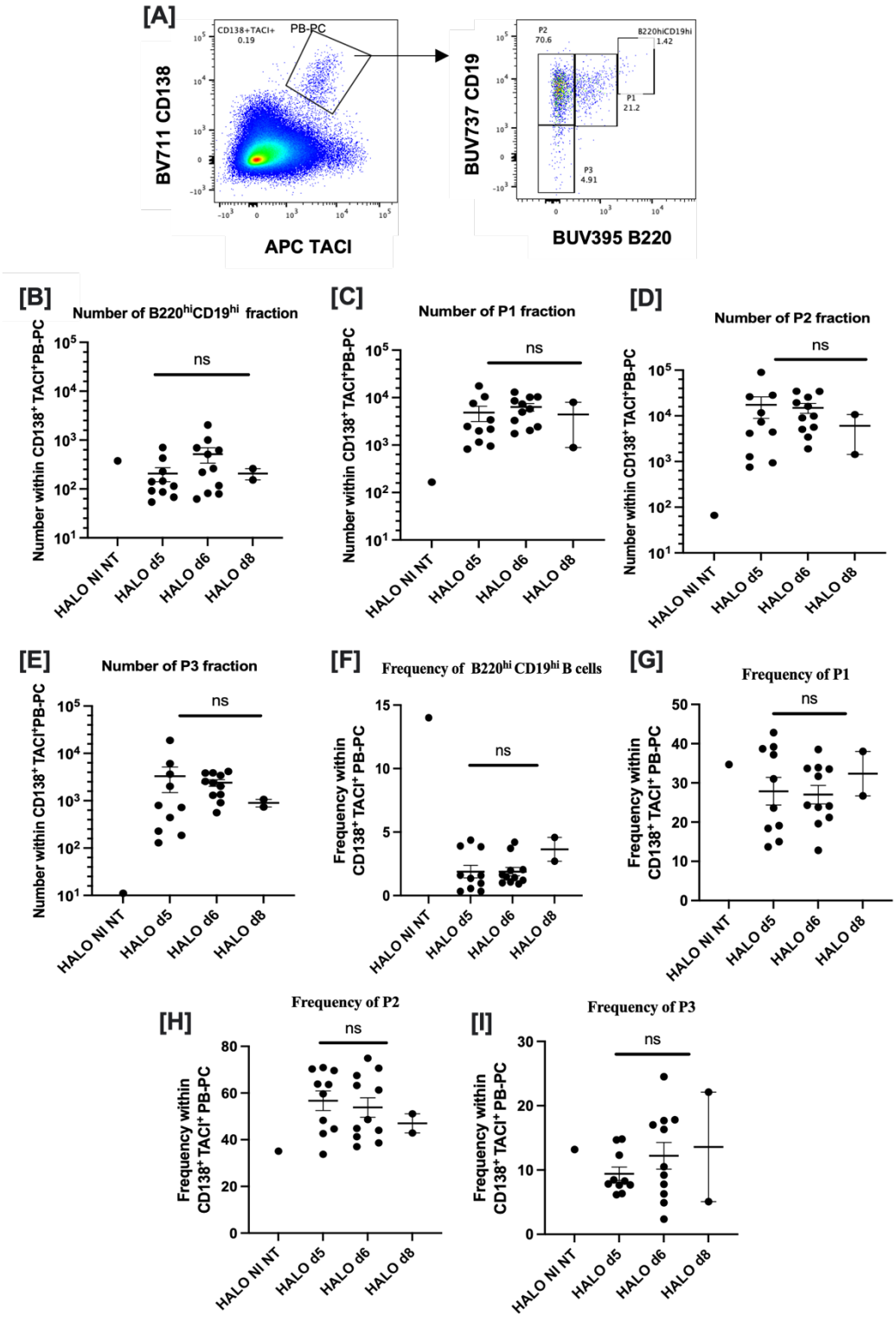


Figure 3.11. Analysis of CD138^{+} TACI^{+} PB-PC fractions in HALO mice following primary SRBCs immunisation.

The experimental protocol is illustrated in Figure 3.2. **(A)** CD138^{+} TACI^{+} PB-PC were fractionated based on B220 and CD19 expression. **(B)** Number of B220^{hi} CD19^{hi} B

cells within CD138^{+} TACI^{+} PB-PC (mean ± SEM). **(C)** Number of B220^{int} CD19^{int} proliferating PB (P1) within CD138^{+} TACI^{+} PB-PC (mean ± SEM). **(D)** Number of B220^{lo} CD19^{int} early non-proliferating PC (P2) within CD138^{+} TACI^{+} PB-PC (mean ± SEM). **(E)** Number of B220^{lo} CD19^{lo} late non-proliferating PC (P3) within CD138^{+} TACI^{+} PB-PC (mean ± SEM). **(F)** Frequency of B220^{hi} CD19^{hi} B cells within CD138^{+} TACI^{+} PB-PC (mean ± SEM). **(G)** Frequency of B220^{int} CD19^{int} proliferating PB (P1) within CD138^{+} TACI^{+} PB-PC (mean ± SEM). **(H)** Frequency of B220^{lo} CD19^{int} early non-proliferating PC (P2) within CD138^{+} TACI^{+} PB-PC (mean ± SEM). **(I)** Frequency of B220^{lo} CD19^{lo} late non-proliferating PC (P3) within CD138^{+} TACI^{+} PB-PC (mean ± SEM). Each symbol represents one mouse. Data were obtained from three independent experiments, with n = 10 on day 5, n = 11 on day 6, and n = 2 on day 8. Statistical tests were performed using one-way ANOVA and the nonparametric Kruskal-Wallis test ($p > 0.05$). HALO NI NT refers to non-immunised and not treated with tamoxifen.

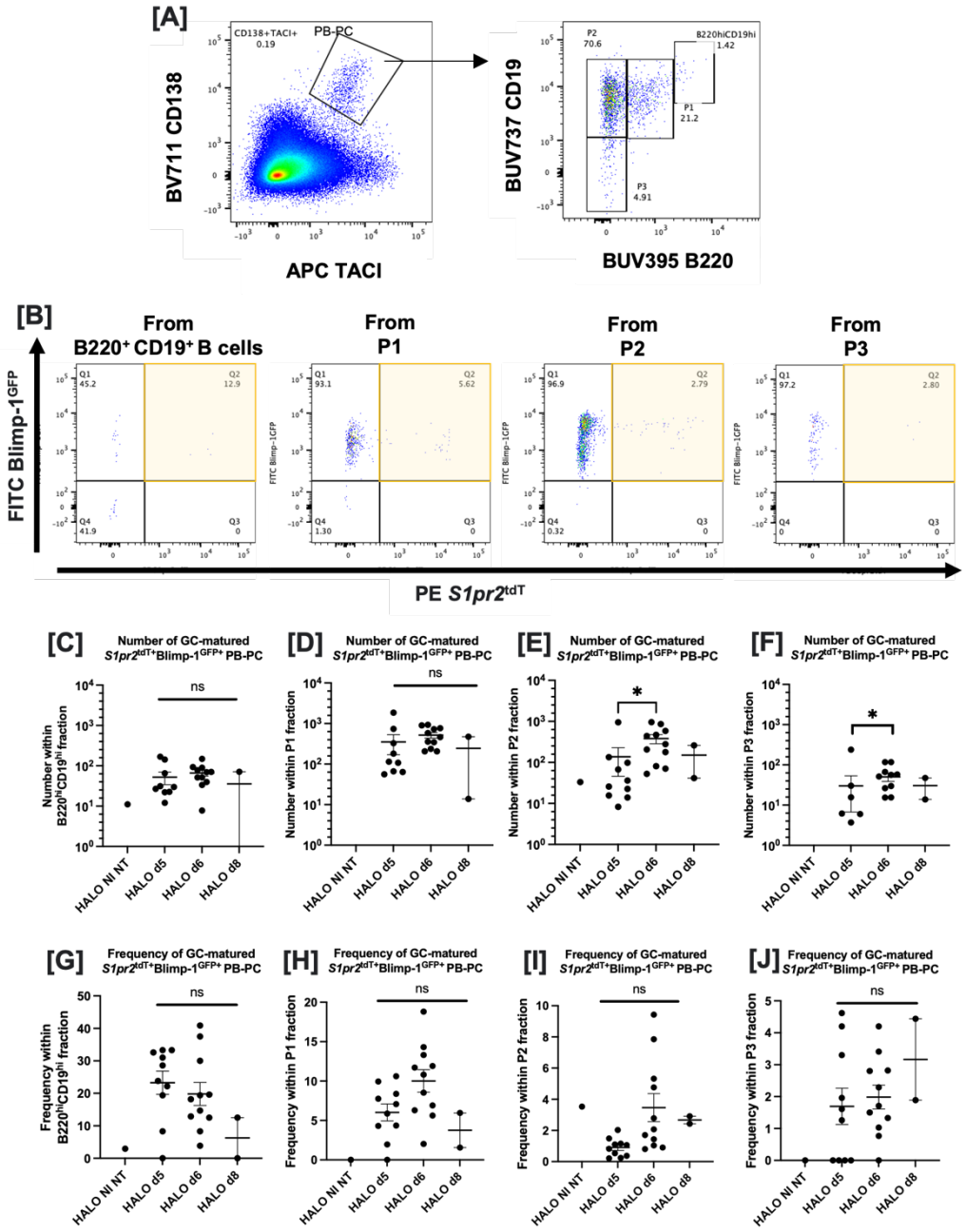


Figure 3.12. The presence of GC-matured *S1pr2*$^{tdT+}$ Blimp-1^{GFP+} PB-PC within CD138^{+} TACI^{+} PB-PC fractions.

The experimental protocol is illustrated in Figure 3.2. **(A)** CD138^{+} TACI^{+} PB-PC were fractionated based on B220 and CD19 expression. **(B)** Each fraction was further analysed to assess the presence of GC-matured *S1pr2*$^{tdT+}$ Blimp-1^{GFP+} PB-PCs. **(C)** Number of GC-matured *S1pr2*$^{tdT+}$ Blimp-1^{GFP+} PB-PC within B220^{hi} CD19^{hi} CD138^{+} TACI^{+} PB-PC (mean ± SEM). **(D)** Number of GC-matured *S1pr2*$^{tdT+}$ Blimp-1^{GFP+} PB-PC within B220^{int} CD19^{int} CD138^{+} TACI^{+} PB-PC (P1) (mean ± SEM). **(E)** Number of GC-matured *S1pr2*$^{tdT+}$ Blimp-1^{GFP+} PB-PC within B220^{lo} CD19^{int} CD138^{+} TACI^{+} PB-PC (P2) (mean ± SEM). **(F)** Number of GC-matured *S1pr2*$^{tdT+}$ Blimp-1^{GFP+} PB-PC within B220^{lo}

CD19^{lo} CD138^{+} TACI^{+} PB-PC (P3) (mean ± SEM). **(G)** Frequency of GC-matured *S1pr2*$^{tdT+}$ Blimp-1^{GFP+} PB-PC within B220^{hi} CD19^{hi} CD138^{+} TACI^{+} PB-PC (mean ± SEM). **(H)** Frequency of GC-matured *S1pr2*$^{tdT+}$ Blimp-1^{GFP+} PB-PC within B220^{int} CD19^{int} CD138^{+} TACI^{+} PB-PC (P1) (mean ± SEM). **(I)** Frequency of GC-matured *S1pr2*$^{tdT+}$ Blimp-1^{GFP+} PB-PC within B220^{lo} CD19^{int} CD138^{+} TACI^{+} PB-PC (P2) (mean ± SEM). **(J)** Frequency of GC-matured *S1pr2*$^{tdT+}$ Blimp-1^{GFP+} PB-PC within B220^{lo} CD19^{lo} CD138^{+} TACI^{+} PB-PC (P3) (mean ± SEM). Each symbol represents one mouse. Data were obtained from three independent experiments, with n = 10 at day 5, n = 11 at day 6, and n = 2 at day 8. Values below the detection limit are out of the scale, indicating a value of zero. Statistical tests were performed by one-way ANOVA, a nonparametric test, and analysis with the Kruskal-Wallis test (ns $p > 0.05$, * $p < 0.05$). HALO NI NT refers to non-immunised, not treated with tamoxifen.

This is also confirmed by the significant increase in the number of GC-derived *S1pr2*$^{tdT+}$ Blimp-1^{GFP+} PB-PC at day 6 compared to day 5 (Figure 3.12E and F). Additionally, the mean frequency of GC-derived *S1pr2*$^{tdT+}$ Blimp-1^{GFP+} PB-PC was higher at day 6, although it was not a statistically significant difference (Figure 3.12I and J). Overall, the fully differentiated GC-derived *S1pr2*$^{tdT+}$ Blimp-1^{GFP+} B220^{lo} CD19^{lo} CD138^{+} TACI^{+} PB-PC occurred at day 6 after the primary immunisation with SRBCs.

3.2.1.6 Dissemination pattern and quantification of PB-PCs in HALO mice using immunofluorescence analysis following SRBC primary immunisation.

The spatial distribution of EF-derived Blimp-1^{GFP+} PB-PC and GC-matured *S1pr2*$^{tdT+}$ Blimp-1^{GFP+} PB-PC was analysed using the splenic sections produced from the experimental protocol described in Figure 3.2. The immunofluorescence staining process was performed on the splenic cryosections as detailed in 2.7.

To guide the interpretation of the image observations, four colours were used to represent different fluorescence channels: white for IgD^{+} follicular B cells, green for the

Blimp-1^{GFP+} signal, and blue for an additional marker used to identify PB-PC, such as IRF4, IgG1, and CD138. GC B cells expressing *S1pr2*$^{tdT+}$ are shown in red colour. CD4^{+} T cells were also displayed in the blue colour to delineate the T cell zone. Upon image merging, green and red double-positive signals appear yellow, green and blue overlap appears turquoise, and blue and red overlap appears pink.

To validate accurate interpretation of fluorescent signals in splenic sections—especially *S1pr2*$^{tdT+}$ and Blimp-1^{GFP+} signals—control spleen sections (Figure 3.13) were obtained from single-reporter mice and processed using the same protocol described in Figure 3.2. These controls enabled validation of anti-GFP staining specificity and assessment of potential channel overlap between the green (GFP) and red (tdT) channels. Observations showed that no GFP signal was detected in the *S1pr2*$^{tdT+}$ section, and GFP fluorescence was specifically restricted to the appropriate channel in the Blimp-1^{GFP+} section. These observations confirmed that the co-localisation detection of GFP and tdT in HALO mice reflects the true signal rather than a background false signal.

Next, we assessed background reporter activity in the absence of immunological stimulation and tamoxifen-induced labelling by examining a splenic section obtained from a HALO mouse that was not immunised but received tamoxifen administration (Figure 3.14). Observations from three zoomed-in views revealed detectable GC-matured *S1pr2*$^{tdT+}$ Blimp-1^{GFP+} PB-PC, consistent with the population detected by flow cytometry analysis (see section 3.2.1).

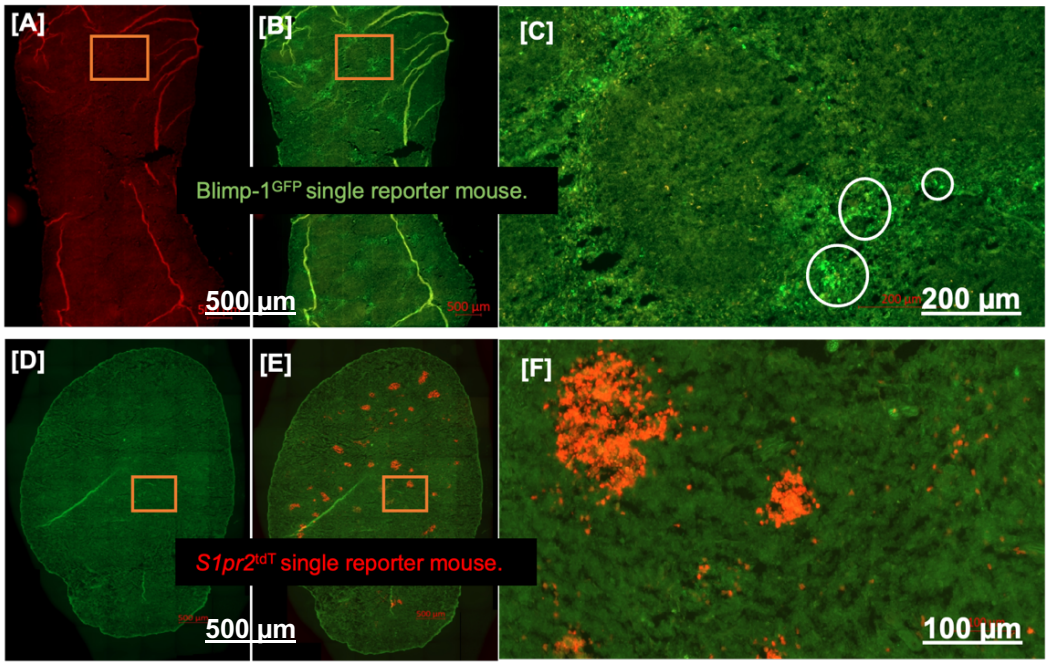
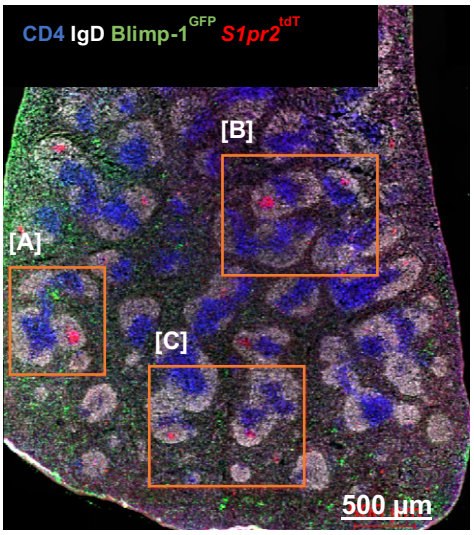
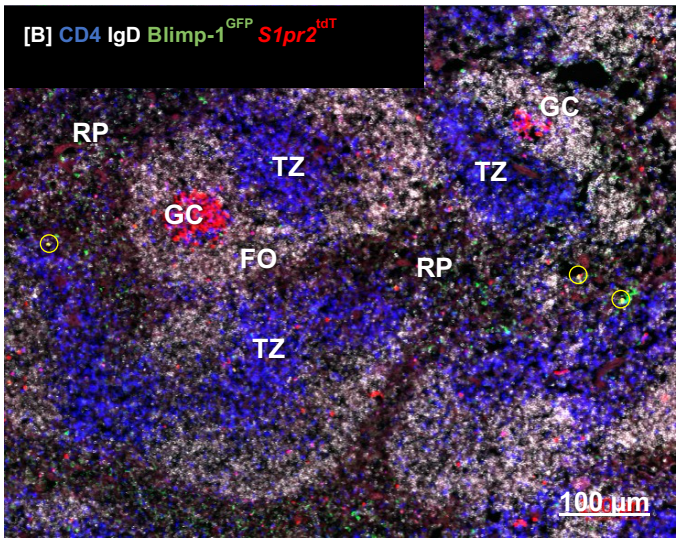
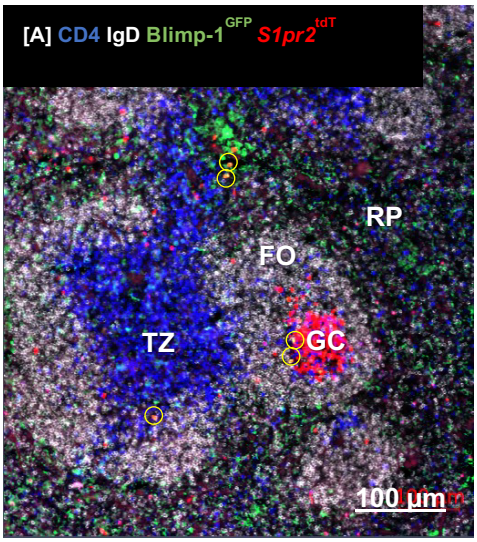


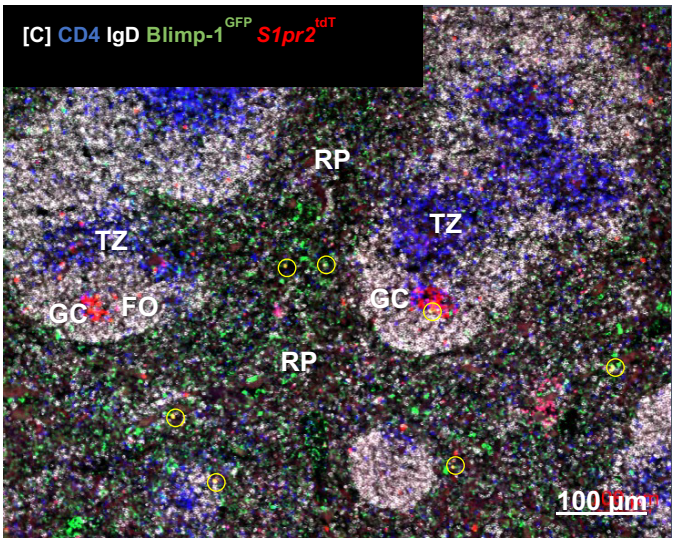
Figure 3.13. Validation of anti-GFP antibody specificity in single reporter mice.

Typical images of splenic sections from an immunised *S1pr2*^{tdT} mouse and a Blimp-1^{GFP} mouse to validate the lack of unspecific binding. Sections were stained with goat anti-GFP (green channel). The *S1pr2*^{tdT} signal is detected as an autofluorescence in the red channel. **(A)** The zoomed-out view shows a Blimp-1^{GFP} mouse spleen section imaged in the red channel. **(B)** The zoomed-out view shows the same Blimp-1^{GFP} mouse spleen section in both red and green channels. **(C)** The zoomed-in view of the selected area shows specific binding of GFP-positive cells in the green channel. **(D)** The zoomed-out view shows an *S1pr2*^{tdT} mouse spleen section imaged in the green channel. **(E)** The zoomed-out view shows the same *S1pr2*^{tdT} mouse spleen section imaged in both red and green channels. **(F)** The zoomed-in view of the selected area confirms that no GFP signal was detected in the green channel. Images were produced by the fluorescent field at 20x magnification using a Zeiss AxioScan Z1 Slide Scanner. Images were processed at 500 µm (zoomed-out images A, B, D, and E), 200 µm (zoomed-in C), and 100 µm (zoomed-in F) with Zen v3.1 (Blue Edition). Both sections were prepared using the protocol described in Figure 3.2. These single reporter mice were processed on day 8 following immunisation with SRBC.


CD4 IgD Blimp-1GFP S1pr2tdT
[B]
[A]
[C]
500 μm


[B] CD4 IgD Blimp-1GFP S1pr2tdT
RP
TZ
GC
TZ
GC
FO
RP
TZ
100 μm


[A] CD4 IgD Blimp-1GFP S1pr2tdT
RP
FO
TZ
GC
100 μm


[C] CD4 IgD Blimp-1GFP S1pr2tdT
RP
TZ
TZ
GC
FO
GC
RP
100 μm

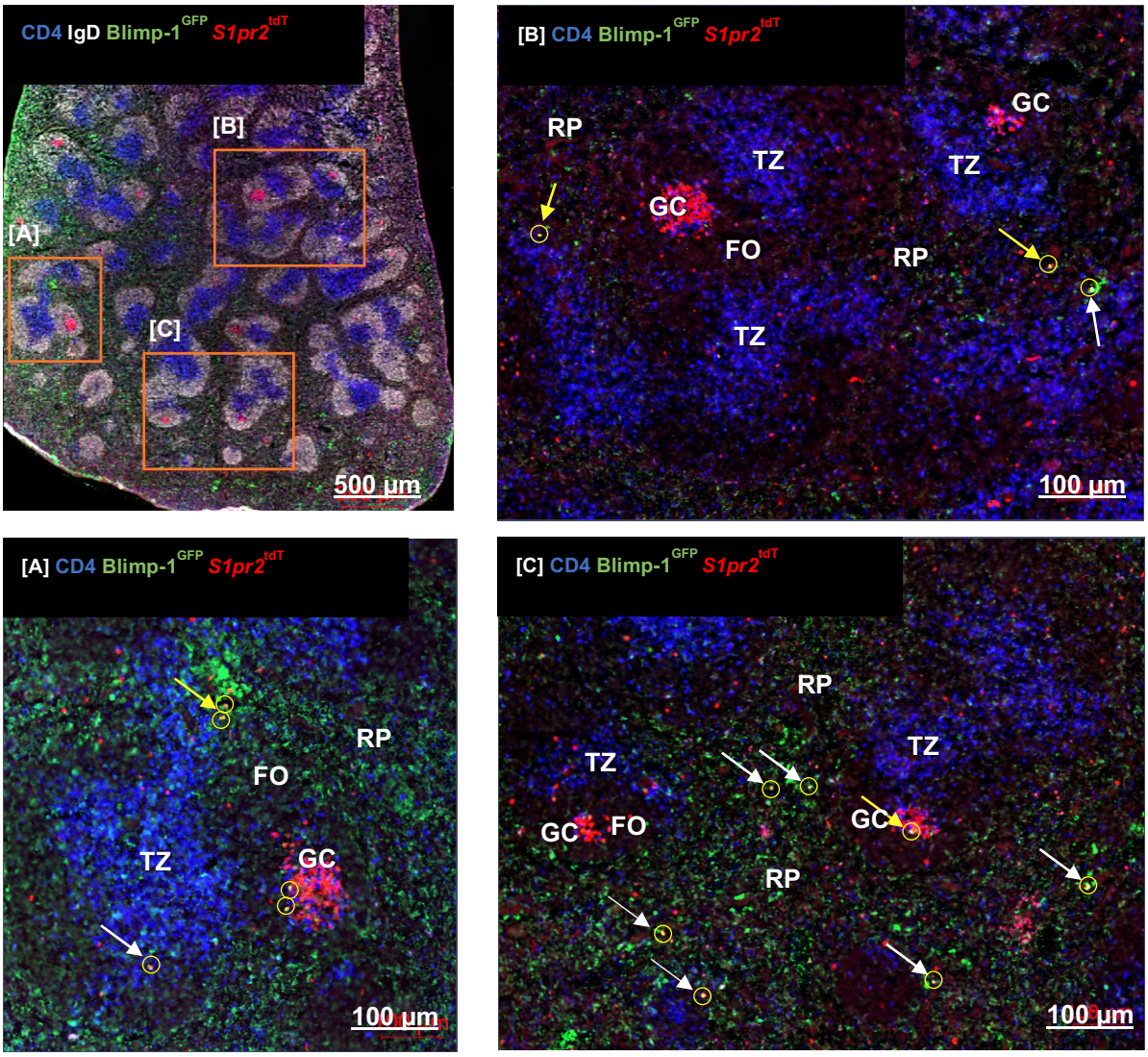


Figure 3.14. GC-matured *S1pr2*$^{tdT+}$ Blimp-1^{GFP+} PB-PCs in a non-treated HALO mouse.

An example image of a splenic section from a HALO mouse that was not immunised but received tamoxifen (see the experimental protocol in Figure 3.2). The upper left image shows the zoom-out of the splenic section stained with antibodies against IgD^{hi} follicular B cells (white channel), CD4^{+} T cells (blue channel), and goat anti-GFP (green channel). The *S1pr2*^{tdT} is detected as auto-fluorescence in the red channel.

(A-C) The zoomed-in images show the dissemination of EF-derived Blimp-1^{GFP+} PB-PCs (green) and GC-matured *S1pr2*$^{tdT+}$ Blimp-1^{GFP+} PB-PCs (yellow) throughout the splenic compartments: **(A)** At the T cell zone (white arrow) and the bridging channel (yellow arrow). **(B)** At the T cell zone (white arrow) and the bridging channel (yellow arrow). **(C)** In the RP (white arrow) and the GC cluster (yellow arrow). Images were produced by the fluorescent field at 20x magnification using a Zeiss AxioScan Z1 Slide Scanner. Images were processed at 500µm (zoom-out image) and 100 µm (zoom-in A-C) with Zen v3.1 (Blue Edition). GC: Germinal centre; FO: Follicular B cells; RP: Red Pulp; TZ: T cells zone.

In contrast, the observations from stimulated HALO mice showed markedly increased distribution of GC-matured *S1pr2*$^{tdT+}$ Blimp-1^{GFP+} PB-PC (Figure 3.15), indicating that the GC-matured *S1pr2*$^{tdT+}$ Blimp-1^{GFP+} PB-PC population expands upon immunisation. GC-matured *S1pr2*$^{tdT+}$ Blimp-1^{GFP+} PB-PCs were observed in the T cell zone-red pulp bridging channel (Figure 3.15A), the red pulp adjacent to the follicle (Figure 3.15B), and extending toward the splenic edge (Figure 3.15C). EF-derived Blimp-1^{GFP+} PB-PC were also detected in high numbers within these regions (Figure 3.15A-C). GC-matured *S1pr2*$^{tdT+}$ Blimp-1^{GFP+} PB-PCs were also captured within GC B cell clusters (Figure 3.16A-B). Figures 3.15 and Figure 3.16 show a representative example of these observations, as no differences in distribution patterns were observed across the experimental time points.

GC-derived *S1pr2*$^{tdT+}$ Blimp-1^{GFP+} PB-PCs were observed at the periphery of the GC, outside the follicle, in regions corresponding to the marginal sinus or marginal zone (Figure 3.17A-C), consistent with the expected egress of LZ-derived PB [172]. This observation was detectable by day 5, when GC clusters were still small or not yet fully developed. The emerging phenomenon at day 5 was observed without (Figure 3.17) or with amplification of Blimp-1^{GFP+} signals (Figure 3.18).

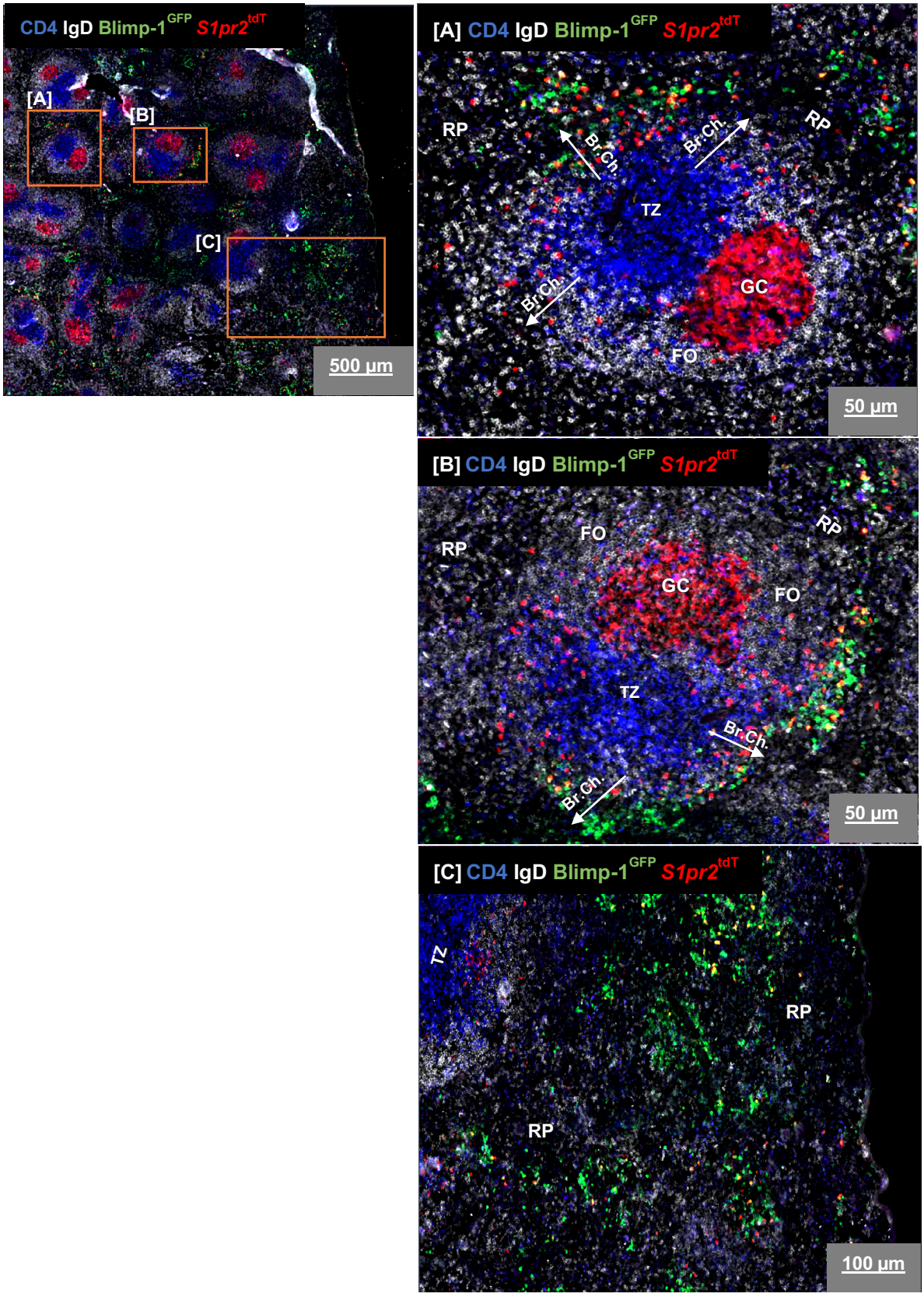


Figure 3.15. Migration pattern of EF-derived Blimp-1^{GFP+} PB-PCs and GC-matured *S1pr2*$^{tdT+}$ Blimp-1^{GFP+} PB-PCs into splenic compartments.

An example image illustrating the migration pattern of EF-derived Blimp-1^{GFP+} PB-PCs and GC-matured *S1pr2*$^{tdT+}$ Blimp-1^{GFP+} PB-PCs (see the experimental protocol in Figure 3.2). The image on the left-hand side shows the zoom-out of the splenic section stained with antibodies against IgD^{hi} follicular B cells (white fluorescence signal), CD4^{+}T cells (blue fluorescence signal), and goat anti-GFP (green fluorescence signal). The *S1pr2*^{tdT} is detected as auto-fluorescence in the red channel. **(A)** Zoom-in shows the migration of EF-derived Blimp-1^{GFP+} PB-PCs and GC-matured *S1pr2*$^{tdT+}$ Blimp-1^{GFP+} PB-PCs through the bridging channel from the T cells zone side. **(B)** Zoom-in image shows the migration of EF-derived Blimp-1^{GFP+} PB-PCs (green cells) and GC-matured *S1pr2*$^{tdT+}$ Blimp-1^{GFP+} PB-PCs (yellow cells) into the red pulp next to the follicle. **(C)** Zoom-in image shows the migration of EF-derived Blimp-1^{GFP+} PB-PCs (green cells) and GC-matured *S1pr2*$^{tdT+}$ Blimp-1^{GFP+} PB-PCs (yellow cells) into the splenic edge. These images were obtained from the spleen of HALO mice 6 days post-immunisation via *i.v.* with SRBCs. Images were produced by the fluorescent field at 20x magnification using a Zeiss AxioScan Z1 Slide Scanner. Images were processed at 500 µm (zoom-out image), 50 µm (zoom-in images A and B) and 100 µm (zoom-in image C) with Zen v3.1 (Blue Edition). GC: Germinal centre; FO: Follicular B cells; RP: Red pulp; TZ: T cells zone; Br.Ch. stands for bridging channel.

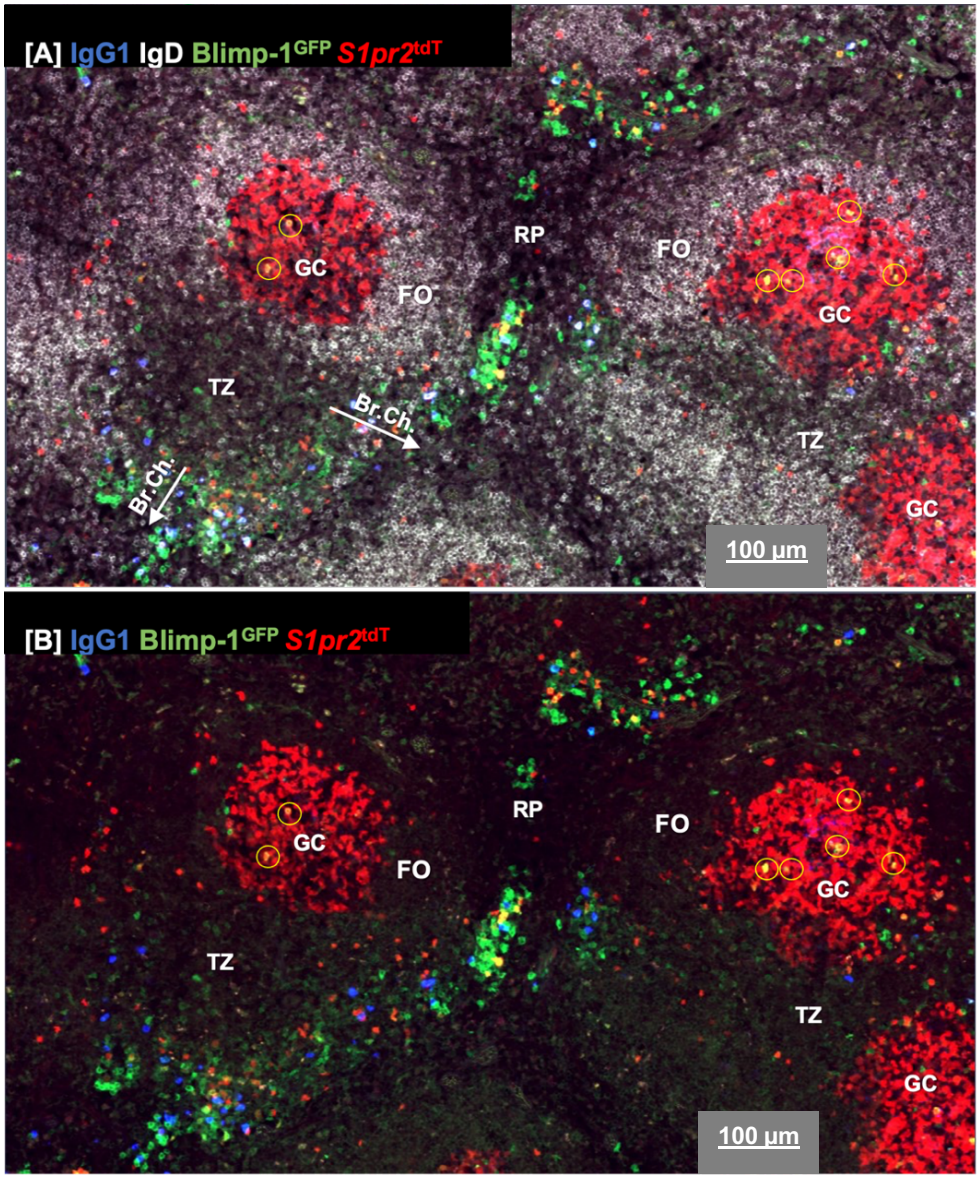


Figure 3.16. Localisation of GC-matured *S1pr2*$^{tdT+}$ Blimp-1^{GFP+} PB-PCs within GC B cell clusters.

An example image of GC-matured *S1pr2*$^{tdT+}$ Blimp-1^{GFP+} PB-PCs located within GC B cell clusters, denoted by yellow empty circles (see the experimental protocol in Figure 3.2). The splenic section was stained with antibodies against IgD^{hi} follicular B cells (white channel), IgG1^{+} antibody-secreting cells (blue channel), and goat anti-GFP (green channel). The *S1pr2*^{tdT} is detected as auto-fluorescence in the red channel. The upper image **(A)** shows the merged view of all channels, and the bottom image **(B)** shows the excluded white channel to enhance the true signals of *S1pr2*$^{tdT+}$ and Blimp-1^{GFP+}. Images were obtained from HALO mouse spleens 6 days after *i.v.* immunisation with SRBCs, using a Zeiss AxioScan Z1 Slide Scanner at 20x magnification. Images were processed at 100 µm with Zen v3.1 (Blue Edition). GC: Germinal centre; FO: Follicular B cells; RP: Red pulp; TZ: T cells zone; Br.Ch. stands for bridging channel.

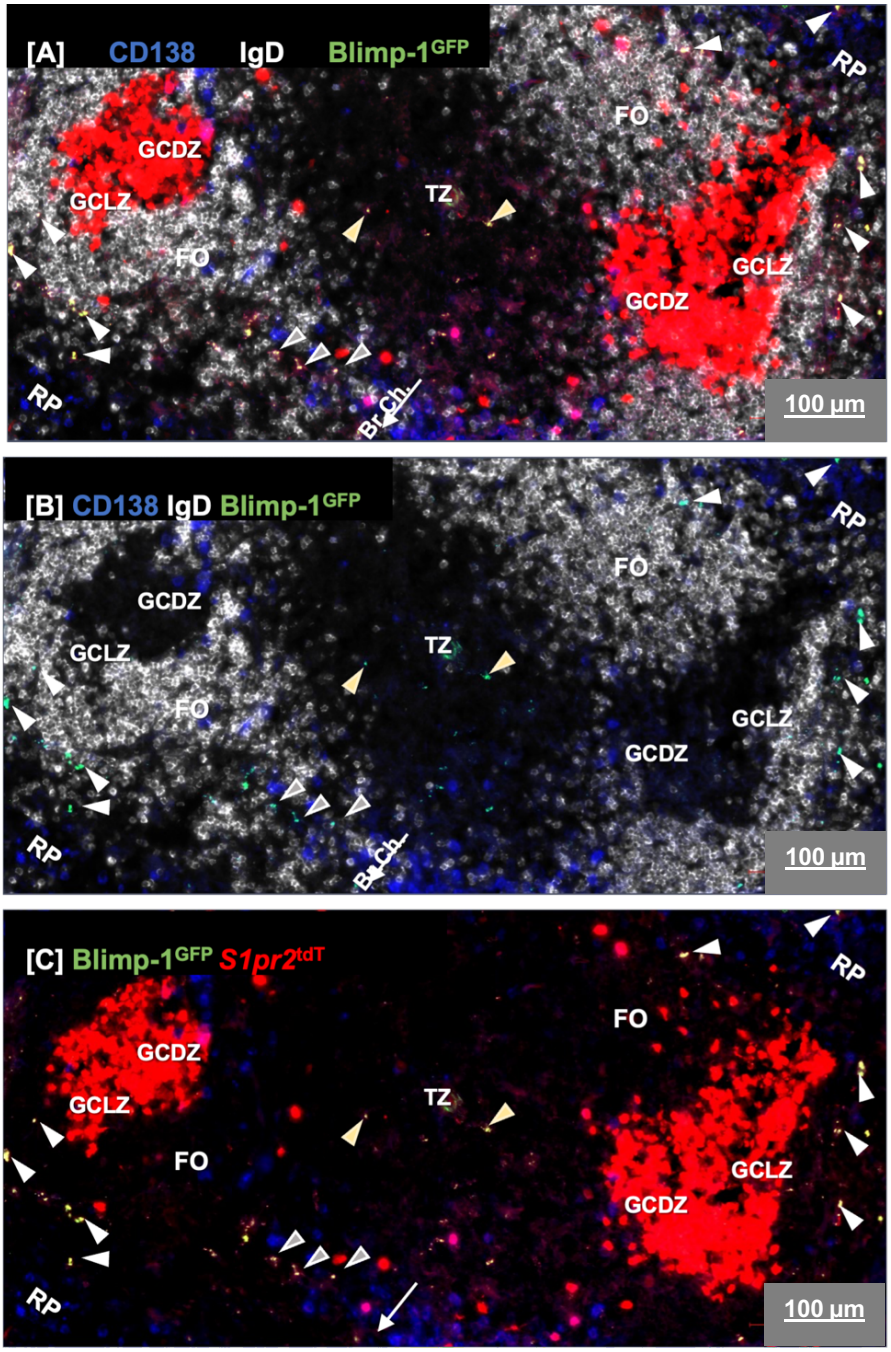
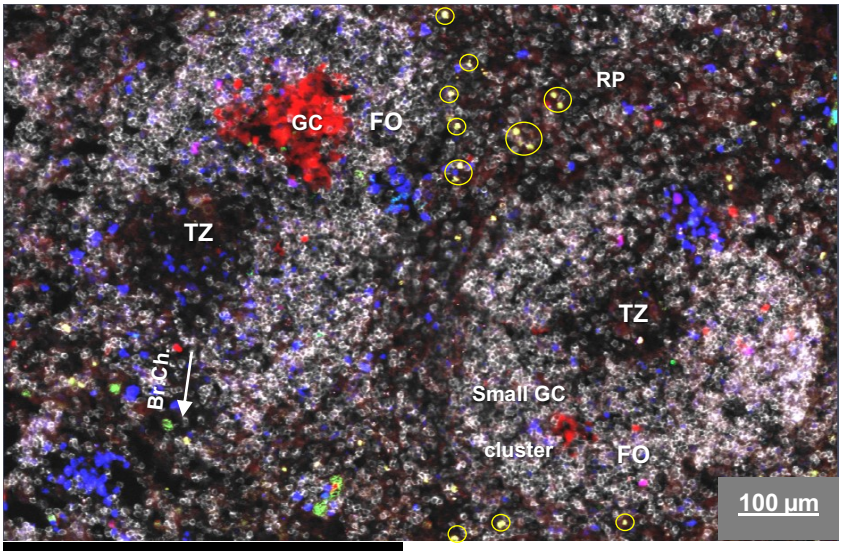


Figure 3.17. GC-matured *S1pr2*$^{tdT+}$ Blimp-1^{GFP+} PB-PCs emerging from the GCLZ side without GFP amplification.

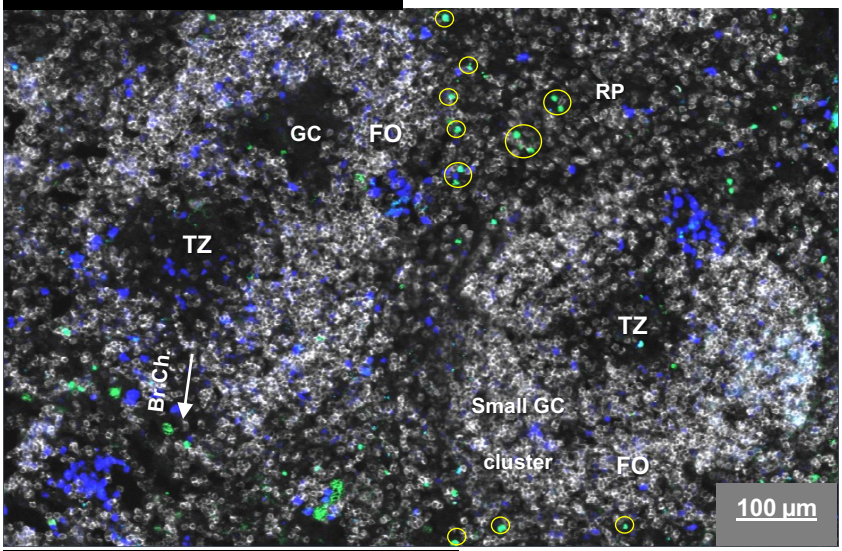
The experimental protocol is illustrated in Figure 3.2. An example image showing the emergence of GC-derived *S1pr2*$^{tdT+}$ Blimp-1^{GFP+} PB-PCs (yellow cells). Splenic section was stained for IgD^{hi} follicular B cells (white cells) and CD138^{+} PB-PCs (blue cells). Blimp-1^{GFP} and *S1pr2*^{tdT} signals were detected by auto-fluorescence. (green and red, respectively). **(A)** An example image of the secondary follicle view illustrating GC-

matured *S1pr2*$^{tdT+}$ Blimp-1^{GFP+} PB-PCs migrating from the light zone side (white arrowheads) towards the T zone (yellow arrowheads) and through the bridging channel (grey arrowheads). **(B)** Same image without the *S1pr2*$^{tdT+}$ red channel. **(C)** Same image without CD138^{+} blue and IgD^{hi} white channels. Images were obtained from the spleens of HALO mice 5 days after *i.v.* SRBCs immunisation acquired at 20x magnification using a Zeiss AxioScan Z1 Slide Scanner and processed at 100 µm in Zen v3.1 (Blue Edition). Abbreviations: GCDZ: Germinal centre dark zone; GCLZ: Germinal centre light zone; FO: Follicular B cells; RP: Red pulp; TZ: T cells zone; Br.Ch. stands for bridging channel.

[A] IRF4 IgD Blimp-1^{GFP} *S1pr2*^{tdT}



[B] IRF4 IgD Blimp-1^{GFP}



[C] IRF4 Blimp-1^{GFP} *S1pr2*^{tdT}

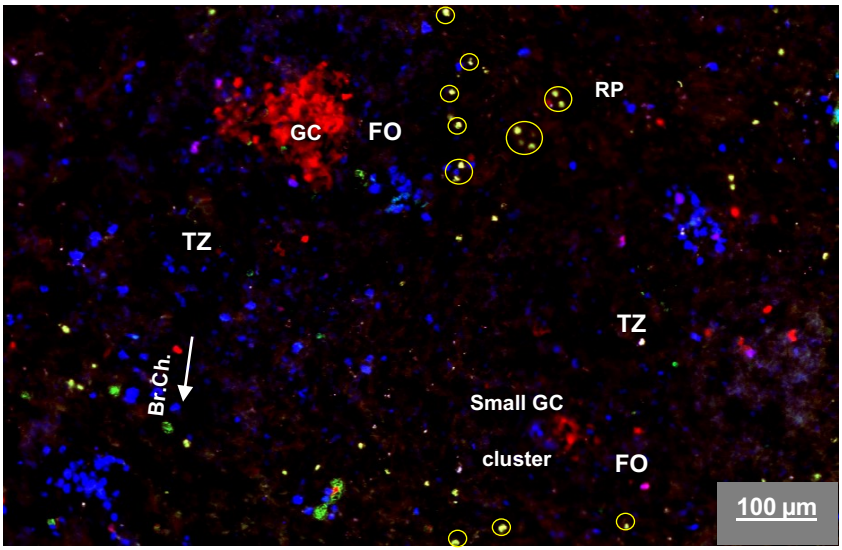


Figure 3.18. GC-matured *S1pr2*$^{tdT+}$ Blimp-1^{GFP+} PB-PCs emerging from the GCLZ side with GFP amplification.

The experimental protocol is illustrated in Figure 3.2. An example image showing the emergence of GC-matured *S1pr2*$^{tdT+}$ Blimp-1^{GFP+} PB-PCs (yellow cells). The splenic section was stained for IgD^{hi} follicular B cells (white cells), CD138^{+} PB-PCs (blue cells), and goat anti-GFP for detecting Blimp-1 expression. The *S1pr2*^{tdT} is detected as auto-fluorescence in the red channel. **(A)** An example image of the secondary follicles view, with merged channels, shows GC-matured *S1pr2*$^{tdT+}$ Blimp-1^{GFP+} PB-PCs emerging from the GC light zone side (denoted by yellow circles), into the T zone (yellow-filled arrowheads). **(B)** Same image without the *S1pr2*$^{tdT+}$ red channel. **(C)** Same image without IgD^{hi} white channels. Images were obtained from spleens of HALO mice 5 days after *i.v.* SRBCs immunisation, acquired at 20x magnification using a Zeiss AxioScan Z1 Slide Scanner and processed at 100 µm in Zen v3.1 (Blue Edition). Abbreviations: GC: Germinal centre B cells; FO: Follicular B cells; RP: red pulp; TZ: T cells zone; Br.Ch. stands for bridging channel.

The CD138 marker, also known as syndecan-1, is a valid approach marker for identifying PB-PC [143, 144, 173], but also a marker for identifying T lymphocytes that share features of both T cells and NK cells [145]. Therefore, CD138^{+} PB-PC was visualised by their dual expression with *S1pr2*$^{tdT+}$ and/or Blimp-1^{GFP+}. In our experimental protocol (see Figure 3.2), CD138^{+}-expressing cells (blue cells) accumulated at the end border between the T cell zone and the red pulp (Figure 3.19), consistent with the previous study performed by Meyer-Hermann and colleagues [147] and further supporting the concept that PB emerges from GC via the GCDZ side [8, 147]. GC-matured CD138^{+} *S1pr2*$^{tdT+}$ PB-PCs were visualised (displayed as pink cells) in the GC cluster, at the GTI region, and the bridging channel (Figure 3.19A-B).

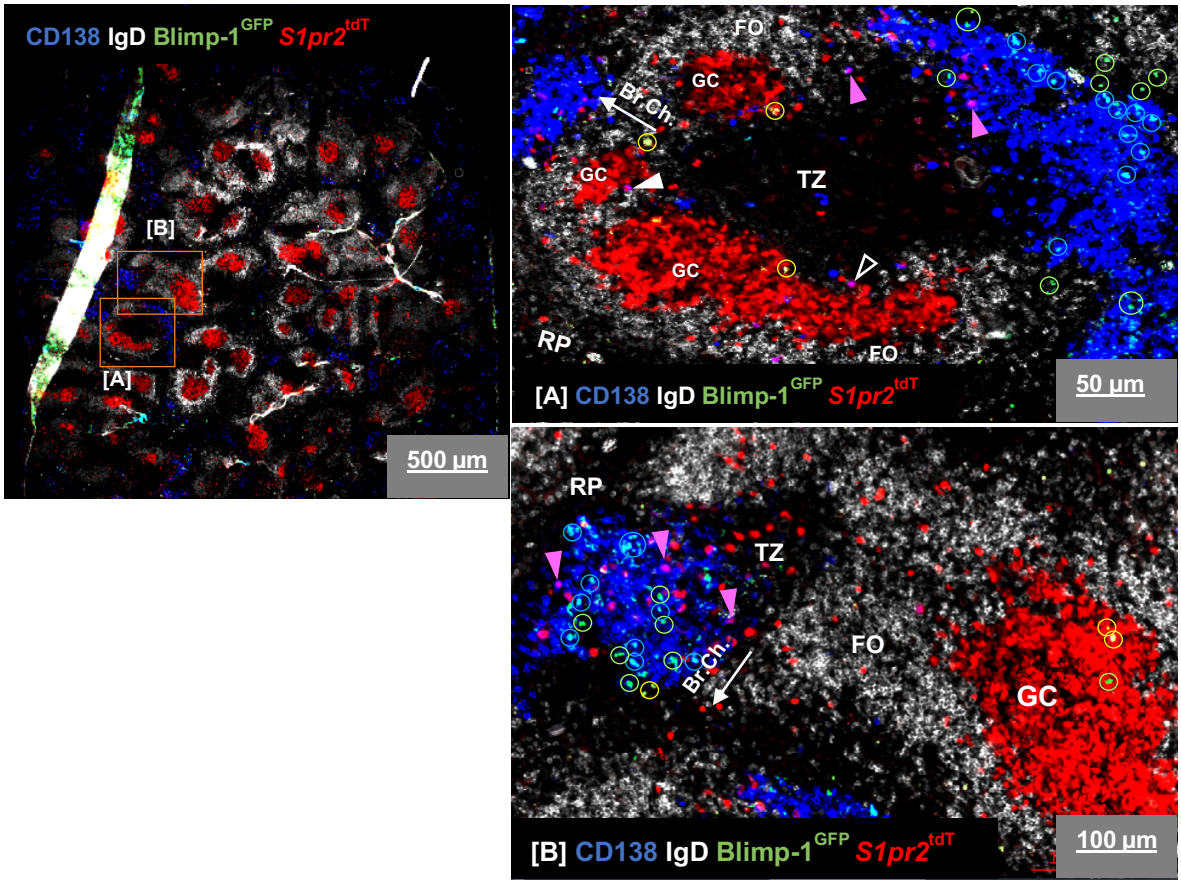


Figure 3.19. Migration pattern of EF-derived and GC-derived CD138^{+} PB-PC.

Example images display the migration pattern of CD138^{+} PB-PCs (blue cells), EF-derived CD138^{+} Blimp-1^{GFP+} PB-PCs (turquoise cells), GC-derived *S1pr2*$^{tdT+}$ CD138^{+} PB-PCs (pink cells), in addition to GC-matured *S1pr2*$^{tdT+}$ Blimp-1^{GFP+} PB-PCs (yellow cells) and EF-derived Blimp-1^{GFP+} PB-PCs (green cells) (see the experimental protocol in Figure 3.2). The splenic section was stained with antibodies against follicular IgD^{hi} B cells (white fluorescence signal), CD138^{+} PCs cells (blue fluorescence signal), and anti-GFP (green fluorescence signal). The *S1pr2*^{tdT} is detected as auto-fluorescence in the red channel. The image on the left-hand side is a zoom-out of the total splenic section. The images on the right-hand side are the zoom-in of the two selected areas (A-B). **(A)** The secondary follicle view represents GC-matured *S1pr2*$^{tdT+}$ Blimp-1^{GFP+} PB-PCs (yellow empty circle) at GTI, GC-derived *S1pr2*$^{tdT+}$ CD138^{+} PB-PCs in the GC cluster (white filled arrowhead), at GTI (white empty arrowhead), and at the bridging channel (pink filled arrowhead). EF-derived CD138^{+} Blimp-1^{GFP+} PB-PCs (blue empty circle) at the end border between the T cell zone and the red pulp. **(B)** Another view from the same secondary follicle represents GC-matured *S1pr2*$^{tdT+}$ Blimp-1^{GFP+} PB-PCs (yellow empty circle) inside the GC cluster and at the RP, GC-derived *S1pr2*$^{tdT+}$ CD138^{+} PB-PCs at the bridging channel and at the RP (pink filled arrowhead), EF-derived CD138^{+} Blimp-1^{GFP+} PB-PCs in the RP (blue empty circle), and EF-derived Blimp-1^{GFP+} PB-P inside the GC cluster and at the red pulp (green empty circle).

These images were obtained from spleens of HALO mice 6 days post-immunisation via *i.v.* with SRBCs. Images were produced by the fluorescent field at 20x magnification using a Zeiss AxioScan Z1 Slide Scanner. Images were processed at 500 µm (zoom-out image), 50 µm (zoom-in image A), and 100 µm (zoom-in image B) with Zen v3.1 (Blue Edition). Abbreviations: GC: Germinal centre; FO: Follicular B cells; RP: Red pulp; TZ: T cells zone; Br.Ch. stands for bridging channel.

EF-matured CD138^{+} Blimp-1^{GFP+} PB-PCs were visualised at the end border between the T cell zone and the red pulp (Figure 3.19A) and in the red pulp (Figure 3.19B). Flow cytometry analysis showed that EF-derived Blimp-1^{GFP+} PB-PCs are present within Fas^{hi} GC B cells, and immunofluorescence confirmed their localisation within the GC cluster (Figure 3.19B and Figure 3.20). This was also identified by Zhang et al. 2018 [8], who identified Blimp-1^{GFP}-expressing cells within the GC, indicating that some B cells can begin to express Blimp-1 ^{GFP} even while still in the GC environment.
However, the presence of Blimp-1 ^{GFP} lacking *S1pr2*$^{tdT+}$ expression in the HALO mouse model raises the question of whether these cells are derived from EF responses and re-enter the GC.

IgG1^{+} PB-PCs (blue) were scattered in the bridging channel at the end border with the T cell zone and within GCLZ in a clustered pattern (Figure 3.21). EF-derived IgG1^{+} Blimp-1^{GFP+} PB-PCs (turquoise) were detected within the T cell zone, in the bridging channel, at the end of the follicle, and in regions corresponding to the marginal sinus or marginal zone. A few GC-matured IgG1^{+} *S1pr2*$^{tdT+}$ Blimp-1^{GFP+} PB-PCs (white) were detected in the bridging channel.

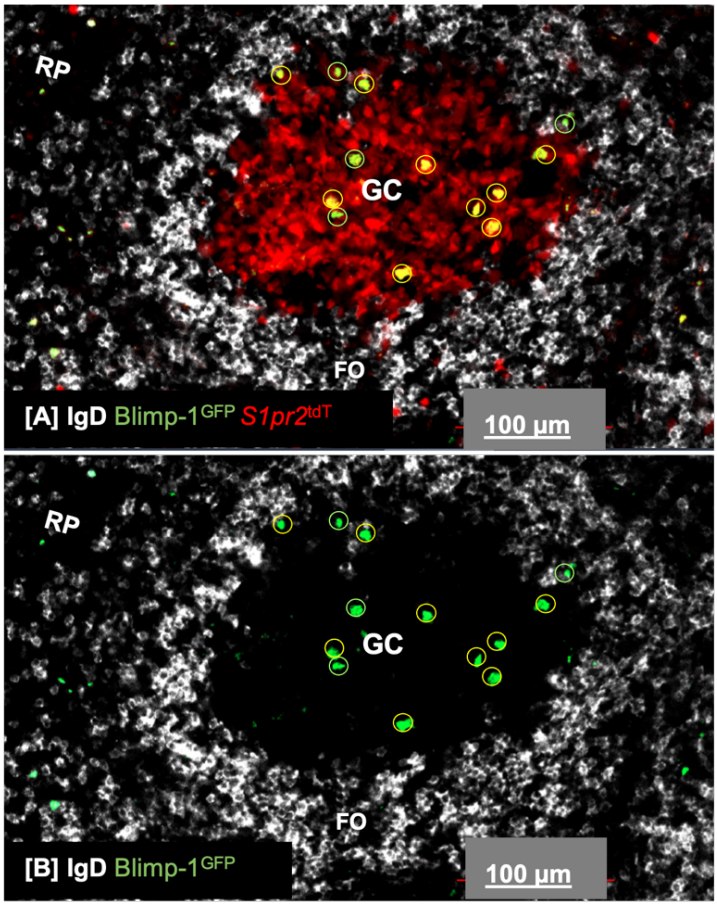


Figure 3.20. EF-derived Blimp-1^{GFP+} PB-PCs inside the GC B cells cluster.
An example image displays the presence of EF-derived Blimp-1^{GFP+} PB-PCs (green cells), inside the GC B cells cluster (see the experimental protocol in Figure 3.2). The splenic section was stained with antibodies against IgD^{hi} follicular B cells (white), and anti-GFP (green). The *S1pr2*^{tdT} is detected as auto-fluorescence in the red channel. **(A)** Zoom-in GC B cells cluster showing EF-derived Blimp-1^{GFP} PB-PCs (green empty circle), and GC-matured *S1pr2*$^{tdT+}$Blimp-1^{GFP+}PB-PCs (yellow empty circle). **(B)** Zoom-in view of the GC B cells cluster, showing the same region as in A, but after the removal of *S1pr2*$^{tdT+}$ auto-fluorescence signal to enhance contrast of the Blimp-1^{GFP} signal. Images were obtained from spleens of HALO mice 6 days post-immunisation via *i.v.* with SRBCs. Images were produced by the fluorescent field at 20x magnification using a Zeiss AxioScan Z1 Slide Scanner. Images were processed at 100 µm with Zen v3.1 (Blue Edition). Abbreviations: GC: Germinal centre; FO: Follicular B cells; RP: Red pulp.

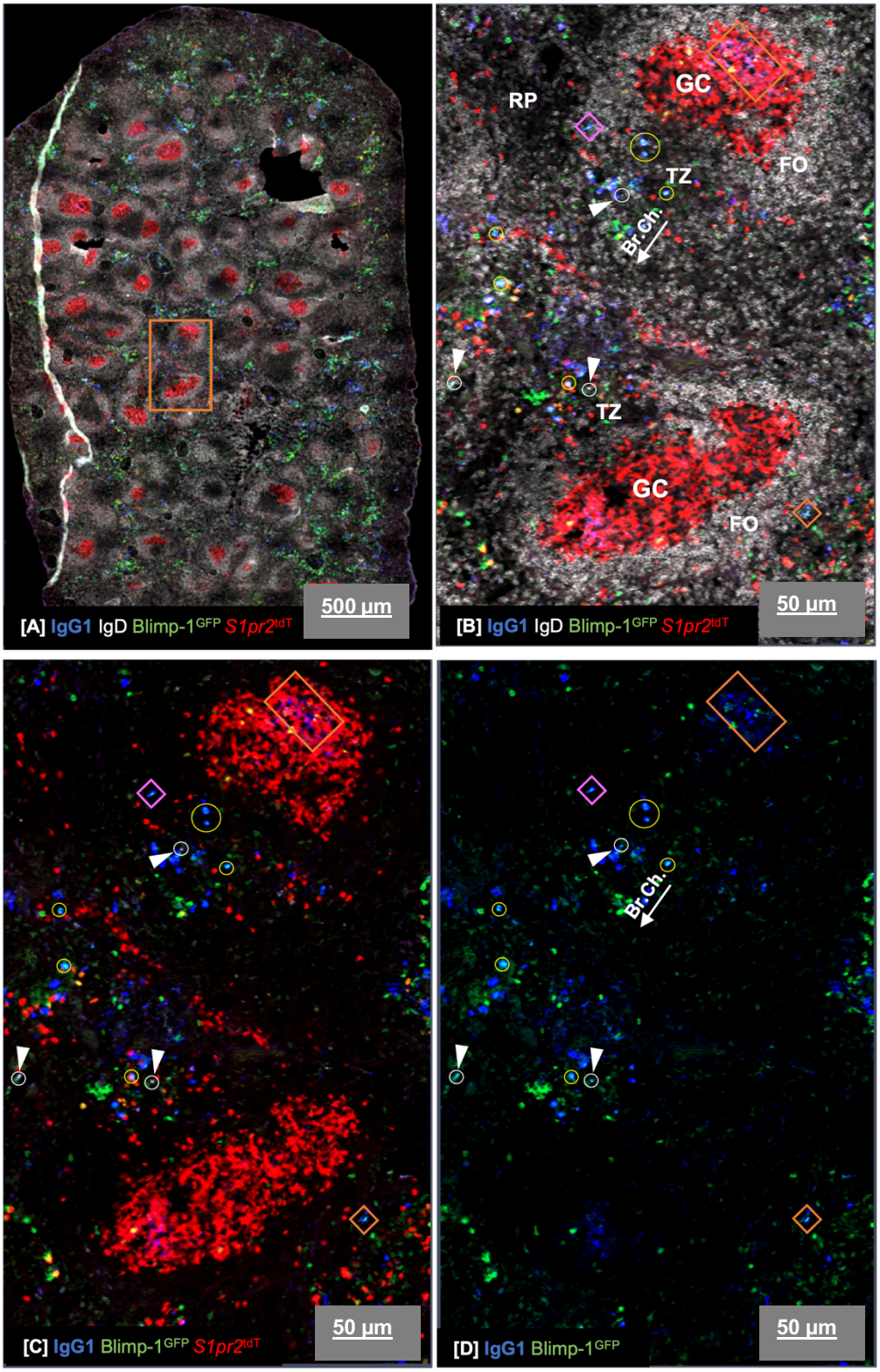

[A] IgG1 IgD Blimp-1GFP S1pr2tdT
500 µm
[B] IgG1 IgD Blimp-1GFP S1pr2tdT
50 µm
RP
GC
FO
TZ
Br.Ch.
TZ
GC
FO
[C] IgG1 Blimp-1GFP S1pr2tdT
50 µm
[D] IgG1 Blimp-1GFP
50 µm
Br.Ch.

Figure 3.21. Example image of IgG1$^+$ response in HALO mice.

Example image displays the IgG1$^+$ response after primary immunisation with SRBC (see the experimental protocol in Figure 3.2). The splenic section was stained with antibodies against IgD^{hi} follicular B cells (white), goat anti-GFP (green), and IgG1$^+$ PB-PC. The *S1pr2*^{tdT} is detected as auto-fluorescence in the red channel. **(A)** The zoomed-out view of the whole splenic section. **(B)** The zoomed-in view of the selected area, highlighted by the orange rectangle line, shows the dissemination pattern of IgG1$^+$ PB-PC. **(C)** The zoomed-in view without IgD channel illustrates the co-expression of GC-matured IgG1$^+$ *S1pr2*$^{tdT+}$ Blimp-1^{GFP+} PB-PCs (white-filled head arrow), EF-derived IgG1$^+$ Blimp-1^{GFP+} PB-PCs (yellow empty circle), IgG1$^+$ inside the GCLZ (orange rectangle), EF-derived IgG1$^+$ Blimp-1^{GFP+} PB-PCs at the end of the follicle (pink square) and EF-derived IgG1$^+$ Blimp-1^{GFP+} PB-PCs in regions corresponding to the marginal sinus or marginal zone (orange square). **(D)** The same view in B without IgD and *S1pr2*^{tdT} channels. Images were derived from the spleen of a HALO mouse 6 days post-immunisation i.v. with SRBCs. Images were produced using a Zeiss AxioScan Z1 Slide Scanner at 20x magnification with the fluorescent field. Images were processed at 500 µm (zoomed-out view) and 50 µm (zoomed-in view) with Zen v3.1 (Blue Edition). Abbreviations: GC: Germinal centre; FO: Follicular B cells; RP: Red pulp; Br.Ch. stands for bridging channel.

3.2.2. Characterisation of the later response of NP-specific GC-matured *S1pr2*$^{tdT+}$ Blimp-1^{GFP+} PB-PC after primary NP$_{27}$-KLH challenge.

It was then of interest to investigate how GC-matured *S1pr2*$^{tdT+}$ Blimp-1^{GFP+} PB-PC respond following NP-KLH immunisation, while also excluding the possibility that SRBC induce short-lived GCs [174], and lack antigen-specific tracking. Overall, SRBC-induced GC B cells displayed characteristics similar to NP-induced GC B cells, including comparable GC kinetics, sustained IgM$^+$ and isotype-switched GC B cell populations, and persistence of founder-like GC B cells during the response [175].

However, NP-derived GC responses exhibit well-defined kinetics. GCs become well-developed by days 8-10, reaching their maximal size around days 12-14 [26, 172, 175]. NP-KLH provides a traceable system for analysing antigen-specific GC maturation and the fate of GC-derived PB-PC. In the Toellner et al. study (1996), it was shown that GC activity strongly increases by day 10 and decreases by day 14, and PC activity increases in medullary cords. These PCs could originate from either the EF or GC [26]. HALO mice can provide simultaneous fate-mapping of GC-derived and EF-PB-PC populations. Therefore, HALO mice were immunised i.p. with 50 µg of precipitated NP_{27}-KLH and heat-inactivated *B. pertussis* as an adjuvant. Eight days later, HALO mice were orally administered a single dose of tamoxifen 48 hours before harvesting on days 10 and 14 post-immunisation (see the experimental protocol in Figure 3.22).

PB-PCs were gated as $CD138^{+}$ $B220^{lo/-}$ cells (Figure 3.23A). There were no significant changes in overall PB-PCs (Figure 3.23B). The analyses of the expression of *S1pr2*$^{tdT+}$ and Blimp-1^{GFP+} were performed by gating $CD138^{+}$ $B220^{lo/-}$ PB-PCs on FITC for Blimp-1^{GFP} expression and PE for *S1pr2*^{tdT} expression (Figure 3.23C). The frequency of GC-matured $CD138^{+}$ *S1pr2*$^{tdT+}$ Blimp-1^{GFP+} PB-PCs declined from a mean of 4% at day 10 to 2.6% at day 14 (Figure 3.23D). In contrast, the mean frequency of EF-matured $CD138^{+}$ Blimp-1^{GFP+} PB-PCs was around 80% at day 10 and 80.5% at day 14 (Figure 3.23E). The mean frequency of GC-derived $CD138^{+}$ *S1pr2*$^{tdT+}$ PB-PCs was lower at day 14 (Figure 3.23F), indicating that the late GC stages (at day 14) produce fewer PB, consistent with the contraction phase. Additionally, O'Connor et al. showed that PC precursors migrate to the BM around day 14 after NP-KLH immunisation [176].

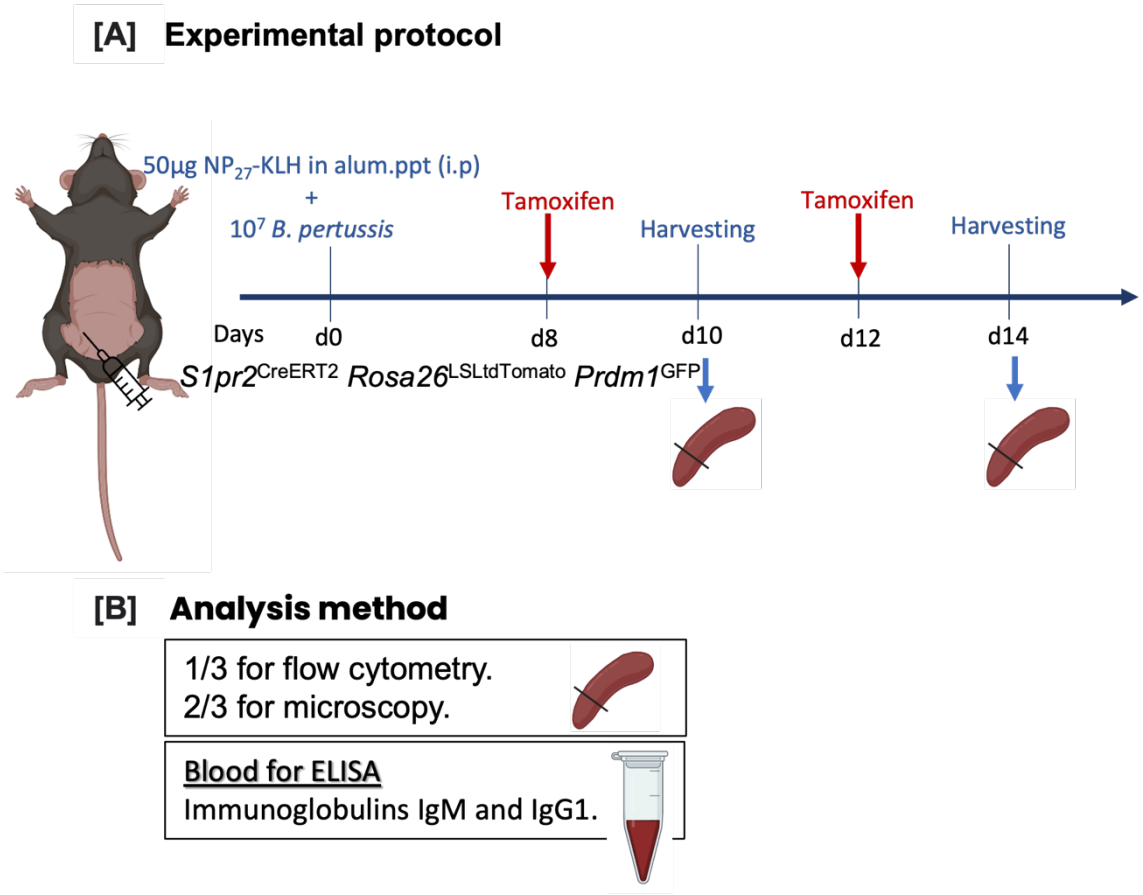


Figure 3.22. Schematic of the experimental procedure for primary immunisation with NP_{27}-KLH in HALO mice.

(A) Twelve to eighteen-week-old mice (5 mice for day 10 and 6 mice for day 14) were immunised i.p. with 50µg NP_{27}-KLH precipitated in 200µL alum on day 0. Mice were treated with tamoxifen (200 µL of 20 mg/mL in corn oil) via oral gavage 48 hours (red arrow) before tissue harvest on day 10 and day 14 (blue arrow). Before culling, mice were bled by cardiac puncture for IgM and IgG1 analysis. **(B)** The analysis method shows that one-third of the spleen was used for flow cytometry analysis, and two-thirds was used for immunofluorescence staining.

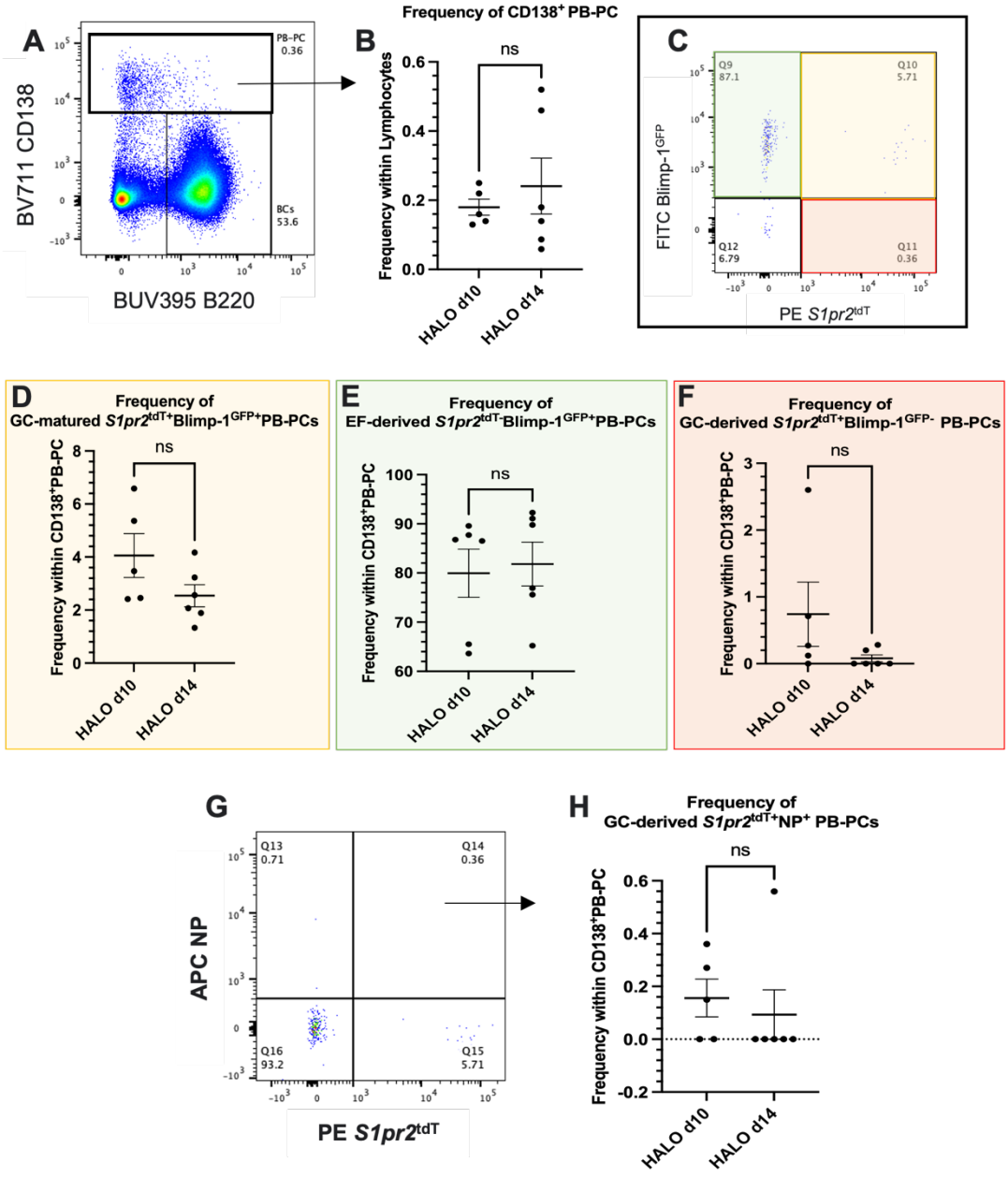


Figure 3.23. Analysis of CD138$^+$ PB-PC in a later response to NP$_{27}$-KLH.
The experimental protocol is illustrated in Figure 3.22. **(A)** CD138$^+$ PB-PC were gated from live cells. **(B)** The frequency of CD138^{hi} PB-PC within the lymphocytes (mean ± SEM). **(C)** CD138$^+$ PB-PC were gated on *S1pr2*^{tdT} and Blimp-1^{GFP}. **(D)** The frequency of GC-derived *S1pr2*$^{tdT+}$ Blimp-1^{GFP+} PB-PC within CD138$^+$ PB-PC. **(E)** The frequency of GC-derived *S1pr2*$^{tdT-}$ Blimp-1^{GFP+} PB-PC within CD138$^+$ PB-PC. **(F)** The frequency of GC-derived *S1pr2*$^{tdT+}$ Blimp-1^{GFP-} memory B cells within CD138$^+$ PB-PC. **(G)** CD138$^+$ PB-PC were gated on NP-specific PB-PC and *S1pr2*^{tdT}. **(H)** The frequency of GC-derived *S1pr2*$^{tdT+}$ NP$^+$ PB-PC. Each symbol represents one mouse. Representative of one experiment where n = 5 mice for the day 10 group and n = 6 for the day 14 group. Statistical tests were performed by an unpaired Welch's t-test, n.s. $p > 0.05$.

CD138^{+} PB-PCs were then gated on NP and *S1pr2*$^{tdT+}$ cells (Figure 3.23G). The mean frequency of NP-specific GC-matured CD138^{+} *S1pr2*$^{tdT+}$ PB-PCs (Figure 3.23H) was higher at day 10 than at day 14; however, this difference did not reach statistical significance.

B220^{+} B cells were gated on CD38 and Fas (Figure 3.24A). GC B cells were identified as CD38^{lo} Fas^{hi} B cells, and non-GC B cells were identified as CD38^{hi} Fas^{lo} B cells. The frequency of Fas^{hi} GC B cells rose on day 10 (Figure 3.24B), while the frequency of CD38^{hi} non-GC B cells was dominant on day 14 (Figure 3.24C). Fas^{hi} GC B cells (Figure 3.25A) were further gated for the proportion of GC-matured *S1pr2*$^{tdT+}$ Blimp-1^{GFP+} PB-PCs (Figure 3.25B) and for the proportion of GC-derived *S1pr2*$^{tdT+}$ B cells (Figure 3.25C). The mean frequency of GC-matured *S1pr2*$^{tdT+}$ Blimp-1^{GFP+} PB-PCs within Fas^{hi} GC B cells was nearly 4% on day 14, compared to just above 2% on day 10 (Figure 3.25D). GC-derived *S1pr2*$^{tdT+}$ Fas^{hi} B cells were 90.4% at day 10 and 90.8% at day 14 (Figure 3.25E). Regarding the specificity to NP (Figure 3.26B), NP-specific B220^{hi} GC B cells showed a slight increase from a mean frequency of 5.8% on day 10 to 11.2% on day 14 (Figure 3.26D). The proportion of NP-specific *S1pr2*$^{tdT+}$ GC B cells (Figure 3.26C) was 7.2% at day 10 and 11.1% at day 14 (Figure 3.26E).

Given the well-established role of the differential expression of the transmembrane proteins CXCR4 and CD86 in defining the GC zones [177], DZ and LZ, this study aimed to analyse whether the Fas^{hi} GC B cells skew towards a particular GC compartment at these time points (Figure 3.27A). DZ B cells were defined as CXCR4^{hi} CD86^{lo} cells, whereas LZ B cells were defined as CXCR4^{lo} CD86^{hi} cells. Gate was applied according to the distribution of CXCR4 and CD86 expression using fluorescence minus one

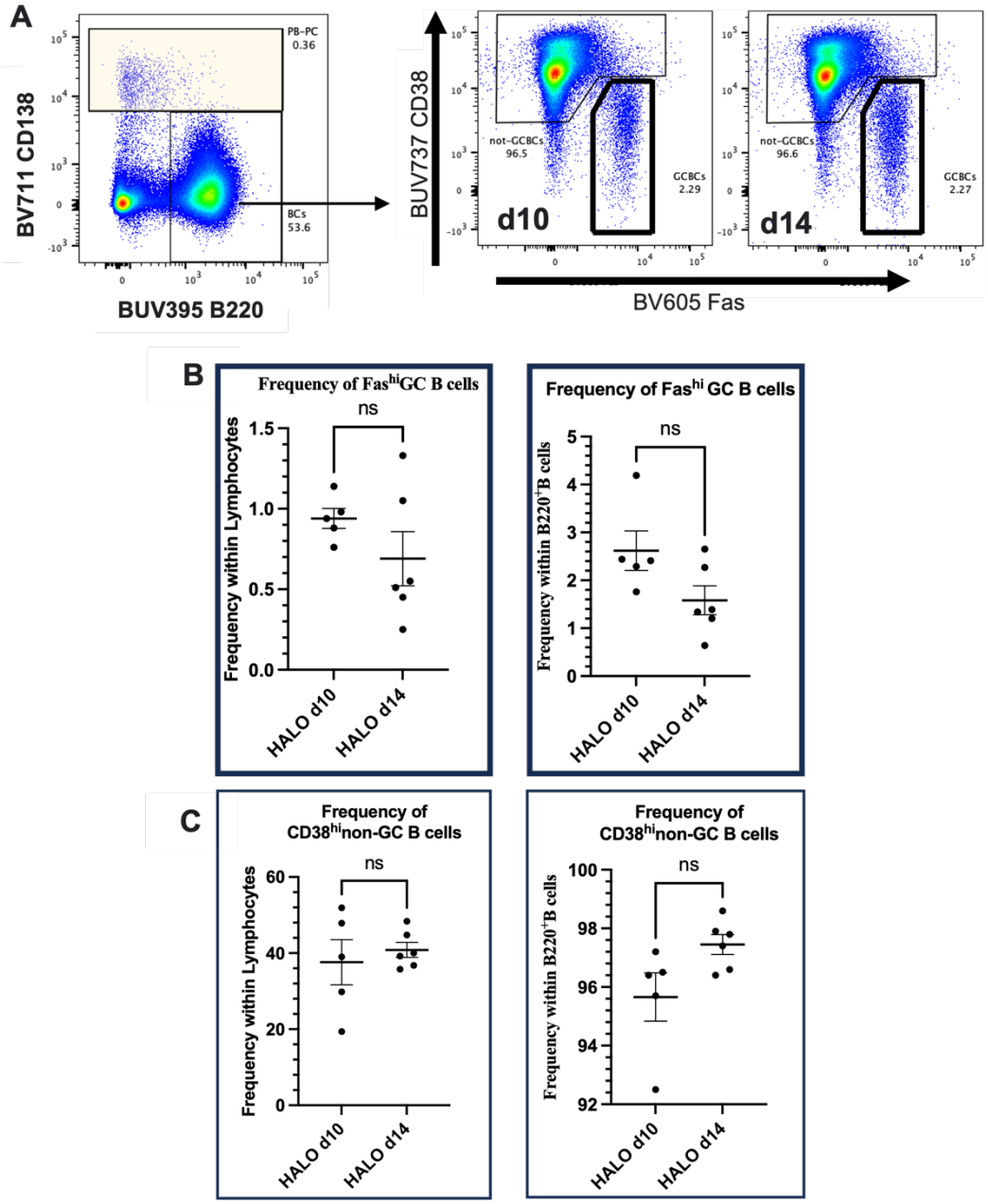


Figure 3.24. Percentage of Fas^{hi} GC B cells at day 10 and day 14 post-NP$_{27}$-KLH immunisation.

The experimental protocol is illustrated in Figure 3.22. **(A)** Representative data plot-based results showing GC B cell response in HALO mice (bold black line) at day 10 and day 14 post-immunisation i.p. with NP$_{27}$-KLH. **(B-C)** Frequency of flow cytometry analysis of **(B)** Fas^{hi} GC B cells (bold black line) **(C)** CD38^{hi} non-GC B cells (thin black line) (mean ± SEM). Each symbol represents one mouse. Representative of one experiment where n = 5 mice for the day 10 group and n = 6 for the day 14 group. Statistical tests were performed by an unpaired Welch's t-test, n.s. $p > 0.05$.

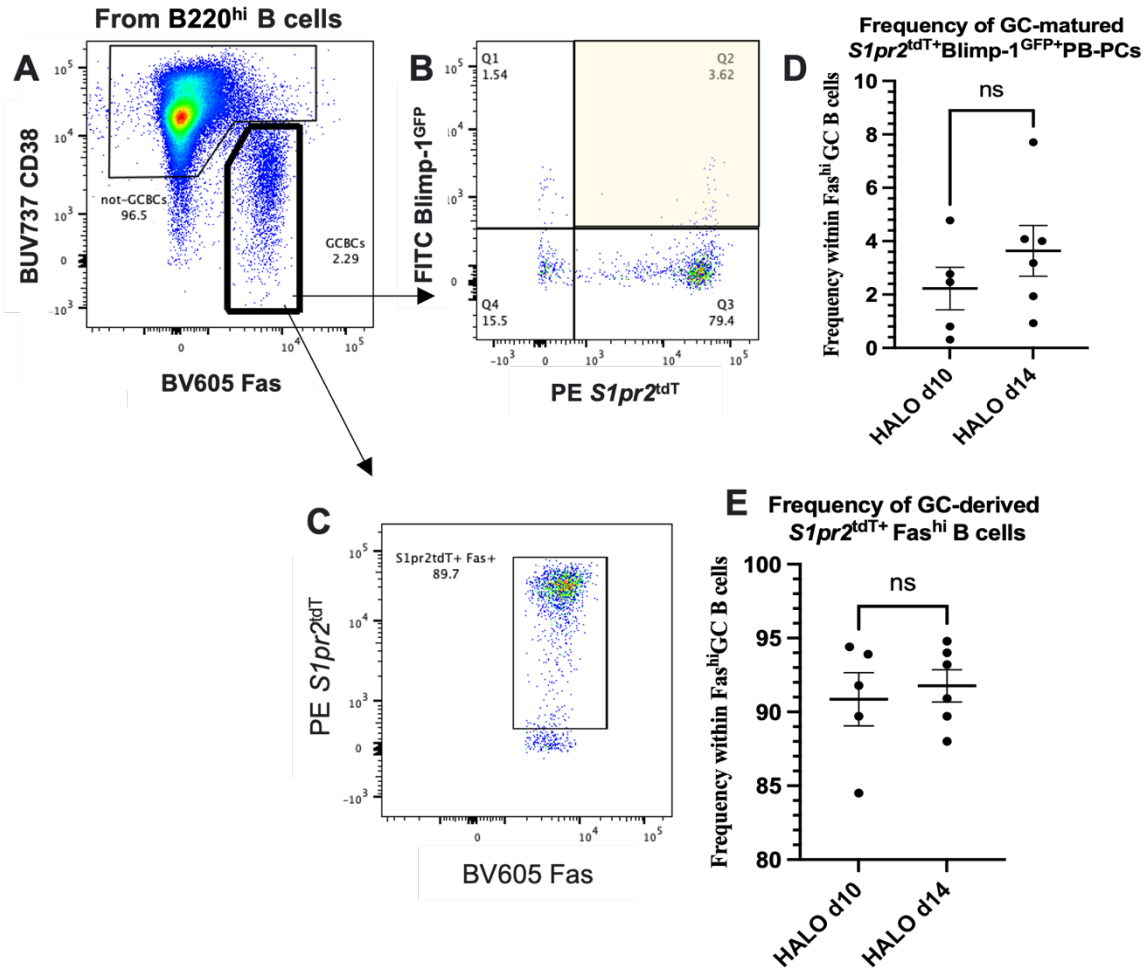


Figure 3.25. GC-matured *S1pr2*$^{tdT+}$ Blimp-1^{GFP+} PB-PC and GC-derived *S1pr2*$^{tdT+}$ Fas^{hi} B cells on day 10 and day 14 post-NP$_{27}$-KLH immunisation.

The experimental protocol is illustrated in Figure 3.22. **(A)** Representative data plots-based results of GC B cells (bold black line) were gated and further analysed for GC-matured *S1pr2*$^{tdT+}$ Blimp-1^{GFP+} PB-PC response (pale yellow square) **(A)**, and GC-derived *S1pr2*$^{tdT+}$ Fas^{hi} B cells response **(C)**. **(D)** Flow cytometric analysis frequency of GC-matured *S1pr2*$^{tdT+}$ Blimp-1^{GFP+} PC within Fas^{hi} GC B cells. **(E)** Flow cytometric analysis frequency of GC-derived *S1pr2*$^{tdT+}$ Fas^{hi} B cells within Fas^{hi} GC B cells (mean ± SEM). Each symbol represents one mouse. Data was obtained from one experiment where n = 5 mice for the day 10 group and n = 6 for the day 14 group. Statistical tests were performed by an unpaired Welch's t-test, n.s. $p > 0.05$.

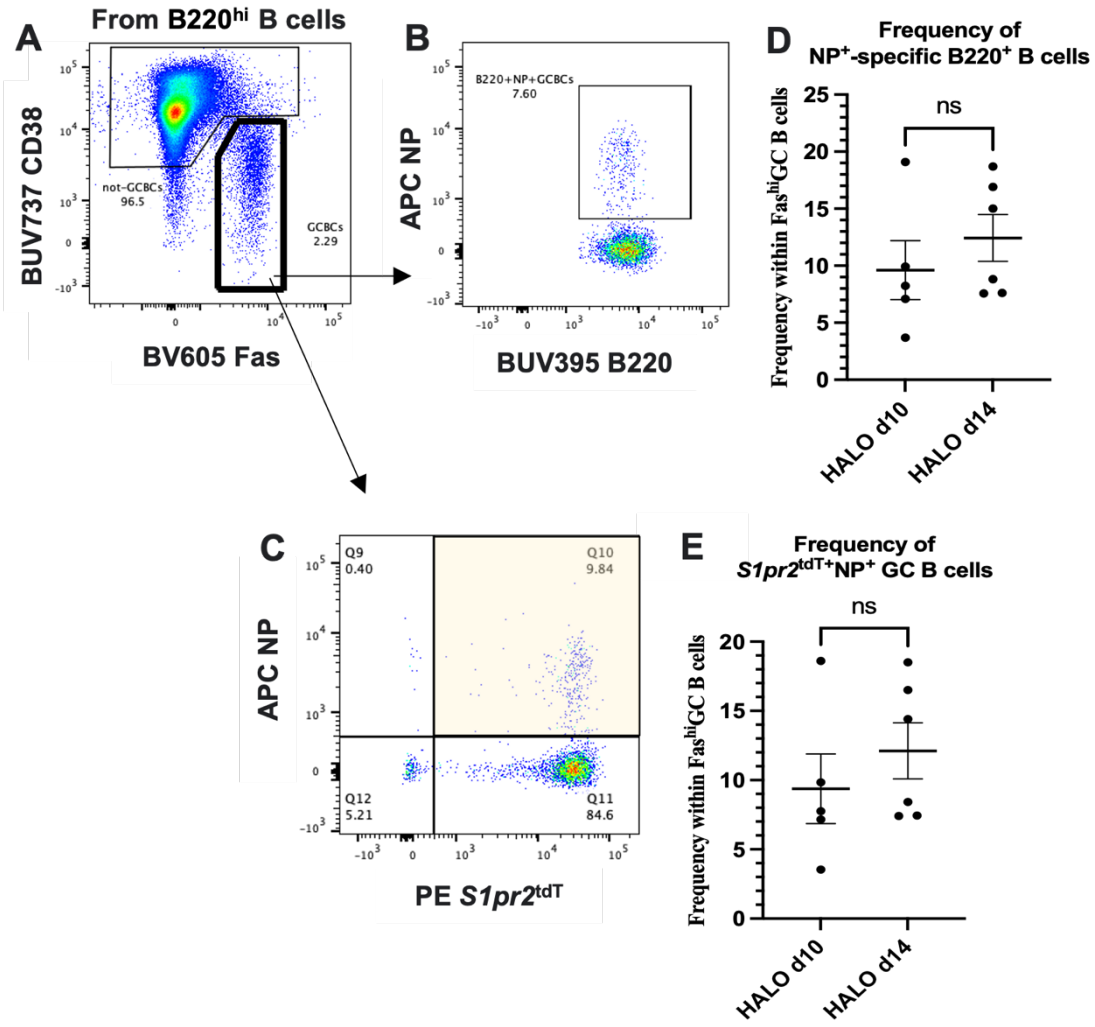


Figure 3.26. NP-specific GC-derived Fas^{hi} B220^{hi} B cells response on days 10 and 14 post-NP$_{27}$-KLH immunisation.

The experimental protocol is illustrated in Figure 3.22. **(A)** Representative data plots-based results of GC B cells (bold black line) were gated, then further analysed for NP-specific B220^{hi} GC B cells response (pale yellow square) **(B)**, and NP-specific *S1pr2*$^{tdT+}$ GC B cells response **(C)**. **(D)** Frequency of flow cytometry analysis of NP-specific B220^{hi} GC B cells within Fas^{hi} GC B cells (mean ± SEM). **(E)** Frequency of flow cytometry analysis of NP-specific *S1pr2*$^{tdT+}$ GC B cells within Fas^{hi} GC B cells (mean ± SEM). Each symbol represents one mouse. Representative of one experiment where n = 5 mice for the day 10 group and n = 6 for the day 14 group. Statistical tests were performed by an unpaired Welch's t-test, n.s. $p > 0.05$.

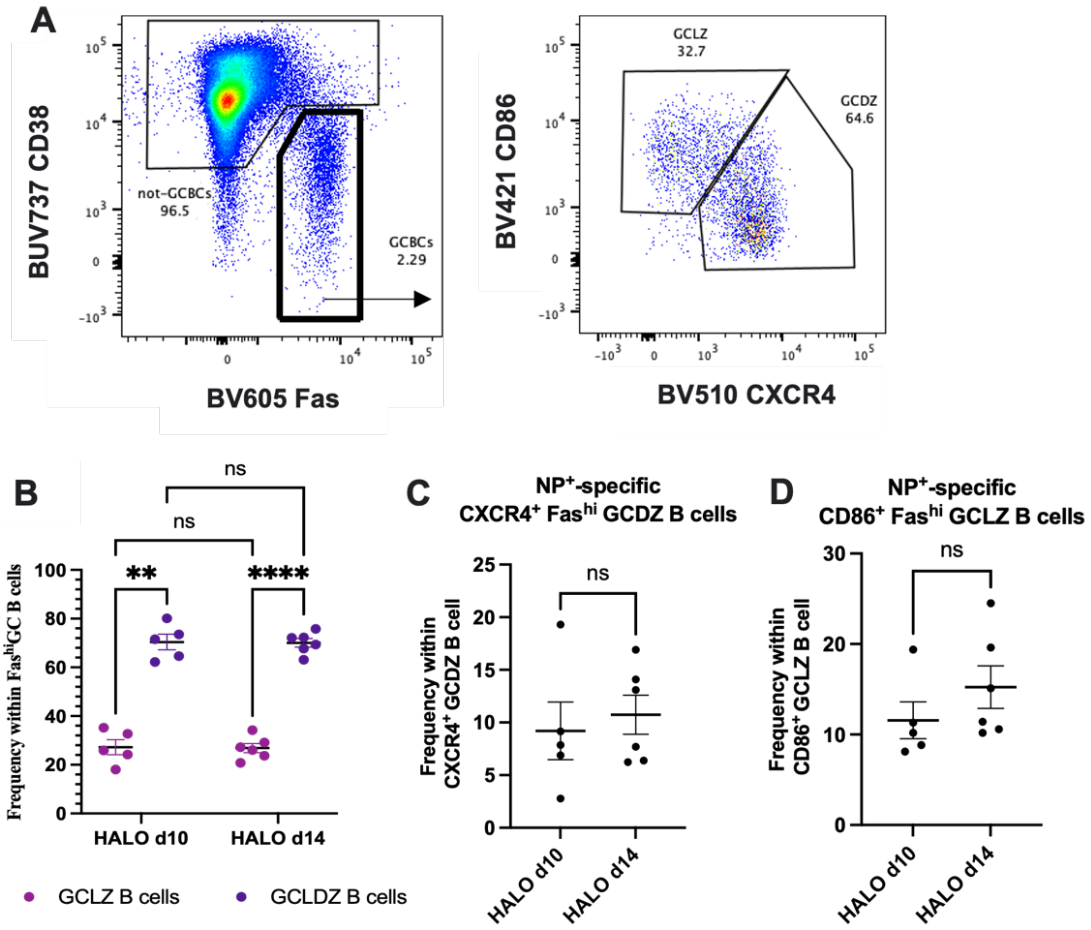


Figure 3.27. GC B cells remain enriched in the GCDZ after 10 and 14 days post-NP_{27}-KLH immunisation.

The experimental protocol is illustrated in Figure 3.22. **(A)** Representative data plots of $CD86^{hi}$ $CXCR4^{lo}$ GCLZ B cells and $CD86^{lo}$ $CXCR4^{hi}$ GCDZ B cells. **(B)** Frequency of flow cytometry analysis of GC zones within Fas^{hi} GC B cells (mean ± SEM). Each symbol represents one mouse. Representative of one experiment where n = 5 mice for the day 10 group and n = 6 for the day 14 group. Statistical tests were performed with mixed-effect analysis with multiple comparisons using two-way ANOVA, ** p <0.01, **** p <0.0001 **(B)**, and unpaired Welch's t-test, n.s. p > 0.05 **(C-D)**.

(FMO). Fas^{hi} GC B cell zone compartment showed consistent distribution of GCDZ and GCLZ B cells across both analysed time points, with approximately 70% of cells displaying $CXCR4^{+}$ and 30% exhibiting $CD86^{+}$ at both days, 10 and 14 post-immunisations (Figure 3.27B). Analysis of the mean frequency of NP-binding GC B cell

subsets showed that CXCR4^{+} GCDZ B cells increased from 5.9% at day 10 to 10.2% at day 14 (Figure 3.27C), indicating sustained proliferation and SHM during the later stage of the response. In contrast, NP-binding CD86^{+} GCLZ B cells increased from 10.2% at day 10 to 15% at day 14 (Figure 3.27D), consistent with ongoing antigen-dependent selection. These data demonstrate that the NP-induced GC remains highly active at day 14.

To further characterise cells that may represent early PC precursors, we next analysed the CD38^{hi} Fas$^{lo/-}$non-GC B cell compartment (Figure 3.28A). CD38^{hi} non-GC B cells were then gated into GC-derived *S1pr2*$^{tdT+}$ memory B cells (Figure 3.28B), GC-derived *S1pr2*$^{tdT+}$ NP^{+} memory B cells (Figure 3.28C), and GC-derived *S1pr2*$^{tdT+}$ Blimp-1^{GFP} PC precursors (Figure 3.28D). The mean frequency of GC-derived *S1pr2*$^{tdT+}$ memory B cells accounted for approximately 0.4% at day 10 and 0.2% at day 14 (Figure 3.28E), GC-derived *S1pr2*$^{tdT+}$ NP^{+} memory B cells 0.05% at day 10 and almost 0.04% at day 14 (Figure 3.28F), and GC-derived *S1pr2*$^{tdT+}$ Blimp-1^{GFP} PC precursors accounted for 0.075% at day 10 and below 0.05% at day 14 (Figure 3.28G). The overall composition of GC-derived cells is consistent with the GC peak to contraction phase [26, 175]. Because surface immunoglobulin (Ig) is progressively downregulated as B cells differentiate into PC, only transient surface Ig expression is expected during the early stages of PB-PC stages, whereas GC B cells retain robust surface BCR.

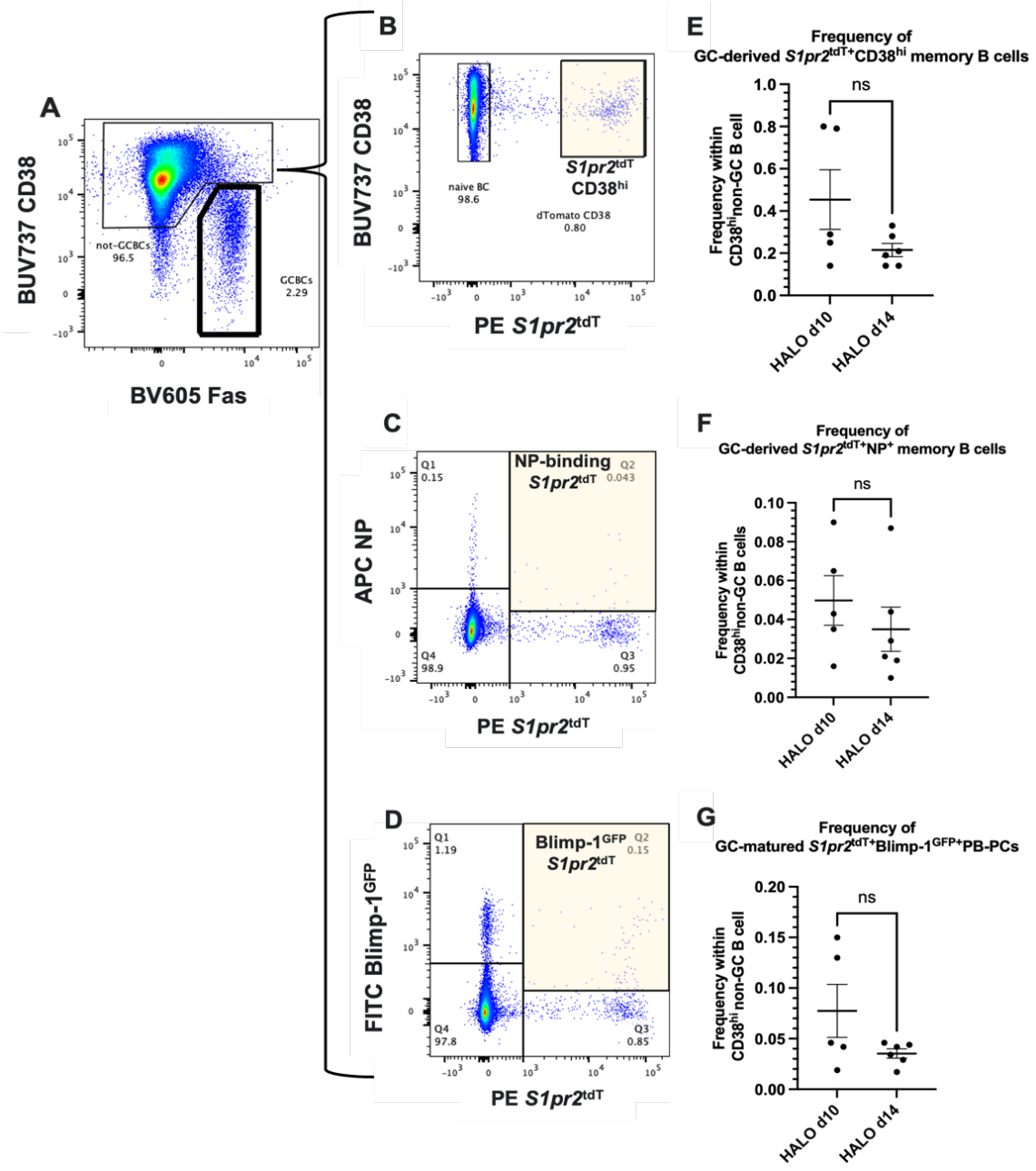


Figure 3.28. Analysis of CD38^{hi} non-GC B cells at days 10 and 14 post-NP$_{27}$-KLH immunisation.

The experimental protocol is illustrated in Figure 3.22. **(A)** CD38^{hi} non-GC B cells were gated into GC-derived *S1pr2*$^{tdT+}$ memory B cells **(B)** (pale yellow squares), GC-derived *S1pr2*$^{tdT+}$ NP^{+} memory B cells **(C)** and GC-derived *S1pr2*$^{tdT+}$ Blimp-1^{GFP+} PC precursor cells **(D)**. **(E-G)** Frequency of flow cytometry analysis of **(E)** *S1pr2*$^{tdT+}$ CD38^{hi} memory B cells, **(F)** GC-derived *S1pr2*$^{tdT+}$ NP^{+} memory B cells and **(G)** *S1pr2*$^{tdT+}$ Blimp-1^{GFP+} PC precursor cells (mean ± SEM). Each symbol represents one mouse. Representative of one experiment where n = 5 mice for the day 10 group and n = 6 for the day 14 group. Statistical tests were performed by an unpaired Welch's t-test, n.s. $p > 0.05$.

To assess membrane-bound IgM and IgG1 levels, we analysed the mean fluorescence intensity (MFI) within $CD138^{hi}$ PB-PC and Fas^{hi} GC B cells (Figure 3.29) at days 10 and 14 post-immunisation. The MFI of IgG1 expression within $CD138^{hi}$ PB-PC was significantly higher at day 10 compared to day 14 (Figure 3.29A), indicating that day 10 includes a higher portion of early PB and more mature PC by day 14. The MFI of IgM and IgG1 expression remained comparable between the two time points within Fas^{hi} GC B cells (Figure 3.29B).

Furthermore, NP_2-specific serum IgM and IgG1 in HALO mice were analysed (Figure 3.30). To establish the background optical density signal from naturally occurring antibodies, sera samples were obtained from the HALO mouse that was not treated (HALO NI NT; neither immunised nor received tamoxifen) and the HALO mouse that only received tamoxifen (HALO NI T). The titration curves in Figure 3.30 A-D demonstrate the decline in optical density values across increasing dilution. The relative titre of high-affinity NP_2-specific IgG1 significantly increased (* $p < 0.05$) at day 10 compared to day 14 (Figure 3.30E). In contrast, the relative titre of avidity NP_2-specific IgM was higher at day 14 (* $p < 0.05$) (Figure 3.30F). This data suggests a shift in the balance of circulating isotypes over this interval, likely reflecting continued production of IgM-secreting PB-PC alongside the contraction of IgG1-secreting PB-PC.

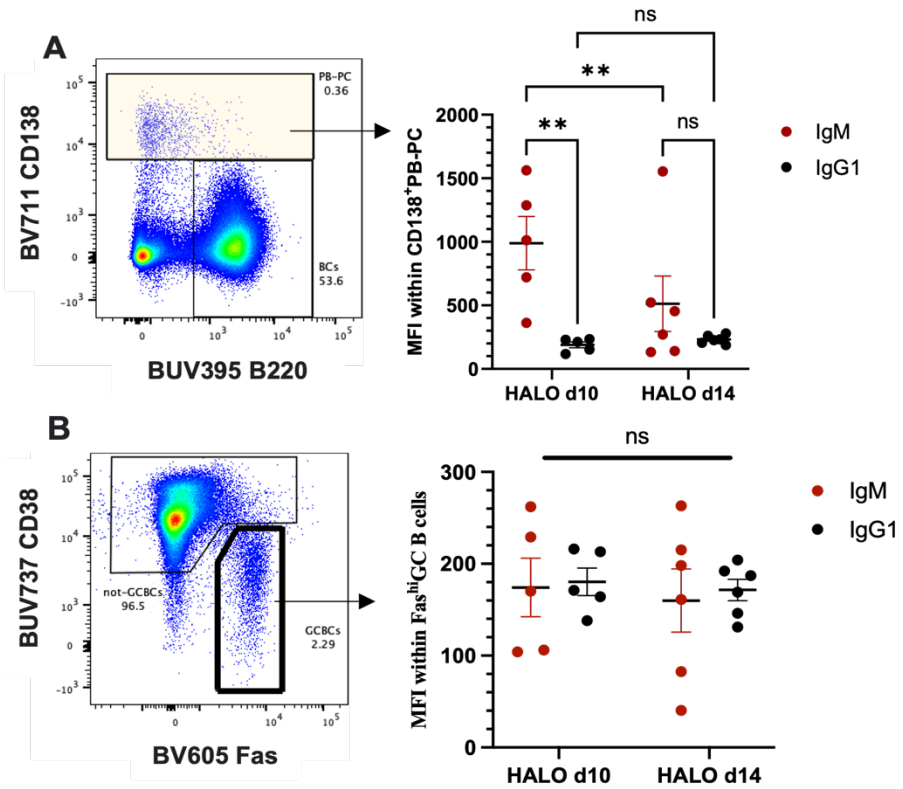


Figure 3.29. MFI of membrane-bound IgG1 and IgM antibodies in a later stage of the CD138^{hi} and Fas^{hi} GC B cells response.

The experimental protocol is illustrated in Figure 3.22. **(A)** MFI of membrane-bound IgM (red) and membrane-bound IgG1 (black) within CD138^{+} PB-PC at days 10 and 14 post-immunisation with NP_{27}-KLH. **(B)** MFI of membrane-bound IgM (red) and membrane-bound IgG1 (black) within Fas^{hi} GC B cells at days 10 and 14 post-immunisation with NP_{27}-KLH. The data on E and F are represented as mean ± SEM. Each symbol represents one mouse. Data was obtained from one experiment, n = 5 mice for the day 10 group and n = 6 for the day 14 group. Statistical tests were performed by an unpaired Welch's t-test, n.s. $p > 0.05$, ** $p < 0.01$.

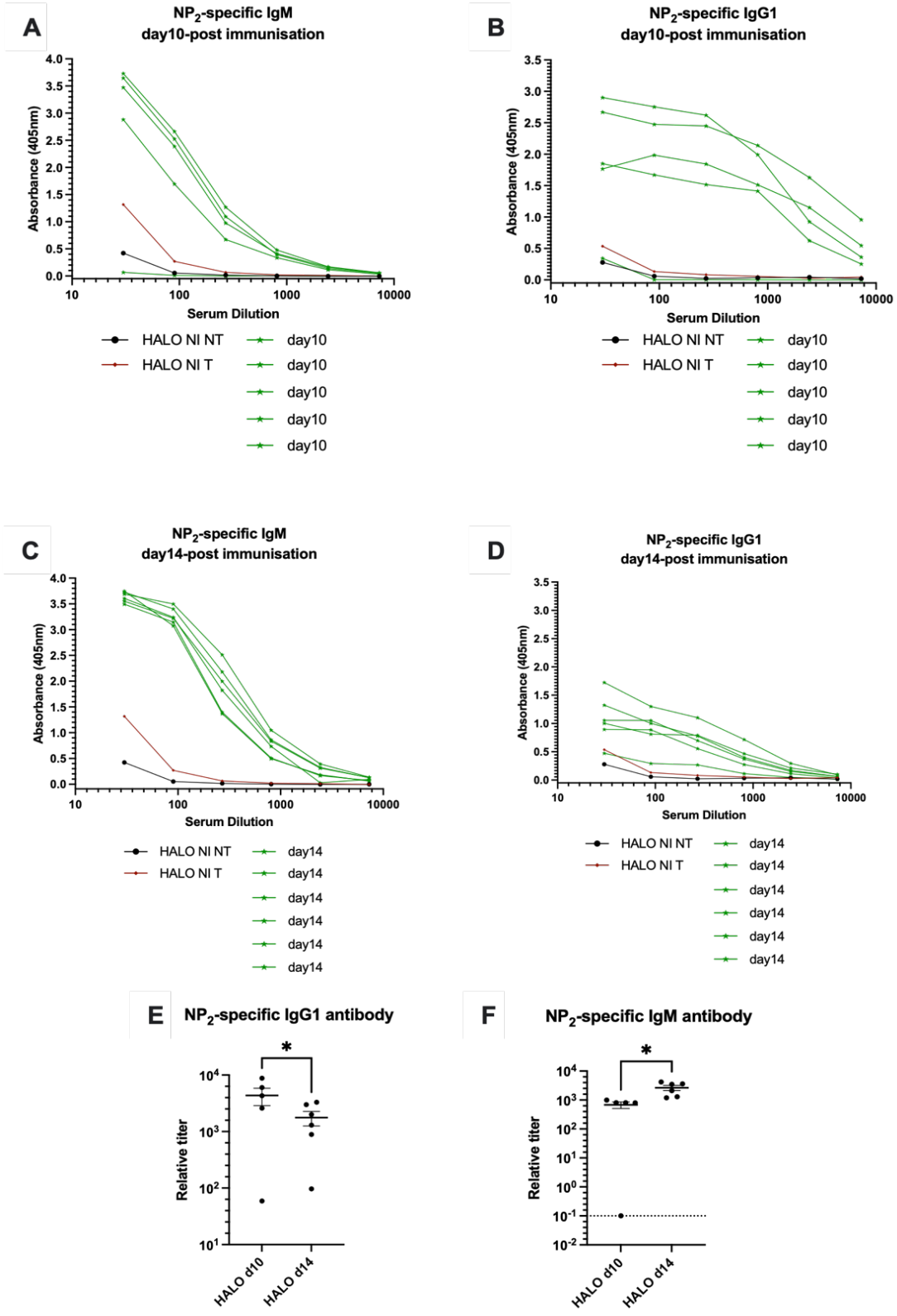


Figure 3.30. NP_2-specific antibody response in a later response to NP_{27}-KLH immunisation.

Mice were immunised as described in Figure 3.22. Sera samples were collected at day 10 and day 14 post-immunisation. NP_2-specific IgM and IgG1 titres were determined

by ELISA. **(A)** Dilution curve for NP_2-specific IgM at day 10 post-immunisation. **(B)** Dilution curve for NP_2-specific IgG1 at day 10 post-immunisation. **(C)** Dilution curve for NP_2-specific IgM at day 14 post-immunisation. **(D)** Dilution curve for NP_2-specific IgG1 at day 14 post-immunisation. **(E)** NP_2-specific IgG1 levels at days 10 and 14 post-immunisation with NP_{27}-KLH. **(F)** NP_2-specific IgM levels at days 10 and 14 post-immunisation with NP_{27}-KLH. The data on E and F are represented as mean ± SEM. Each symbol represents one mouse. Data was obtained from one experiment, n = 5 mice for the day 10 group and n = 6 for the day 14 group. Statistical tests were performed by a paired parametric t-test, * $p < 0.05$.

Together, primary immunisation of HALO mice with NP_{27}-KLH showed that GC-matured CD138$^+$ *S1pr2*$^{tdT+}$ Blimp-1^{GFP+} PB-PCs, GC-derived *S1pr2*$^{tdT+}$ memory B cells, GC-derived *S1pr2*$^{tdT+}$ NP$^+$ memory B cells, GC-derived *S1pr2*$^{tdT+}$ Blimp-1^{GFP} PC precursors, and serum IgG1 levels were predominant at day 10. However, these differences did not reach statistical significance, and a larger cohort of mice may be required to determine whether these trends reflect meaningful biological changes over time.

3.2.3. Characterisation of GC-matured *S1pr2*$^{tdT+}$ Blimp-1^{GFP+} PB-PC in HALO mice following secondary NP_{27}-KLH challenge.

3.2.3.1. GC-derived CD38$^+$ PC precursors peaked at day 5, with a high proportion of GC-matured CD138$^+$ PB-PC at day 8 following secondary challenge.

The primary response depends on the nature of the antigen and the route of entry. The response following primary immunisation with the T-dependent antigen NP-KLH can

be well developed for 12-14 days and generate antigen-specific memory B cells [175, 178]. The affinity maturation of these antigen-specific memory B cells can be enhanced by further exposure to the initial antigen. The secreting-antibody levels in the circulation start declining around 4 weeks [178]. In this study, precipitated NP-KLH and adjuvant were administered via the i.p. route, a standard method in murine immunology for achieving systemic distribution and accumulation within the spleen. A secondary i.v. challenge directly targets the spleen, triggering a rapid expansion of the pre-existing immune response.

GC-matured CD138^{+} *S1pr2*$^{tdT+}$ Blimp-1^{GFP+} PB-PCs were tested using a carrier-priming followed by a boost strategy (see the experimental protocol in Figure 3.31). Mice were initially primed i.p. with alum-precipitated NP_{27}-KLH along with *B. pertussis*. On days 28 and 29, mice were boosted i.v. with soluble NP_{27}-KLH. This immunisation route follows the same procedure described by the Toellner et al. study [26]. To induce tdT expression for tracking GC-derived B cells, mice were assigned to two tamoxifen-treatment groups:

1) a single-dose group, receiving tamoxifen on day 32 and harvested 48 hours later on day 34; this group corresponded to the day 5 post-boosting time point.
2) a double-dose group, receiving tamoxifen on days 32 and 34 and harvested 96 hours later on day 36; this group corresponded to the day 8 post-boosting time point.
3) The third group of HALO mice was assigned to the non-boosted group.

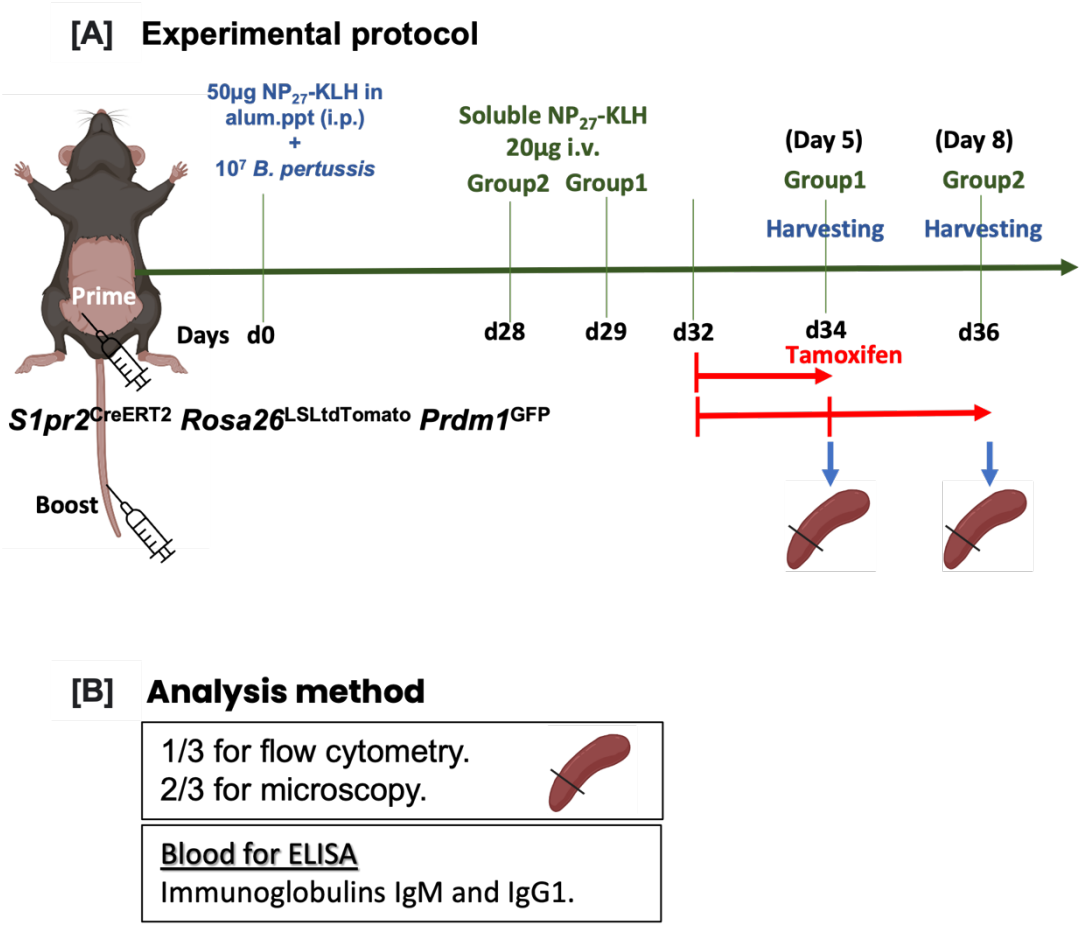


Figure 3.31. Schematic of the experimental procedure for secondary immunisation in HALO mice.

(A) Schematic of the immunisation and treatment protocol. HALO mice were primed i.p. with NP_{27}-KLH in alum on day 0. On days 28 and 29, one cohort of HALO mice received an i.v. boost with soluble NP_{27}-KLH, while a second cohort remained unboosted. For analysis at day 5 post-boost (Group 1, G1; n = 8), mice received a single dose of tamoxifen (200 µL of 20 mg/mL in corn oil) 48 hours prior to the harvest time point. For analysis at day 8 post-boost (Group 2, G2; n =7), mice received a pulse dose of tamoxifen (200 µL of 20 mg/mL in corn oil) 96 hours prior to the harvest time point. **(B)** The chart of the analysis method and the tissues used.

The selection of day 5 and day 8 post-boosting corresponds to the lag phase, which typically lasts 2-5 days before antibody titres begin to rise, and captures the secondary response, with active GC and PB-C output at day 8 [178]. We first characterised three compartments of splenic B cells by gating on CD138 and B220, followed by subdividing $B220^{hi}$ B cells into $CD38^{+}$ non-GC B cells and Fas^{hi} GC B cells (Figure 3.32A and B). Boosting was associated with a significant increase in the number of these three compartments at day 5 compared to day 8 (Figure 3.32C-E). In the absence of boosting, day 8 exhibited a rise in these compartments' response, although it was not statistically different. These three compartments—$CD138^{+}$ PB-PC, $CD38^{+}$ non-GC B cells, and Fas^{hi} GC B cells—were further subdivided based on the expression of *S1pr2*^{tdT} and Blimp-1^{GFP} to characterise the phenotypic diversity of antibody-secreting cells generated following boosting, as examined in subsequent analyses.

Figure 3.33A investigates three fractions within the $CD138^{+}$ PB-PC compartment: EF-derived $CD138^{+}$ Blimp-1^{GFP+} PB-PC (Figure 3.33B), GC-matured *S1pr2*$^{tdT+}$ Blimp-1^{GFP+} PB-PC (Figure 3.33C), and GC-matured *S1pr2*$^{tdT+}$ PB-PC (Figure 3.33D). The number of EF-derived $CD138^{+}$ Blimp-1^{GFP+} PB-PC was the predominant subset at both time points and showed a significant decrease from day 5 to day 8 post-boosting (* $p < 0.05$). On day 5, boosting is associated with a higher proportion of EF-derived $CD138^{+}$ Blimp-1^{GFP+} PB-PC compared to non-boosting controls (~92.9% vs ~76.9%) (Figure 3.33B). On day 8, the boosted group shows a lower proportion than the non-boosted group (~70.8% vs ~82.2%) (Figure 3.33B). These data indicate that EF-derived $CD138^{+}$ Blimp-1^{GFP+} PB-PC dominate the $CD138^{+}$ compartment early after boosting, particularly at day 5.

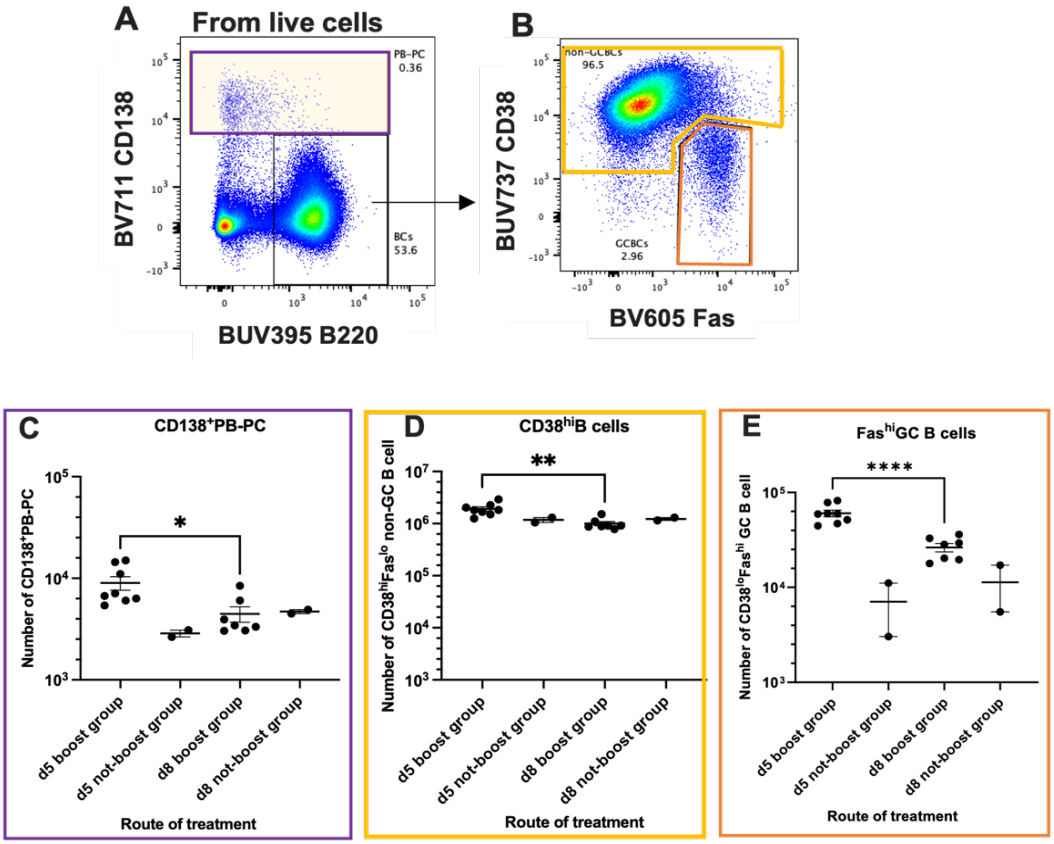


Figure 3.32. Analysis of splenic B cell populations in HALO mice.

The experimental protocol is illustrated in Figure 3.31. **(A)** A flow cytometry analysis of CD138^{+} PB-PC gated from live cells. **(B)** A flow cytometry analysis of B220+ B cells was gated on Fas^{hi} GC B cells and CD38^{hi} non-GC B cells. **(C)** Number of CD138^{+}PB-PC. **(D)** Number of CD38^{hi} non-GC B cells. **(E)** Number of Fas^{hi} GC B cells. Data are represented as mean ± SEM. Each symbol represents one mouse. Data are representative of two independent experiments, with n = 8 mice for the day 5 post-boosting group, n = 7 for the day 8 post-boosting group, and n = 2 for the non-boosted group at each time point. Statistical tests were performed using ordinary one-way ANOVA. * p <0.05, ** p <0.01, **** p <0.0001.

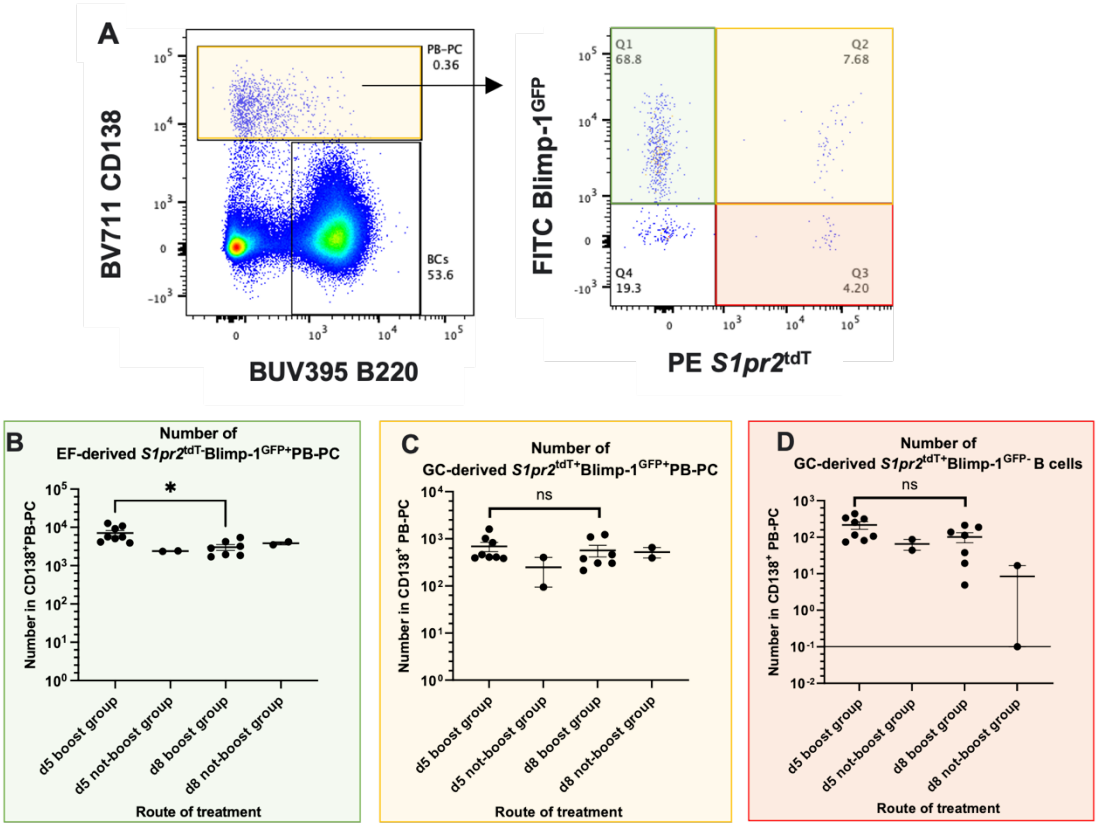


Figure 3.33. Analysis of the maturation of CD138⁺ PB-PC.

The experimental protocol is illustrated in Figure 3.31. **(A)** A flow cytometry analysis of CD138⁺ PB-PCs was gated and further analysed based on the expression of *S1pr2*^{tdT} and Blimp-1^{GFP}. **(B)** Number of EF-derived CD138⁺*S1pr2*$^{tdT-}$ Blimp-1^{GFP+} PB-PC. **(C)** Number of GC-derived CD138⁺*S1pr2*$^{tdT+}$ Blimp-1^{GFP+} PB-PC**. (D)** Number of GC-derived CD138⁺*S1pr2*$^{tdT+}$ Blimp-1^{GFP-} PB-PC. Values below the detection limit are out of the scale, indicating a value of zero. Data are represented as mean ± SEM. Each symbol represents one mouse. Data are representative of two independent experiments, with n = 8 mice for the day 5 post-boosting group, n = 7 for the day 8 post-boosting group, and n = 2 for the non-boosted group at each time point. Statistical tests were performed using ordinary one-way ANOVA (B-D) and two-way ANOVA (E-G). n.s. $p > 0.05$, * $p < 0.05$, ** $p < 0.01$, *** $p < 0.001$, **** $p < 0.0001$.

Moreover, the proportion of GC-matured *S1pr2*$^{tdT+}$ Blimp-1^{GFP+} PB-PC accounted for 9.3% in the boosted compared to 9.4% in the non-boosted group at day 5 (Figure 3.33C), which is nearly identical. By day 8, this proportion increased to 11% in the boosted group and was comparable to that observed in the non-boosted group (10.7%). These data indicate that GC-matured *S1pr2*$^{tdT+}$ Blimp-1^{GFP+} PB-PC constitute a minor fraction of the CD138^{+} compartment at both time points, with only a slight proportion increased at day 8 compared to day 5. Figure 3.33D shows the number of GC-derived *S1pr2*$^{tdT+}$ PB-PC within the CD138^{+} compartment. Boosting is associated with a higher proportion of GC-derived *S1pr2*$^{tdT+}$ CD138^{+} PB-PC compared to non-boosted controls—3.8% vs 1.7% at day 5 and 2.8% vs 1.8% at day 8. Therefore, GC-derived *S1pr2*$^{tdT+}$ CD138^{+} PB-PC represent a minor subset. Boosting consistently increases their relative contribution compared to non-boosted controls at both time points. However, the magnitude of the fraction decreased from day 5 to day 8 in boosted mice.

Overall, the three CD138^{+} PB-PC fractions showed the same hierarchical output pattern observed in the primary response to SRBC, with EF-derived PB-PC being the most abundant population, followed by GC-matured PB-PC, and finally GC-derived PB-PC as the least abundant. However, the primary immunisation with SRBC is associated with a higher number of EF-derived CD138^{+} Blimp-1^{GFP+} PB-PC at both time points and a higher number of GC-derived CD138^{+} *S1pr2*$^{tdT+}$ Blimp-1^{GFP+} PB-PC at day 5 (Figure 3.6D and E). In contrast, the secondary immunisation with NP_{27}-KLH is associated with a higher number of GC-derived CD138^{+} *S1pr2*$^{tdT+}$ Blimp-1^{GFP+} PB-PC at day 8 and GC-derived CD138^{+} *S1pr2*$^{tdT+}$ PB-PC at both time points (Figure 3.33C and D). Taken together, the EF response contributes strongly early after primary SRBC

immunisation, with GC-matured PB-PC constituting the predominant population at day 5. In contrast, following secondary immunisation with NP_{27}-KLH, GC-matured PB-PC become predominant at day 8. Moreover, the contribution of GC-derived $CD138^+$ *S1pr2*$^{tdT+}$ PB-PC is associated primarily with secondary immunisation with NP_{27}-KLH. (Figure 3.33D) compared to primary immunisation (Figure 3.6F).

The number of NP-specific GC-derived $CD138^+$ PB-PC provides an additional readout of GC-derived P1 and P2 PB-PC following boosting. Accordingly, $CD138^+$ PB-PC were gated based on NP binding and *S1pr2*^{tdT} expression (Figure 3.34A). The mean number of NP-specific GC-derived *S1pr2*^{tdT} $CD138^+$ PB-PC did not differ significantly between the boosted groups at the two time points (Figure 3.34B).

Moreover, the relative contributions of the three fractions–EF PB-PCs, GC-matured PB-PCs, and GC-derived memory B cells within the Fas^{hi} GC B cell compartment–were investigated at days 5 and 8, before and after boosting (Figure 3.35A-D). On day 5 before boosting, these fractions accounted for 10.8%, 9.8%, and 76.1% of the Fas^{hi} GC B cell compartment, respectively. After boosting, the EF-derived and GC-matured PB-PCs fractions decreased to 4.7% and 7.8%, respectively, whereas GC-derived memory B cells increased to 99.2%. This suggests that boosting reduces the proportional contribution of EF-derived and GC-matured PB-PC while increasing the fraction of memory B cells. By day 8 before boosting, EF PB-PCs, GC-matured PB-PCs, and GC-derived memory B cells represented 9.7%, 9.6%, and 95.2% of the Fas^{hi} GC B cell compartment, respectively. Following the boost, the contribution of EF-derived and GC-matured PB-PCs further decreased to 1.4% and 2.2%, respectively, while GC-derived memory B cells accounted for 79.8% of the compartment.

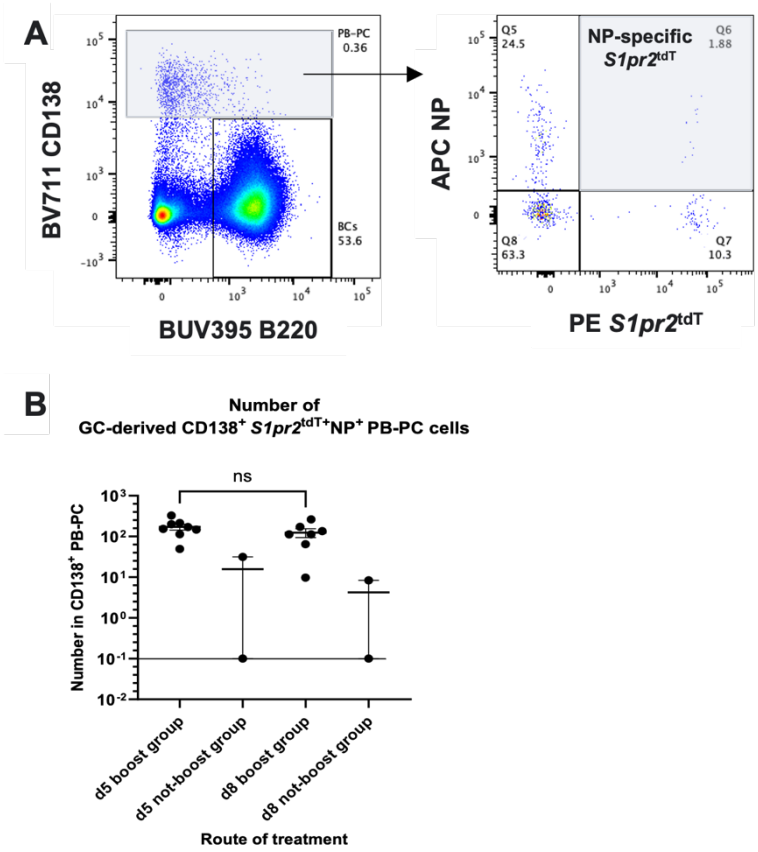


Figure 3.34. GC-derived CD138^{+} *S1pr2*$^{tdT+}$ NP^{+} PB-PC.

The experimental protocol is illustrated in Figure 3.31. **(A)** A flow cytometry analysis of CD138^{+} PB-PC gated and further analysed based on the expression of NP^{+} *S1pr2*$^{tdT+}$. **(B)** The number of NP^{+}-binding GC-derived CD138^{+} *S1pr2*$^{tdT+}$ PB-PC. Values below the detection limit are out of the scale, indicating a value of zero. Data are represented as mean ± SEM. Each symbol represents one mouse. Data are representative of two independent experiments, with n = 8 mice for the day 5 post-boosting group, n = 7 for the day 8 post-boosting group, and n = 2 for the non-boosted group at each time point. Statistical tests were performed using One-way ANOVA, a nonparametric test, and analysis with the Kruskal-Wallis test. n.s. $p > 0.05$.

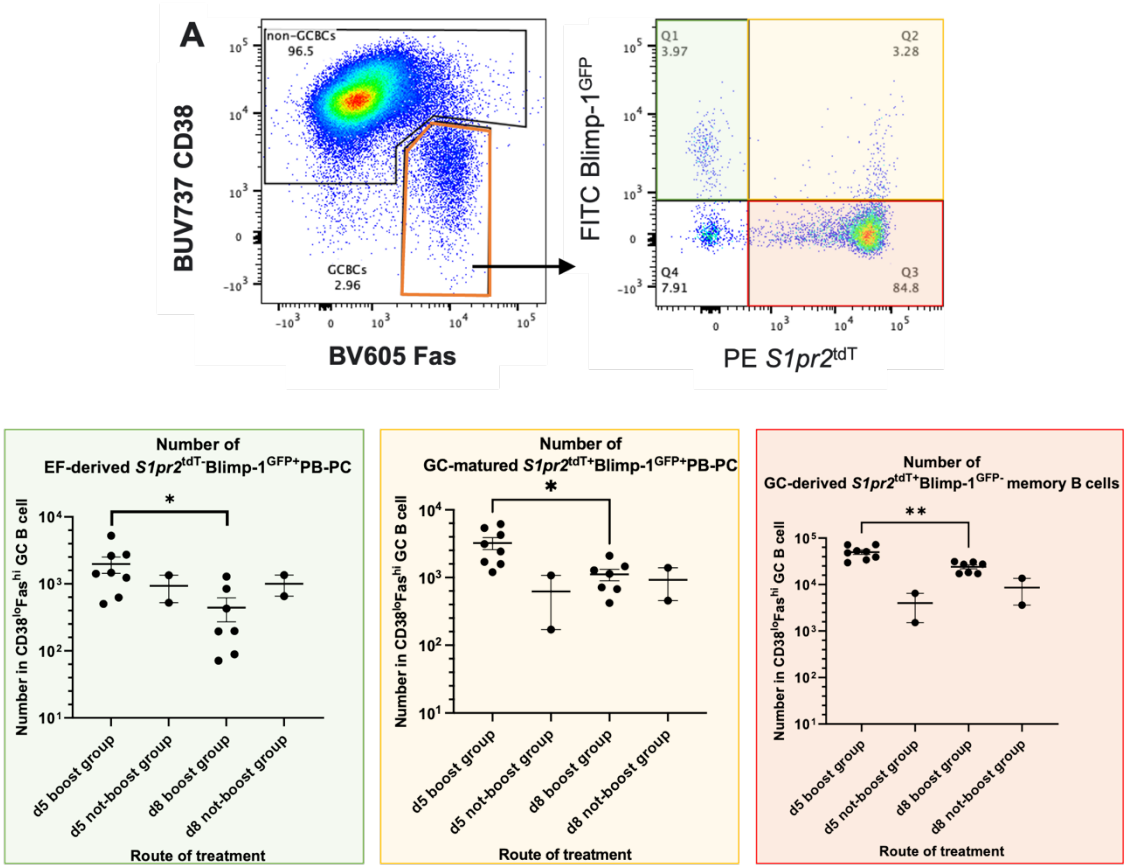


Figure 3.35. Analysis of GC B cell reaction during recall responses to NP_{27}-KLH immunisation.

The experimental protocol is illustrated in Figure 3.31. **(A)** A flow cytometry analysis of Fas^{hi} GC B cells was gated and further analysed based on the expression of *S1pr2*^{tdT} and Blimp-1^{GFP}. **(B)** Number of EF-derived *S1pr2*$^{tdT-}$ Blimp-1^{GFP+} PB-PC. **(C)** Number of GC-derived *S1pr2*$^{tdT+}$ Blimp-1^{GFP+} PB-PC. **(D)** Number of GC-derived *S1pr2*$^{tdT+}$ Blimp-1^{GFP-} PB-PC. Data are represented as mean ± SEM. Each symbol represents one mouse. Data are representative of two independent experiments, with n = 8 mice for the day 5 post-boosting group, n = 7 for the day 8 post-boosting group, and n = 2 for the non-boosted group at each time point. Statistical tests were performed using ordinary one-way ANOVA. * p <0.05, ** p <0.01.

This indicates a similar reduction in the contribution of EF-derived and GC-matured PB-PC after boosting as observed at day 5; however, the fraction of memory B cells displayed a different pattern, being lower following boosting. Overall, boosting was associated with a reduced proportional contribution of EF-derived and GC-matured PB-PCs within the Fas^{hi} GC B cell compartment, but it was associated with an increase in GC-derived memory B cells at day 5 that was not maintained at day 8.

For NP-specific GC B cells (Figure 3.36), day 5 showed a significantly higher number of NP-specific *S1pr2*$^{tdT+}$ GC B cells and NP-specific $B220^{+}$ B cells (Figure 3.36C and E) compared to day 8. In contrast, NP-specific *S1pr2*$^{tdT+}$ GC B cells were not detected in the non-boosted group on day 8 (Figure 3.36C). Despite these differences in cell numbers, the relative contribution of NP-specific *S1pr2*$^{tdT+}$ GC B cells within the Fas^{hi} GC B cell compartment did not differ significantly between the boosted groups at the two time points.

Figure 3.37 shows GC-matured $CD38^{+}$ *S1pr2*$^{tdT+}$ Blimp-1^{GFP+} PC precursors and NP-specific GC-derived $CD38^{+}$ *S1pr2*$^{tdT+}$ memory B cells. Following boosting, the number of GC-derived precursors was approximately 750 cells at day 5, decreasing to 390 cells at day 8, representing a ~52% reduction (Figure 3.37C). In contrast, before boosting, the number of these precursors increased from ~150 at day 5 to 380 at day 8. Notably, the mean number of GC-derived PC precursors did not differ between non-boosted and boosted groups at day 8. This indicates that GC-derived PC precursors increased in the absence of boosting at day 8, while boosting was associated with a higher number of these precursors early at day 5 after boosting.

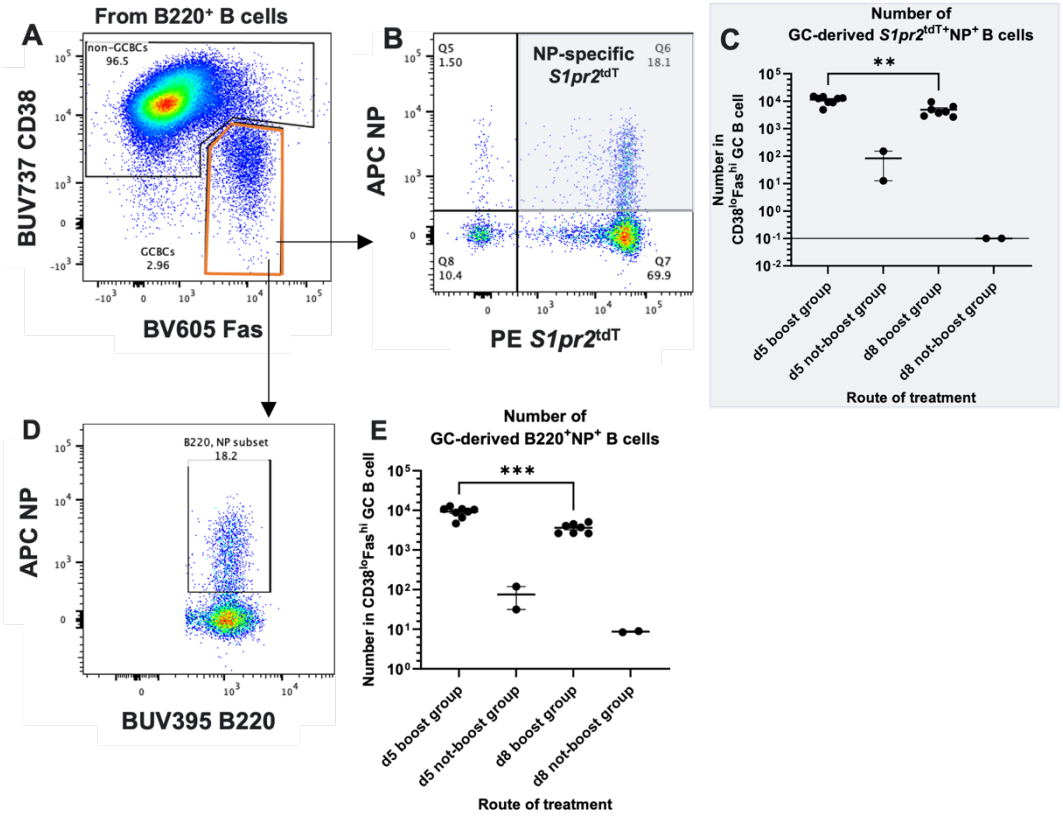


Figure 3.36. Analysis of NP-specific GC-derived B cells during recall responses to NP_{27}-KLH immunisation.

The experimental protocol is illustrated in Figure 3.31. **(A)** A flow cytometry analysis of Fas^{hi} GC B cells was gated from $B220^{hi}$ B cells. **(B)** A flow cytometry analysis of GC-derived NP^+ *S1pr2*^{tdT} B cells. **(C)** Number of GC-derived NP^+ *S1pr2*$^{tdT+}$ B cells within Fas^{hi} GC B cells. Values below the detection limit are out of the scale, indicating a value of zero. **(D)** A flow cytometry analysis of GC-derived NP^+ $B220^+$ B cells. **(E)** Number of GC-derived NP^+ $B220^+$ B cells within Fas^{hi} GC B cells. Data are represented as mean ± SEM. Each symbol represents one mouse. Data are representative of two independent experiments, with n = 8 mice for the day 5 post-boosting group, n = 7 for the day 8 post-boosting group, and n = 2 for the non-boosted group at each time point. Statistical tests were performed using ordinary one-way ANOVA. ** p <0.01, *** p <0.001.

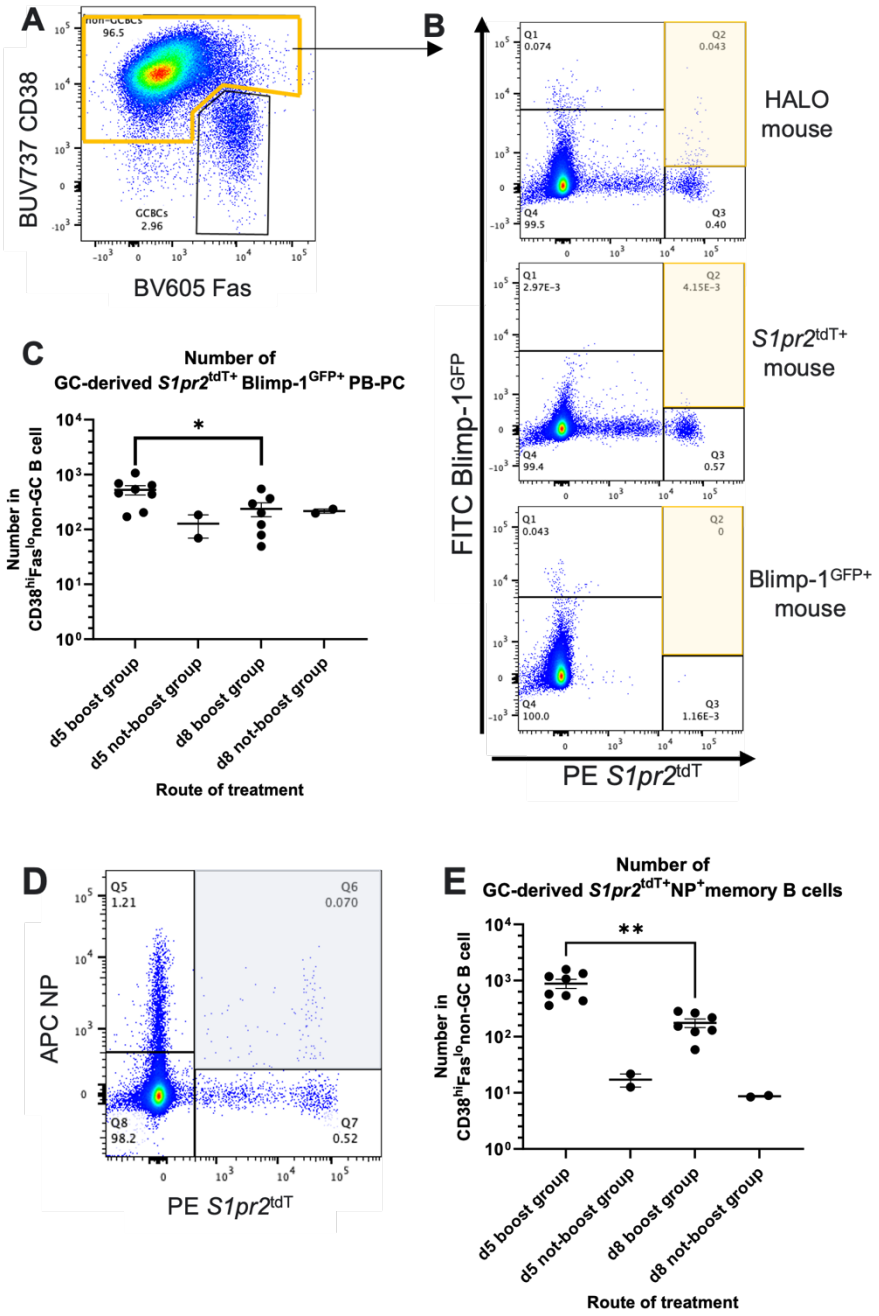


Figure 3.37. Analysis of non-GC B cell reaction during recall responses to NP_{27}-KLH immunisation.

The experimental protocol is illustrated in Figure 3.31.
(A) A flow cytometry analysis of CD38^{+} non-GC B cells was gated from B220^{+} B cells. **(B)** Flow cytometric analysis of GC-matured *S1pr2*$^{tdT+}$ Blimp-1^{GFP+} PB-PC gated from the CD38^{+} non-GC B cell compartment. Thresholds for reporter positivity were defined using single-reporter control mice. Plots shown are representative of boosted samples. **(C)** Number of GC-matured *S1pr2*$^{tdT+}$ Blimp-1^{GFP+} PB-PC within CD38^{hi} non-GC B cells. **(D)** A flow cytometry analysis of GC-derived NP^{+} *S1pr2*$^{tdT+}$ memory B cells gated from CD38^{+} non-GC B cells. **(E)** Number of GC-derived NP^{+} *S1pr2*$^{tdT+}$ memory B cells

within CD38^{hi} non-GC B cells. The data are represented as mean ± SEM. Each symbol represents one mouse. Data were obtained from two independent experiments. n = 8 mice for the day 5 post-boosting group, n = 7 for the day 8 post-boosting group, and n = 2 for the non-boosted group at each time point. Statistical tests were performed using ordinary one-way ANOVA. * p <0.05, ** p <0.01.

The number of GC-derived *S1pr2*$^{tdT+}$ NP^{+} memory B cells decreased significantly from ~980 cells at day 5 to ~310 cells at day 8 (p = 0.011), representing a 31.6% reduction (Figure 3.37E). Before boosting, a reduction was observed, representing approximately a 3.2-fold decrease from day 5 to day 8 (Figure 3.37E). Overall, NP-binding was more abundant at day 5 than at day 8, with a comparable reduction observed both before and after boosting, indicating that this decline is not specifically driven by boosting.

3.2.3.2. GC-matured CD19^{lo} B220^{lo} CD138^{+} TACI^{+} *S1pr2*$^{tdT+}$ Blimp-1^{GFP+} PB-PC occurs on day 8 post-boosting immunisation to NP$_{27}$-KLH.

We investigated the discrimination between PB-PC subsets after primary immunisation with SRBCs at three time points (see the experimental protocol, Figure 3.2). In the recall response experiment, we had the opportunity to repeat the analysis of PB-PC maturation stages using six mice — three at each time point — following the same protocol described in Figure 3.31. Correspondingly, splenic B cells were gated on CD138 and TACI (Figure 3.38A), showing CD138^{+} TACI^{+} PB-PC accounted for 10^4 at day 5, which decreased to 5,000 at day 8 (Figure 3.38B). CD138^{+} TACI^{+} PB-PC was further analysed for GC-matured *S1pr2*$^{tdT+}$ Blimp-1^{GFP+} PB-PC (Figure 3.38C).

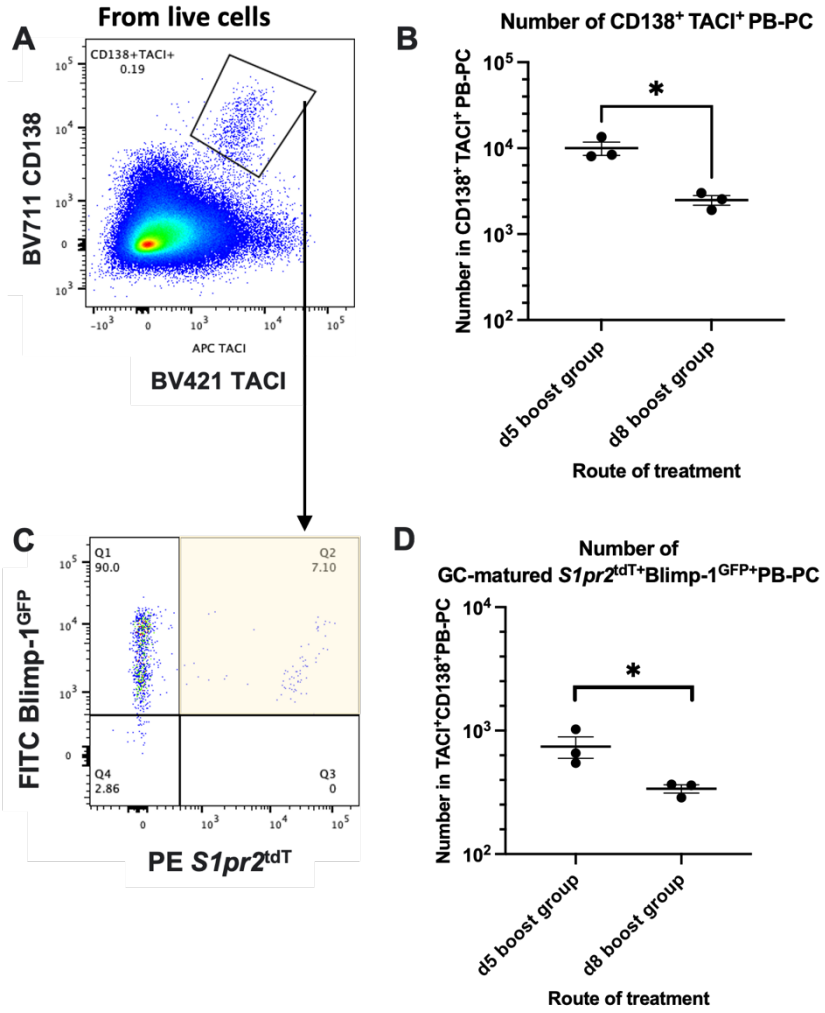


Figure 3.38. Analysis of GC-matured CD138^{hi} TACI^{hi} *S1pr2*$^{tdT+}$ Blimp-1^{GFP+} PB-PC during recall responses to NP$_{27}$-KLH immunisation.

The experimental protocol is illustrated in Figure 3.31. **(A)** A flow cytometry analysis of CD138^{hi} TACI^{hi} PB-PC was gated from live cells. **(B)** Number of CD138^{hi} TACI^{hi} PB-PC. **(C)** A flow cytometry analysis of GC-matured *S1pr2*$^{tdT+}$ Blimp-1^{GFP+} PB-PC gated from CD138^{hi} TACI^{hi} PB-PC. **(D)** Number of GC-matured *S1pr2*$^{tdT+}$ Blimp-1^{GFP+} PB-PC within CD138^{hi} TACI^{hi} PB-PC. The data are represented as mean ± SEM. Each symbol represents one mouse. Data were derived from a single experiment, with n = 3 mice for the day 5 post-boosting group, n = 3 for the day 8 post-boosting group. Statistical tests were performed by an unpaired Welch's t-test, * p <0.05.

As expected from the early rapid recall response, day 5 post-boosting showed a significant increase in GC-matured CD138^{+} TACI^{+} *S1pr2*$^{tdT+}$ Blimp-1^{GFP+} PB-PC. The proportion of GC-matured PB-PC accounted for approximately 8% of CD138^{+} TACI^{+} PB-PC at day 5, but this proportion increased to ~11% of CD138^{+} TACI^{+} PB-PC by day 8 (Figure 3.38D). Then, CD138^{+} TACI^{+} PB-PC was fractioned into B220^{hi} CD19^{hi} B cells, B220^{int} CD19^{int} proliferating PB (P1), B220^{lo} CD19^{int} early non-proliferating PC (P2), and B220^{lo} CD19^{lo} late non-proliferating PC (P3) (Figure 3.39A-B) [148]. CD138^{+} TACI^{+} PB-PC fractions were identified by Blimp-1^{GFP} fluorescence intensity, with Blimp-1^{GFP} additionally applied as a third parameter within the CD19/B220 gate (Figure 3.39C).

The number of the minor fraction of B220^{hi} CD19^{hi} B cells remained steady during all tamoxifen labelling (Figure 3.40C). The P1 fraction displayed an increasing output at day 5 and decreased 72 hours later; however, it was not statistically significant (Figure 3.40D). The early and late nonproliferating PC (P2 and P3 fractions) displayed statistically significant responses on day 5. Overall, boosting was associated with the dominance of the P1 fraction at both time points. Together, primary SRBC immunisation was associated with the dominance of the P2 fraction (Figure 3.11D and H), whereas P1 was associated with secondary challenge with NP_{27}-KLH. Furthermore, the CD138^{+} TACI^{+} PB-PC fractions were investigated for their maturity into *S1pr2*^{tdT} and Blimp-1^{GFP} expression (Figure 3.41A). Generally, among all maturity fractions, the P2 fraction showed a significant difference in the number of GC-matured PB-PC at day 5 compared to day 8 (Figure 3.41B-E). However, the proportion of GC-matured PB-PC was ~18% at day 5 vs ~35.5% at day 8 of the B220^{hi} CD19^{hi} fraction (Figure 3.40C and Figure 3.41B).

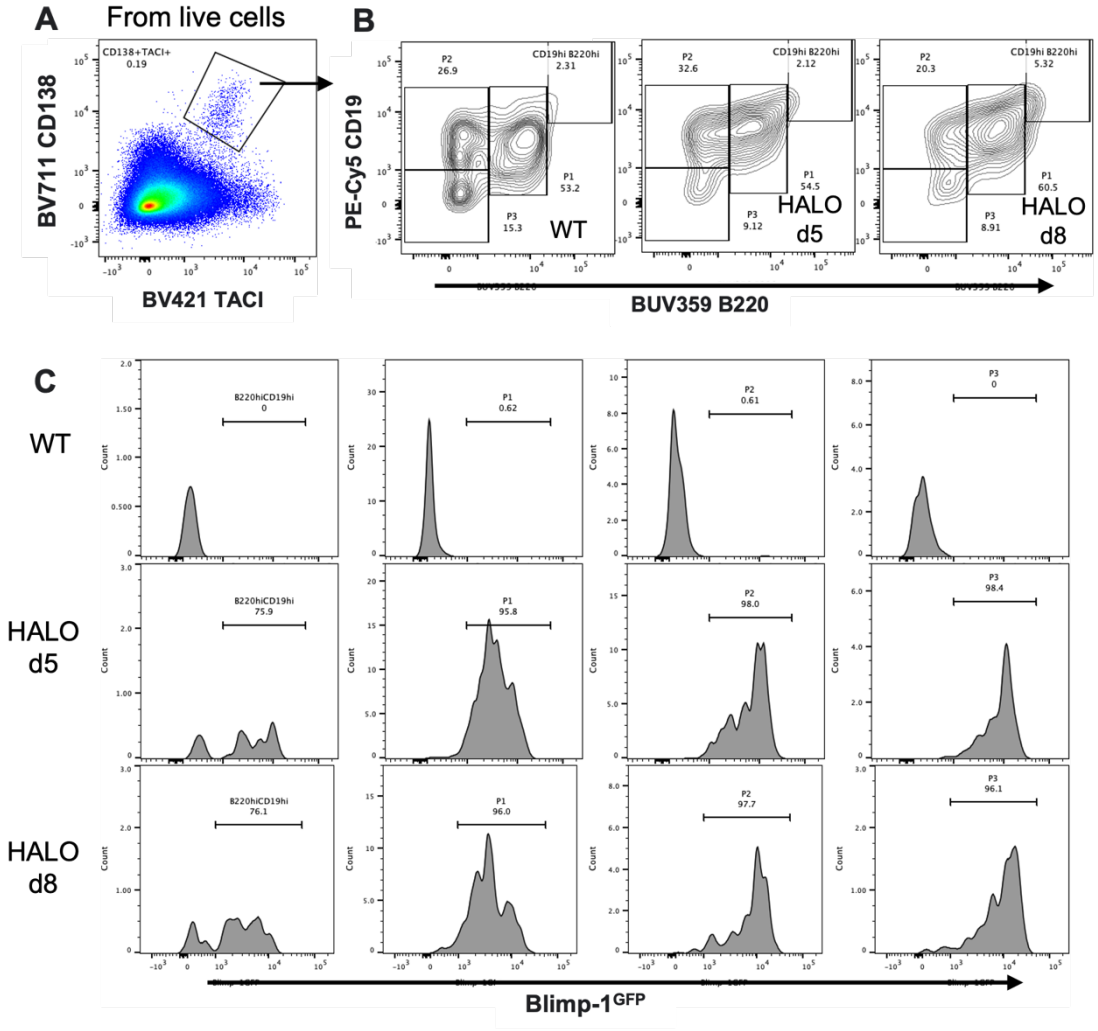


Figure 3.39. Analysis of CD138^{hi} TACI^{hi} PB-PC fractions during recall responses to NP$_{27}$-KLH immunisation.

The experimental protocol is illustrated in Figure 3.31. **(A)** A flow cytometry analysis of CD138^{hi} TACI^{hi} PB-PC was gated from live cells. **(B)** A flow cytometry analysis of PB-PC fractions, based on the expression level of B220 and CD19, in wild-type (WT), HALO mice on day 5 and day 8 post-boosting. **(C)** A histogram analysis of Blimp-1^{GFP+} expression level on each fraction of CD138^{hi} TACI^{hi} PB-PC. WT was used as a negative control of Blimp-1^{GFP+} expression. Data were derived from one experiment, with n = 3 mice for the day 5 post-boosting group and n = 3 for the day 8 post-boosting group.

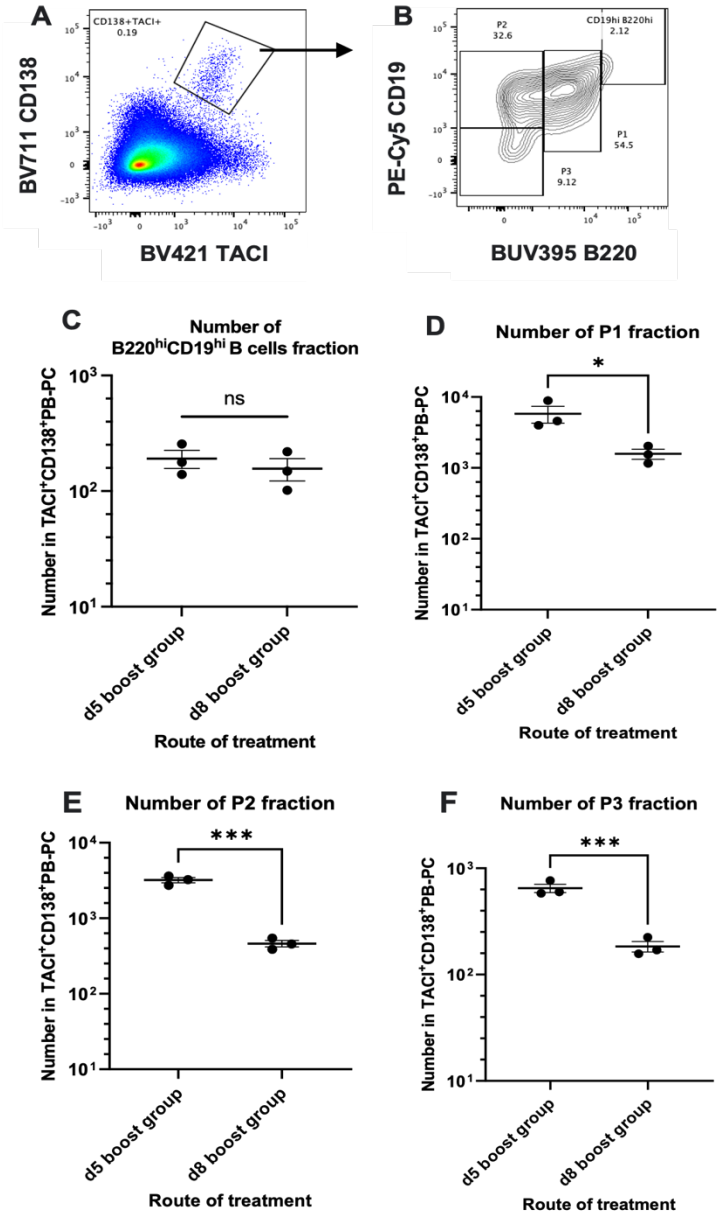


Figure 3.40. Number of CD138^{hi} TACI^{hi} PB-PC fractions during recall responses to NP$_{27}$-KLH immunisation.

The experimental protocol is illustrated in Figure 3.31. **(A)** A flow cytometry analysis of CD138^{hi} TACI^{hi} PB-PC was gated from live cells. **(B)** A flow cytometry analysis of PB-PC fractions, based on the expression level of B220 and CD19. **(C)** Number of B220^{hi} CD19^{hi} B cell fractions within CD138^{hi} TACI^{hi} PB-PC. **(D)** Number of PB-PC (P1) fractions within CD138^{hi} TACI^{hi} PB-PC. **(E)** Number of early PC (P2) fractions within CD138^{hi} TACI^{hi} PB-PC. **(F)** Number of late PC (P3) fraction within CD138^{hi} TACI^{hi} PB-PC. The data is represented as mean ± SEM. Each symbol represents one mouse. Data was obtained from one experiment, with n = 3 mice for the day 5 post-boosting group, n = 3 for the day 8 post-boosting group. Statistical tests were performed using an unpaired t-test. n.s. p >0.05, *p <0.05, ***p <0.001.

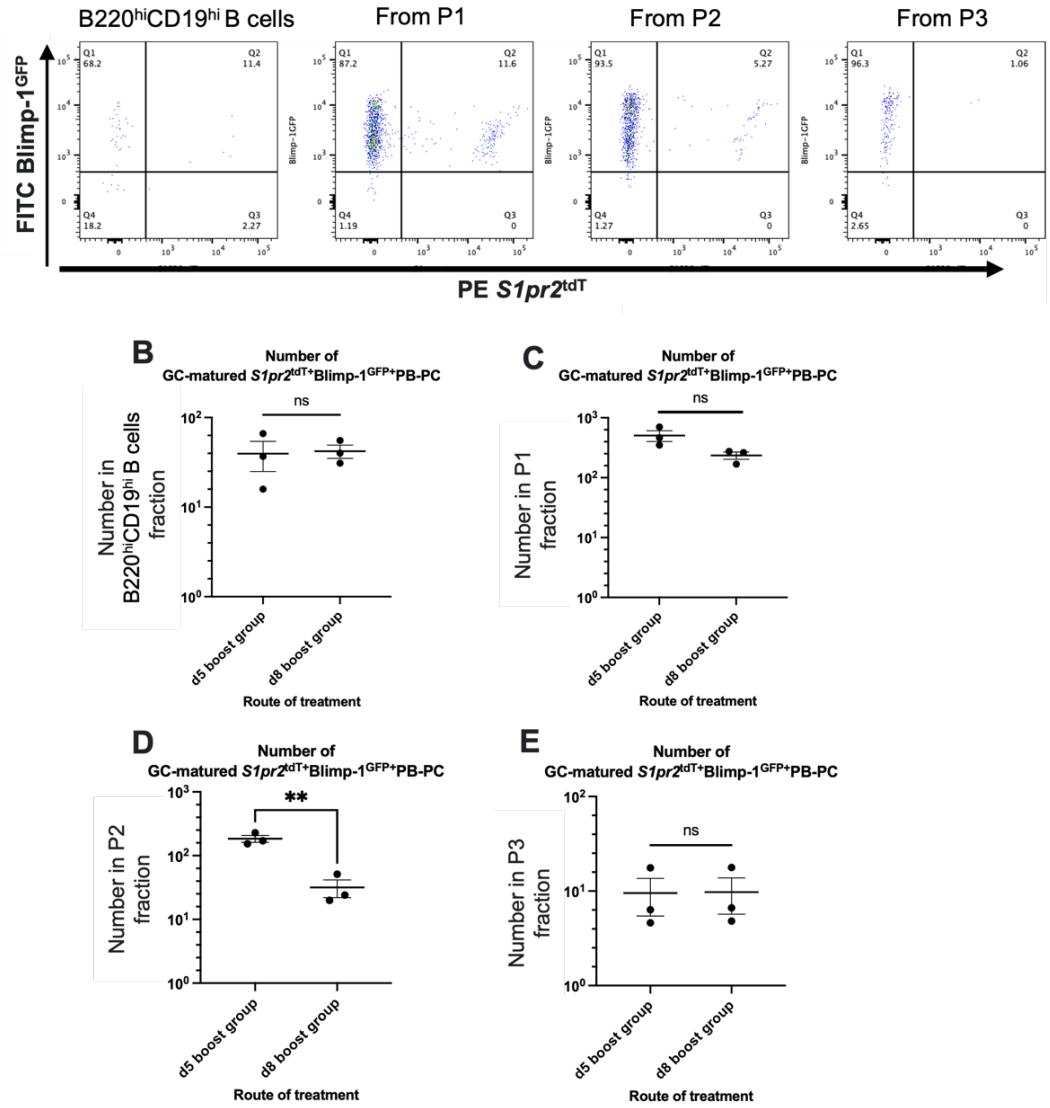


Figure 3.41. Analysis and number of GC-matured CD138^{hi} TACI^{hi} *S1pr2*$^{tdT+}$ Blimp-1^{GFP+} PB-PC during recall responses to NP$_{27}$-KLH immunisation.

The experimental protocol is illustrated in Figure 3.31. **(A)** A flow cytometry analysis of GC-matured *S1pr2*$^{tdT+}$ Blimp-1^{GFP+} PB-PC gated from CD138^{hi} TACI^{hi} PB-PC fractions. **(B)** Number of GC-matured *S1pr2*$^{tdT+}$ Blimp-1^{GFP+} PB-PC within B220^{hi} CD19^{hi} B cells fraction. **(C)** Number of GC-matured *S1pr2*$^{tdT+}$ Blimp-1^{GFP+} PB-PC within PB-PC (P1) fraction. **(D)** Number of GC-matured *S1pr2*$^{tdT+}$ Blimp-1^{GFP+} PB-PC within early PC (P2) fraction. **(E)** Number of GC-matured *S1pr2*$^{tdT+}$ Blimp-1^{GFP+} PB-PC within late PC (P3) fraction. Data is represented as mean ± SEM. Each symbol represents one mouse. Data was obtained from one experiment, with n = 3 mice for the day 5 post-boosting group, n = 3 for the day 8 post-boosting group. Statistical tests were performed by an unpaired Welch's t-test. n.s. $p > 0.05$, ** $p < 0.01$.

The proportion of GC-derived *S1pr2*$^{tdT+}$ Blimp-1^{GFP+} PB-PCs within the P1 fraction increased from 9.5% on day 5 to 16% on day 8 (Figure 3.40D and Figure 3.41C). Within the P2 fraction, GC-derived *S1pr2*$^{tdT+}$ Blimp-1^{GFP+} PB-PC represented 5.8% on day 5 and 7.6% on day 8 (Figure 3.40E and Figure 3.41D). in the more mature P3 fraction, these cells accounted for 1.1% on day 5 and 3% on day 8 (Figure 3.40F and Figure 3.41E). Overall, a higher proportion of mature PB-PC was observed at day 8 across all CD138^{+} TACI^{+} PB-PC fractions.

3.2.3.3. NP_2-specific IgG1 antibody titre was enhanced at day 8 post-boosting.

High-affinity of IgG1 and high-avidity of IgM responses to NP_2 were assessed using sera samples collected by cardiac puncture (see section 2.8) from boosted mice at days 5 and 8 post-boosting. Serum samples were collected only during the second experimental repeat; therefore, ELISA analysis was performed exclusively on boosted groups, as non-boosted mice were not included in this repeat due to the limited availability of HALO mice. At day 5, NP_2-specific IgM and IgG1 titres were present at almost comparable levels (Figure 3.42C and D). By day 8, NP_2-specific IgM had declined, with an increase observed in only a single sample, whereas NP_2-specific IgG1 titres increased significantly compared to day 5 (Figure 3.42D).

Together, the increased NP_2-specific IgG1 titres by day 8 are consistent with the higher proportion of mature CD138^{+} TACI^{+} PB-PCs observed at this time point, suggesting progressive differentiation of antibody-secreting cells during the recall response in a short time frame. A caveat of this analysis is the absence of a non-boosted group.

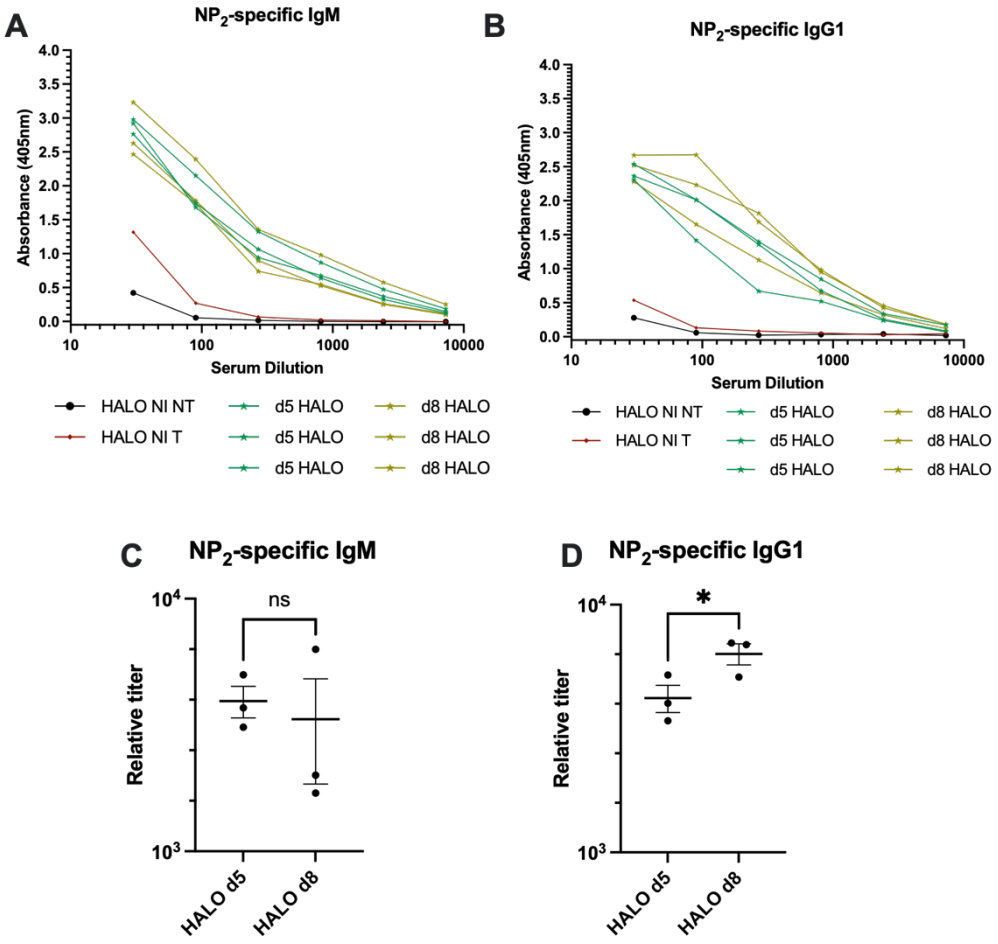


Figure 3.42. NP_2-specific antibody response after recall responses to NP_{27}-KLH immunisation.

Mice were immunised as described in Figure 3.31. Sera samples were collected on day 5 and day 8 post-boosting. NP_2-specific IgM and IgG1 titres were determined by ELISA. **(A)** Dilution curve for NP_2-specific IgM. **(B)** Dilution curve for NP_2-specific IgG1. **(C)** NP_2-specific IgM levels at days 5 and 8 post-boosting with NP_{27}-KLH. **(D)** NP_2-specific IgG1 levels at days 5 and 8 post-boosting with NP_{27}-KLH. The data on C and D are represented as mean ± SEM. Each symbol represents one mouse. Data was obtained from one experiment, with n = 3 mice for the day 5 post-boosting group, n = 3 for the day 8 post-boosting group. Statistical tests were performed by a paired parametric t-test. n.s. $p > 0.05$, * $p < 0.05$.

Additionally, the present analysis captures only the titres of high-affinity IgG1 and high-avidity IgM NP-specific antibodies; therefore, the use of NP_2/NP_{15} or NP_2/NP_{27} relative titre ratios would provide a direct measure of affinity maturation.

Figure 3.43 and Figure 3.44 present typical examples of splenic sections obtained following the secondary immunisation protocol outlined in Figure 3.31, highlighting the spatial localisation of NP-specific EF-derived Blimp-1^{GFP} PB-PCs and NP-specific GC-derived *S1pr2*$^{tdT+}$ B cells.

3.2.4. Histology quantification of GC-matured *S1pr2*$^{tdT+}$ Blimp-1^{GFP+} PB-PC.

GC-matured *S1pr2*$^{tdT+}$ Blimp-1^{GFP+} PB-PCs were quantified within three anatomical regions: per mm^2 of spleen section (Figure 3.45A), per mm^2 of T cell zone (Figure 3.45B), and per mm^2 of GC B cells area (Figure 3.45C) using immunofluorescence imaging. The splenic sections used in GC-matured PB-PC quantification were prepared according to the experimental protocol illustrated in Figure 3.2. Sections were stained with IgD to identify B cell follicles, CD4 to define T cell zones, and anti-GFP to detect Blimp-1^{GFP} PB-PCs. Images were uploaded into Qupath software, and qualification was performed as described in section 2.7.4. The number of GC-matured *S1pr2*$^{tdT+}$ Blimp-1^{GFP+} PB-PCs per mm^2 of spleen section increased significantly on day 6 compared to day 5. When quantified per mm^2 of T cell zone, the number GC-matured *S1pr2*$^{tdT+}$ Blimp-1^{GFP+} PB-PCs varied across time points, with a non-significant increase observed on day 8. In contrast, the density of GC-matured *S1pr2*$^{tdT+}$ Blimp-1^{GFP+} PB-PCs per mm^2 of GC area remained relatively comparable across the

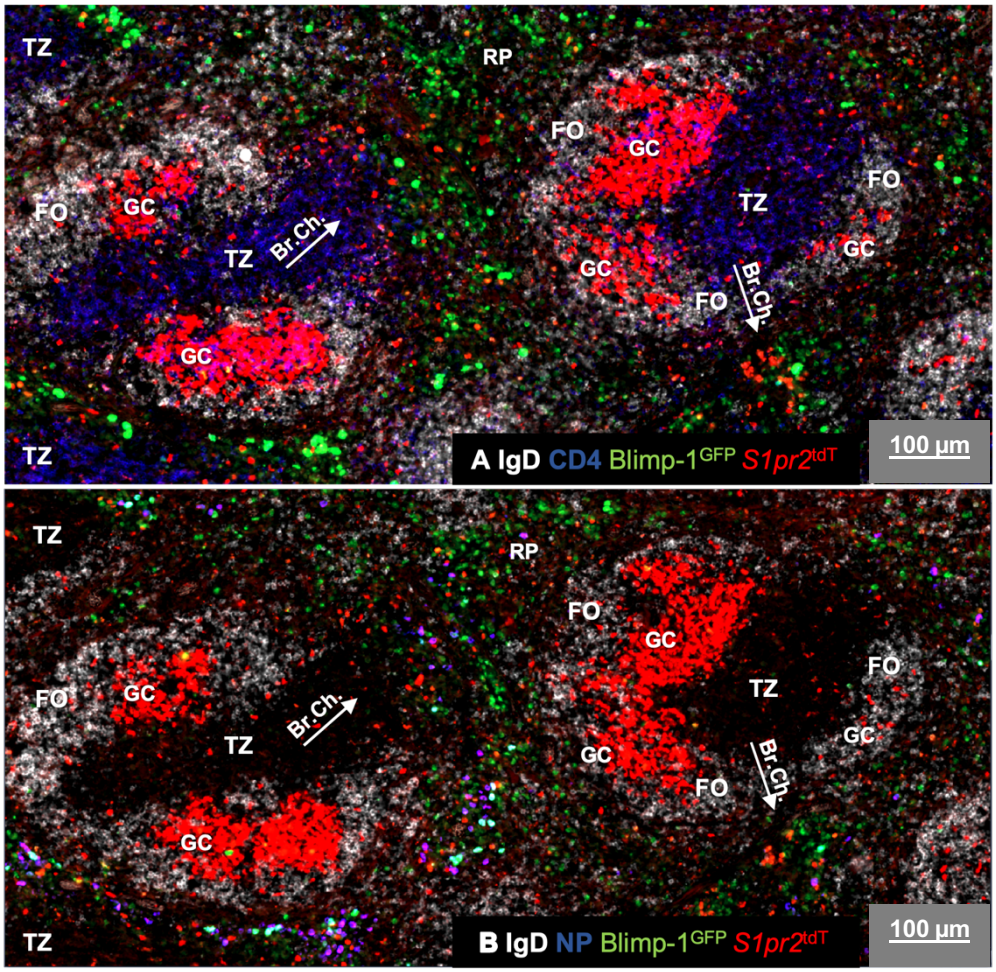


Figure 3.43. An example image of NP-specific B cells in a recall response on day 5 post-boosting.

The splenic sections were obtained from the protocol illustrated in Figure 3.31. The splenic sections were stained with antibodies against IgD^{hi} follicular B cells (white), anti-GFP (green), CD4^{+} T cells (blue cells in view A), and NP^{+} cells (blue cells in view B). The *S1pr2*^{tdT} signal is detected as auto-fluorescence in the red channel. **(A)** Zoomed-in view of the secondary follicles, showing the T cell zones. **(B)** Zoomed-in view of the same secondary follicles in A, showing NP-specific GC-derived *S1pr2*$^{tdT+}$ B cells around the secondary follicle (purple cells, NP *S1pr2*^{tdT}) and NP-specific EF-derived Blimp-1^{GFP} PB-PCs (turquoise cells, NP Blimp-1^{GFP}). These images were obtained from the spleen of HALO mice 5 days post-boosting. Images were produced by the fluorescent field at 20x magnification using a Zeiss AxioScan Z1 Slide Scanner. Images were processed at 100 µm with Zen v3.1 (Blue Edition). GC: Germinal centre; FO: Follicular B cells; RP: Red pulp; TZ: T cell zone; Br.Ch. stands for bridging channel.

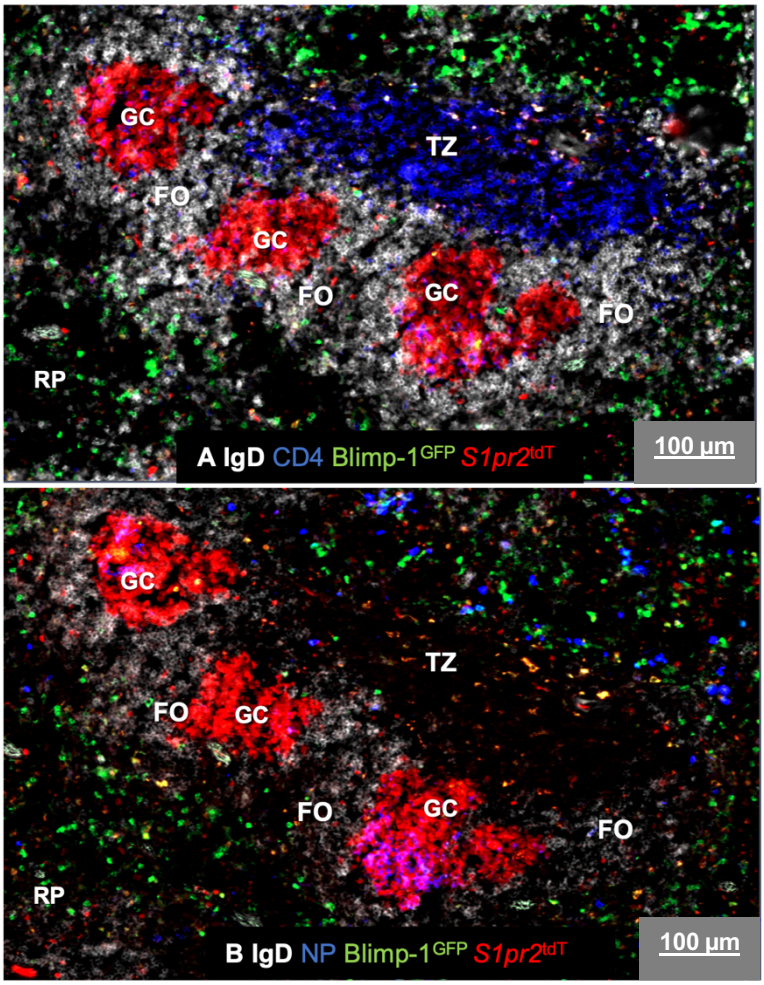


Figure 3.44. An example image of NP-specific B cells in a recall response on day 8 post-boosting.

The splenic sections were obtained from the protocol illustrated in Figure 3.31. The splenic sections were stained with antibodies against IgD^{hi} follicular B cells (white), anti-GFP (green), $CD4^{+}$ T cells (blue in view A), and NP^{+} cells (blue in view B). The *S1pr2*^{tdT} signal is detected as auto-fluorescence in the red channel. **(A)** Zoomed-in view of the secondary follicles, showing the T cell zones staining. **(B)** Zoomed-in view of the same secondary follicles in A, showing NP-specific activated cells within the GC dark zone side are denoted with a grey-filled triangle, NP-specific EF-derived Blimp-1^{GFP} PB-PCs are denoted with yellow circles, trafficking towards the bridging channel during the T cell border, and NP-specific B cells are denoted with a white-filled triangle. These images were derived from the spleen of HALO mice 8 days post-boosting. Images were produced by the fluorescent field at 20x magnification using a Zeiss AxioScan Z1 Slide Scanner. Images were processed at 100 µm with Zen v3.1 (Blue Edition). GC: Germinal centre; FO: Follicular B cells; RP: Red pulp; TZ: T cell zone; Br.Ch. stands for bridging channel.

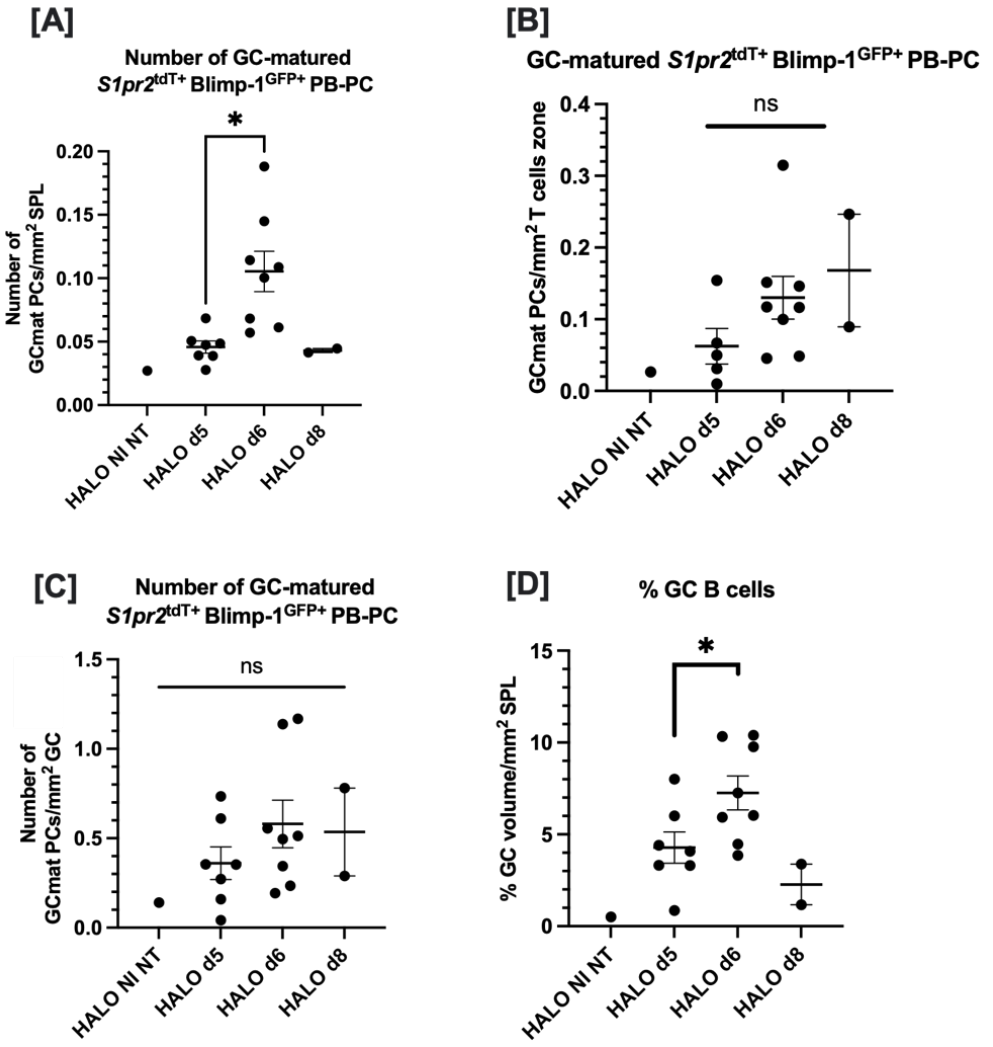


Figure 3.45. Histology quantification of GC-matured *S1pr2*$^{tdT+}$ Blimp-1^{GFP+} PB-PC in HALO mice in response to SRBCs.

The experimental protocol is illustrated in Figure 3.2. **(A)** The number of GC-matured *S1pr2*$^{tdT+}$ Blimp-1^{GFP+} PB-PC per square millimetre of the SPL section. **(B)** The number of GC-matured *S1pr2*$^{tdT+}$ Blimp-1^{GFP+} PB-PC per square millimetre of T zone. **(C)** The number of GC-matured *S1pr2*$^{tdT+}$ Blimp-1^{GFP+} PB-PC per square millimetre relative to the GC' size. **(D)** GC B cells volume per square millimetre of the spleen. Each symbol represents one mouse. Data was obtained from two independent experiments where n = 7 at day 5, n = 8 at day 6, and n = 2 at day 8. Statistical tests were performed by One-way ANOVA, a nonparametric test, and analysis with the Kruskal-Wallis test (n.s. $p > 0.05$, * $p < 0.05$). The quantification was performed manually using Qupath software (v0.4.4).

time points. The GC area was also quantified as a percentage of the total spleen section area. GC size peaked on day 6, corresponding with the increased number of GC-matured *S1pr2*$^{tdT+}$ Blimp-1^{GFP+} PB-PCs per mm^2 of spleen observed at the same time point. The increased localisation of GC-matured *S1pr2*$^{tdT+}$ Blimp-1^{GFP+} PB-PCs within the splenic section on day 6 corresponded with the flow cytometric findings, which demonstrated peaked frequencies of GC-matured CD138$^+$ TACI$^+$ *S1pr2*$^{tdT+}$ Blimp-1^{GFP+} PB-PCs and GC B cells at the same time point (see sections 3.2.1.1, 3.2.1.2, and 3.2.1.4). Collectively, these findings indicate that day 6 represents the peak of GC activity and GC-derived PB-PC generation following primary SRBC immunisation.

3.2.5. Histology identification and quantification of GC-associated IRF4$^+$PB-PC.

IRF4 is an early inducer after B cell activation, promotes differentiation and suppresses the GC programme [8]. High levels of IRF4-associated GC are located at the GTI after SRBC or NP-carrier immunisation [8]. Here, we exploited the advantage of the HALO mice model to locate and quantify GC-matured *S1pr2*$^{tdT+}$ IRF4$^+$ Blimp-1^{GFP+} PB-PC at the GTI region.

Figure 3.46 and Figure 3.47 were obtained from the experimental protocol illustrated in Figure 3.2 – primary immunisation with SRBC – and Figure 3.48 was obtained from the experimental protocol illustrated in Figure 3.31 – recall response immunisation with NP_{27}-KLH. These images are typical examples of GC-matured *S1pr2*$^{tdT+}$ IRF4$^+$ Blimp-1^{GFP+} PB-PCs found at the GTI, in the bridging channel, and the red pulp.

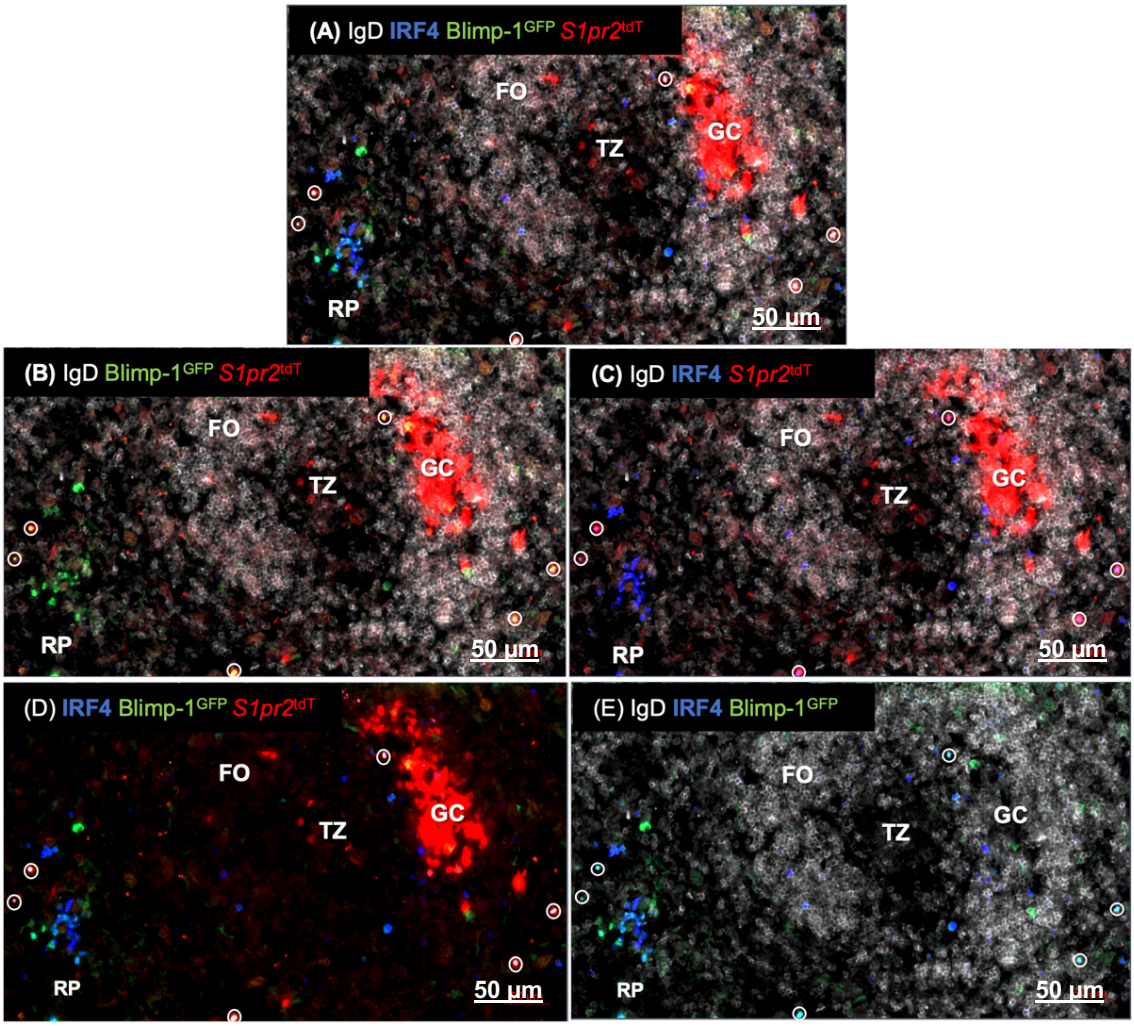


Figure 3.46. Identification of GC-matured *S1pr2*$^{tdT+}$ Blimp-1^{GFP+} IRF4^{hi} PB-PCs in a small GC cluster.

An example image displays the appearance of GC-associated *S1pr2*$^{tdT+}$ Blimp-1^{GFP+} IRF4^{hi} PB-PCs (white circle). The splenic section was stained with antibodies against follicular IgD^{hi} B cells (white), IRF4^{+} cells (blue), and anti-GFP (green). The *S1pr2*^{tdT} is detected as auto-fluorescence in the red channel. This image was obtained from the spleen of HALO mice 5 days post-immunisation with SRBC via *i.v*. The image was produced by the fluorescent field at 20x magnification using a Zeiss AxioScan.Z1 Slide Scanner and processed at 50 µm with Zen v3.1 (Blue Edition). GC: Germinal centre; FO: Follicular B cells; RP: Red pulp; TZ: T cell zone.

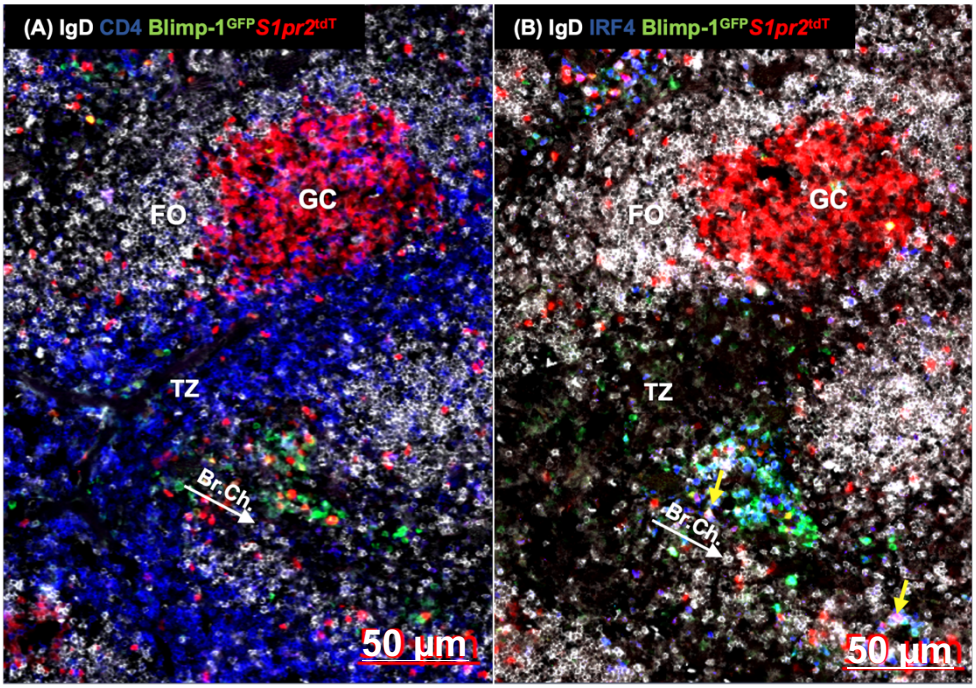


Figure 3.47. Identification of GC-matured *S1pr2*$^{tdT+}$ Blimp-1^{GFP+} IRF4^{hi} PB-PCs in the bridging channel.

An example image displays the appearance of GC-matured Blimp-1^{GFP+} *S1pr2*$^{tdT+}$ IRF4^{hi} PB-PC in the bridging channel (yellow-headed arrow). The splenic section was stained with antibodies against follicular IgD^{hi} B cells (white), CD4^{+} T cells (A) IRF4^{+} cells (B) (blue), and anti-GFP (green). The *S1pr2*^{tdT} is detected as auto-fluorescence in the red channel. Image **(A)** is zoomed-in view showing the CD4^{+} T cell zone. Image **(B)** is zoomed-in on the same view showing migration of GC-matured Blimp-1^{GFP+} *S1pr2*$^{tdT+}$ IRF4^{hi} PB-PC. These images were obtained from the spleens of HALO mice 6 days post-immunisation with SRBC via *i.v*. Images were produced by the fluorescent field at 20x magnification using a Zeiss AxioScan Z1 Slide Scanner. Images were processed at 50 µm with Zen v3.1 (Blue Edition). GC: Germinal centre; FO: Folicular B cells; TZ: T cell zone; Br.Ch. stands for bridging channel.

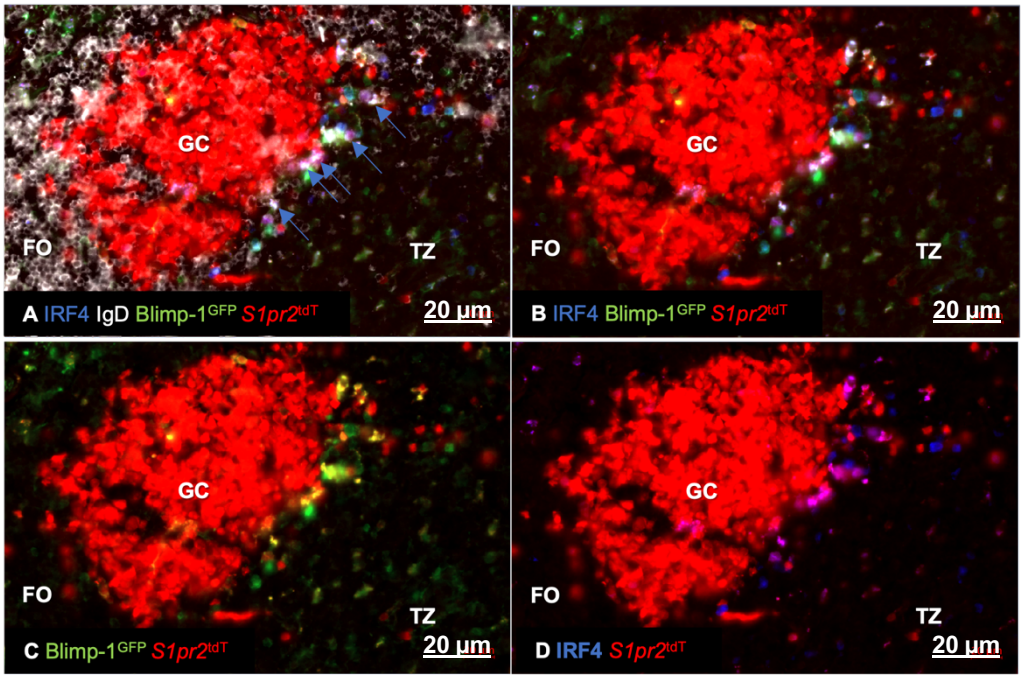


Figure 3.48. Identification of GC-matured *S1pr2*$^{tdT+}$ Blimp-1^{GFP+} IRF4^{hi} PB-PCs at the GTI of matured GC.

An example images display the appearance of GC-matured Blimp-1^{GFP+} *S1pr2*$^{tdT+}$ IRF4^{hi} PB-PC at the GTI region. The splenic section was stained with antibodies against follicular IgD^{hi} B cells (white), IRF4^{+} cells (blue), and anti-GFP (green). The *S1pr2*^{tdT} is detected as auto-fluorescence in the red channel. This image was obtained from the spleen of HALO mice at 8 days post-boosting with NP_{27}-KLH. The image was produced by the fluorescent field at 20x magnification using a Zeiss AxioScan Z1 Slide Scanner. Image was processed at 20 µm with Zen v3.1 (Blue Edition). Abbreviations: GC: Germinal centre; FO: Follicular B cells.

GTI is a narrow strip between IgD^{-} GC and IgD^{+} follicular/T-zone regions, where GC B cells receive signals that trigger exit from the GC and initiation of PB differentiation [8]. Therefore, we wanted to quantify the *S1pr2*$^{tdT+}$ IRF4^{+} Blimp-1^{GFP+} PB-PCs-associated GC. The quantification of GC-matured *S1pr2*$^{tdT+}$ IRF4^{+} Blimp-1^{GFP+} PB-PCs at the GTI was determined according to the region definition described in 2.7.4. **Table 3.2** shows the number of mice analysed at the denoted time points, the total merged GC area, and the number of GC regions included in the quantification.

Table 3.2. Quantification of GC-matured IRF4^{+} *S1pr2*$^{tdT+}$ Blimp-1^{GFP+} PB-PC at GTI.

Day5

Sample ID	Merge annotated GCs.	Total GC-IRF4^{+} *S1pr2*^{tdT} cells at GTI	Blimp-1^{GFP+} expression among them	% of Blimp-1^{GFP+} expression
Mouse A	42733.3 µm^2 **4 GC**	4 cells	2 cells	50%
Mouse B	143776.9 µm^2 **6 GC**	13 cells	7 cells	53%

Day6

Sample ID	Merge annotated GCs.	Total GC-IRF4^{+} *S1pr2*^{tdT} cells at GTI	Blimp-1^{GFP+} expression among them	% of Blimp-1^{GFP+} expression
Mouse A	348234.4 µm^2 **17 GC**	42 cells	11 cells	26.2%
Mouse B	99452.8 µm^2 **6 GC**	17 cells	5 cells	29.4%
Mouse C	145874.6 µm^2 **13 GC**	31 cells	10 cells	32.3%

Day8

Sample ID	Merge annotated GCs.	Total GC-IRF4^{+} *S1pr2*^{tdT} cells at GTI	Blimp-1^{GFP+} expression among them	% of Blimp-1^{GFP+} expression
Mouse A	54951.2 µm^2 **8 GC**	27 cells	19 cells	70.4%
Mouse B	35485.7 µm^2 **5 GC**	17 cells	7 cells	41.2%

The experimental protocol is illustrated in Figure 3.2. GC-matured IRF4^{+} *S1pr2*$^{tdT+}$ PB-PC at GTI were quantified, and then how many of them are expressing Blimp-1^{GFP+} PB-P. The quantification was performed manually using Qupath software (v0.4.4).

GC-matured *S1pr2*$^{tdT+}$ IRF4^{+} PB-PCs were first identified, and the fraction of these cells that co-expressed Blimp-1^{GFP+} PB-PCs was subsequently determined. At day 5, approximately half of GC-matured *S1pr2*$^{tdT+}$ IRF4^{+} PB-PCs expressed Blimp-1^{GFP+} (50% and 53%). By day 6, the proportion of Blimp-1^{GFP+} cells was lower, ranging from 26.2% to 32.3% across samples. At day 8, the proportion increased again but showed greater variability between mice (41.2% and 70.4%). Due to the small number of samples analysed at each time point, variability between mice limits definitive conclusions. Overall, this observation is consistent with the previous report, showing that, at early stages, IRF4 high populations are heterogeneous and comprise both Blimp-1$^{low/-}$ and Blimp-1^{+} cells [8]. Importantly, the absence of a detectable Blimp-1^{GFP} signal does not necessarily indicate a true lack of Blimp-1 expression [148].

3.2.6. GC-resident Tfh cells in HALO mice.

Tfh cells promote GC B cell selection by delivering survival signals through CD40L and cytokines like IL-21, and are also implicated in directing GC B cells toward PC or memory B cell fates [90, 91]. We wanted to assess the phenotype of GC-resident Tfh cells at days 5 and 6 post-SRBC immunisation (Figure 3.2) by flow cytometric analysis (Figure 3.49). GC-resident Tfh cells are identified by high expression of CXCR5 and PD-1 and reduced expression of CD90.2 [92], Figure 3.49A and B. In addition, elevated *S1pr2*$^{tdT+}$ expression contributes to the retention of Tfh cells within the GC microenvironment [87]. Flow cytometric analysis revealed a significant increase in the number of GC-resident *S1pr2*$^{tdT+}$ CXCR5^{hi} PD-1^{hi} CD90.2^{lo} Tfh cells on day 6 compared to day 5 (Figure 3.49E). Notably, the expansion of this GC-resident Tfh population

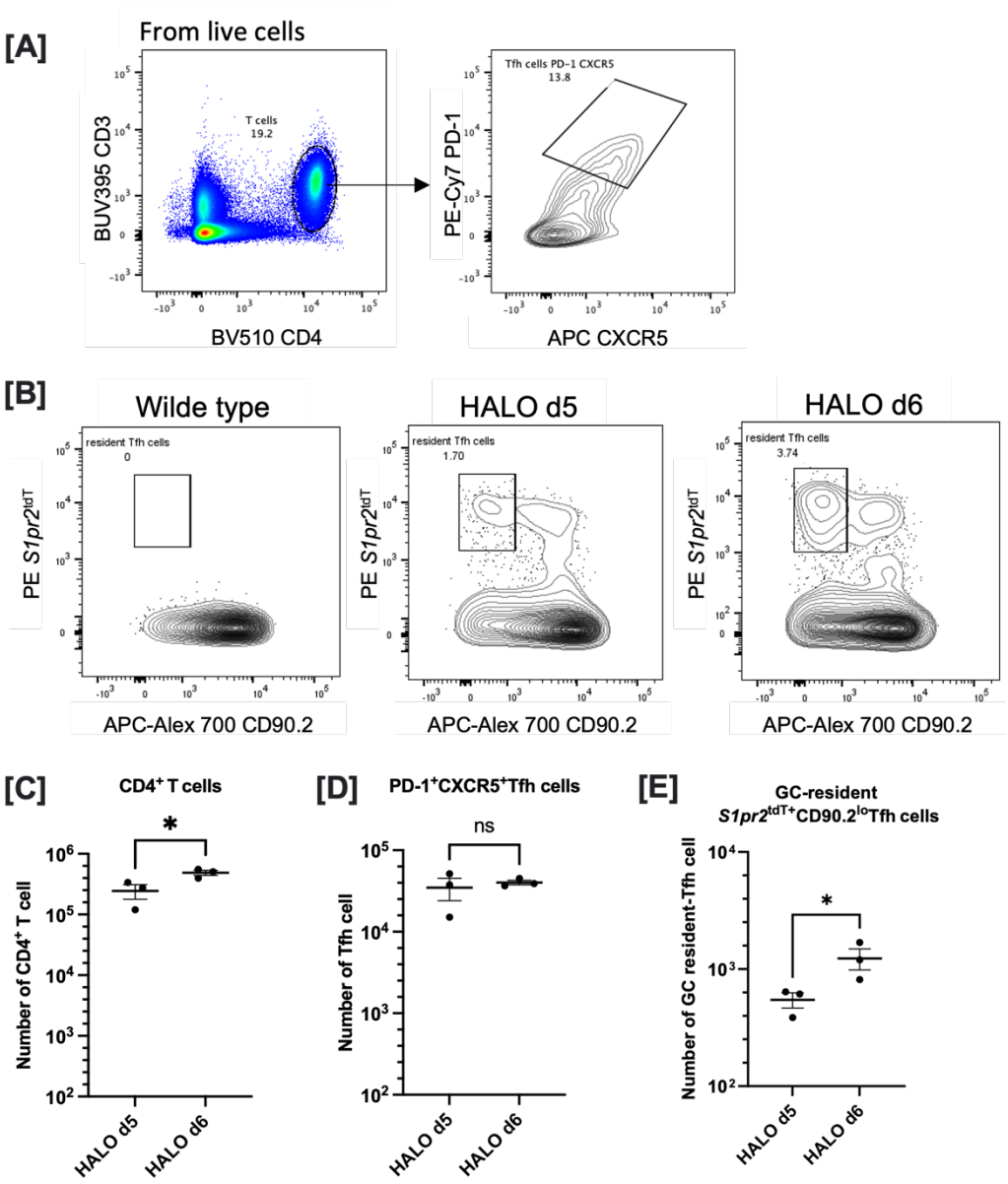


Figure 3.49. GC-resident Tfh cells in HALO mice.

The experimental protocol is illustrated in Figure 3.2. **(A)** $CD4^+$ T cells were gated and further analysed for Tfh-expressing PD-1 and CXCR5 cells. **(B)** GC-resident Tfh cells identified as $CXCR5^{hi}$ $PD\text{-}1^{hi}$ *S1pr2*^{tdThi} $CD90.2^{lo}$. **(C)** Number of $CD4^+$ T cells. **(D)** Number of $CXCR5^{hi}$ $PD\text{-}1^{hi}$ Tfh cells. **(E)** Number of GC-resident $CXCR5^{hi}$ $PD\text{-}1^{hi}$ *S1pr2*^{tdThi} $CD90.2^{lo}$ Tfh cells. Data were obtained from a single experiment using splenic HALO mice at day 5 (n = 3) and day 6 (n = 3) post-immunisation via *i.v.* with SRBCs. Statistical tests were performed by an unpaired Welch's t-test. n.s. $p > 0.05$, * $p < 0.05$.

occurred in parallel with GC expansion, suggesting coordinated regulation of GC architecture and Tfh cell abundance. Maintenance and expansion of GC-resident Tfh cells are known to depend on sustained cognate interactions with antigen-presenting by MHC II GC B cells [92]. Therefore, the observed increase in GC-resident Tfh cells at day 6 is consistent with the peak in GC size at this time point, and Tfh cell accumulation is driven by GC expansion.

3.2.7. Investigation of *S1pr2*^{tdT} and Blimp-1^{GFP} expression in splenic CD4^{+} and CD3^{+} T cells.

The *S1pr2* receptor is involved in the migration and localisation of B cells and T cells within the GC [87, 96]. Moreover, Blimp-1 is also expressed in T cells and plays an antagonistic role in Tfh cell differentiation by repressing Bcl6 [96]. In contrast, Blimp-1 expression in B cells drives their differentiation into PC. Initial image analysis showed *S1pr2*^{tdT} and Blimp-1^{GFP} labelling within CD4^{+} T cells (Figure 3.50), leading to subsequent flow cytometric analysis of *S1pr2*^{tdT} and Blimp-1^{GFP} expression in CD4^{+} CD3^{+} T cells. To validate the specificity of the HALO fate-mapping system, *S1pr2*^{tdT} and Blimp-1^{GFP} expression were investigated in CD4^{+} (Figure 3.51) and CD3^{+} T cells (Figure 3.52) in the HALO mice at days 5 and 6 post-SRBC immunisation (Figure 3.2). Overall, as expected, the MFI of Blimp-1^{GFP} expression was low in CD3^{+} and CD4^{+} T cells (Figure 3.53A), with a slight increase observed at day 6 compared to day 5. When Blimp-1^{GFP} MFI in CD3^{+} and CD4^{+} T cells (Figure 3.53A) was compared with that in CD138^{+} TACI^{+} PB-PC (Figure 3.53B), Blimp-1^{GFP} expression was markedly lower in T cells, confirming that high-level Blimp-1^{GFP} expression is lineage-specific to PB-PC

differentiation. Consistent with the previous reports, Blimp-1 expression in T cells is low in the naive state and induced following TCR stimulation, with gradual upregulation occurring between days 3-6 [179]. In contrast, *S1pr2*$^{tdT+}$ expression was detectable in CD3^{+} and CD4^{+} T cells (Figure 3.53C) but was substantially higher in CD138^{+} TACI^{+} PB-PC (Figure 3.53D). This differential expression is consistent with the established role of *S1pr2*$^{tdT+}$ in GC residency and retention. Accordingly, *S1pr2*$^{tdT+}$ expression within the T cell compartment likely reflects GC-resident Tfh populations.

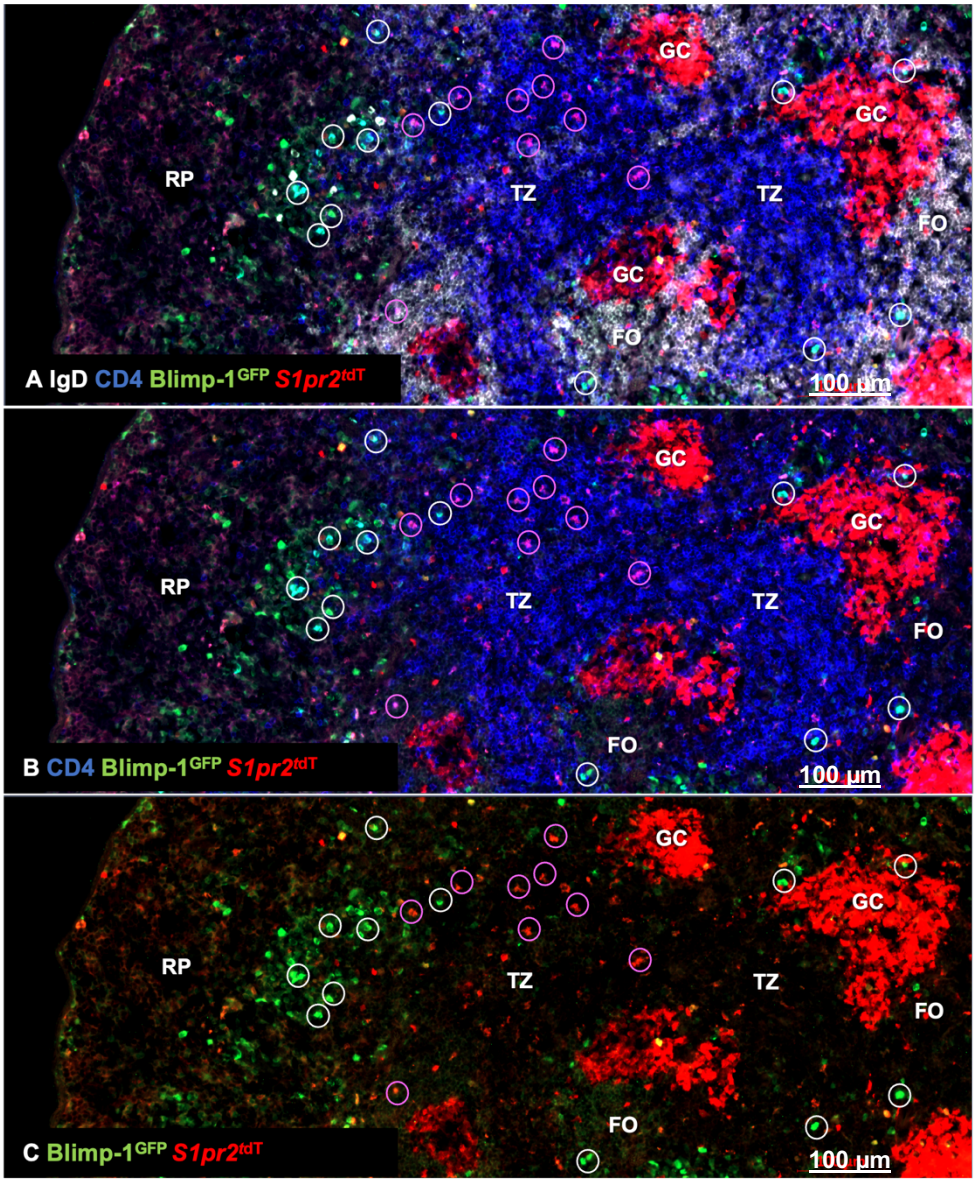


Figure 3.50. Typical image of *S1pr2*$^{tdT+}$ and Blimp-1^{GFP+} expression in CD4^{+} T cells.

An example image displays the expression of *S1pr2*$^{tdT+}$ (pink empty circle) and Blimp-1^{GFP+} (white empty circle) in CD4^{+} T cells. The spleen section was stained with antibodies against follicular IgD^{hi} B cells (white), CD4^{+} T cells (blue) and anti-GFP (green). The *S1pr2*^{tdT} signal was detected as an autofluorescence in the red channels. This image was obtained from the spleen of HALO mice 6 days post-immunisation via *i.v.* with SRBCs. Imaging was performed at 100 µm using a Zeiss AxioScan Z1 Slide Scanner and processed with Zen v3.1 (Blue Edition). Abbreviations: GC: Germinal centre; FO: Follicular zone B cells; RP: Red pulp; TZ: T cell zone.

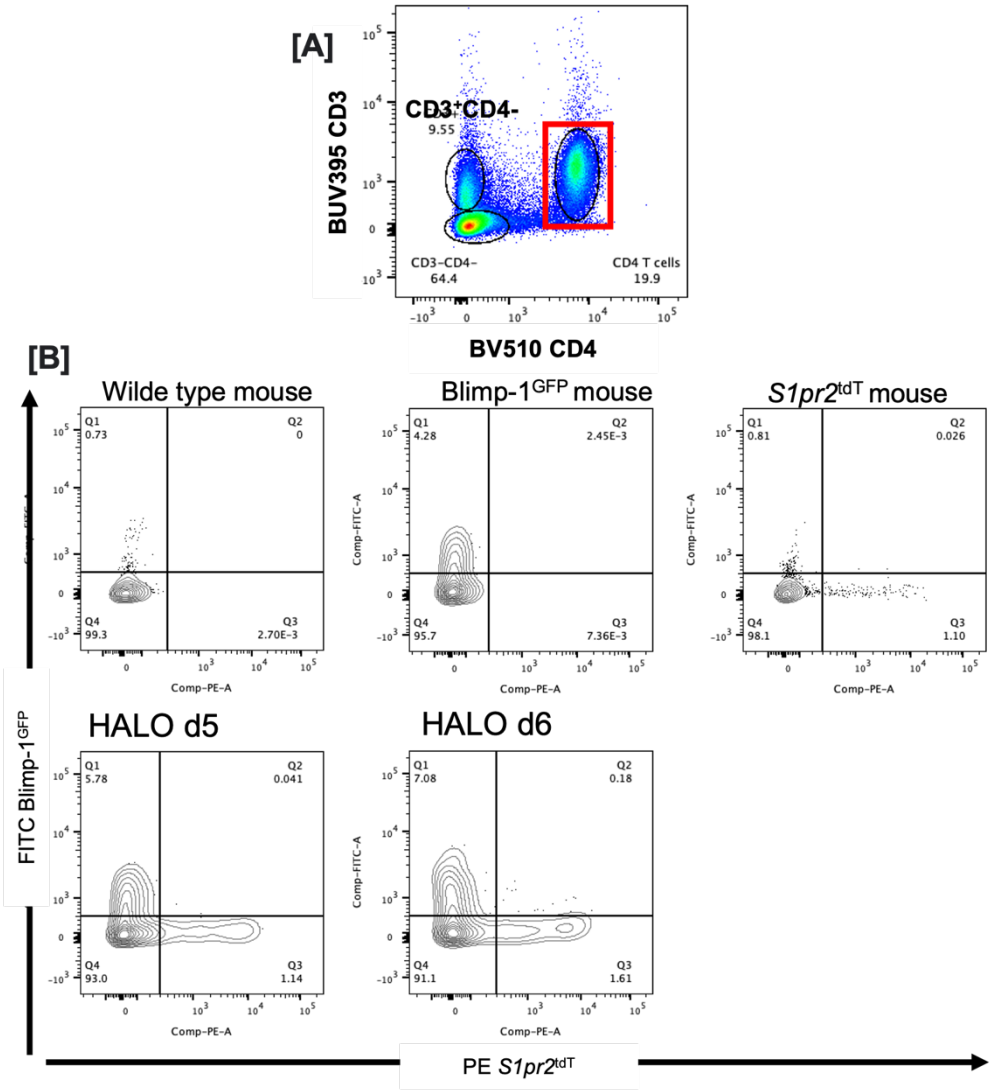


Figure 3.51. Analysis of *S1pr2*^{tdT} and Blimp-1^{GFP} expression in CD4^{+} CD3^{-} T cells in HALO mice.

The experimental protocol is illustrated in Figure 3.2. **(A)** CD4^{+} T cells were gated and further analysed for *S1pr2*^{tdT} and Blimp-1^{GFP} expression. **(B)** Representative expression of *S1pr2*^{tdT} and Blimp-1^{GFP} in CD4^{+} T cells within the denoted mouse model. Wild-type mice served as a baseline control for red and green autofluorescence. Blimp-1^{GFP}-only and *S1pr2*^{tdT}-only mice were used to define GFP and tdTomato fluorescence gates. HALO mice data were obtained from a single experiment using splenic HALO mice at day 5 (n = 3) and day 6 (n = 3) post-immunisation via *i.v.* with SRBCs.

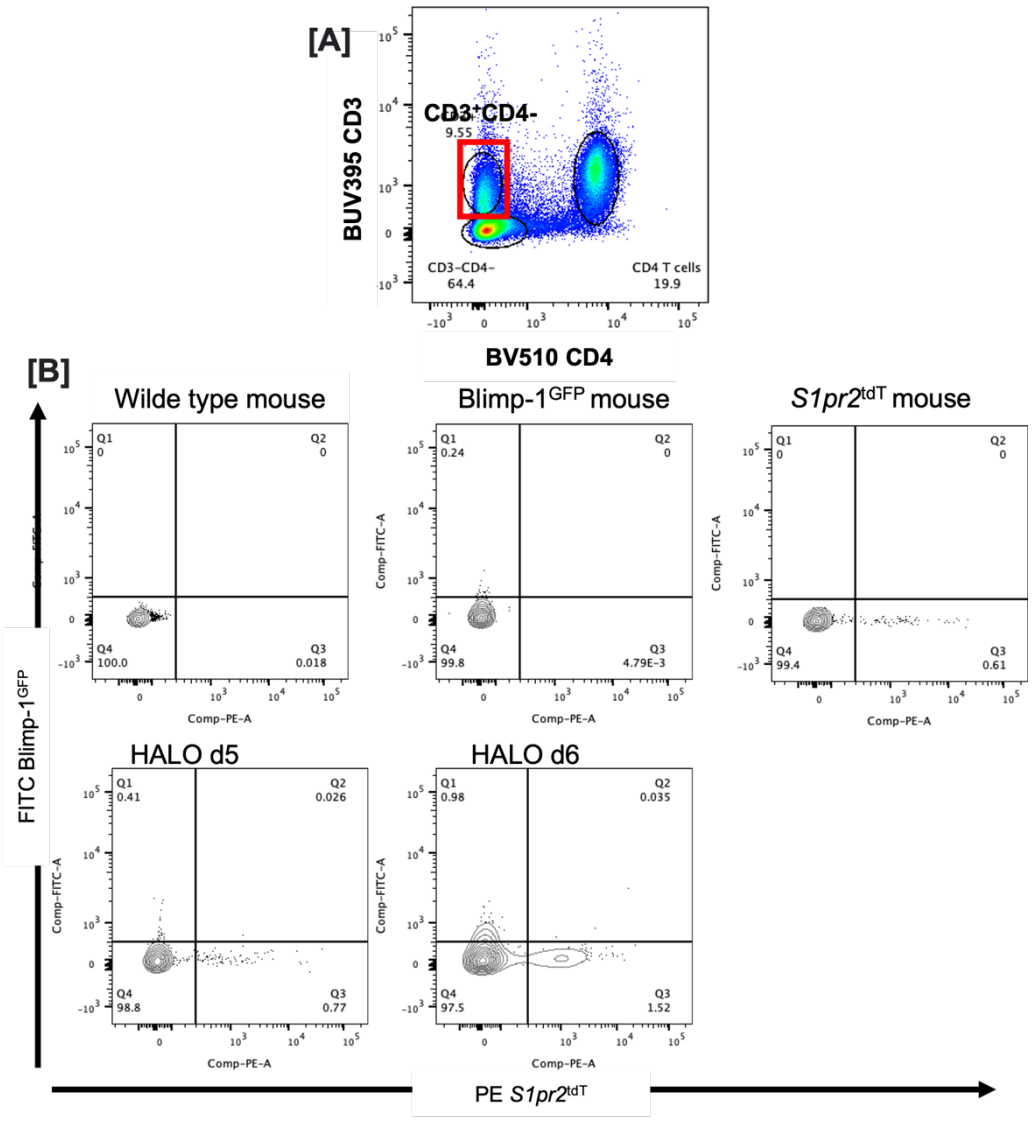


Figure 3.52. Analysis of *S1pr2*^{tdT} and Blimp-1^{GFP} expression in CD3^{+} CD4^{-} T cells in HALO mice.

The experimental protocol is illustrated in Figure 3.2. **(A)** CD3^{+} CD4^{-} T cells were gated and further analysed for *S1pr2*^{tdT} and Blimp-1^{GFP} expression. **(B)** Representative expression of *S1pr2*^{tdT} and Blimp-1^{GFP} in CD3^{+} CD4^{-} T cells within the denoted mouse model. Wild-type mice served as a baseline control for red and green autofluorescence. Blimp-1^{GFP}-only and *S1pr2*^{tdT}-only mice were used to define GFP and tdTomato fluorescence gates. HALO mice data were obtained from a single experiment using splenic HALO mice at day 5 (n = 3) and day 6 (n = 3) post-immunisation with SRBCs (Figure 3.2).

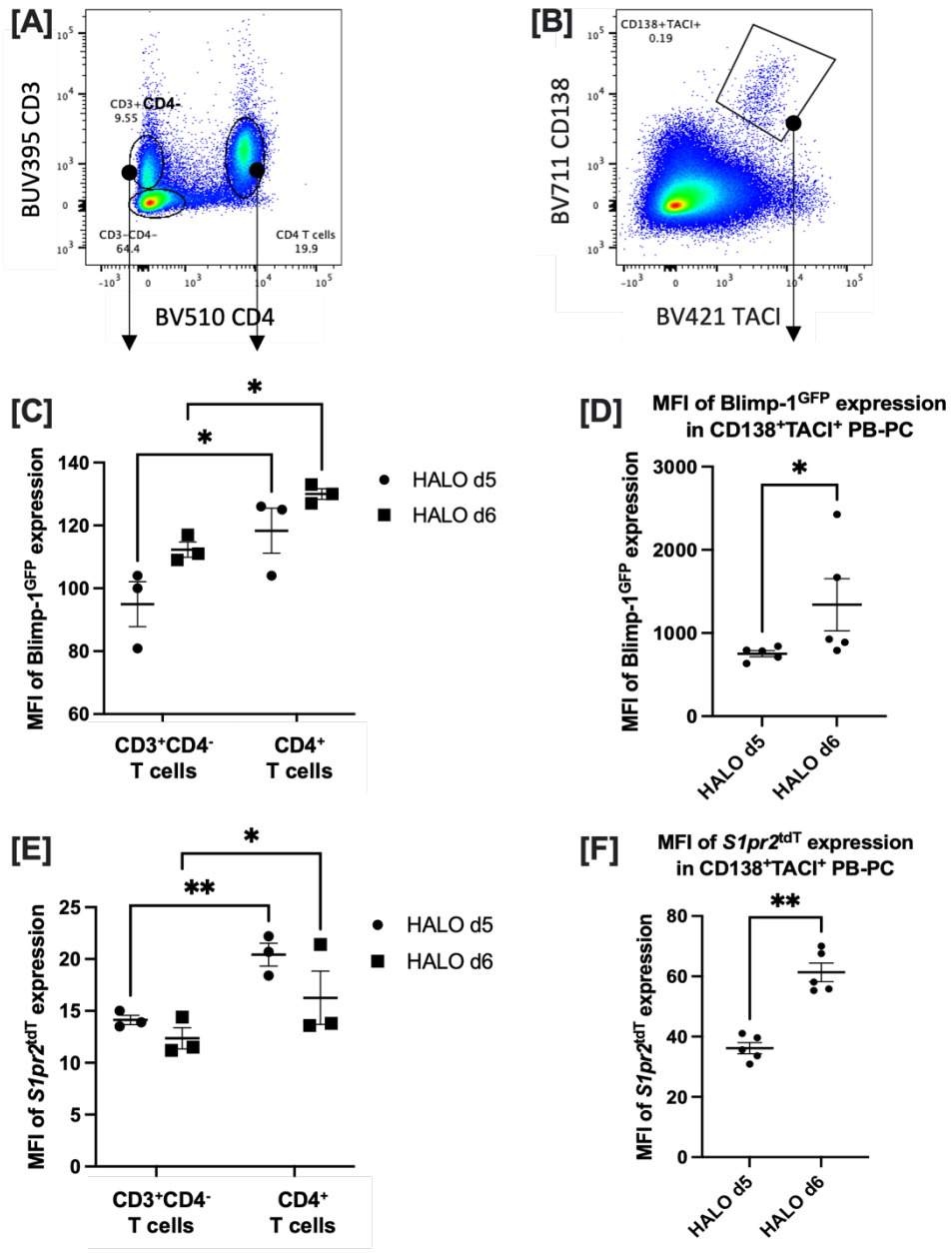


Figure 3.53. Analysis of *S1pr2*^{tdT} and Blimp-1^{GFP} expression in CD3^{+} CD4^{-} and CD4^{+} T cells in HALO mice.

The experimental protocol is illustrated in Figure 3.2. **(A)** MFI of Blimp-1^{GFP} expression in CD3^{+} CD4^{-} and CD4^{+} T cells. **(B)** MFI of Blimp-1^{GFP} expression in CD138^{+} TACI^{+} PB-PC. **(C)** MFI of *S1pr2*^{tdT} expression in CD3^{+} CD4^{-} and CD4^{+} T cells. **(D)** MFI of *S1pr2*^{tdT} expression in CD138^{+} TACI^{+} PB-PC. Wild-type mice served as a baseline control for red and green autofluorescence. Blimp-1^{GFP}-only and *S1pr2*^{tdT}-only mice were used to define GFP and tdTomato fluorescence gates. HALO mice data were obtained from a single experiment using splenic HALO mice at day 5 (n = 3) and day 6 (n = 3) post-immunisation with SRBCs (Figure 3.2). Statistical tests were performed by Two-way ANOVA (A and C) and by the Mann-Whitney test (B and D). * p <0.05, ** p <0.01.

Table 3.3. Summary of the main findings from the HALO mice experiments.

Experimental approach	Main observation
Primary SRBCs immunisation	1- GC-derived PB-PCs were detected early post-immunisation at day 5 and identified as B220^{hi} CD19^{hi} CD138^{+} TACI^{+} *S1pr2*$^{tdT+}$ Blimp-1^{GFP+} cells. 2- GC-matured PB-PCs accumulated and peaked at day 6, characterised by a B220^{lo} CD19^{lo} CD138^{+} TACI^{+} *S1pr2*$^{tdT+}$ Blimp-1^{GFP+} phenotype. 3- GC-derived CD38^{+} Blimp-1^{GFP+} *S1pr2*$^{tdT+}$ PB-PC precursors peaked at day 5. 4- Increased GC-derived memory B cells was observed at day 6 alongside accumulation of GC-derived *S1pr2*$^{tdT+}$ CD138^{+} TACI^{+} PB-PCs.
Primary NP_{27}-KLH immunisation	1- GC-derived PB-PCs and NP_2-specific IgG1 responses were prominent at day 10. 2- Generally, GC-derived PB-PC frequencies were relatively low.
Secondary NP_{27}-KLH challenge	1- Increased GC-derived PB-PC responses and GC-derived CD38^{+} Blimp-1^{GFP+} *S1pr2*$^{tdT+}$ PB-PC precursors peaked at day 5 following boosting. 2- GC-matured B220^{lo} CD19^{lo} CD138^{+} TACI^{+} *S1pr2*$^{tdT+}$ Blimp-1^{GFP+} PB-PC and NP_2-specific IgG1 titres increased at day 8 following boosting.

1.3 Discussion.

The results presented in this chapter demonstrated that the *S1pr2*^{CreERT2} *Rosa26*^{LSLtdTomato} *Prdm1*^{GFP} (HALO) mouse model enables the identification of GC-matured *S1pr2*$^{tdT+}$ Blimp-1^{GFP+} PB-PC, thereby distinguishing these cells from EF-derived Blimp-1^{GFP+} PB-PC that did not enter a GC during the same immune response. Flow cytometry and histological analyses revealed the presence of a few EF-derived Blimp-1^{GFP+} PB-PCs and GC-matured *S1pr2*$^{tdT+}$ Blimp-1^{GFP+} PB-PCs in the spleen under steady-state conditions, suggesting low-level reporter expression independent of immunisation. Fluorochrome-conjugated antibody labelling of markers such as CD19, B220, CD138 and TACI allows further discrimination of PB-PC developmental stages [148, 180].

Earlier work by Zhang et al. showed that GC-derived PB-PC appeared as early as day 5 post-immunisation, emerging at the GTI, where their differentiation is induced by IL-21 and CD40-ligation and supported by APRIL signalling [8]. The study was powerful in identifying the anatomical localisation and signalling environment of GC-derived PB-PC, relying on indirect or induced fate-mapping approaches. Moreover, studies using SRBC or haptenated protein for immunisation has reported the appearance of GC-derived PB-PC as early as day 5 post-immunisation [8, 181, 182]. Therefore, we established day 5 post-immunisation as the initial time point, based on these reports about the onset of GC-derived PB-PC output. To ensure consistency across all time points— days 5, 6, and 8, tamoxifen was administered 48 hours prior to spleen collection in each group, thereby inducing reporter activation under identical conditions. This approach ensured that observed differences in EF-derived Blimp-

1^{GFP+} PB-PCs and GC-matured *S1pr2*$^{tdT+}$ Blimp-1^{GFP+} PB-PCs reflected true biological variation over time rather than differences in labelling efficiency or timing.

Quantitative increases in Blimp-1 expression define PC differentiation, and its levels correlate with loss of B cell markers (CD19, B220, MHC II), reduced proliferation, and increased longevity [159]. While expression of CD138 is heterogeneous and not definitive for all antibody-secreting cells [159]. Blimp-$1^{GFPlo/int}$ often $CD138^{-}$ and correlates with PB, while Blimp-1^{GFPhi} can be $CD138^{-}$ or $CD138^{+}$, correlates with PC, especially in the BM [159]. Two independent studies, led by Wilmore et al. and Prachet et al., advanced the identification of antibody-secreting cells beyond the conventional CD138/Blimp-1 marker combination [148, 180]. Refining PB-PC identification using markers such as TACI, CD19, B220, Sca-1, CD138, and Blimp-1 deepens understanding of PB-PC differentiation states and developmental stage [148, 180]. The HALO mouse model further enhances PB-PC analysis by enabling simultaneous assessment of differentiation status and migratory patterns. Moreover, the HALO mouse model enables the characterisation of distinct PB-PC populations based on *S1pr2*$^{tdT+}$ Blimp-1^{GFP+} expression. Using this approach, two PB-PC populations were identified: 1) $CD138^{+}$ *S1pr2*$^{tdT+}$ Blimp-1^{GFP-} PB-PC; and 2) $CD138^{-}$ Blimp-1^{GFP+} Fas^{hi} PB-PC. The absence of Blimp-1^{GFP} in the first population implies the limitations of IRES-dependent—reflects reporter sensitivity—and does not indicate a complete absence of Blimp-1 expression [148, 159]. Blimp-1^{GFP} reporter mice defined the $CD138^{hi}$ $B220^{lo}$ PC gate, which contains a substantial fraction of GFP-negative cells [148, 159]. The second population raises the question of why these cells lack *S1pr2*^{tdT} expression in the HALO mouse model. Blimp-$1^{GFP+\ B}$ cells are developed within Fas^{hi} GC B cells during the active tamoxifen window, as tamoxifen is still present and Cre

recombination continues to label new cells [183]. Alternatively, these cells may be positioned within Fas^{hi} due to antibody feedback [77, 184-186]. Another possibility is incomplete GC labelling [187], as the *S1pr2*^{ERT2Cre}*Rosa26*^{LSLtdTomato} system labels around 80% of GC B cells (Figure 3.7J). In Kallies et al.'s study, CD138^{-} Blimp-1^{GFP+} PB-PCs represent an early or transitional state of PC differentiation, illustrating that Blimp-1 upregulation precedes and is not synchronised with CD138 expression [159].

Following primary SRBC immunisation of HALO mice, GC-derived PB-PCs were detected early post-immunisation at day 5, identified as B220^{hi} CD19^{hi} CD138^{+} TACI^{+} *S1pr2*$^{tdT+}$ Blimp-1^{GFP+} cells. GC-matured PB-PCs accumulated to peak levels at day 6, characterised by a B220^{lo} CD19^{lo} CD138^{+} TACI^{+} *S1pr2*$^{tdT+}$ Blimp-1^{GFP+} phenotype. The phenotypic shift from B220^{hi} CD19^{hi} to B220^{lo} CD19^{lo} reflects the developmental maturation, marking the loss of B cell identity and BCR signalling as cells commit to the PC lineage. In a study conducted in the absence of an immunogenic antigen, B220^{hi} MHC-II^{hi} Blimp-1^{tdT+} PB-PC were identified as an early-generated PC population arising from both GC-independent and -dependent pathways and were detected in BM at day 0 [188]. Approximately four weeks after entry into the BM, B220^{hi} MHC-II^{hi} Blimp-1^{tdT+} PB-PC differentiate into B220^{lo} MHC-II^{lo} Blimp-1^{tdT+} long-lived PC [188]. In NP-CGG immunisation, NP-specific PC detected in the BM around day 7 were predominantly derived from GC-independent pathways, whereas PCs generated through GC-dependent differentiation were preferentially detected at day 56 post-immunisation [188]. Approximately 10-20% of B220^{hi} MHC-II^{hi} Blimp-1^{tdT+} PB-PC differentiate into B220^{lo} MHC-II^{lo} Blimp-1^{tdT+} long-lived PC, while the remaining cells either undergo cell death or fail to differentiate. Overall, both GC-independent and GC-

derived PB-PCs display similar survival and decay kinetics, indicating that GC-experienced is not required for PCs to contribute to the long-lived compartment [188].

The HALO mouse model has been established to identify the affinity of GC-matured PB-PC. The generation of affinity-matured PB-PC from GC is an essential process for producing antibodies with high specificity and functional efficacy. During the later stages of the GC response – typically around 21 days post-immunisation and onwards – the GC environment is thought to favour the selection and differentiation of B cells with higher-affinity receptors, contributing to long-lasting humoral immunity [189]. However, recent studies have challenged this traditional view, demonstrating that both high- and low-affinity B cells can give rise to PB-PCs throughout different phases of the immune response, not just the late GC phase [105, 107, 108]. These findings suggest that high affinity is not the sole factor driving the maturation of the antibody repertoire. Comparative analyses between infection and immunisation models further support this notion, showing that while the efficiency of PB-PC output may vary, both models give rise to PB-PC with a broad range of antibody affinities [105]. The V186.2 is a commonly studied VH gene in B cells undergoing affinity maturation, especially in response to NP-carrier antigens [190, 191]. Therefore, to test whether the GC-matured B220^{lo} CD19^{lo} CD138^{+} TACI^{+} *S1pr2*$^{tdT+}$ Blimp-1^{GFP+} PB-PCs identified at day 6 have undergone high-affinity maturation, molecular validation of hallmark somatic hypermutations – specifically the W33L and K59R mutations in the V186.2 heavy chain gene – is required.

GC-derived *S1pr2*$^{tdT+}$ Blimp-1^{GFP+} PB-PC appeared within CD38^{+} populations. PC differentiation starts within follicles—in the GCLZ—with low CD38 expression, which

increases progressively during PC differentiation and relocates to extrafollicular regions [192]. Blimp-1^{GFP+} CD38^{+} cells represent early PC precursors or PB with an intermediate level of Blimp-1 [159]. They have initiated the PC transcriptional program but have not yet reached the fully differentiated CD138^{+} Blimp-1^{hi} PC stage [159]. CD38 enhances BCR signalling in mice by activating downstream pathways such as the PI3K-Akt signalling pathway, which is involved in B cell activation, survival and differentiation; however, PI3K-Akt signalling is normally attenuated in GC B cells [193]. The functional role of CD38 could be tested by combining the HALO mouse model with a conditional CD38 knockout, enabling assessment of how CD38 loss affects GC-derived PB-PC differentiation.

Following primary i.p. immunisation with NP-KLH, GCs increased in frequency on day 10 and declined by day 14. In contrast to the primary NP-CGG response, GC size increases through day 10 and reaches a maximum around day 14 before declining thereafter [26]. In the context of SRBC immunisation, GC volume instead peaks around days 6-7 and declines by days 10 and 14 [8]. In their study, GC response was quantified using histological measurements of GC area, whereas in this study, GC response was assessed by the frequency of GC B cells. Using HALO mice, GC-matured CD138^{+} *S1pr2*$^{tdT+}$ Blimp-1^{GFP+} PB-PCs accumulated alongside a high-affinity titre of NP_2-specific IgG1 at day 10, consistent with prior evidence that IgG1 class-switch-associated transcription is induced early after primary immunisation and remains detectable through day 10 before declining by day 14 [8].

Another insight into the dynamic of GC-matured *S1pr2*$^{tdT+}$ Blimp-1^{GFP+} PB-PCs was obtained by performing a recall response in HALO mice. Mice were primed via i.p. to

rapidly induce the antigen into the cavity and, four weeks later, boosted into the bloodstream to magnify the immune response [181]. The time frame for receiving the tamoxifen was a single dose over 48 hours and a double dose over 92 hours before harvesting the spleens on days 5 and 8, respectively. The short window focuses on the immediate early wave of the recall response, and the longer window focuses on labelling the broader and slightly delayed phase of the recall response. The analyses revealed that day 8 was prioritised as the time point characterised by the highest proportional expansion of high-affinity GC-matured $CD19^{lo}$ $B220^{lo}$ $CD138^{+}$ $TACI^{+}$ *S1pr2*$^{tdT+}$ Blimp-1^{GFP+} PB-PC (P3), together with increased P1 and P2 populations, aligning with the peak NP-specific IgG1 titre. This is consistent with classical secondary response kinetics, where high-affinity IgG dominates at this period of time [178]. GC-experienced PB-PC most likely originate from previously GC-experienced memory B cells [194, 195]. However, it may either differentiate directly into PB-PC, re-enter GC for further affinity maturation before differentiation, or generate secondary memory B cells [194-196]. A human study analysing peripheral blood following tetanus booster immunisation demonstrated that antigen-specific PC and memory B cells are clonally related and can exhibit either an identical mutation pattern or have additional unique mutation patterns, indicating that recall responses may involve both direct differentiation and continued diversification [196]. However, these findings were derived from circulating cells. Using HALO mice would determine whether GC-matured PB-PC observed at day 8 shared clonal ancestry with memory B cells and whether additional mutation occurs following boosting.

At the histology level, we analysed the output of GC-matured *S1pr2*$^{tdT+}$ Blimp-1^{GFP+} PB-PCs in three measured environments (see section 3.2.4). Immunofluorescence histology of spleen sections taken 5, 6, and 8 days after SRBC immunisation showed a non-significant increase of GC-matured *S1pr2*$^{tdT+}$ Blimp-1^{GFP+} PB-PCs on day 8 within the T cell zone, compared to days 5 and 6. The presence of GC-matured PB-PC in the T zone reflects a transitional migratory phase following GCDZ exit before reaching a survival niche, such as red pulp, BM, and splenic bridging channel. PB initially migrate through the T zone with higher motility and becomes slower, more confined movement upon reaching the medullary niches [197]. The fibroblastic reticular cell network within the T zone, enriched in CCL19, CCL12 and detectable CXCL12 provides a structural scaffold guiding their migration toward survival sites. The increased presence of GC-matured *S1pr2*$^{tdT+}$ Blimp-1^{GFP+} PB-PCs within the T cell zone may provide insight into their accumulation at the GTI [8]. However, due to the limited number of biological replicates analysed on day 8, larger cohorts will be required to determine whether these spatial patterns are consistent. The GTI represents the earliest anatomical site where GC-derived PB-PC exit the GC and initiate transcriptional commitment to the PC fate, characterised by downregulation of Bcl6 and upregulation of IRF4 and Blimp-1.

A key finding of SRBC immunisation is the emergence of GC-derived *S1pr2*^{tdT} Blimp-1^{GFP} PB-PCs as early as day 5 and localise next to the GCLZ side. This spatial distribution is consistent with previous reports indicating that PBs egress from LZ following selection. A 2019 study examined how GC B cells exit the GC by mapping their spatial distribution within intact LN using whole-organ imaging [172]. It was shown that most GC-experienced B cells accumulated predominantly within the LN cortex in

proximity to GC structures, rather than in the T cell zone. Dissemination was shown to occur primarily from the LZ, where B cells migrate to the GC periphery before gradually entering the surrounding follicular mantle. Most AID-experienced B cells detected outside the GC appeared to be in a transitional state, with only a small fraction corresponding to PB or classical memory B cells. Mechanistically, BCR affinity played a role as high-affinity clones efficiently populated the cortex, whereas low-affinity cells showed impaired dissemination. Additionally, CCR6-dependent signalling was required for effective accumulation of B cells in the cortex. Notably, substantial heterogeneity was observed among individual GCs in their capacity to release cells, suggesting that GC output is not uniform [172]. These observations were made at day 12-14 post-immunisation using NP-OVA in alum, compared to an earlier time point following SRBC immunisation in the present study. This suggests that dissemination from GC may occur earlier than previously appreciated.

Identification of GC-matured *S1pr2*$^{tdT+}$ IRF4^{+} Blimp-1^{GFP+} PB-PCs by flow cytometry proved challenging (data not shown). An IRF4 staining panel was therefore included to assess the impact of fixation and intercellular staining conditions on GFP and tdTomato signals. These conditions had a pronounced effect on the GFP fluorescence and a modest effect on the tdTomato signal. However, the triple expression GC-matured *S1pr2*$^{tdT+}$ IRF4^{+} Blimp-1^{GFP+} PB-PCs was successfully identified in situ. The increase in Blimp-1^{GFP} expression observed at day 8, if confirmed in larger cohorts, could reflect a wave of PB-PC maturation and migration through the GTI. This interpretation is consistent with the increased number of GC-matured *S1pr2*$^{tdT+}$ Blimp-1^{GFP+} PB-PCs per μm² of the T zone at this time point. The GTI contains specialised GC-T zone interface reticular cells (GTIRCs) enriched in chemokines such as CXCL12,

cytokines including APRIL, and adhesion molecules such as ICAM-1 and VCAM-1 [8]. Together with Tfh cell-derived signals, including IL-21, these factors are thought to support the differentiation, retention, and migration of PB-PCs emerging from the GC. The caveat is that the HALO mouse model requires optimisation of tissue fixation and intercellular staining conditions to preserve Blimp-1^{GFP} fluorescence while enabling reliable detection of IRF4. Furthermore, the cost and time required for breeding HALO mice limited the feasibility of pilot optimisation and experimental replication.

While the present study focused on early GC output, future work could extend this analysis to later stages of the response. Building on the current findings, future studies should exploit the fate-mapping capability of the HALO mouse model to investigate the molecular and functional properties of GC-derived PC. This could include sorting defined PC subsets—GC-matured PC, EF-derived PC, and GC-derived PC precursors—for molecular profiling to further characterise differences associated with affinity-maturation. In addition, the intrinsic fluorescence of HALO mice could be used for advanced imaging approaches, such as light-sheet microscopy of whole lymph nodes, to map PC niches. Moreover, HALO mice could be exploited as a platform for monoclonal antibody discovery, as they enable the isolation of GC-experienced cells at the P1 and P2 stages through intrinsic fluorescent reporters, rather than relying on antigen binding.

1.4 Conclusion.

The HALO mouse model represents an advanced transgenic system that enables simultaneous tracking of two fluorescent reporters within the same immune stimulation.

Using this system, it was possible to directly identify GC-matured PB-PCs and distinguish them from non-GC-derived PB-PCs in combination with conventional phenotypic markers. Different immunisation routes were investigated to enrich GC-derived ASC that are candidates for hybridoma fusion without needing antigen-labelled sorting. Alternatively, single-cell cloning of Ig genes from these population provides recover high antibody affinity.

Chapter 4. Investigating the Impact of the Chimeric Tail of IgMg1 on Germinal Centre Response in the Context of AID Deletion.

4.1 Introduction

The BCR plays a critical role in B cell activation and GC responses by facilitating antigen capture for presentation to Tfh cells. In naive or non-switched B cells, membrane IgM transmits signals through the Igα/β complex, while in B cells which are IgG isotype-switched, BCRs can transmit signals directly via their cytoplasmic tail [198]. The engineered BCR allows for the assessment of how changes in BCR signalling affect B cell behaviour during immune response. In a collaborative effort, our lab developed an IgMg1 mouse model in which the cytoplasmic tail of IgG1 replaces the cytoplasmic tail of IgM, creating a chimeric IgMg1 BCR [199]. The purpose of constructing IgMg1 mice was to test whether the IgG1 signalling tail induces hyperresponsive naive B cells—due to the intrinsic BCR signal transduction capacity of the IgG1 cytoplasmic region—while keeping a normal polyclonal B cell repertoire. Therefore, this model was used to investigate the behaviour and function of IgMg1 B cells, with a focus on how this chimeric BCR affects a B cell's ability to participate in GC reactions, differentiate into PC, and influence the differentiation of Tfh cells. The findings revealed that IgMg1 B cells leave the BM as anergic cells, retaining a wild-type repertoire of BCR specificities and exhibiting normal IgD expression [199, 200]. Despite the anergy state, IgMg1 B cells can normally engage in GC reactions in response to TD antigens; however showed subdued responses to TI antigens [199,

200]. In response to the TD antigen NP-CGG, IgMg1 GC B cells showed an increased rate of apoptosis and an improved rate of proliferation six days after primary immunisation [199]. By day eight after primary immunisation, the total number of GC B cells in IgMg1 mice was comparable to that in wild-type mice [199]. In response to NP-KLH, apoptosis levels were higher among IgMg1 GC B cells eight days after immunisation compared to wild-type mice [200]. While wild-type mice exhibit a decline in NP-specific GC B cells, GC B cells in IgMg1 mice maintain a higher percentage of NP-specific GC B cells at eight days after immunisation with NP conjugated to either CGG or KLH [199, 200]. This retention suggests alterations in BCR signalling in IgMg1 GC B cells.

Moreover, the studies revealed that IgMg1 mice exhibit an increased number of Tfh cells compared to wild-type mice [199, 200] as well as heightened TCR signalling following immunisation [200]. This suggests that the altered BCR signalling in IgMg1 mice may enhance Tfh cell differentiation, which contributes to increased class switching.

Anergic IgMg1 B cells were able to differentiate into PCs. However, the overall impact on PC differentiation was significantly impaired in response to primary immunisation with TI antigen NP-Ficoll (at day 5) and TD antigen NP-CGG (at day 8) compared to wild-type B cells [199]. In contrast, the differentiation of anergic IgMg1 B cells into PCs was slightly reduced in response to NP-Ficoll (at day 6), but it remained unchanged compared to wild-type when exposed to TD antigen NP-KLH (at day 8) [200].

In response to primary immunisation with TD antigen NP-KLH, the researchers found that the frequency of $IgG1^+$ GC B cells in IgMg1 is dominant even more than in wild-

type GC B cells [199, 200], and correspondingly, the frequency of IgM^+ GC B cells is reduced compared to wild-type GC. Following isotype switching, these cells no longer display the chimeric IgMg1 BCR and instead express a conventional BCR corresponding to their new isotype. The researchers considered several possibilities and provided evidence against some of the possible explanations. Caspase-3 activity was higher in both $IgG1^+$ and IgM^+ IgMg1 GC B cell compartments, suggesting it was not the primary reason for the reduction of IgM^+ GC B cells. Given the similar DZ/LZ ratio for both IgM^+ and $IgG1^+$ GC B cells, this indicates that the lower frequency of IgM^+ GC B cells is not from being excluded from selection into GCDZ. Finally, the possibility that the reduction in IgM^+ GC B cells resulted from increased IgM^+ PCs output was not reasonable, as overall PC numbers were not significantly different, and IgM^+ anti-NP_2 serum titres showed a slight reduction compared with the wild-type counterpart. Based on these observations, the researchers proposed two main explanations for the reduction of IgM^+ GC B cells in IgMg1 mice: increased class-switching and reduced ability of IgM^+ IgMg1 B cells to enter the GC. To further investigate this, $IgMg1AID^{Cre}$ mice were generated (see Section 2.2.6 and Figure 4.1), allowing us to study the effect of the chimeric IgMg1 BCR on GC B cells' response in the presence of the homozygosity of the AID^{Cre} allele, where B cells are unable to class-switch. Notably, the absence of AID leads to large GC structures, as observed in humans and mice, due to a low apoptosis rate and a high proliferation rate [81, 83]. Further, the PC phenotype in AID^{Cre} mice is mostly IgM with lower affinity [201]. Therefore, the $IgMg1AID^{Cre}$ model provides an opportunity to study how chimeric BCR signalling influences B cell responses in the absence of AID activity. Utilising the $IgMg1AID^{Cre}$ mouse model could significantly contribute to the investigation of altered BCR

signalling on B cell activation and the development of autoimmunity related to class switching and AID activity. In this chapter, the following aims were addressed:

1. To investigate the CD138^{+} PB-PC response in IgMg1AID^{Cre} mice.
2. To investigate the kinetics of the Fas^{+} GC response B cell compartments.
3. To investigate the expansion of CXCR5^{+} PD1^{+} Tfh cells in IgMg1AID^{Cre} mice.

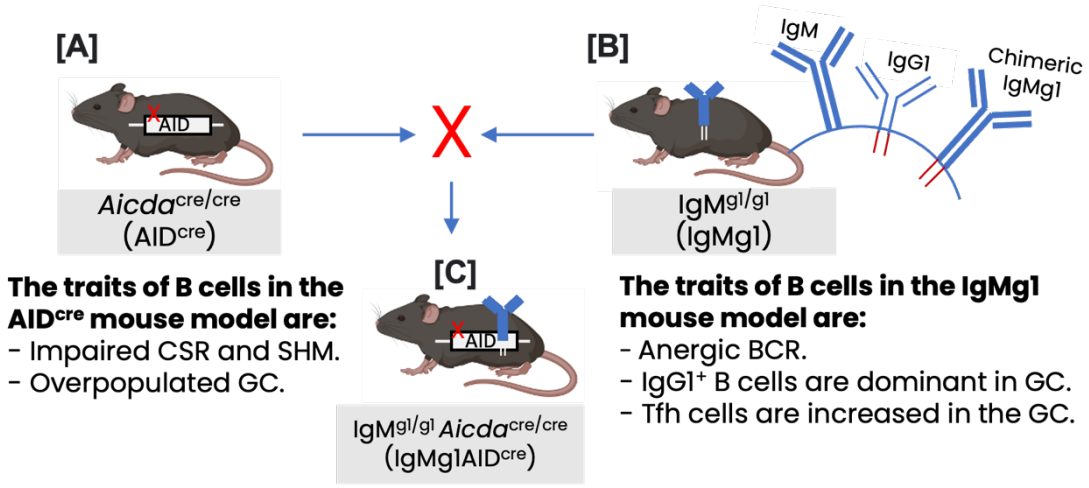


Figure 4.1. Schematic overview of the IgMgAID^{Cre} mouse models.

(A) The AID^{Cre} mouse model and its associated B cell traits. **(B)** The IgMg1 mouse model and its associated B cell traits. **(C)** IgMg1AID^{Cre} mouse model that is bred by mating the two mouse models.

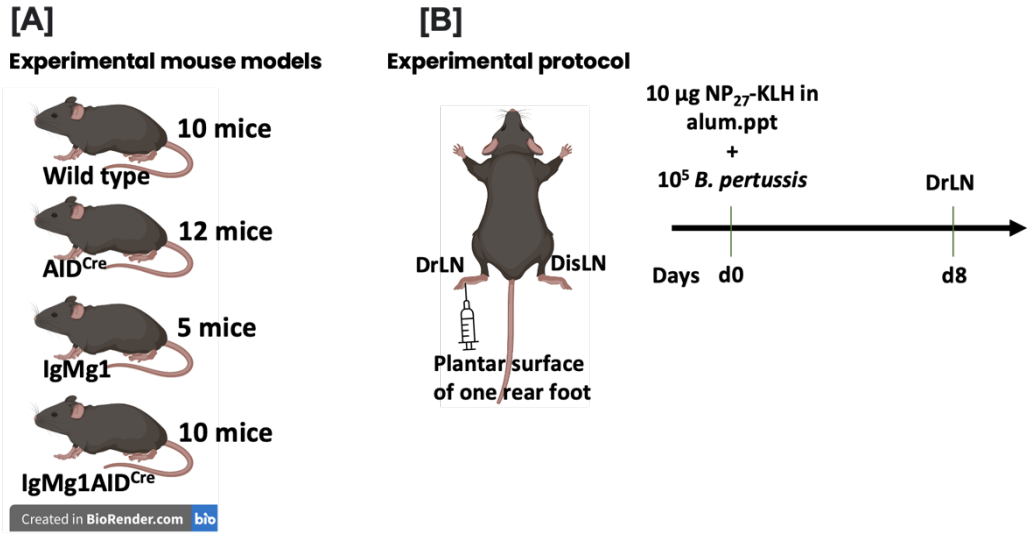
4.2. Results.

4.2.1. Experimental design for studying IgMg1AID^{Cre} mice.

Mice (Figure 4.2A) were immunised on the plantar surface of one rear foot with 10 µg NP_{27}-KLH in alum and heat-inactivated *B. pertussis* (Figure 4.2B). The draining lymph nodes (DrLN; injection site) were analysed by flow cytometry at day 8 after immunisation. Day 8 was selected based on previous work from our group, which employed the same immunisation protocol in the IgMg1 mouse model to evaluate B cell responses [199, 200]. The table in Figure 4.2C summarises the presence and absence of the GC processes, CSR and SHM, in the four different mouse models used in this chapter. The detailed description of the genetic modifications and characteristics of these mouse models is described in sections 2.2.1 2.2.5, and 2.2.6.

4.2.2. CD138^{+} PB-PC are impaired in the IgMg1AID^{Cre} mouse model.

Given that the AID^{Cre} model predominantly generates IgM-expressing PC [201], we wanted to examine how the transgenic IgMg1 allele affects PC differentiation in the IgMg1AID^{Cre} model (Figure 4.3). Following the immunisation schedule outlined in Figure 4.2B, there was a significant reduction in the frequency of CD138^{+} PB-PC in the lymph nodes of IgMg1AID^{Cre} mice compared to IgMg1 and wild-type mice (**** $p < 0.0001$), while it was similar to that observed in AID^{Cre} mice (Figure 4.3C). The number of CD138^{+} PB-PC shows a significant reduction in IgMg1AID^{Cre} mice compared to the AID^{Cre} model (** $p < 0.01$) and IgMg1 model (* $p < 0.05$) and did not show a significant difference compared to wild-type (Figure 4.3D). Overall, the results suggest that the PB-PC response to NP-KLH immunisation is strongly impaired in IgMg1AID^{Cre} mice.



[C]

Mouse model	Class switch recombination (CSR)	Somatic hypermutation (SHM)
Wild type	✓	✓
AIDCre	x	x
IgMg1	✓	✓
IgMg1AIDCre	x	?

Figure 4.2. Schematic of the experimental mouse models and the protocol.

(A) The number and strains of mouse models. **(B)** Each mouse model was immunised on the plantar surface of one rear foot with the precipitated antigen. Draining lymph nodes (DrLN) were harvested on day 8. **(C)** An overview of the capability of CSR and SHM in each mouse model.

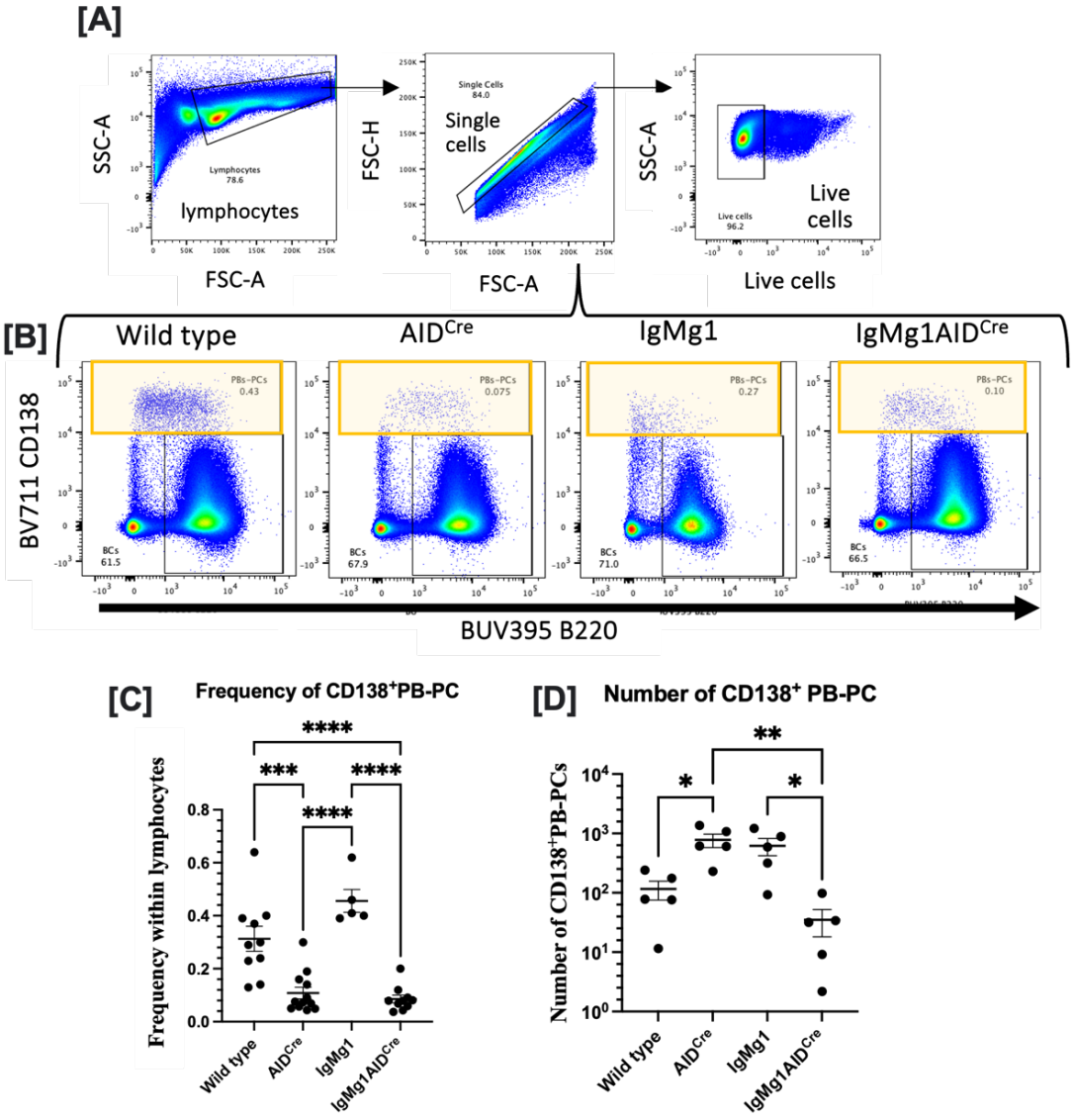


Figure 4.3. Analysis of the CD138⁺ PB-PC response.
The experimental protocol is illustrated in Figure 4.2. **(A)** The gating strategy of the lymph nodes. **(B)** Representative flow cytometry plots of CD138⁺ PB-PC in each mouse model. **(C)** The frequency of CD138⁺ PB-PC (mean ± SEM) within lymphocytes obtained from n=2 independent experiments (wild type = 10, AID^{Cre} = 12, IgMg1 = 5, and $IgMg1AID^{cre}$ = 10). **(D)** The number of CD138⁺ PB-PC (mean ± SEM) (wild type = 5, AID^{Cre} = 5, IgMg1 = 5, and $IgMg1AID^{cre}$ = 5). Data were derived from a single experiment, as CountBeads were accidentally used only in this experiment. Each symbol represents one mouse. Statistical tests were performed using ordinary one-way ANOVA. * $p < 0.05$, ** $p < 0.01$, *** $p < 0.001$, **** $p < 0.0001$.

The percentage and number of NP-specific CD138^{+} PB-PC (Figure 4.4B and C) were found to be reduced in IgMg1AID^{Cre} mice compared to the AID^{Cre} and IgMg1 models. Among the five samples of IgMg1AID^{Cre}, two exhibited no detectable response (Figure 4.4C), while the remaining three showed a markedly impaired NP-specific CD138^{+} PB-PC response compared to AID^{Cre} and IgMg1 models and no significant difference from the wild-type model. In both the IgMg1AID^{Cre} and AID^{Cre} mouse models, the results exhibited an absence of NP-specific IgG1^{+} CD138^{+} PB-PC (Figure 4.5D), which is expected. Overall, the decreased NP-specific CD138^{+} PB-PC response in the IgMg1AID^{Cre} model implies the impairment of PB-PC differentiation.

Surface IgM and IgG1 BCR expression was examined by flow cytometry staining with anti-BCR antibodies (Figure 4.6A-E). The frequency of IgG1 expression in the wild-type model showed 4% compared to 6% in the IgMg1 model (Figure 4.6B-C). These findings are consistent with the Hudson report that IgMg1 mice exhibit no significant increase in IgG1 PB-PC following primary NP-KLH immunisation [200]. As expected, IgG1 was absent in the AID^{Cre} model due to disrupted CSR, and the same was observed in the IgMg1AID^{Cre} model as a consequence of the AID^{Cre} background (Figure 4.6B and C). Accordingly, BCR expression in the IgMg1AID^{Cre} model is expected to remain a chimeric BCR, comprising an IgM extracellular region and carrying an IgG1 cytoplasmic tail. In contrast, the total frequency and number of IgM^{+} PB-PC in the IgMg1 model exhibited a reduction relative to the wild-type model (Figure 4.6D and E), which is consistent with Hudson's report [200].

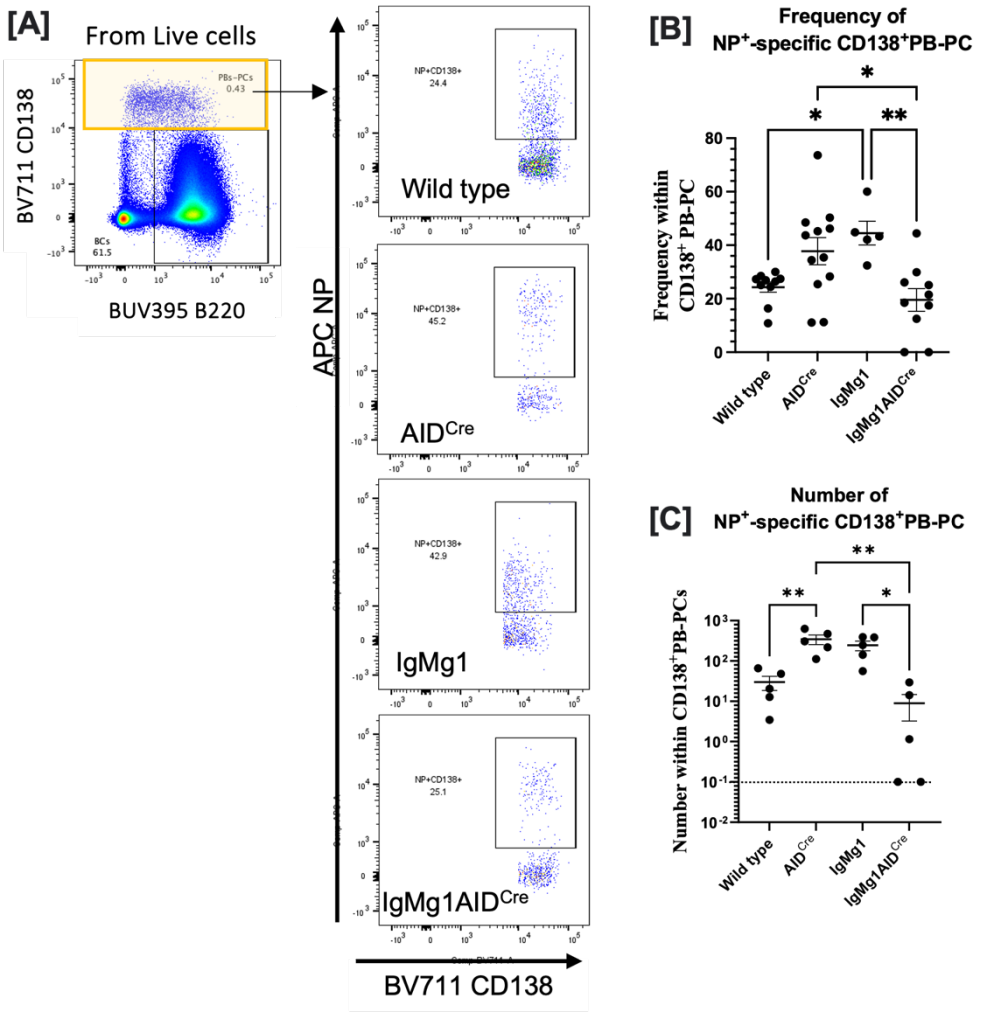


Figure 4.4. Analysis of the NP$^+$-specific CD138$^+$ PB-PC response.

The experimental protocol is illustrated in Figure 4.2. **(A)** Representative flow cytometry plots of CD138$^+$ PB-PC paired with NP and CD138. **(B)** The frequency of NP$^+$-specific CD138$^+$ PB-PC (mean ± SEM) within CD138$^+$ PB-PC, obtained from n=2 independent experiments (wild type = 10, AID^{Cre} = 12, IgMg1 = 5, and IgMg1AID^{cre} = 10). **(C)** The number of NP$^+$-specific CD138$^+$ PB-PC (mean ± SEM) within CD138$^+$ PB-PC (wild type = 5, AID^{Cre} = 5, IgMg1 = 5, and IgMg1AID^{Cre} = 5). Data in (C) was derived from a single experiment, as CountBeads were accidentally used only in this experiment. Each symbol represents one mouse. Samples with zero frequency were plotted at the lower limit of detection (10^{-1}) to allow visualisation on a logarithmic scale. Statistical tests were performed using ordinary one-way ANOVA. * $p < 0.05$, ** $p < 0.01$.

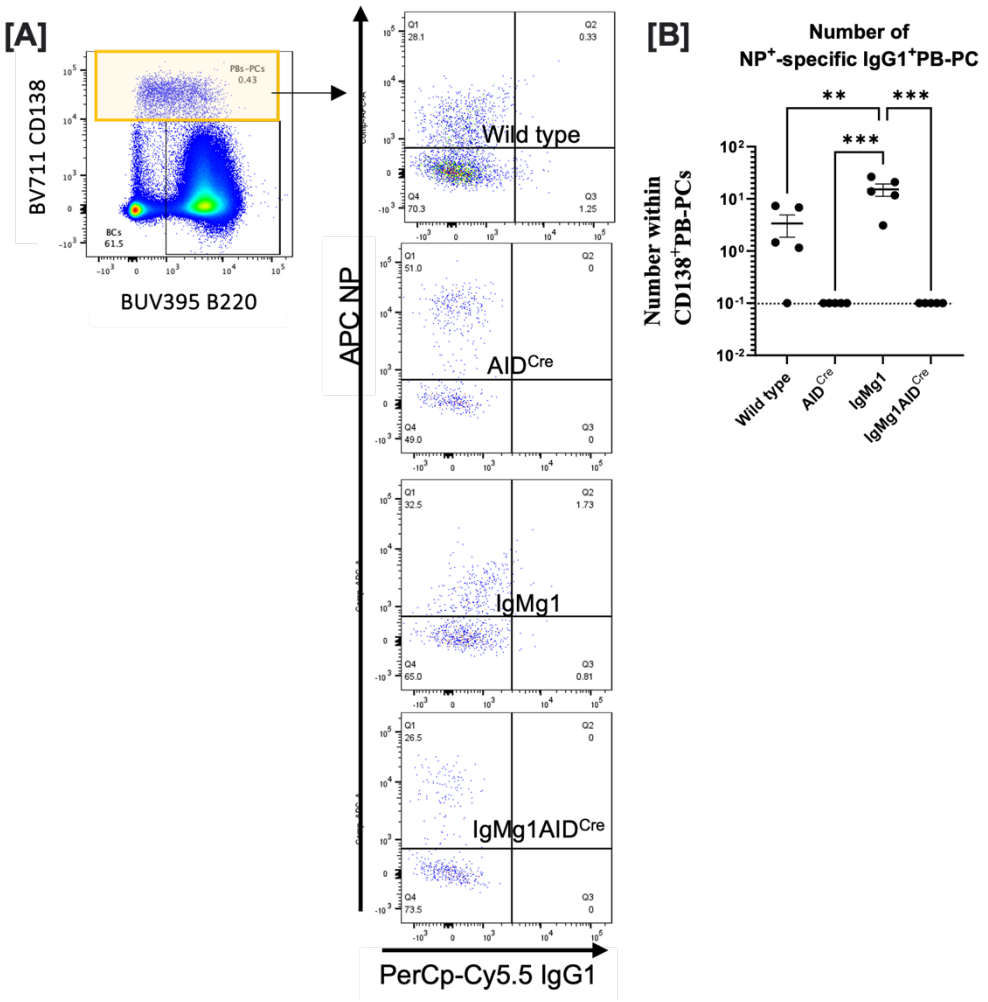


Figure 4.5. Analysis of the NP^{+}-specific IgG1^{+} CD138^{+} PB-PC response.

The experimental protocol is illustrated in Figure 4.2. **(A)** Representative flow cytometry plots of CD138^{+} PB-PC paired with NP and IgG1. **(B)** The number of NP^{+}-specific IgG1 PB-PC (mean ± SEM) within CD138^{+} PB-PC (wild type = 5, AID^{Cre} = 5, IgMg1 = 5, and IgMg1AID^{Cre} = 5). Data in (B) was derived from a single experiment, as CountBeads were accidentally used only in this experiment. Data points with zero detectable were plotted at the lower limit of detection (10^{-1}) to allow visualisation on a logarithmic scale. Each symbol represents one mouse. Statistical tests were performed using ordinary one-way ANOVA. * $p < 0.05$, ** $p < 0.01$, *** $p < 0.001$.

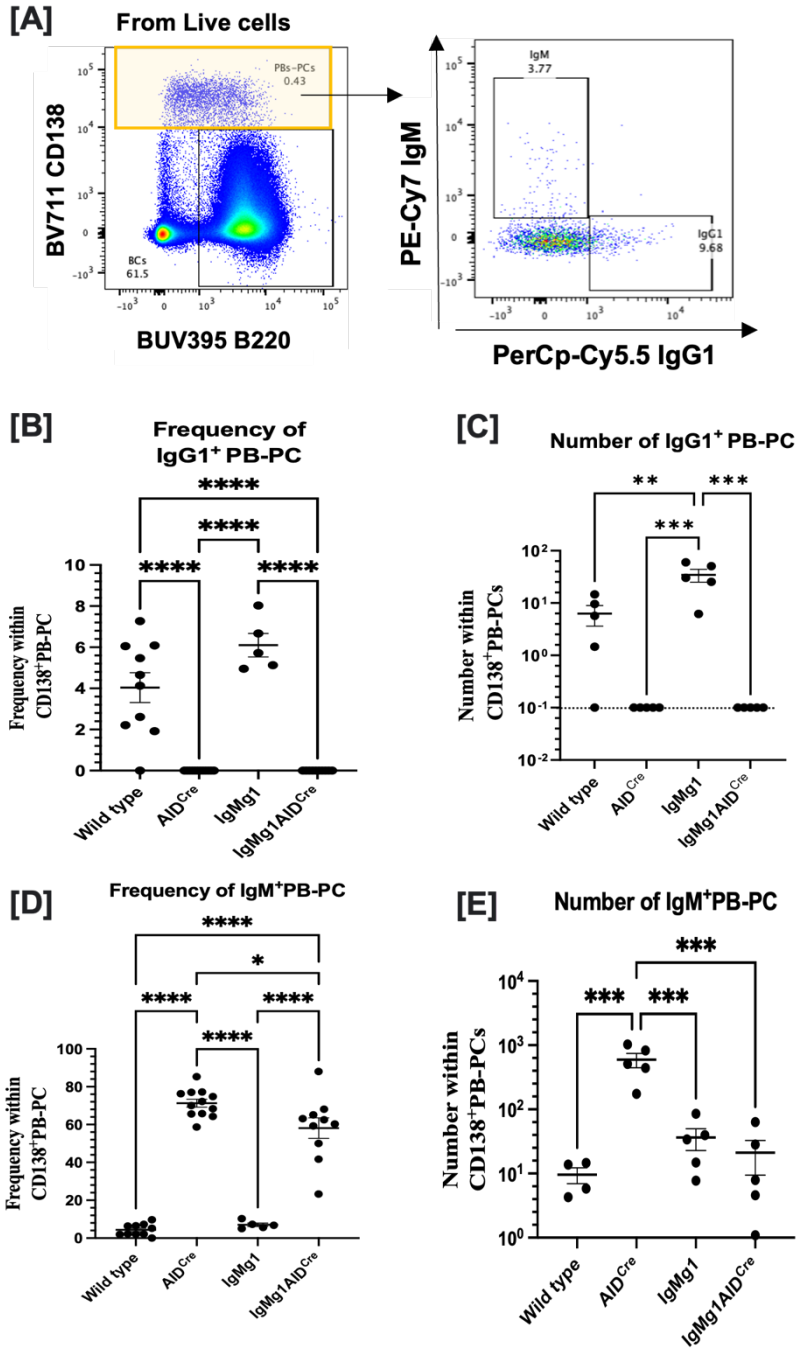


Figure 4.6. Analysis of IgG1$^+$ and IgM$^+$ CD138$^+$ PB-PC response.

The experimental protocol is illustrated in Figure 4.2. **(A)** Representative flow cytometry plots of CD138$^+$ PB-PC paired with IgM and IgG1. **(B)** The frequency of IgG1$^+$ CD138$^+$ PB-PC (mean ± SEM) within CD138$^+$ PB-PC, obtained from n=2 independent experiments (wild type = 10, AID^{Cre} = 12, IgMg1 = 5, and IgMg1AID^{Cre} = 10). **(C)** The number of IgG1$^+$ CD138$^+$ PB-PC (mean ± SEM) within CD138$^+$ PB-PC (wild type = 5, AID^{Cre} = 5, IgMg1 = 5, and IgMg1AID^{cre} = 5). Data points with zero detectable were plotted at the lower limit of detection (10^{-1}) to allow visualisation on a

logarithmic scale. **(D)** The frequency of IgM$^+$ CD138$^+$ PB-PC (mean ± SEM) within CD138$^+$ PB-PC, obtained from n=2 independent experiments (wild type = 10, AID^{Cre} = 12, IgMg1 = 5, and IgMg1AID^{Cre} = 10). **(E)** The number of IgM$^+$ CD138$^+$ PB-PC (mean ± SEM) within CD138$^+$ PB-PC (wild type = 5, AID^{Cre} = 5, IgMg1 = 5, and IgMg1AID^{Cre} = 5). Each symbol represents one mouse. Data in C and E were derived from a single experiment, as CountBeads were accidentally used only in this experiment. Samples with zero frequency were plotted at the lower limit of detection (10^{-1}) to allow visualisation on a logarithmic scale. Statistical tests were performed using ordinary one-way ANOVA. * $p < 0.05$, ** $p < 0.01$, *** $p < 0.001$, **** $p < 0.0001$.

The frequency and number of IgM$^+$ PB-PC in the AID^{Cre} mouse model were significantly expanded compared to wild-type and IgMg1 models, which is expected as PB-PC differentiation is restricted to the IgM isotype in the absence of AID activity. In IgMg1AID^{Cre} mice, the frequency and number of IgM$^+$ PB-PCs were dampened compared with the AID^{Cre} model (Figure 4.6D and E). The frequency of IgM$^+$ CD138$^+$ PB-PCs is almost 60% in the IgMg1AID^{Cre} model and about 70% in the AID^{Cre} (* $p < 0.05$) (Figure 4.6D and E). In contrast, the number of IgM$^+$ CD138$^+$ PB-PCs in the IgMg1AID^{Cre} model exhibited a reduction (*** $p < 0.001$) compared with the AID^{Cre} model but equivalence with wild-type and IgMg1 mice models. Overall, while both AID^{cre} mice and IgMg1 mice individually exhibit an increased PC output, IgMg1AID^{cre} displayed an impairment of the PC response at day 8 after primary immunisation with NP-KLH.

4.2.3. IgMg1AID^{Cre} impairs IgM$^+$ GC B cell recruitment.

GC reaction is shaped by a complex interplay of molecular and cellular factors. GC in the AID^{Cre} model are known to be considerably larger [81, 83]. IgG1$^+$-dominated GC B cells were found in the IgMg1 model [199, 200]. In the IgMg1AID^{Cre} model, we wanted

to examine how the IgMg1 allele modifies GC response when IgM cells cannot class switch and therefore continue to express the IgMg1 allele (Figure 4.7). Numbers of Fas^+ GC B cells in the IgMg1AID^{Cre} strain were similar to wild-type mice, highlighted by similar frequencies within total lymphocytes (Figure 4.7C) and $B220^+$ B cells (Figure 4.7D) and by the number of Fas^+ GC B cells (Figure 4.7E). The elevation of GC B cells in the AID^{Cre} model was expected, indicating a role for AID in constraining GC size by introducing somatic mutations that reduce antigen affinity or specificity, thereby limiting clonal persistence within the GC [202]. GC B cell size was reduced in the new transgenic IgMg1AID^{Cre} model. This suggests that the IgMg1 BCR induces weaker signalling or downstream GC-regulating molecules than when the GC B cells class switch to IgG.

Next, we examined how the IgMg1 allele modifies GC IgM-expressing B cells in the IgMg1AID^{Cre} model (Figure 4.8). First, as expected, AID^{Cre} B cells can only be IgM^+-expressing GC B cells. The quantification of IgM^+ GC B cells in IgMg1 mice showed a reduction compared to the quantification of $IgG1^+$ GC B cells, which is in line with results described previously by Hudson that $IgG1^+$ GC B cells are proportionally increased [200]. However, the frequency of IgM expression in the IgMg1AID^{Cre} model was higher than in the IgMg1 and wild-type models but lower than in the AID^{Cre} model (Figure 4.8C). In contrast, the number of IgM-expressing cells in the IgMg1AID^{Cre} model showed no significant difference compared to the wild-type and IgMg1 models (Figure 4.8D). Although the absence of CSR in the AID^{Cre} background, IgM^+ GC B cells in the IgMg1AID^{Cre} model displayed reduced participation, as their numbers were not increased relative to wild-type mice (Figure 4.8E). Consistent with this, Hudson reported that the apparent shift toward $IgG1^+$ GC B cells in the IgMg1 model is not

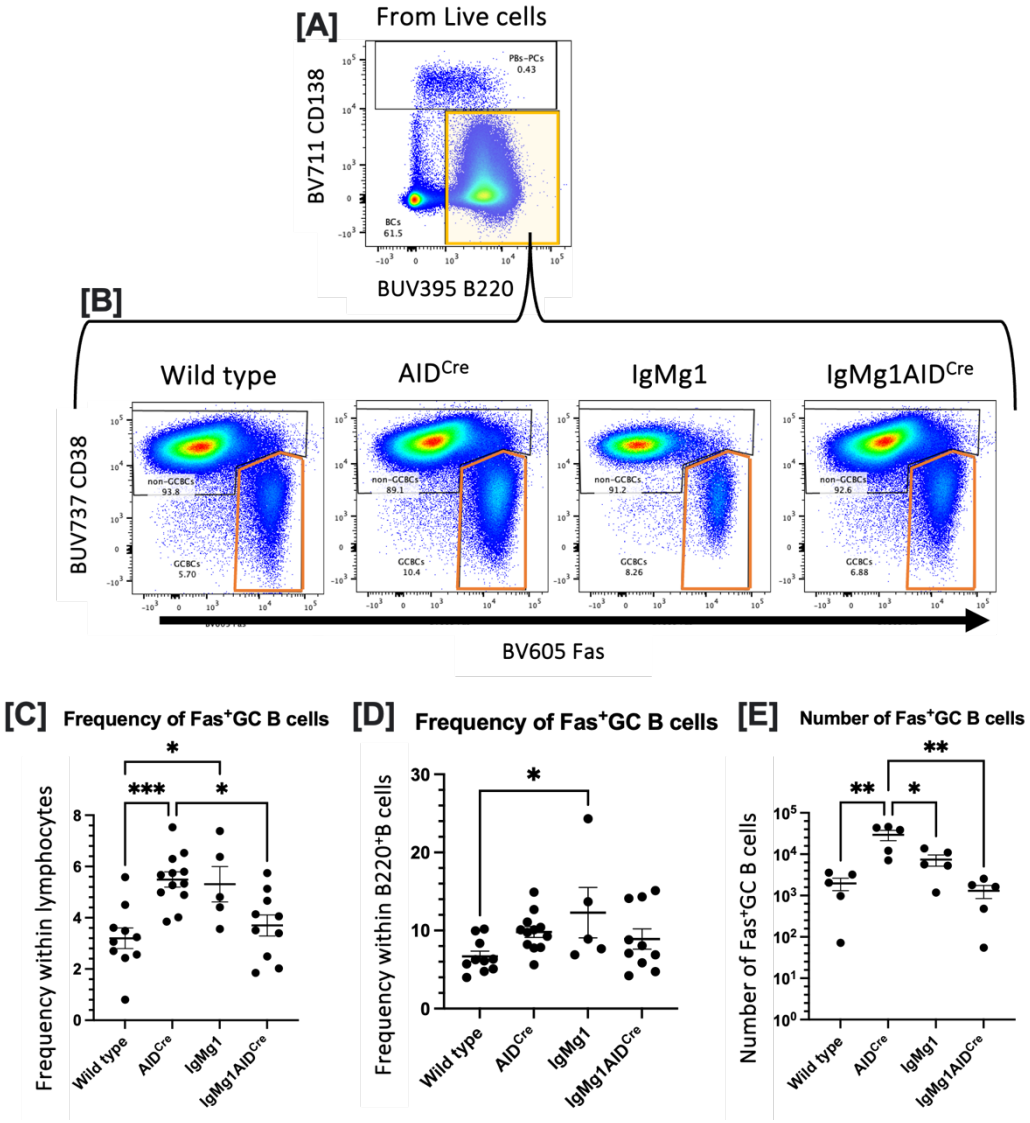


Figure 4.7. Analysis of the Fas⁺ GC B cell response.

The experimental protocol is illustrated in Figure 4.2. **(A)** Representative flow cytometry plots of B220⁺ B cells. **(B)** Representative flow cytometry plots of Fas⁺ GC B cells in each mouse model. **(C)** The frequency of Fas⁺ GC B cells (mean ± SEM) within lymphocytes, obtained from n=2 independent experiments (wild type = 10, AID^{Cre} = 12, IgMg1 = 5, and $IgMg1AID^{cre}$ = 10). **(D)** The frequency of Fas⁺ GC B cells (mean ± SEM) within B220⁺ B cells, obtained from n=2 independent experiments (wild type = 10, AID^{Cre} = 12, IgMg1 = 5, and $IgMg1AID^{cre}$ = 10). **(E)** The number of Fas⁺ GC B cells (mean ± SEM) (wild type = 5, AID^{Cre} = 5, IgMg1 = 5, and $IgMg1AID^{cre}$ = 5). Data in (C) and (D) were derived from two independent experiments. Data in (E) a single experiment, as CountBeads were accidentally used only in this experiment. Each symbol represents one mouse. Statistical tests were performed using ordinary one-way ANOVA. * $p < 0.05$, ** $p < 0.01$, *** $p < 0.001$.

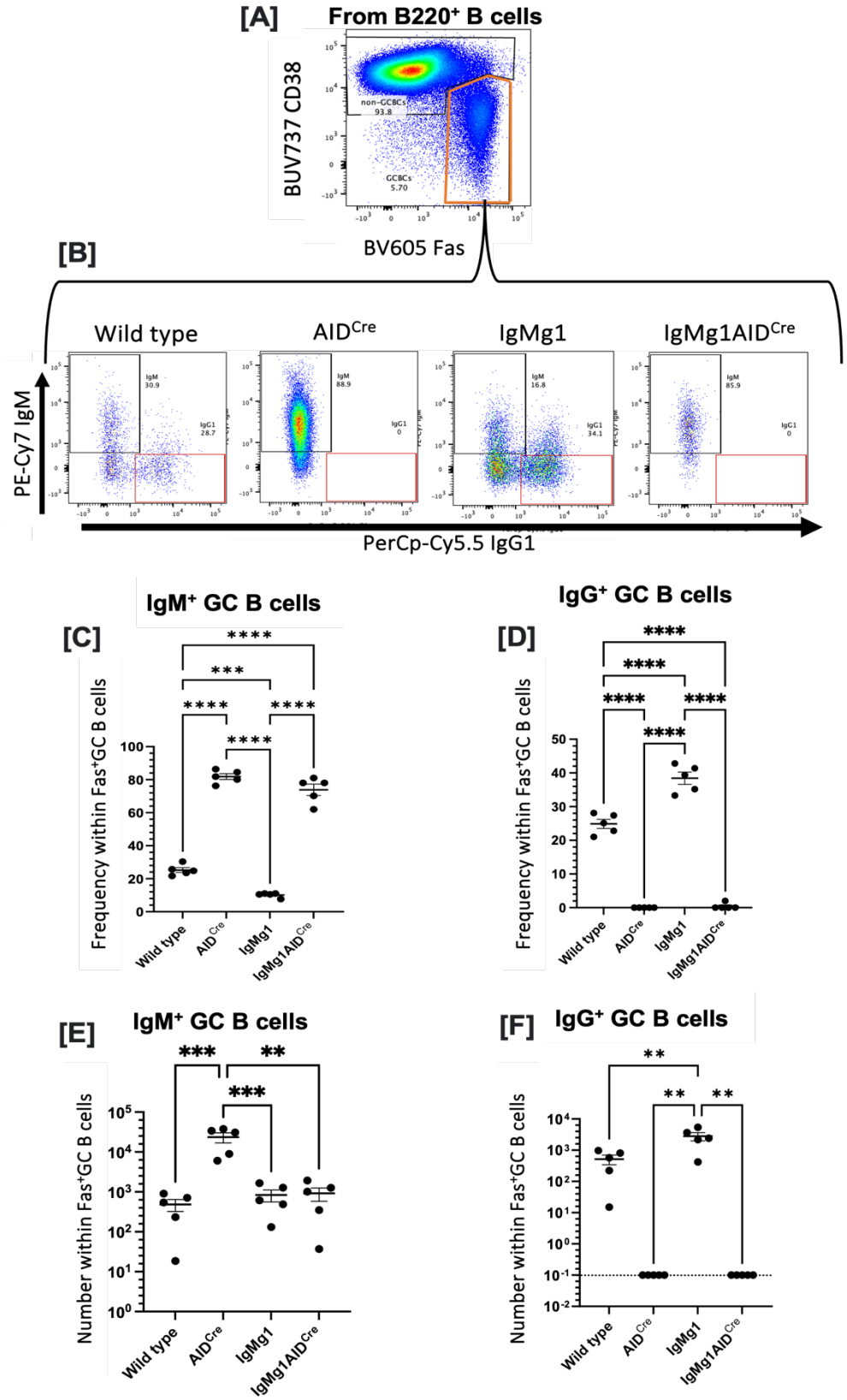


Figure 4.8. Analysis of IgG1$^+$ and IgM$^+$ B220$^+$ Fas$^+$ GC B cell response.

The experimental protocol is illustrated in Figure 4.2. **(A)** Representative plots of Fas^+ GC B cells. **(B)** Representative plots of $IgG1^+$ and IgM^+ gated from Fas^+ GC B cells. **(C)** The frequency of IgM^+ in $B220^+$ Fas^+ GC B cells (mean ± SEM) (wild type = 5, AID^{Cre} = 5, IgMg1 = 5, and $IgMg1AID^{cre}$ = 5). **(D)** The frequency of $IgG1^+$ in $B220^+$ Fas^+ GC B cells (mean ± SEM) (wild type = 5, AID^{Cre} = 5, IgMg1 = 5, and $IgMg1AID^{cre}$ = 5). The one detected value did not represent a genuine signal. **(E)** The number of IgM^+ within Fas^+ GC B cells (mean ± SEM) (wild type = 5, AID^{Cre} = 5, IgMg1 = 5, and $IgMg1AID^{Cre}$ = 5). **(F)** The number of $IgG1^+$ within Fas^+ GC B cells (mean ± SEM) (wild type = 5, AID^{Cre} = 5, IgMg1 = 5, and $IgMg1AID^{Cre}$ = 5). Data points with zero detectable were plotted at the lower limit of detection (10^{-1}) to allow visualisation on a logarithmic scale. Each symbol represents one mouse. Data were derived from a single experiment. Statistical tests were performed using ordinary one-way ANOVA. ** $p < 0.01$, *** $p < 0.001$, **** $p < 0.0001$.

driven by increased $IgG1^+$ switching but instead reflects reduced participation and survival of IgM^+ GC B cells, as their numbers were likewise not increased relative to those of wild-type mice [200]. Together, these findings indicate that altered BCR signalling in the IgMg1 background limits IgM^+ B cell participation in GCs independently of CSR. Overall, the $IgMg1AID^{Cre}$ model showed a greater reduction in the total number of IgM GC B cells than the AID^{Cre} model, indicating that the IgMg1 transgenic BCR may impose additional constraints on GC entry and/or survival when AID protein is absent.

The frequency and the number of NP-binding GC B cells within the GC compartment were increased in IgMg1 mice compared to wild-type in response to NP-CGG and NP-KLH [199, 200]. Therefore, we wanted to assess the involvement of NP-specific Fas^+ $B220^+$ GC B cells in the $IgMg1AID^{Cre}$ model (Figure 4.9). The frequency of NP-specific GC B cells within total GC B cells fell within a similar range without significant variation (Figure 4.9C). The number of NP-specific GC B cells in $IgMg1AID^{Cre}$ was comparable to wild-type mice but significantly lower than AID^{Cre} mice, decreasing from ~6,000 to

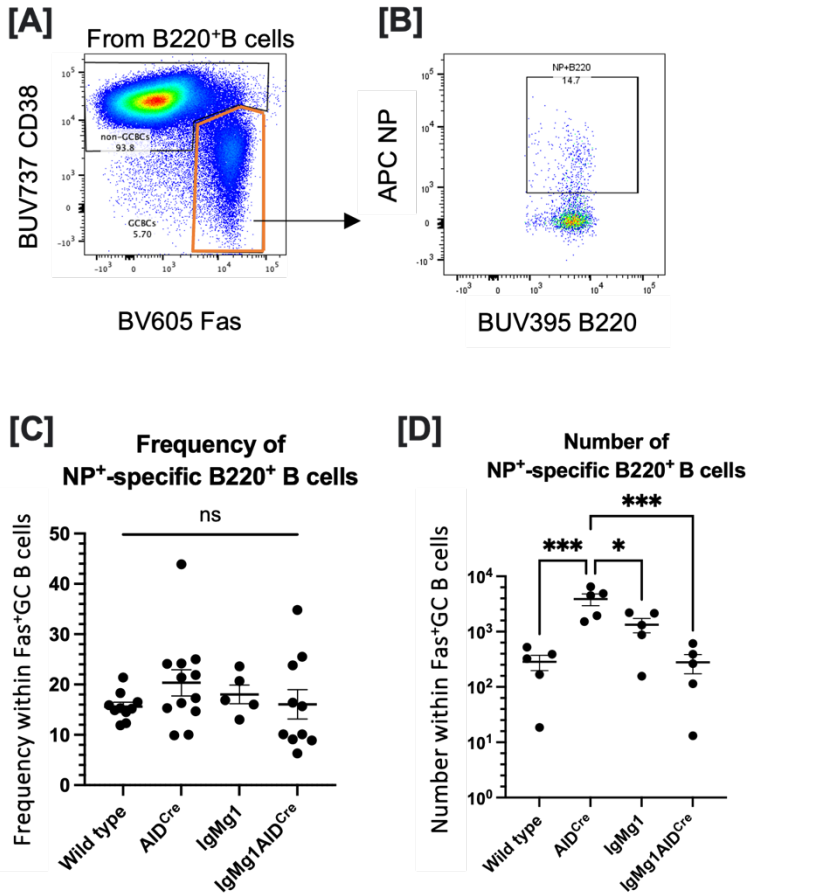


Figure 4.9. Analysis of the NP$^+$-specific B220$^+$ GC B cell response.

The experimental protocol is illustrated in Figure 4.2. **(A)** Representative flow cytometry plots of Fas$^+$ GC B cells paired with NP and B220. **(B)** Representative flow cytometry plots of NP$^+$-specific B220$^+$ GC B cells gated from Fas$^+$ GC B cells. **(C)** The frequency of NP$^+$-specific B220$^+$ B cells (mean ± SEM) within Fas$^+$ GC B cells. Data were obtained from n=2 independent experiments (wild type = 10, AID^{Cre} = 12, IgMg1 = 5, and IgMg1AID^{Cre} = 10). **(D)** The number of NP$^+$-specific B220$^+$ B cells (mean ± SEM) within Fas$^+$ GC B cells. Data were obtained from one single experiment (wild type = 5, AID^{Cre} = 5, IgMg1 = 5, and IgMg1AID^{Cre} = 5), as CountBeads were accidentally used only in this experiment. Each symbol represents one mouse. Statistical tests were performed using ordinary one-way ANOVA. n.s. $p > 0.05$, * $p < 0.05$, *** $p < 0.001$.

500 cells (Figure 4.9D). Notably, NP-specific GC B cell numbers in the IgMg1AID^{Cre} model were also reduced relative to the IgMg1 model, decreasing from ~1,500 to 500 cells. Together, these data indicate that the number of NP-specific GC B cells observed in the IgMg1 model is not maintained in the IgMg1AID^{Cre} model, reflecting impaired GC formation. Regarding NP-specific IgG1^{+} GC B cells in IgMg1 mice (Figure 4.10), they showed a higher number compared to wild-type (** $p < 0.01$), consistent with a previous finding [200]. A caveat of the detected IgG1 events in both AID^{Cre} and IgMg1AID^{Cre} mice is that they likely reflect non-specific antibody binding.

Following this, we tested the GC dynamics in IgMg1AID^{Cre} mice. GC B cells within the DZ and the LZ can be identified by staining for Fas^{+} GC B cells and CXCR4^{+} and CD86^{+} [177]. DZ B cells were defined as CXCR4^{hi} CD86^{lo} cells, whereas LZ B cells were defined as CXCR4^{lo} CD86^{hi} cells. Gates were applied according to the distribution of CXCR4 and CD86 expression using FMO. The frequencies of GCDZ and GCLZ B cells in the IgMg1 were similar to those in wild-type mice, with a greater proportion positioned in the DZ (Figure 4.11C), consistent with the previous findings [200]. AID^{Cre} mice showed a tendency to have a more equal distribution between GC zones. However, the IgMg1AID^{Cre} mice showed a GC zone distribution that appeared intermediate between the wild-type / IgMg1 and AID^{Cre} phenotypes, with a relatively increased proportion of GCDZ B cells and decreased proportion of GCLZ B cells. Analysis of the number of GC B cells within each zone revealed a distribution similar to that of wild-type mice (Figure 4.11D). Overall, the data suggest that altered BCR signalling in the IgMg1AID^{Cre} mice results in a reduction or survival in GC B cell recruitment compared to the AID^{Cre} model at day 8 after primary immunisation with NP-KLH.

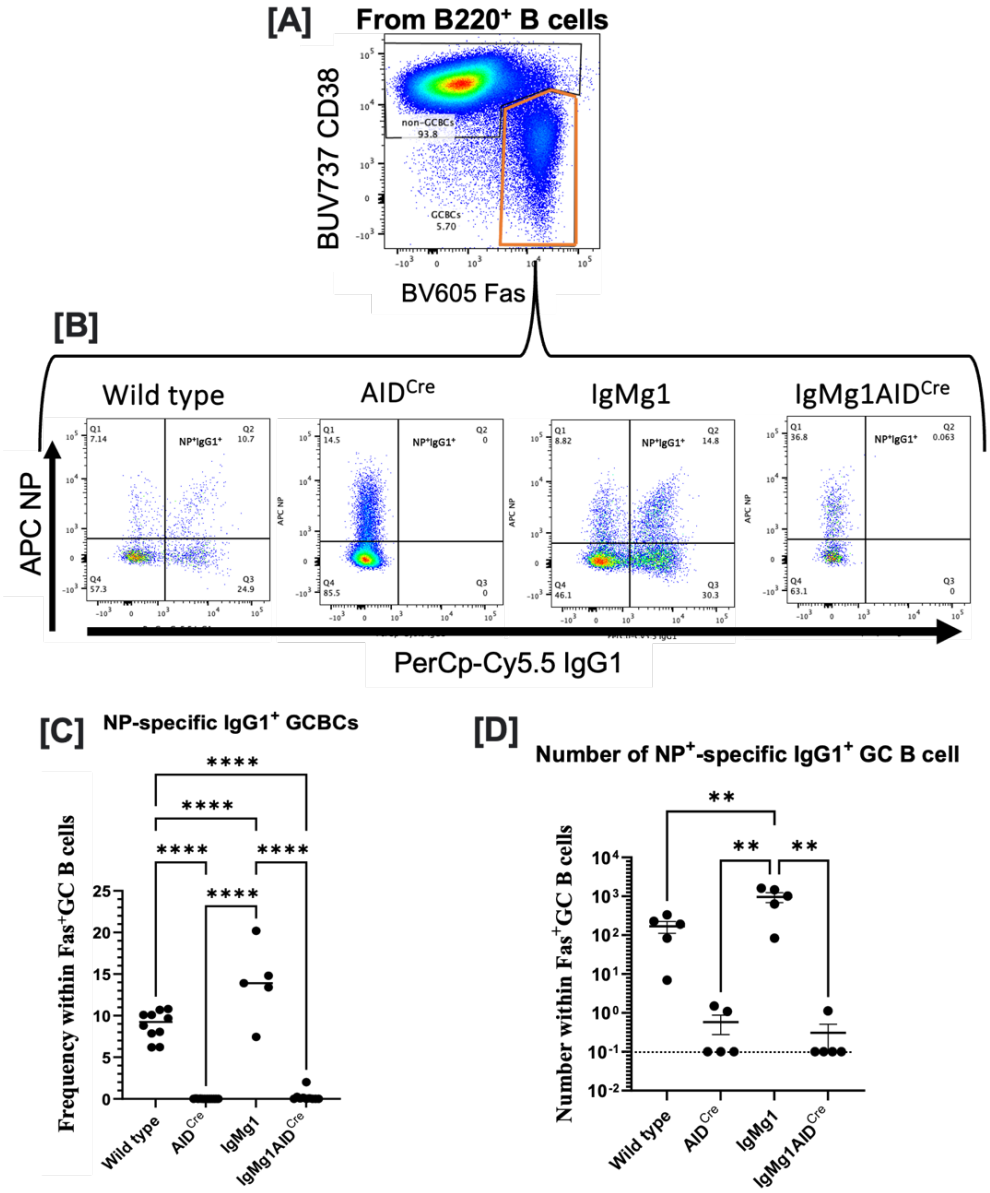


Figure 4.10. Analysis of the NP⁺-specific IgG1⁺ GC B cells response.

The experimental protocol is illustrated in Figure 4.2. **(A)** Representative flow cytometry plots of Fas⁺ GC B cells. **(B)** Representative flow cytometry plots of NP-specific IgG1⁺ PB-PC gated from Fas⁺ GC B cells. **(C)** The Frequency of NP-specific IgG1⁺ GC B cells (mean ± SEM) within Fas⁺ GC B cells, obtained from n=2 independent experiments (wild type = 10, AID^{Cre} = 12, IgMg1 = 5, and IgMg1AID^{Cre} = 10). **(D)** The number of NP-specific IgG1⁺ GC B cells (mean ± SEM) within Fas⁺ GC B cells, obtained from a single experiment (wild type = 5, AID^{Cre} = 5, IgMg1 = 5, and IgMg1AID^{Cre} = 5), as CountBeads were accidentally used only in this experiment. Each symbol represents one mouse. Samples with zero frequency were plotted at the lower limit of detection (10^{-1}) to allow visualisation on a logarithmic scale. Statistical tests were performed using ordinary one-way ANOVA. ** $p < 0.01$, **** $p < 0.0001$.

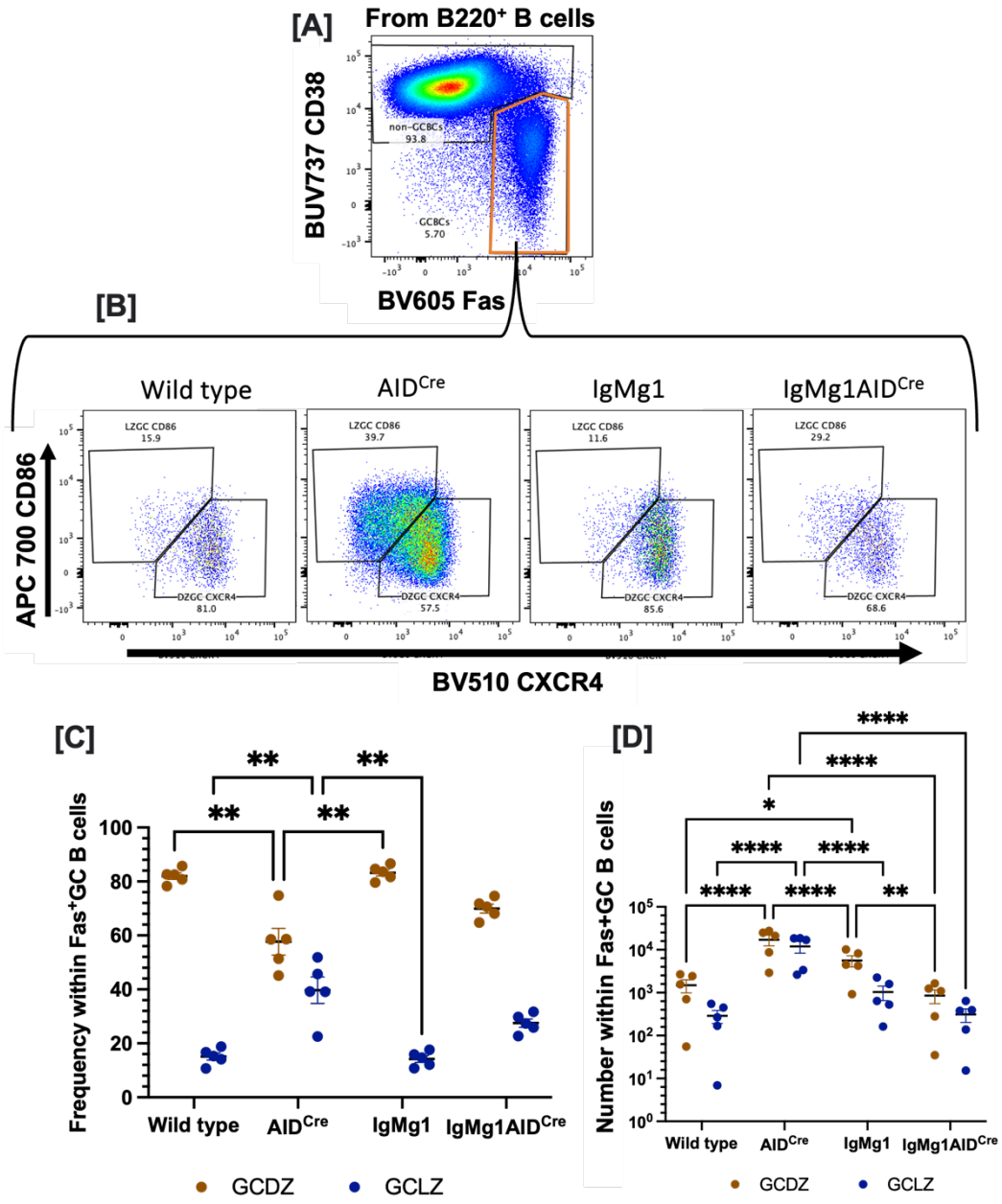


Figure 4.11. Analysis of the GC zones' response.

The experimental protocol is illustrated in Figure 4.2. **(A)** Representative flow cytometry plots of Fas$^+$ GC B cells. **(B)** Representative flow cytometry plots of CXCR4$^+$ GCDZ B cells and CD86$^+$ GCLZ B cells gated from Fas$^+$ GC B cells. **(C)** The frequency of CXCR4$^+$ GCDZ B cells and CD86$^+$ GCLZ B cells PC (mean ± SEM) within Fas$^+$ GC B cells. **(D)** The number of CXCR4$^+$ GCDZ B cells and CD86$^+$ GCLZ B cells (mean ± SEM) within Fas$^+$ GC B cells. Data were obtained from a single experiment (wild type = 5, AID^{Cre} = 5, IgMg1 = 5, and IgMg1AID^{Cre} = 5), as the second experiment failed to yield reliable GC zones staining. Each symbol represents one mouse. Statistical tests were performed using two-way ANOVA. * $p < 0.05$, ** $p < 0.01$, **** $p < 0.0001$.

4.2.4. IgMg1 BCR in the IgMg1AID^{Cre} model contributes to the regulation of IgM$^+$ CD38$^+$ B cells.

The CD38 marker was used to distinguish GC from non-GC B cells in IgMg1 mice, as CD38 is downregulated in GC B cells [172]. This was then further analysed for the number and the frequency of IgM$^+$ and IgG1$^+$ expressing CD38$^+$ non-GC B cells (Figure 4.12A-E).

The detectable frequency and number of IgG1 in AID^{Cre} and IgMg1AID^{Cre} CD38$^+$ non-GC B cells may represent either non-specific binding or background noise from the acquisition instrument, as IgG1 expression is not expected in the absence of AID protein (Figure 4.12B and C). The IgMg1 model displayed a high frequency and number of IgG1$^+$ B cells compared to the wild-type. Moreover, the IgMg1 model showed a significant reduction in the frequency of IgM$^+$ B cells, accounting for **** $p < 0.0001$ compared to AID^{Cre} and wild-type models and ** $p < 0.01$ compared to the IgMg1AID^{Cre} model (Figure 4.12D). Thus, the characteristic of the IgMg1 model is consistent with the ability of the IgMg1 BCR to allow escape from anergy through class switching [200]. In the IgMg1AID^{Cre} model, the frequency of IgM$^+$ B cells was significantly reduced relative to the AID^{Cre} and wild-type models—consistent with the impaired PC and GC responses—but significantly increased compared with the IgMg1 model (Figure 4.12D). However, the number of IgM$^+$ B cells displayed a significant decrease compared to those observed in the AID^{Cre} model and those observed in the wild-type and IgMg1 model, although it was not statistically significant (Figure 4.12E). Together, the data indicate that BCR signalling of IgMg1 BCR in the IgMg1AID^{Cre} model contributes to the regulation of IgM$^+$ CD38$^+$ B cells.

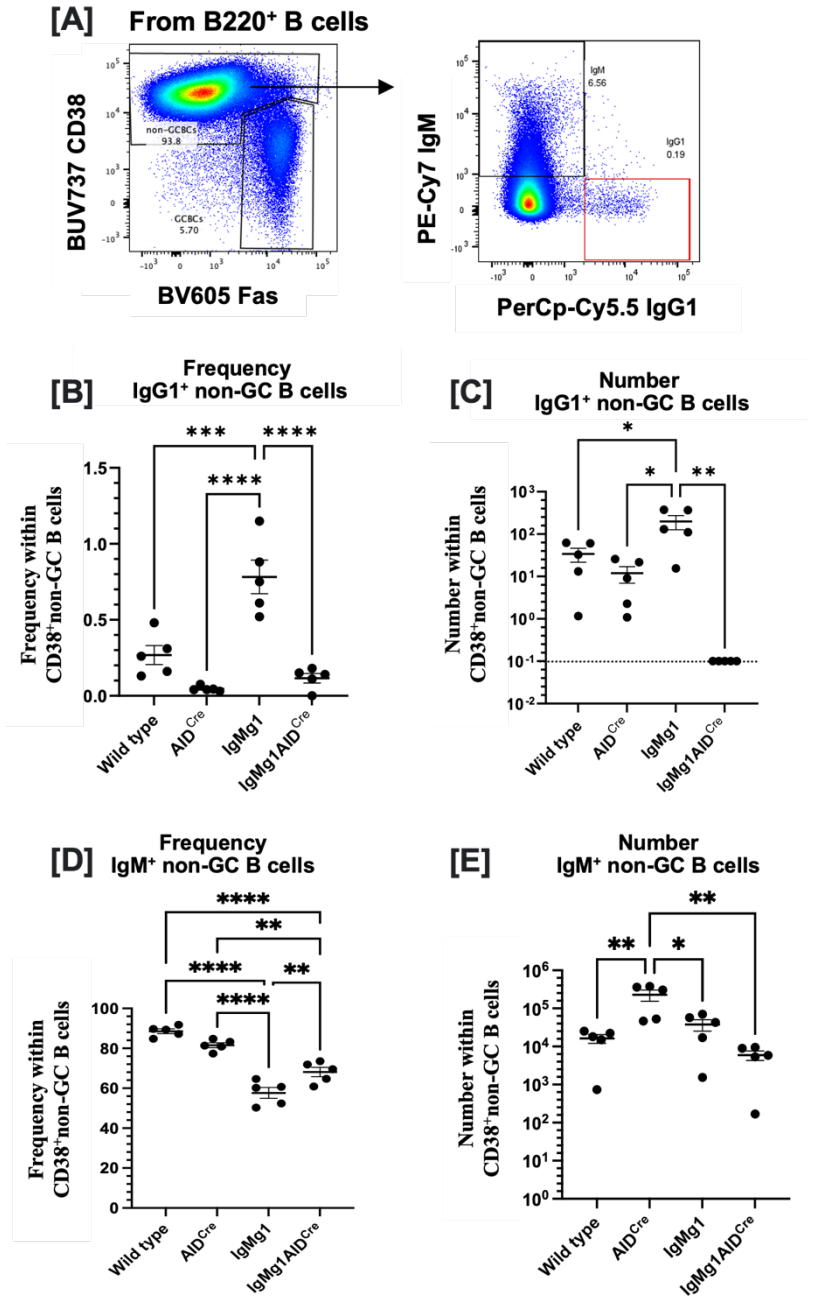


Figure 4.12. Analysis of IgG1$^+$ and IgM$^+$ CD38$^+$ non-GC B cell response.

The experimental protocol is illustrated in Figure 4.2. **(A)** Representative flow cytometry plots of CD38$^+$ non-GC B cells were gated from B220$^+$ B cells and further gated on IgM and IgG1 expression. **(B)** The frequency of IgG1$^+$-expressing CD38$^+$ non-GC B cells (mean ± SEM) within CD38$^+$ non-GC B cells. **(C)** The number of IgG1$^+$-expressing CD38$^+$ non-GC B cells (mean ± SEM) within CD38$^+$ non-GC B cells. Data points with zero detectable were plotted at the lower limit of detection (10^{-1}) to allow visualisation on a logarithmic scale. The detected IgG1 data in the **(B)** IgMg1AID^{Cre} and **(B and C)** AID^{Cre} models may not represent genuine signals. (D) The frequency of IgG1$^+$-expressing CD38$^+$ non-GC B cells (mean ± SEM) within CD38$^+$ non-GC B cells.

(E) The number of IgG1$^+$-expressing CD38$^+$ non-GC B cells (mean ± SEM) within CD38$^+$ non-GC B cells. Data were obtained from a single experiment (wild type = 5, AID^{Cre} = 5, IgMg1 = 5, and IgMg1AID^{cre} = 5). Each symbol represents one mouse. Statistical tests were performed using ordinary one-way ANOVA. * $p < 0.05$, ** $p < 0.01$, *** $p < 0.001$, **** $p < 0.0001$.

A caveat of this investigation is that IgM and IgG1 staining in the second experiment was suboptimal and therefore excluded from the analysis, limiting the assessment to a single experimental replicate.

The NP-specific non-GC B cells were quantified as NP-specific CD38$^+$ Fas^{lo} B cells and NP-specific IgG1$^+$ CD38$^+$ Fas^{lo} B cells (Figure 4.13A-C). IgMg1AID^{Cre} mice showed no significant difference in the frequency of NP-specific CD38$^+$ non-GC B cells compared with the other mouse models (Figure 4.13D). However, the number of NP-specific CD38$^+$ non-GC B cells was significantly reduced in IgMg1AID^{Cre} relative to the AID^{Cre} (Figure 4.13E). The number of NP-specific CD38$^+$ non-GC B cells expressing IgG1$^+$ in IgMg1AID^{Cre} mice was detected in only two out of five analysed samples, compared with AID^{Cre} mice, where four out of five analysed samples were positive for IgG1$^+$ expression. As CSR cannot occur in the absence of functional AID, these events are unexpected and likely reflect non-specific staining or background signal rather than genuine IgG1 expression (Figure 4.13F). Overall, these data suggest that at day 8 after primary immunisation with NP-KLH, CD38$^+$ non-GC B cell response to model antigen NP was strongly impaired in IgMg1AID^{Cre} mice compared with AID^{Cre} mice. NP-specific CD38$^+$ non-GC B cells may be GC-derived memory B cells or include activated NP-specific follicular B cells that retain the potential to enter GCs, differentiate into PB-PC, or give rise to GC-independent memory B cells.

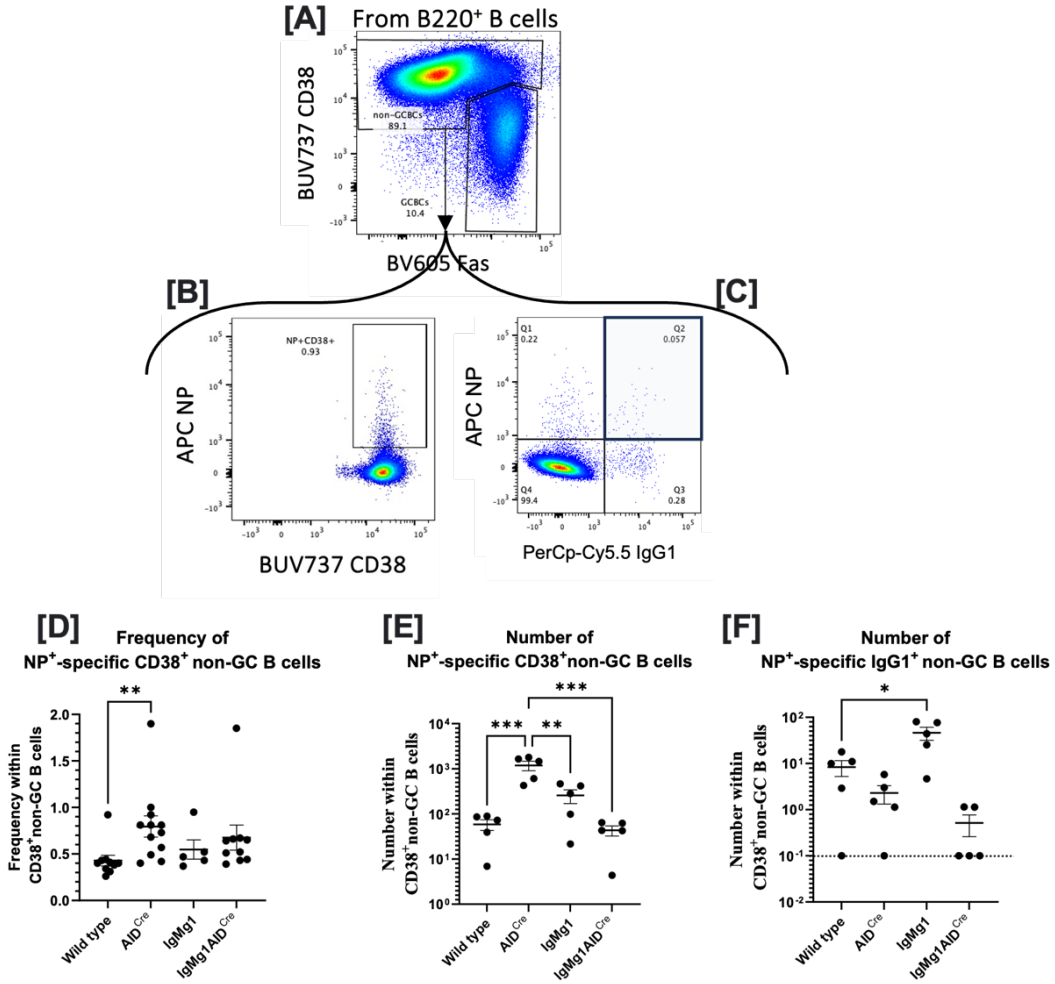


Figure 4.13. Analysis of NP$^+$-specific CD38$^+$ non-GC B cell response.

The experimental protocol is illustrated in Figure 4.2. **(A)** Representative flow cytometry plots of CD38$^+$ non-GC B cells. **(B)** Representative flow cytometry plots of NP$^+$-specific CD38$^+$ non-GC B cells derived from the IgMg1 model. **(C)** A typical example of flow cytometry plots of NP$^+$-specific IgG1$^+$ expression within CD38$^+$ non-GC B cells derived from the IgMg1 model. **(D)** The frequency of NP$^+$-specific CD38$^+$ non-GC B cells (mean ± SEM) within CD38$^+$ non-GC B cells obtained from n=2 independent experiments (wild type = 10, AID^{Cre} = 12, IgMg1 = 5, and IgMg1AID^{cre} = 10). **(E)** The number of NP$^+$-specific CD38$^+$ non-GC B cells (mean ± SEM) within CD38$^+$ non-GC B cells obtained from a single experiment (wild type = 5, AID^{Cre} = 5, and IgMg1AID^{Cre} = 5), as CountBeads were accidentally used only in this experiment. **(F)** The number of NP$^+$-specific CD38$^+$ non-GC B cells that expressed IgG1$^+$ (mean ± SEM) within CD38$^+$ non-GC B cells obtained from a single experiment (wild type = 5, AID^{Cre} = 5, and IgMg1AID^{Cre} = 5), as CountBeads were accidentally used only in this experiment. Data points with zero detectable were plotted at the lower limit of detection (10^{-1}) to allow visualisation on a logarithmic scale. The data points in the AID^{Cre} and IgMg1AID^{Cre} models may not genuine responses. Each symbol represents one mouse.

Statistical tests were performed using ordinary one-way ANOVA. * $p < 0.05$, ** $p < 0.01$, *** $p < 0.001$.

4.2.5. Tfh cells are reduced in the IgMg1AID^{Cre} model.

IgMg1 mice exhibited increased Tfh cell differentiation during the primary response to NP-KLH at day 8 [200]. Preliminary data from our group indicate that there is no significant difference in Tfh cell responses between AID^{Cre} mice and wild-type mice (unpublished thesis data). Here, we wanted to examine how the IgMg1 allele modifies Tfh cell differentiation in the IgMg1AID^{Cre} model. Tfh cells are identified as CD4$^+$ CD62L$^-$ CD44$^+$ CXCR5$^+$ PD-1$^+$ (Figure 4.14). The number of CD4$^+$ T cells was significantly reduced in the IgMg1AID^{Cre} model compared with the AID^{Cre} model (*** $p < 0.001$; Figure 4.14B) and showed a trend toward reduction relative to the IgMg1 and wild-type models, although this difference did not reach statistical significance. The number of CD62L$^-$ CD44$^+$ activated T cells was significantly reduced in IgMg1AID^{Cre} mice compared with AID^{Cre} mice (** $p < 0.01$; Figure 4.14C) and was also lower than in the IgMg1 and wild-type models, although these differences did not reach statistical significance. In contrast, the frequency of CD44$^+$ activated T cells within CD4$^+$ T cells accounted for ~15.4% in the IgMg1AID^{Cre} model, compared with ~14.1% in the AID^{Cre} model and ~30.7% in the IgMg1 model.

Tfh cells were identified based on high co-expression of CXCR5 and PD-1, consistent with what was previously established by Moriyama et. al. (2014) [87]. The frequency of CXCR5$^+$ PD-1$^+$ Tfh cells within CD62L$^-$ CD44$^+$ activated T cells (Figure 4.15C) showed a significant decrease of 12% in the IgMg1AID^{Cre} model compared with the

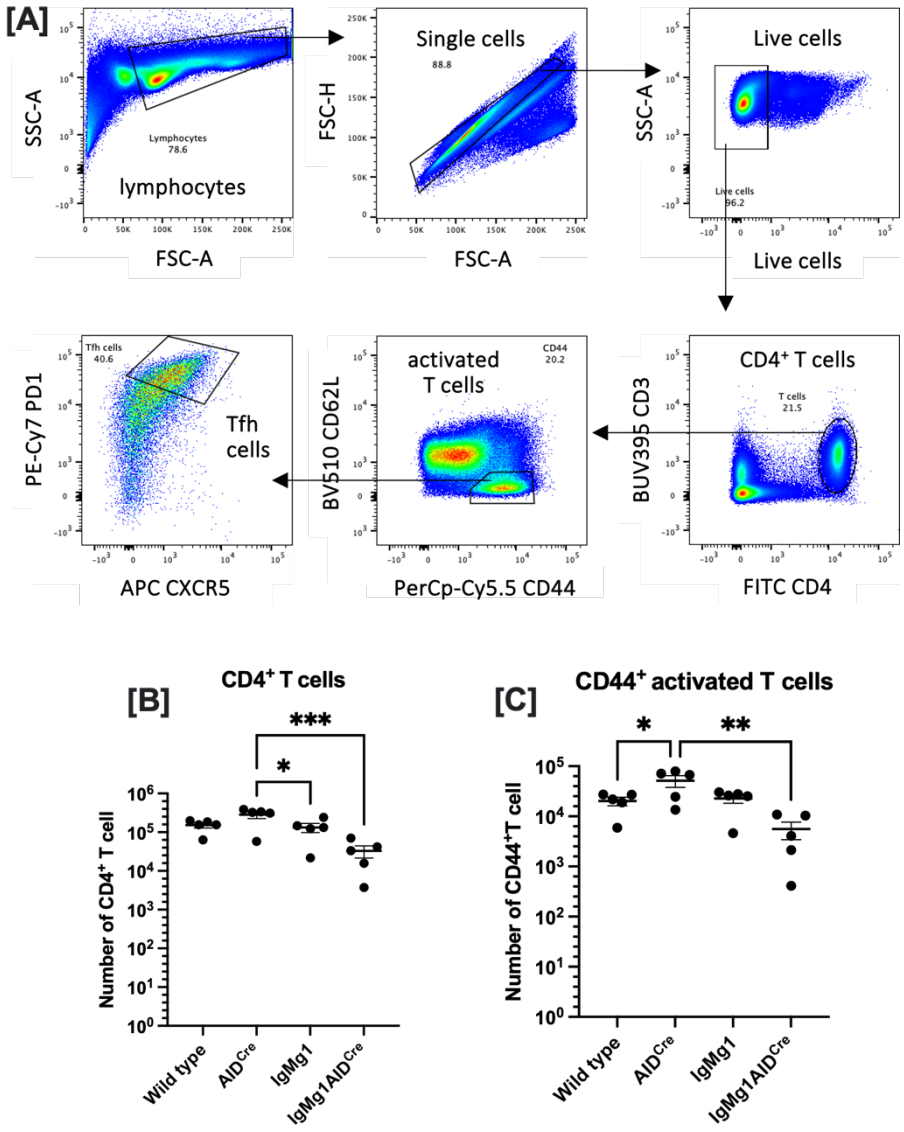


Figure 4.14. Analysis of CD44⁺ T cell response.

The experimental protocol is illustrated in Figure 4.2. **(A)** Representative flow cytometry gating strategy plots of splenocytes, showing gating on CD4⁺ T cells followed by gating on CD44⁺ activated T cells. **(B)** The number of CD4⁺ T cells (mean ± SEM). **(C)** The number of CD44⁺ activated T cells (mean ± SEM). Data obtained from a single experiment (wild type = 5, AID^{Cre} = 5, IgMg1 = 5, and $IgMg1AID^{cre}$ = 5), as CountBeads were accidentally used only in this experiment. Each symbol represents one mouse. Statistical tests were performed using ordinary one-way ANOVA. * $p < 0.05$, ** $p < 0.01$, *** $p < 0.001$.

IgMg1 model. However, the number of CXCR5$^+$ PD-1$^+$ Tfh cells (Figure 4.15D) showed only a significant decrease in the IgMg1AID^{Cre} model compared with AID^{Cre} mice, representing an ~10-fold reduction. The reduction of Tfh cell response in IgMg1AID^{Cre} mice was ~5-fold compared to IgMg1 and wild-type mice, although it was not statistically significant (Figure 4.15D). The frequency of CXCR5$^+$ PD-1$^+$ Tfh cells within all CD4$^+$ T cells decreased significantly in the IgMg1AID^{Cre} model compared with those in the IgMg1 model (** $p < 0.01$).

An increase in Tfh cells was observed in IgMg1 mice, which may reflect altered interactions between GC B cells and T cells, potentially creating a microenvironment that favours Tfh differentiation and expansion [200]. Combining the IgMg1 modification with AID^{Cre}, which stops B cells from switching away from the IgMg1 B cell receptor (and also inhibits affinity maturation), shows that the increased Tfh cell differentiation is lost if class switching is inhibited. This may indicate that Tfh differentiation is affected by the IgMg1 BCR, maybe due to changes in BCR signalling or the amount of antigen presentation of GC B cells to Tfh cells.

Although the frequencies of Tfh cells within T cells change substantially, the reduction of Tfh cell number may also partly reflect the substantially decreased GC B cell numbers in this model, as the IgMg1AID^{Cre} model exhibits markedly fewer GC B cells compared with both AID^{Cre} and IgMg1 models (Figure 4.7E).

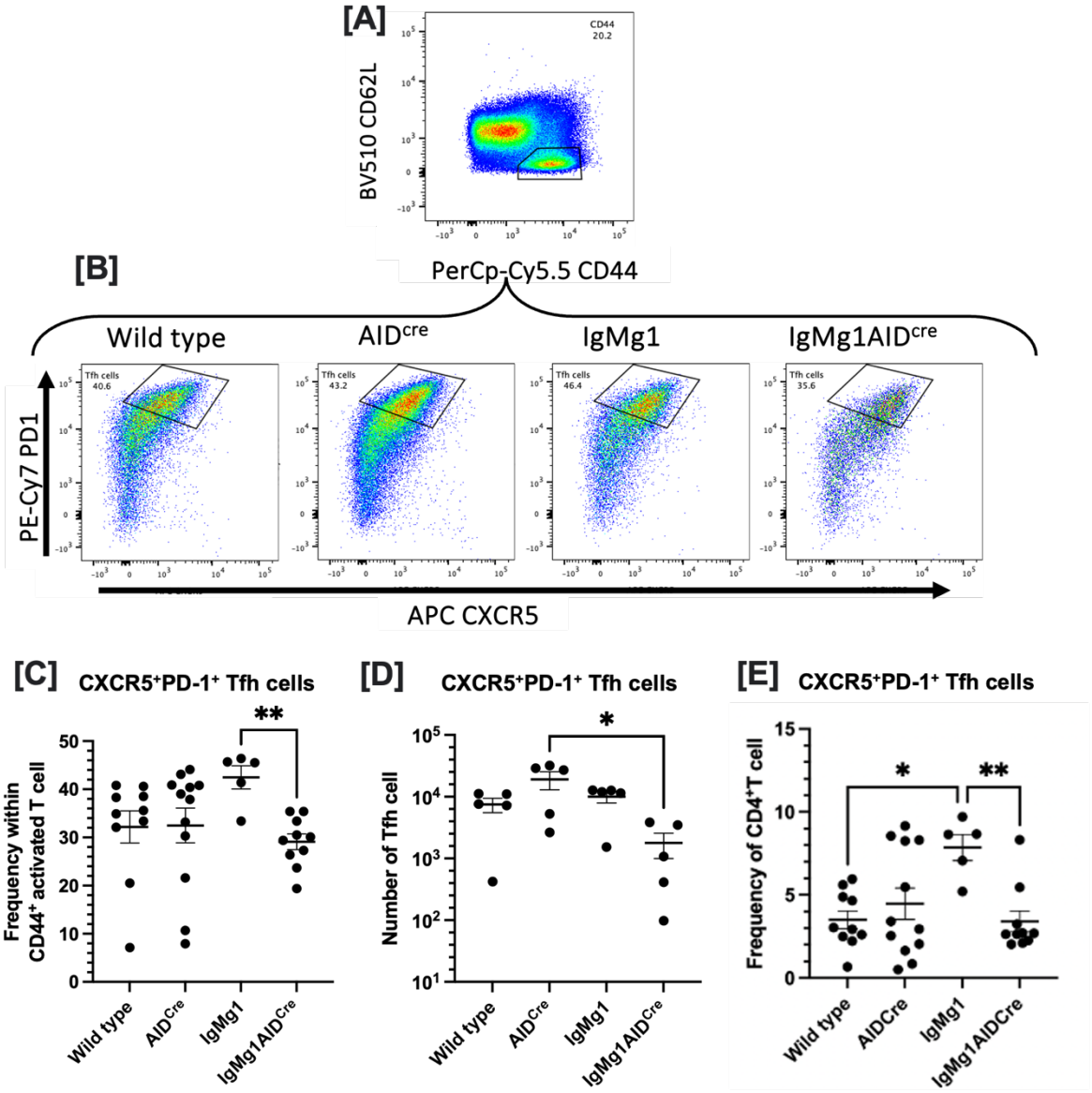


Figure 4.15. Analysis of CXCR5⁺ PD-1⁺ Tfh cells response.
The experimental protocol is illustrated in Figure 4.2. **(A)** Representative flow cytometry plots of CD44⁺ activated T cells. **(B)** Representative flow cytometry plots of CXCR5⁺ PD-1⁺ Tfh cells in each mouse model. **(C)** The frequency of CXCR5⁺ PD-1⁺ Tfh cells (mean ± SEM) within CD44⁺ activated T cells obtained from n=2 independent experiments (wild type = 10, AID^{Cre} = 12, IgMg1 = 5, and IgMg1AID^{cre} = 10). **(D)** The number of CXCR5⁺ PD-1⁺ Tfh cells (mean ± SEM). Data obtained from a single experiment (wild type = 5, AID^{Cre} = 5, IgMg1 = 5, and IgMg1AID^{cre} = 5), as CountBeads were accidentally used only in this experiment. **(E)** The frequency of CXCR5⁺ PD-1⁺ Tfh cells (mean ± SEM) within CD4⁺ activated T cells obtained from n=2 independent experiments (wild type = 10, AID^{Cre} = 12, IgMg1 = 5, and IgMg1AID^{cre} = 10). Each symbol represents one mouse. Statistical tests were performed using ordinary one-way ANOVA. * $p < 0.05$, ** $p < 0.01$.

4.3 Discussion.

This chapter aimed to investigate the behaviour of the IgMg1 BCR in the context of a non-functional AID, following the observation of increased IgG1 GC B cells and reduced IgM GC B cells. The experiments with the IgMg1AID^{Cre} mouse model provide an opportunity to investigate IgM^{+} CD138^{+} PB-PC, GC B cell, and Tfh cell numbers and frequencies in comparison with those observed in the IgMg1 and AID^{Cre} models.

The present results showed an apparent increase in both the frequency and the number of PB-PC responses in the IgMg1 model relative to wild-type mice following NP-KLH immunisation. This contrasts with previous studies, which reported no substantial differences in PB-PC frequency or number between IgMg1 and wild-type mice in response to TD antigens (NP-CGG and NP-KLH) [199, 200]. This difference may reflect that the DrLN size can fluctuate with the magnitude of the immune response; lymphocyte numbers were quantified using counting beads.

The IgMg1AID^{cre} strain displayed a reduction in IgM^{+} CD138^{+} PB-PC compared with their prominence in the AID^{cre} strain, while remaining equivalent with the IgMg1 strain. This observation likely reflects an alteration in BCR signalling and reduced support from the T cell and cytokine environment. This could be tested by assessing BCR-induced signalling responses using phospho-flow cytometry, for example, by measuring phosphorylation of SYK, BLNK, BTK, or ERK following BCR engagement. As BCR signal strength influences subsequent interaction with Tfh cells, the contribution of T cell-derived signals could be further evaluated by assessing key cytokines such as IL-4 and IL-21, which synergise with BCR signalling to promote the induction of IRF4 and Blimp-1. Notably, as only cell surface staining was performed,

the IgM^+ and $IgG1^+$ PB-PCs analysed in this study correspond to the P1 and P2 differentiation stages. Fully mature P3 PCs, which lack surface immunoglobulin expression, would therefore not be captured in this analysis [148].

Moreover, the IgMg1AID^{Cre} mouse model provided an insight into other biological aspects. B cells within the GC undergo apoptosis in the DZ when they acquire damaging mutations in their BCR through SHM and in the LZ when they are not positively selected [103]. Fas receptor ligation on GC B cells triggers the downstream caspase 8-mediated apoptosis [203]. This is essential for maintaining both B and T cell populations within the GC. Wild-type GC B cells exhibit increased activity of caspases 3, 8, and 9, reflecting apoptosis activity, while $AID^{-/-}$ GC B cells show caspase activity at background levels [81]. Therefore, $AID^{-/-}$ models exhibit expanded GC B cell pools [81, 204]. Caspase activity has an impact on the IgMg1 model, as shown by a greater proportion of GC B cells positive for active caspase 3 at day 8 after primary immunisation with TD antigens [199, 200]. Notably, a rise in apoptotic IgMg1 GC B cells was observed 6 days following primary immunisation with NP-CGG [199]. After 8 days, the frequency of IgMg1 GC B cells, in comparison to wild-type, was shown to increase in response to 20 µg of precipitated NP-CGG with heat-inactivated *B. pertussis* [199], but to decrease in response to 10 µg of precipitated NP-KLH with heat-inactivated *B. pertussis* [200]. In contrast, the present results demonstrated a significant increase in IgMg1 GC B cells in response to 10 µg of precipitated NP-KLH and heat-inactivated *B. pertussis* than was observed in wild-type. The IgMg1AID^{Cre} model showed a reduction in both the frequency and number of Fas^+ GC B cells compared with the AID^{Cre} and IgMg1 models. The reason for this reduction requires further investigation, including assessment of caspase 3 activity under this new altered

BCR signalling condition. This could be investigated experimentally by quantifying active caspase 3 in splenic Fas^+ GC B cells by intracellular flow cytometry staining, allowing comparison of the proportion of apoptotic cells between genotypes.

The analysis of $IgG1^+$ and IgM^+ GC B cells was based on surface staining and represents a single experiment, as IgM and IgG1 staining in the initial experiment was suboptimal and excluded. Consequently, the reproducibility of these observations and potential variability in staining efficiency or biological response could not be assessed. Low-frequency $IgG1^+$ events were detected within GC and non-GC B cell populations. Given that class-switch recombination is not expected in the AID^{Cre} or $IgMg1AID^{Cre}$ mouse models, $IgG1^+$ events may reflect nonspecific staining or background signal. However, without replication, a biological contribution cannot be excluded. Therefore, the presence of $IgG1^+$ events introduce uncertainty in the interpretation of class-switch status in these populations, and further experiments would be required to confirm whether these signals represent artefact or low-level staining variability. In contrast, following class-switch recombination in the IgMg1 model, cells are expected to lose expression of the chimeric IgMg1 BCR and instead express a conventional IgG1 BCR. However, in the $IgMg1AID^{Cre}$ model, CSR cannot occur, and the chimeric receptor is predicted to be retained.

The present results showed that the $IgMg1AID^{Cre}$ model exhibits a reduced GC B cell response and an intermediate GC zone distribution relative to wild-type, AID^{Cre}, and IgMg1 models. The NP-specific $B220^+$ Fas^+ GC B cell was decreased compared with both the AID^{Cre} and IgMg1 models. In parallel, phenotypic analysis revealed a reduction in Tfh cells in the $IgMg1AID^{Cre}$ model, in contrast to their expansion in the

AID^{Cre} and IgMg1 models. The IgMg1 model has previously been associated with an increased GC B cell response and a higher fraction of NP-specific B220^{+} Fas^{+} GC B cells [199, 200]. Collectively, these findings suggest that IgMg1 GC B cells have an impaired ability to compete for Tfh-derived survival signals in the absence of AID-dependent selection mechanisms.

During GC response, Tfh cells expand in proportion to the strength of TCR engagement with peptide-MHC II complexes and compete based on antigen-recognition affinity [90]. BCR affinity influences this process by regulating the amount of antigen presented by GC B cells and thereby the strength of TCR signalling received by Tfh cells. In the IgMg1 model, enhanced class switching to IgG1 and the ability to undergo somatic hypermutation potentially strengthen their interactions with Tfh cells and promote greater Tfh expansion. In contrast, AID^{Cre} mice retain wild-type IgM signalling and lack SHM, leading to an enlarged GC B cell compartment with limited output; this may increase the demand for Tfh support to sustain the expansion. However, in IgMg1AID^{Cre} mice, where CSR is blocked and only the transgenic IgMg1 BCR is expressed, antigen engagement is likely to induce qualitatively altered signalling. This reflects the combination of conventional Igα/β-mediated signalling with signals derived from the IgG1 cytoplasmic tail, which may modify downstream activation and reduce the efficiency of Tfh cell engagement. This could be tested experimentally by measuring BCR signalling directly in IgMg1AID^{Cre} GC B cells using a Nur77/Nr4a1 reporter system, which provides a sensitive readout of antigen receptor signalling [205]. For example, if possible, crossing Nur77/Nr4a1-eGFP reporter with IgMg1AID^{Cre} mice would enable visualisation of real-time signalling intensity in vivo.

The IgM and IgG BCR complexes adopt fundamentally different spatial alignments relative to the cell membrane and their co-receptors Igα/β [206]. IgM BCR sits closer to the cell membrane and interacts with the Igα/β signalling dimer in a side-by-side orientation. While IgG1 BCR is spaced further out from the membrane due to its distinct hinge region and sits on top of the Igα/β signalling complex in a head-by-side alignment [206]. Therefore, the signalling output of a BCR is not just a sum of its parts but depends critically on the integrated structure of the entire receptor complex and appropriate presentation to downstream signalling machinery and organelles such as the mitochondria.

The IgMg1AID^{Cre} mouse model did not provide insight into why GCs in the IgMg1 model are dominated by class-switched IgG1 B cells and why IgM^{+} GC B cells are reduced. This reduction was previously attributed to GC entry failure. However, the GC in the IgMg1AID^{Cre} mouse model suggests that entry failure is not the cause. Another explanation proposed was that cells escape anergy by switching from the chimeric IgMg1 BCR to IgG1. However, it remains unclear whether the dominance of IgG1 GC B cells in the IgMg1 mouse model is a result of the IgG1 tail. The study by Sundling et al. demonstrated that the decline in IgM GC B cells is independent of ongoing CSR processes, pointing instead to alternative mechanisms at play within the GC reaction. To assess the fate of IgM GC B cells, Sundling et al. set up an experimental design involving MD4 and SWHEL mice sharing the same antigen specificity (HEL antigen), but MD4 mice are genetically modified to lack the capability to undergo the CSR process [110]. Both MD4 and SWHEL B cells were co-transferred into wild-type recipient mice. By comparing B cells over time post-antigen challenge, they found that IgM GC B cells (from both MD4 and SWHEL) were depleted similarly, regardless of

the presence or absence of CSR capabilities [110]. IgM$^+$ GC B cells exhibit normal functionality for SHM at the same rate as IgG1$^+$ GC B cells; however, high-affinity clones of IgM$^+$ GC B cells fail to accumulate within the GC [110]. This lack of retention is attributed to a selection process that favours high-affinity clones of IgG1$^+$ GC B cells over IgM$^+$ GC B cells. Notably, the positive selection of IgG1$^+$ GC B cells is not mediated by the cytoplasmic tail of the IgG1 molecule but rather by other molecular and cellular processes that drive the selection within the GC [110]. Therefore, the IgMg1 BCR may escape anergy by switching to an IgG1-driven pathway through molecular processes.

A caveat with the IgMg1AID^{Cre} mouse model is that B cell development has not been examined, as is standard for many newly generated mouse models. Altered BCR signalling can skew transitional B cell fate toward MZ or FO lineage, which is relative to the signalling strength. Weaker BCR signalling appears to promote the differentiation into an MZ B cell phenotype, while relatively strong BCR signalling favours an FO B cell phenotype [13, 14, 207]. However, it has also been reported that mouse models with strong BCR signalling favour an MZ phenotype [208-211]. Because MZ and FO B cells contribute differently to influence the immune response, shifts in the MZ and FO ratio can significantly affect GC recruitment, Tfh frequency, and PC output. IgMg1 mice exhibit a developmental skewing toward the FO phenotype and a reduction in MZ B cells [199, 200]. Therefore, the IgMg1AID^{Cre} mouse model may contribute to their distinct immunological phenotypes, explaining the alterations in GC recruitment, Tfh frequency, and PC output.

A further caveat with the IgMg1AID^{Cre} mouse model is that the experiments were performed with a limited number of mice in only two independent experiments. The flow cytometric analysis of IgM-expressing GC and non-GC B cells, including their staining, may not be fully accurate. The IgMg1AID^{Cre} mouse model would not be a proper system to investigate the dominance of class-switched GC B cells over IgM cells due to the inability to undergo CSR. Rather, the IgMg1AID^{Cre} mouse model provides an opportunity to further investigate GC B cell and Tfh cell behaviours observed in IgMg1 and AID^{Cre} models. Given that BCR signalling shapes both GC B cell survival, selection, and Tfh engagement, assessing calcium flux, oxidative phosphorylation, and caspase 3 activity in the IgMg1AID^{Cre} B cells will be essential for understanding how altered signalling and the absence of AID protein together influence GC dynamics.

4.4. Conclusion.

The IgMg1AID^{Cre} model presented in this chapter showed that an altered BCR enables the separation of the AID-dependent mechanism from the BCR-dependent metabolic and survival pathways. By removing the AID protein while preserving the IgMg1 signalling, this model reveals how BCR structure alone shapes GC entry and Tfh engagement. The impaired GC B cell recruitment, reduced NP-specific GC B cells, PC output, and altered Tfh frequencies observed in the IgMg1 and AID^{Cre} models highlight the combined impacts of BCR-intrinsic signalling in the IgMg1AID^{Cre} model. Even when CSR is ablated, IgM^{+} GC B cells do not accumulate as observed in the IgMg1 mouse model, demonstrating that their reduced representation reflects impaired survival and/or selection rather than conversion into class-switched or PC fates. Consistent

with this is the reduction in PB-PC output in the IgMg1AID^{Cre} mouse model compared to the AID^{Cre} model. This model therefore offers valuable insight into both the basic biology of GC selection and the immunological defects characteristic of AID deficiency.

Chapter 5. The Impact of Antigen Localisation on the Induction and Persistence of Memory B Cells.

5.1 Introduction

Migration of memory B cells to different localisations is an important aspect of adaptive immunity, ensuring a rapid and effective response upon re-exposure to an antigen. Memory B cells exhibit multiple fates on re-encountering the antigen [212, 213], involving rapid proliferation and differentiation into antibody-secreting cells [153, 213], re-entering the GC for modification of their BCR [213-215], or returning to their resting state [153, 213]. However, there is an ongoing debate about the participation of memory B cells in forming the secondary GC [64, 212, 213, 216, 217]. The fate and efficiency of memory B cell responses after secondary challenge rely on the proximity of the booster immunisation to the initial priming site [218]. While vaccination and microbial infection can establish memory B cells both locally and in distal lymphoid tissues [218-220], some memory B cells—such as those in the lung after pulmonary influenza virus infection—remain tissue-resident and do not circulate [221]. These resident memory B cells can rapidly differentiate into PCs upon re-exposure, providing effective local protection [221]. When booster immunisations are administered at sites distant from the original priming, the magnitude and quality of the recall response may be altered, potentially due to the limited redistribution of memory B cells across lymphoid compartments. These observations suggest that memory B cells preferentially home to familiar microenvironments, possibly due to the persistence of local antigen depots or retained antigen-presenting cells that provide continued stimulation. In contrast, when a

booster immunisation is delivered at a site distant from the original priming location, memory B cells may require additional signalling cues to effectively migrate and participate in the secondary response. This spatial dependence has important implications for vaccination design. If the anatomical site of antigen exposure influences the magnitude and quality of the memory B cell recall, then site-specific immunisation approaches could be optimised to improve protective outcomes [218]. Beyond localisation and trafficking, the intrinsic properties of memory B cells also contribute to superior responsiveness [213, 222]. Compared to naive B cells, memory B cells possess pre-formed signalling networks that enable them to respond more rapidly, re-enter the cell cycle, and expand efficiently upon re-exposure to antigen [213, 222]. Several studies have highlighted the importance of the anatomical site in shaping memory B cell recall responses. Kuraoka et al. (2022) demonstrated that boosting at the original priming site enhances recall GC responses and antibody affinity compared to distal boosting [218]. However, their analysis focused on clonal composition and antibody output rather than spatially resolved lymph node dynamics or the differentiation fate of memory B cells. Shenoy et al. (2012) showed that memory B cells require local inflammation to access distal lymph nodes, but did not examine the quality or fate of recall responses under physiological conditions, nor whether memory B cells re-enter the GC or differentiate into PB-PC at these sites [219]. Baine and Thorbecke (1982) provided early evidence that local boosting produces stronger responses than systemic challenge, but lacked the cellular resolution to define B cell subsets [223]. Together, these studies reveal a key question in our knowledge of how anatomical context shapes the dynamics of memory B cell recall.

In this chapter, recall memory B cell responses were assessed against a lower dose of the TD antigen precipitated-NP_{27}-KLH. We tracked the GC-derived B cells, using the inducible reporter model *S1pr2*^{CreERT2} *Rosa26*^{LSLtdTomato}, which does not label GC-independent activated B cells. We also assessed the persistence of humoral memory by analysing the PB-PC population and antibody production. The immunisation scheme targeted two lymphatic regions: the draining lymph node (DrLN), which is ipsilateral to the injection site, representing the local response; and the distal lymph node (DisLN), which is contralateral to the injection site, representing the systemic response.

Therefore, mice were immunised with 10 µg of precipitated NP_{27}-KLH via the plantar surface of the left rear foot (Figure 5.1A). To induce CreERT2 activity, mice received three doses of tamoxifen shortly after priming. As GC typically become fully established within 5-6 days of a primary response [8, 224, 225], tamoxifen was administered on days 5, 7, and 9. Tamoxifen-induced recombination is temporally restricted, as tamoxifen and its active metabolites are degraded within approximately one week after immunisation [226]. Therefore, tamoxifen administration during priming is unlikely to label cells that are activated and re-enter the GC after boosting on day 30.

Thirty days after priming, a cohort of mice received a booster with the soluble form of the same antigen in both rear feet—targeting the initial site (DrLN-boosted, DrLN-B) and the distal site (DisLN-boosted, DisLN-B) (Table 5.1). Popliteal lymph nodes from non-boosted mice served as controls: DrLN-non-boosted (DrLN-NB), reflecting the primary response, and DisLN-non-boosted (DisLN-NB), reflecting systemic dissemination from the draining site. Samples, including popliteal lymph nodes

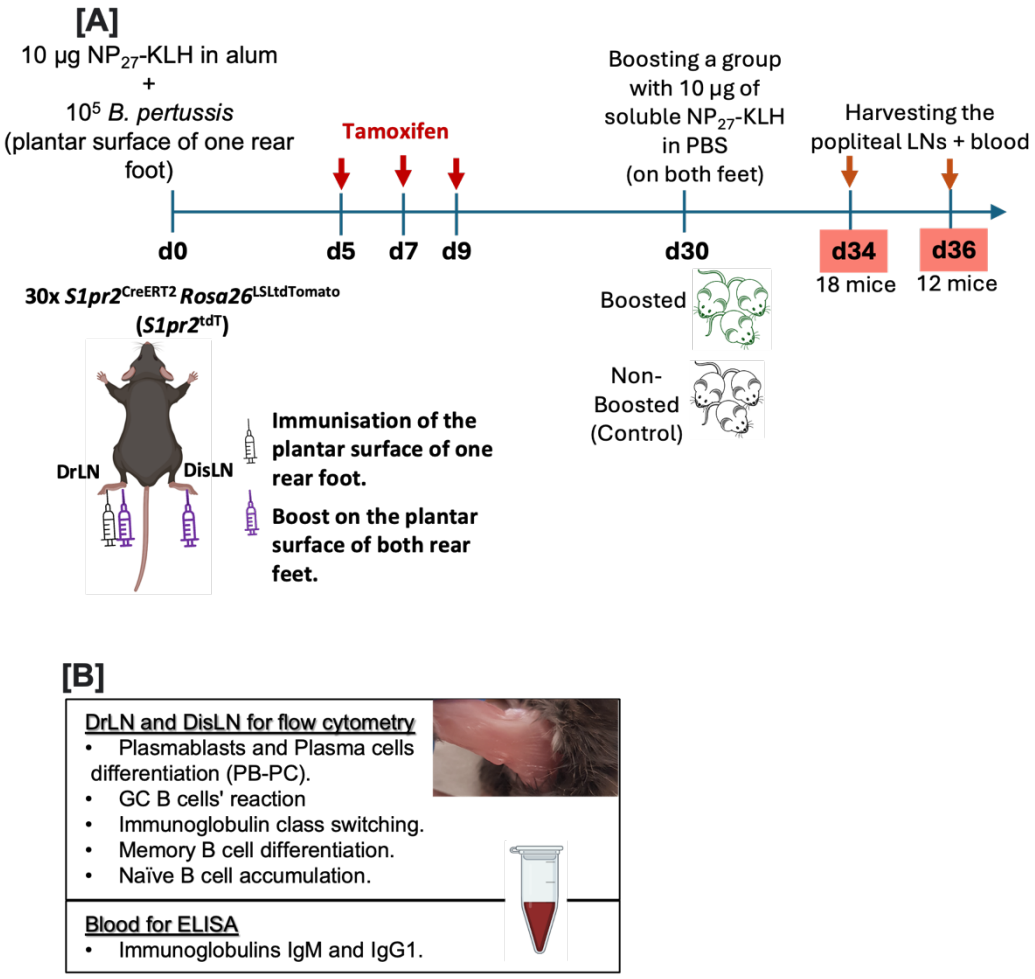


Figure 5.1. Schematic of the experimental procedure for studying recall memory B cell responses.

(A) It shows the immunisation protocol. 30 mice of *S1pr2*^{tdT} (14 male and 16 female), ranging from 8 to 15 weeks old, were immunised on day 0 with 20 µL of PBS containing 10 µg of NP_{27}-KLH in alum plus 10^5 of *B. pertussis* (denoted with a white syringe) and then administered by gavage with 200 µL of tamoxifen containing 20 mg/mL in corn oil at the indicated time points. Thirty days later, a cohort of mice (n = 15) was boosted with 20 µL of PBS containing 10 µg of NP_{27}-KLH (denoted by a purple syringe), and another cohort of mice (n = 15) served as a control. Four and six days later, the popliteal lymph nodes (LNs) and blood were harvested for flow cytometry and ELISA analysis, respectively. **(B)** The chart of the analysis method and the tissues used.

Table 5.1. Description of lymph nodes abbreviations used in this study.

Group	Prime	Boost	Description
DrLN-B	✓	✓	Draining lymph node, primed and boosted.
DrLN-NB	✓	x	Draining lymph node, only primed.
DisLN-B	⬅ Migrated cells	✓	Distal lymph nodes are seeded with migrated primed B cells and boosted later.
DisLN-NB	⬅ Migrated cells	x	Distal lymph nodes are only seeded with migrated primed B cells from the draining site.

(section 2.6) and blood (section 2.8), were harvested and analysed on days 4 and 6 following boosting or at the corresponding time points in non-boosted mice (Figure 5.1B). The selection of days 4 and 6 post-boosting is supported by findings from Zhan et al. (2022), demonstrating that antigen-specific GC B cells emerge as early as day 4 and peak between days 6-10 [26, 227]. This experimental design allowed us to investigate the local and systemic dissemination of B cell recall response following homologous boosting with 10 µg antigen at an intermediate interval of 30 days.

The following aims were addressed in this chapter:

1. Analysing GC-derived $CD38^{+}$ *S1pr2*$^{tdT+}$ memory B cell differentiation with a focus on their anatomical redistribution.
2. Investigating GC B cell dynamics to determine the differences between before and after boosting.
3. Characterising PB-PC differentiation across DrLN and DisLN to assess the extent of antibody-secreting cell responses during recall.
4. Measuring the systemic IgG1 and IgM titres by ELISA.

5.2 Results

5.2.1. The number of memory B cells declines at distal sites 6 days after boosting.

A prime and boost antigen was used to investigate how the location of a booster dose affects the quality of recall memory formation. Both humoral and cellular components of the primary response begin to decline as antigen levels decrease [178]. GC responses last ~2-4 weeks in most systems following primary immunisation with conventional antigen exposure [228]. However, GC responses can persist for up to 6 months in a slow-delivery immunisation with HIV Env protein [228]. This study investigated early memory formation by administering the booster on day 30, enabling us to analyse a secondary response while minimising interference from the waning primary response—without artificially disrupting the primary GC response (for instance, using MR-1 antibody). However, it has been reported that GC and GC-derived responses are indistinguishable between MR-1-treated (CD40L-blocked) and untreated mice [218].

GC-derived $CD38^{+}$ *S1pr2*$^{tdT+}$ B cells are the classical memory B cell phenotype (Figure 5.2A), from which can differentiate into multiple fates, including PC precursors. The mean number of memory B cells was 50,000 in DrLN-NB, which decreased to approximately 10,000 after boosting (DrLN-B) on day 4 (Figure 5.2B), representing a 5-fold reduction. A similar reduction was observed two days later, which was 5,000 in DrLN-NB and decreased 5-fold after boosting (Figure 5.2D). This represents an 80% reduction between primed and boosted lymph nodes, indicating that boosting activates these cells, perhaps towards PC precursors or re-entry to the GC.

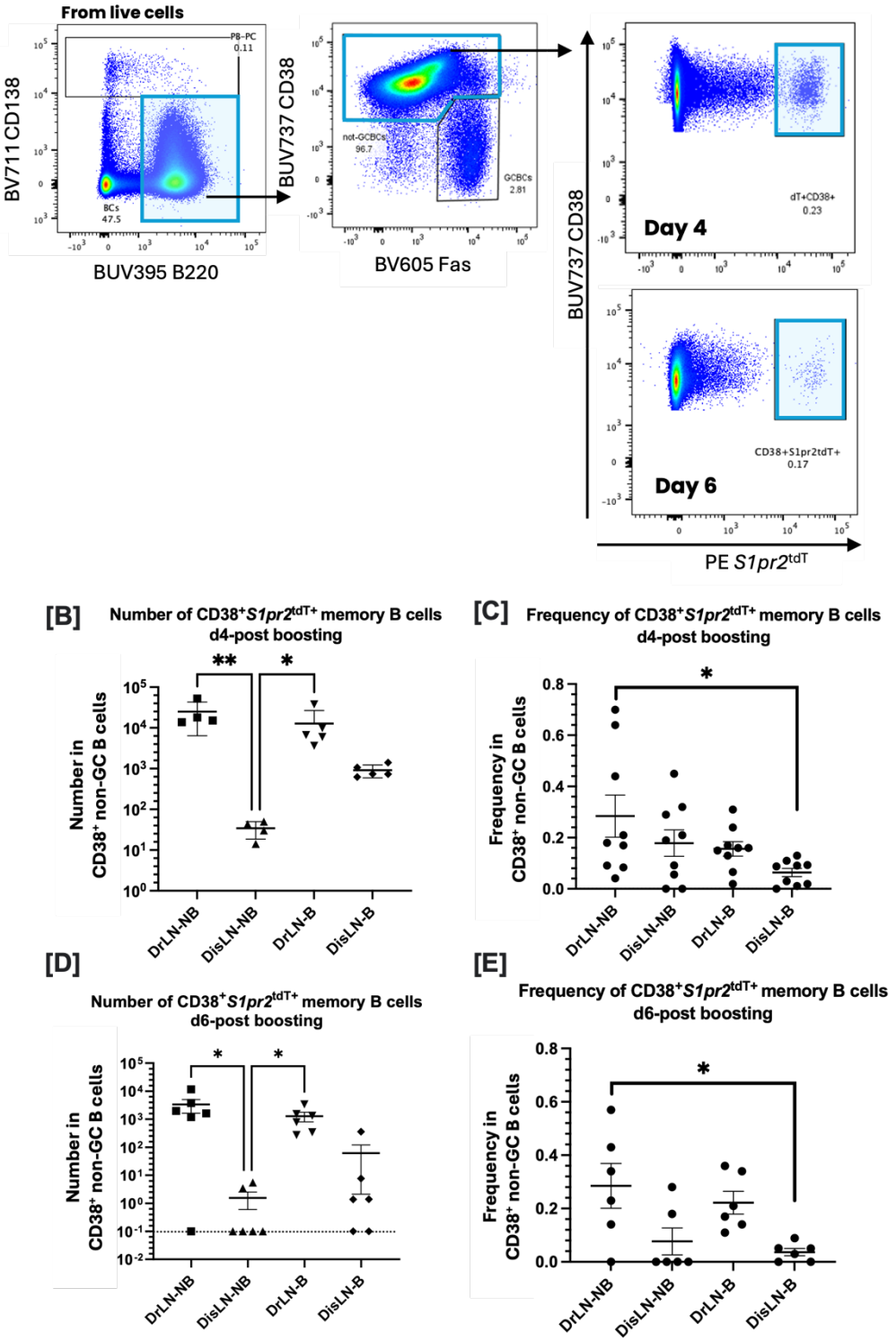


Figure 5.2. Analysis of CD38$^+$ *S1pr2*$^{tdT+}$ memory B cells after recall responses.

The experimental protocol is illustrated in Figure 5.1. **(A)** A typical flow cytometry example from DrLN-B, showing gating on CD38$^+$ non-GC B cells and subsequent gating on CD38$^+$ *S1pr2*$^{tdT+}$ memory B cells (blue outlines). **(B)** The number of CD38$^+$ *S1pr2*$^{tdT+}$ memory B cells (mean ± SEM) on day 4 post-boosting. Data were derived

from a single experiment (5 mice for the boosted group and 4 mice for the non-boosted group), as CountBeads were accidentally used only in this experiment. **(C)** The frequency of CD38^{+} *S1pr2*$^{tdT+}$ memory B cells within CD38^{+} non-GC B cells (mean ± SEM) on day 4 post-boosting. Data obtained from two independent experiments (9 mice for the boosted group and 9 mice for the non-boosted group). **(D)** The number of CD38^{+} *S1pr2*$^{tdT+}$ memory B cells (mean ± SEM) on day 6 post-boosting (mean ± SEM). Data obtained from a single experiment (6 mice for the boosted group and 6 mice for the non-boosted group). **(E)** The frequency of CD38^{+} *S1pr2*$^{tdT+}$ memory B cells within CD38^{+} non-GC B cells (mean ± SEM) on day 6 post-boosting (mean ± SEM). Data obtained from a single experiment (6 mice for the boosted group and 6 mice for the non-boosted group). Each symbol represents one mouse. Data points with zero detectable were plotted at the lower limit of detection (10^{-1}) to allow visualisation on a logarithmic scale. Statistical tests were performed using a one-way ANOVA, a nonparametric test, and the Kruskal-Wallis test. * $p < 0.05$, ** $p < 0.01$.

The number of memory B cells in the draining lymph nodes, whether primed or boosted, was 10-fold higher on day 4 than on day 6 (Figure 5.2B and D), indicating the reduced expansion of these post-GC memory cells at day 6. Alternatively, it may be due to different efficiency in cell preparation on different days, as there was no difference in the frequency of these cells. In contrast, the number of memory B cells in the distal sites of mice which received primed circulating cells only was very low (a mean of 60 cells) and increased 17-fold four days after boosting (Figure 5.2B). However, the number of these cells in the distal sites (DisLN-NB and DisLN-B) was lower on day 6 (Figure 5.2D) than on day 4.

The frequency of GC-derived CD38^{+} *S1pr2*$^{tdT+}$ memory B cells in DrLN-NB that were only primed was significantly higher than the distal site that received a boost (DisLN-B) at both time points (Figure 5.2C and E). The retention of memory B cells is preferentially maintained at the initial immunisation site compared with distal boost sites, likely reflecting the larger pre-existing pool of memory B cells in the primed draining lymph nodes and the rapid replenishment of memory B cells through

extrafollicular and GC differentiation. Notably, although the mean frequency of memory B cells in DrLN-NB was comparable at both time points, the wide distribution at day 6 suggests increased biological variability between samples.

Antigen-specific memory B cells determine where these cells physically reside after immunisation. To address the NP-binding in our study, NP-specific GC-derived $CD38^{+}$ $S1pr2^{tdT+}$ memory B cells were analysed on day 6 (Figure 5.3A). NP-specific GC-derived $CD38^{+}$ $S1pr2^{tdT+}$ memory B cells were present at comparable numbers in the draining lymph nodes before and after boosting. Most samples exhibited around 2,000 cells, with one sample reaching ~4,000 (Figure 5.3B). The distal sites showed a negative response, except for a single sample in boosted distal lymph nodes. A caveat to this investigation is that NP-specific B cells were not investigated after 4 days post-boosting.

Overall, these findings suggest that GC-derived $CD38^{+}$ $S1pr2^{tdT+}$ memory B cells are preferentially retained within the primed draining lymph nodes, whereas only limited recruitment occurs at distal lymph nodes following boosting.

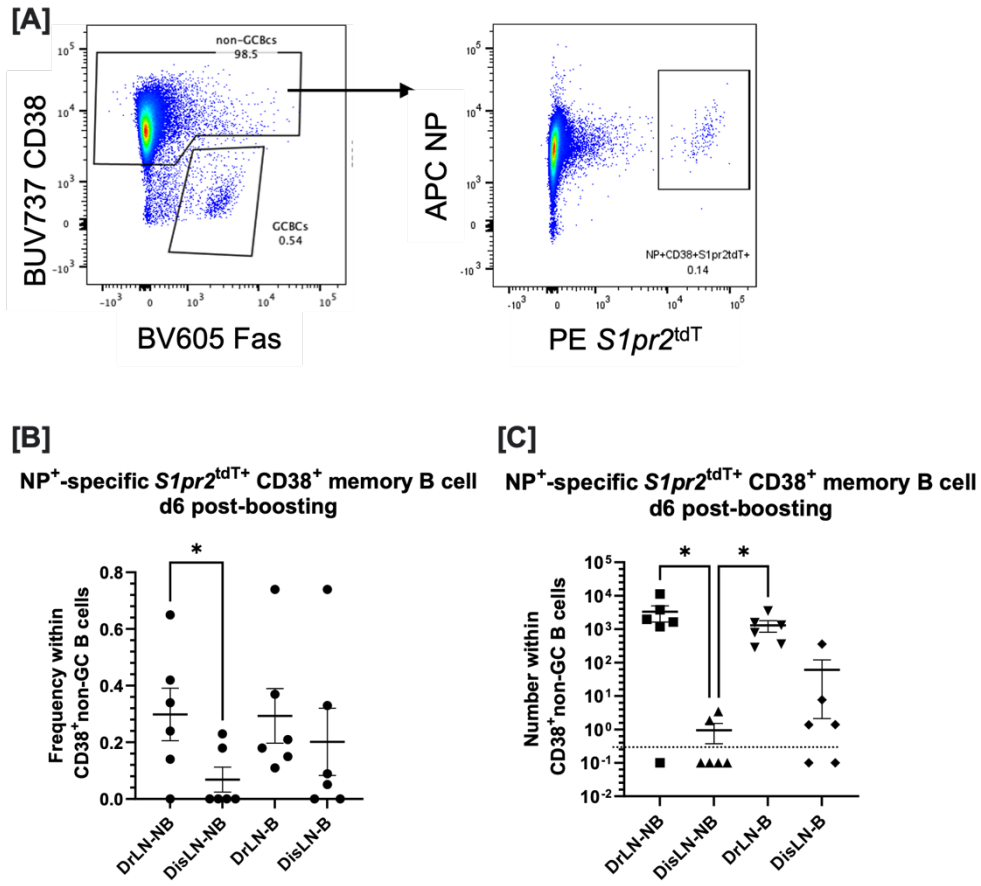


Figure 5.3. Analysis of NP$^+$-Specific *S1pr2*$^{tdT+}$ CD38$^+$ B cells after recall responses.

The experimental protocol is illustrated in Figure 5.1. **(A)** A typical flow cytometry example gated on CD38$^+$ non-GC B cells and further gated on NP$^+$-Specific *S1pr2*$^{tdT+}$ B cells. **(B)** The frequency of NP$^+$-Specific *S1pr2*$^{tdT+}$ B cells within CD38$^+$ non-GC B cells (mean ± SEM) on day 6 post-boosting. Data were derived from a single experiment (6 mice for the boosted group and 6 mice for the non-boosted group). **(C)** The number of NP$^+$-Specific *S1pr2*$^{tdT+}$ B cells within CD38$^+$ non-GC B cells (mean ± SEM) on day 6 post-boosting. Data were derived from a single experiment (6 mice for the boosted group and 6 mice for the non-boosted group). Each symbol represents one mouse. Samples with zero frequency were plotted at the lower limit of detection (10^{-1}) to allow visualisation on a logarithmic scale. Statistical tests were performed using a one-way ANOVA, a non-parametric test, and an analysis with the Kruskal-Wallis test. * $p < 0.05$.

5.2.2. Sustained distal GC activity may require adjuvant-driven inflammation during rechallenge.

Studies have reported that GC can remain detectable for extended periods—up to 60 days after NP-CGG immunisation in alum [229] and even 100 days following vesicular stomatitis virus infection [230]. Here, our study is consistent with that by showing the number of Fas^+ GC B cells remained detectable in the local primed sites 34 and 36 days after the initial immunisation, declining ~10-fold from day 4 to day 6 post-boost, likely reflecting the rapid contraction of the response after its early peak (Figure 5.4B and E). The detection of GC B cells in the non-boosted distal site was unexpected (Figure 5.4B-D). A plausible explanation is that a small fraction of the antigen may have entered systemic circulation—potentially facilitated by minor local bleeding during footpad injection—allowing low-level antigen delivery to distal lymph nodes.

After boosting the DrLN-NB, GC B cells decreased by a ~5.7-fold compared to non-boosted primed draining lymph nodes (Figure 5.4B) and a ~5-fold reduction compared to day 6 (Figure 5.4B and E). When distant lymph nodes received a boost, the number of GC B cells increased up to 7,400 cells compared to only the primed group, representing a 13-fold increase on day 4 (from 600 cells without a boost to an average of 8,000 cells). By day 6, numbers had reduced again to approximately 2 logs fewer than on day 4. The frequency of GC B cells within lymphocytes did not differ significantly between groups. In contrast, the frequency of DrLN-B at day 6 showed greater changes with an increase of GC B cells compared to their counterpart at day 4 (Figure 5.4C-D and F-G).

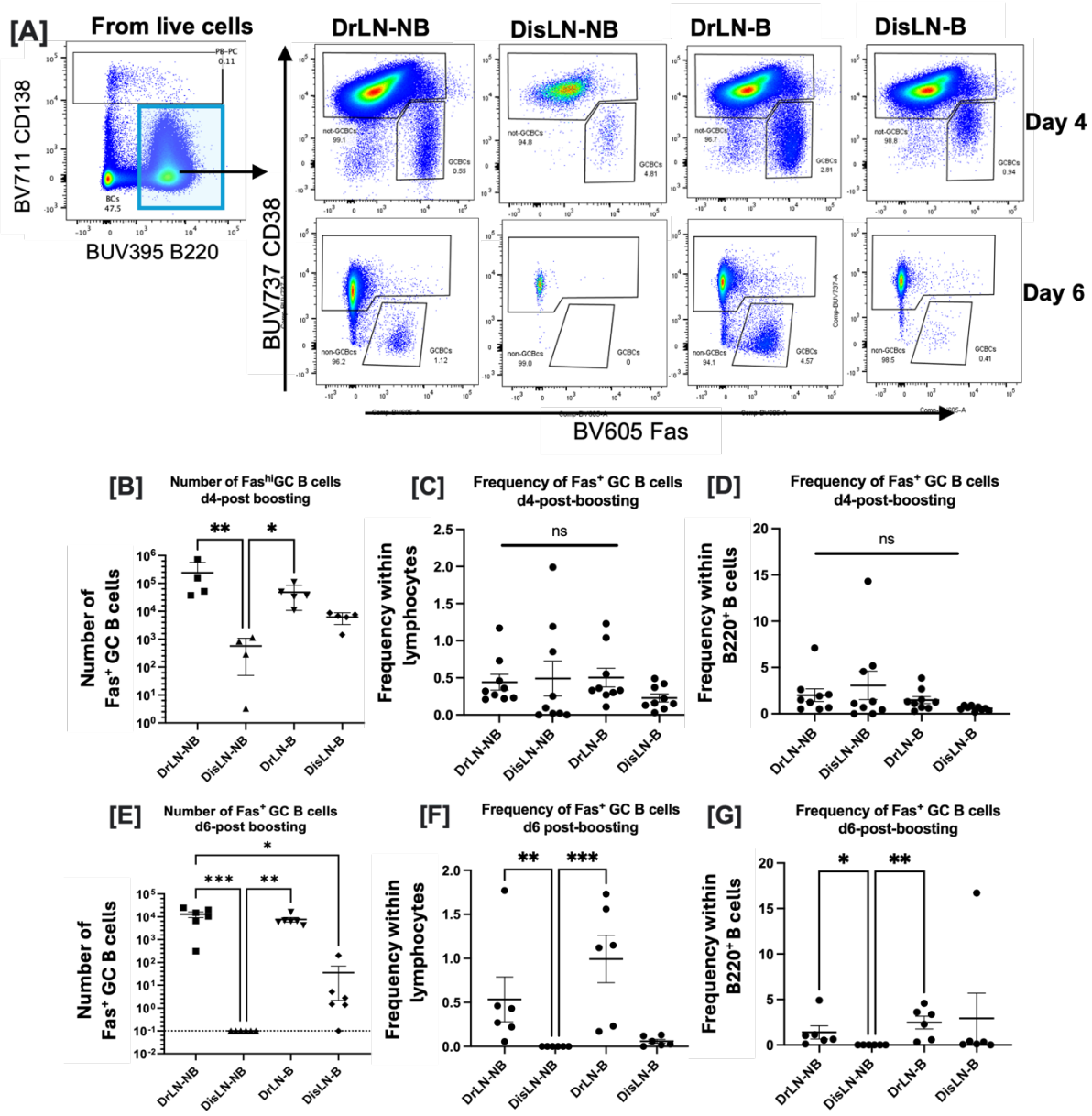


Figure 5.4. Analysis of Fas⁺ GC B cells after recall responses.

The experimental protocol is illustrated in Figure 5.1. **(A)** Typical flow cytometry example showing gating on B220⁺ B cells and subsequent gating on Fas⁺ GC B cells. **(B-D)** The number and the frequency of Fas⁺ GC B cells (mean ± SEM) on day 4 post-boosting. **(B)** Data were derived from a single experiment (5 mice for the boosted group and 4 mice for the non-boosted group), as CountBeads were accidentally used only in this experiment. **(C-D)** Data were derived from two individual experiments (9 mice for the boosted group and 9 mice for the non-boosted group). **(E-G)** The number and the frequency of Fas⁺ GC B cells (mean ± SEM) on day 6 post-boosting. Data were derived from a single experiment (6 mice for the boosted group and 6 mice for the non-boosted group). Each symbol represents one mouse. Samples with zero frequency were plotted at the lower limit of detection (10^{-1}) to allow visualisation on a logarithmic scale.

Statistical tests were performed using a one-way ANOVA, a non-parametric test, and an analysis with the Kruskal-Wallis test. ns $p > 0.05$, * $p < 0.05$, ** $p < 0.01$, *** $p < 0.001$.

The GC B cell response observed in the DisLN-B lymph nodes may be driven by naive B cells responding to antigen delivered during boosting, although the limited re-entry of GC-experienced memory B cell clones from the primary response cannot be excluded [64]. To test whether GC B cells after boosting are derived from memory or naive B cells, Fas$^+$ GC B cells were gated on B220$^+$ and *S1pr2*$^{tdT+}$ cells to compare the distribution of B220$^+$ *S1pr2*$^{tdT+}$ GC B cells (Figure 5.5A). The number of B220$^+$ *S1pr2*$^{tdT+}$ GC B cells in the DrLNs, between priming and boosting, mirrored the pattern observed for total GC B cells at both time points. Within the total GC B cell number population on day 4, approximately 200 cells of *S1pr2*$^{tdT+}$ B cells were detected among 8,000 GC B cells in the DisLN-B. Whereas only ~60 of *S1pr2*$^{tdT+}$ B cells were observed among 800 GC B cells in the DisLN-NB (Figure 5.5). On day 6, *S1pr2*$^{tdT+}$ GC B cells were detected in 2 out of 5 DisLN-B samples (Figure 5.5E). In contrast, the frequency of *S1pr2*$^{tdT+}$ GC B cells in the draining lymph nodes was slightly higher on day 6 than on day 4, reaching approximately 60% (Figure 5.5C and D). Overall, the analysis of the total numbers of GC B cells and *S1pr2*$^{tdT+}$ GC B cells revealed a relatively high number and frequency of GC B cells persisting in the DrLN 30 days after priming. This finding was unexpected, as the experimental design aimed to investigate GC reactivation after the waning of the primary GC response. In some T-dependent immunisation models, the primary GC response is substantially reduced by this time point, allowing the secondary response to be more readily distinguished from residual primary GC activity [218].

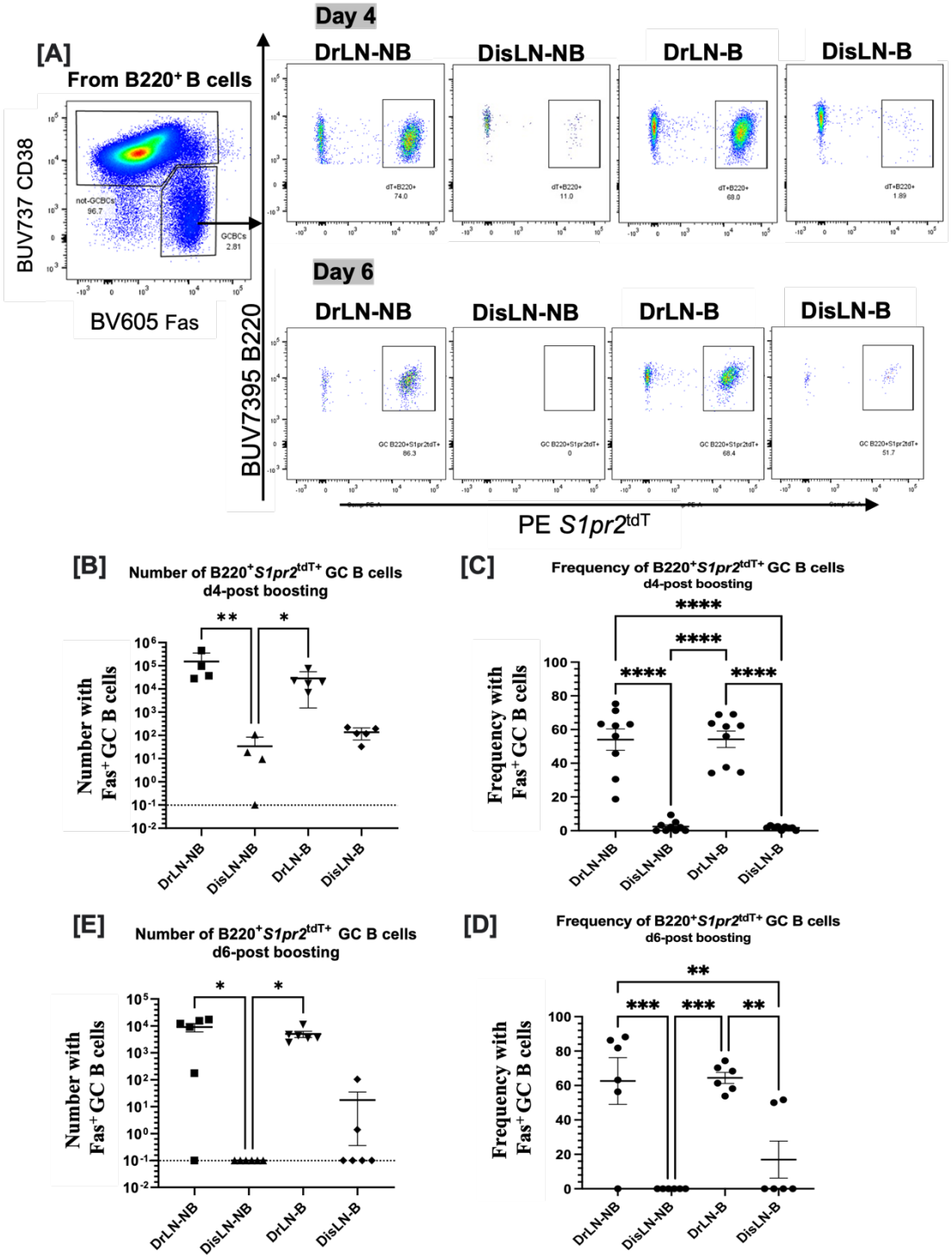


Figure 5.5. Analysis of B220$^+$ *S1pr2*$^{tdT+}$ GC B cells after recall responses.

The experimental protocol is illustrated in Figure 5.1. **(A)** Typical flow cytometry examples showing gating on Fas$^+$ GC B cells and further gating on B220$^+$ and *S1pr2*$^{tdT+}$ GC B cells. **(B-C)** The number and the frequency of B220$^+$ and *S1pr2*$^{tdT+}$ GC B cells within Fas$^+$ GC B cells (mean ± SEM) on day 4 post-boosting. **(B)** Data were derived

from a single experiment (5 mice for the boosted group and 4 mice for the non-boosted group), as CountBeads were accidentally used only in this experiment. **(C)** Data were derived from two individual experiments (9 mice for the boosted group and 9 mice for the non-boosted group). **(E-D)** The number and the frequency of $B220^{+}$ and *S1pr2*$^{tdT+}$ GC B cells within Fas^{+} GC B cells (mean ± SEM) on day 6 post-boosting. Data were derived from a single experiment (6 mice for the boosted group and 6 mice for the non-boosted group). Each symbol represents one mouse. Samples with zero frequency were plotted at the lower limit of detection (10^{-1}) to allow visualisation on a logarithmic scale. Statistical tests were performed using a one-way ANOVA, a non-parametric test, and an analysis with the Kruskal-Wallis test, * $p < 0.05$, ** $p < 0.01$, *** $p < 0.001$, **** $p < 0.0001$.

Consequently, the continued presence of primary GC B cells limits the extent to which conclusions can be drawn regarding memory B cell reactivation within DrLN. In contrast, the data suggest that GCs forming in the DisLN are predominantly derived from naive B cells rather than memory B cells.

TACI expression increases as GC B cells begin to differentiate into PB-PC and prepare to exit GC [8, 231]. Therefore, we used TACI expression as a marker to identify GC B cells transitioning toward a post-GC fate (Figure 5.6A). On day 4, the number of $TACI^{+}$ *S1pr2*$^{tdT+}$ GC B cells in DrLN-NB (Figure 5.6B) showed a broad heterogeneity, ranging approximately from 10^{2} to 10^{5}, while after boosting, it reduced to a narrow cluster around ~10^{2} to 10^{3}. The distal sites showed low numbers and no major effect of boosting. By day 6, $TACI^{+}$ *S1pr2*$^{tdT+}$ GC B cells no longer displayed the broad heterogeneity observed at day 4, and the upper range of this population was reduced by ~10^{3}. At this later time point, no significant differences were observed following boosting (Figure 5.6C), and distal lymph nodes did not support a substantial expansion of this population.

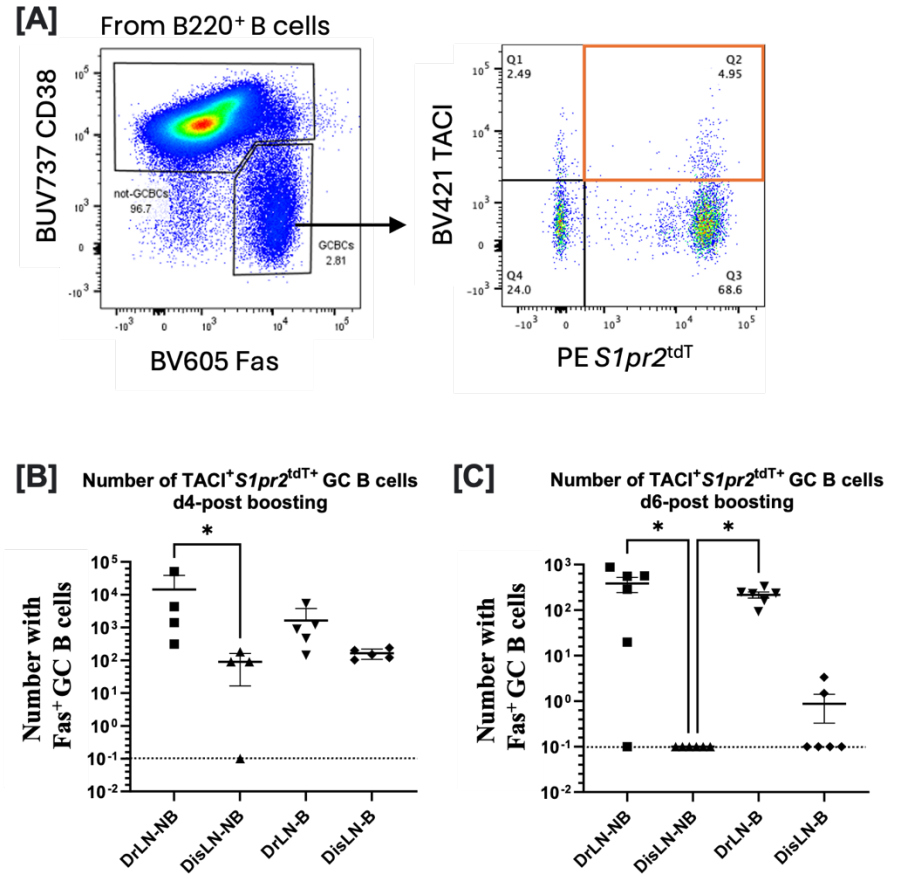


Figure 5.6. Analysis of TACI^{+} *S1pr2*$^{tdT+}$ GC B cells after recall responses.

The experimental protocol is illustrated in Figure 5.1. **(A)** A typical flow cytometry example derived from day 4, showing gating on Fas^{+} GC B cells and further gating on TACI^{+} and *S1pr2*$^{tdT+}$ positive cells (orange outlines). **(B)** Data were derived from a single experiment (5 mice for the boosted group and 4 mice for the non-boosted group), as CountBeads were accidentally used only in this experiment. **(C)** The number of B220^{+} and *S1pr2*$^{tdT+}$ GC B cells within Fas^{+} GC B cells (mean ± SEM) on day 6 post-boosting. Data obtained from a single experiment (6 mice for the boosted group and 6 mice for the non-boosted group). Each symbol represents one mouse. Data points with zero detectable were plotted at the lower limit of detection (10^{-1}) to allow visualisation on a logarithmic scale. Statistical tests were performed using a one-way ANOVA, a non-parametric test, and an analysis with the Kruskal-Wallis test, * $p < 0.05$.

Together, these data suggest that TACI^{+} *S1pr2*$^{tdT+}$ GC B cells represent a transient GC exit population whose induction depends on the strength of local differentiation signals. Overall, these findings may reflect a greater propensity of memory B cells seeding GCs in the draining lymph node to differentiate towards the PB pathway. In contrast, GCs in the distal lymph nodes, which are predominantly seeded by naive B cells, do not appear to exhibit the same tendency for rapid PB differentiation.

Antigen specificity amongst GC B cells was analysed at day 6 (Figure 5.7). The persistence of NP-specific *S1pr2*$^{tdT+}$ GC B cells varied from near zero to ~18,000, compared to intermediate numbers of around 3,000-5,000 in most mice (Figure 5.7B), suggesting that boosting does not expand NP-binding GC B cells. DisLN-B had zero NP-binding GC B cells, indicating that naive B cells going into the response after a booster immunisation are mainly specific to other epitopes on the carrier protein rather than to NP. This is consistent with antibody feedback blocking excess to epitopes that dominated the primary response, leading to epitope spreading [80, 184, 185, 232].

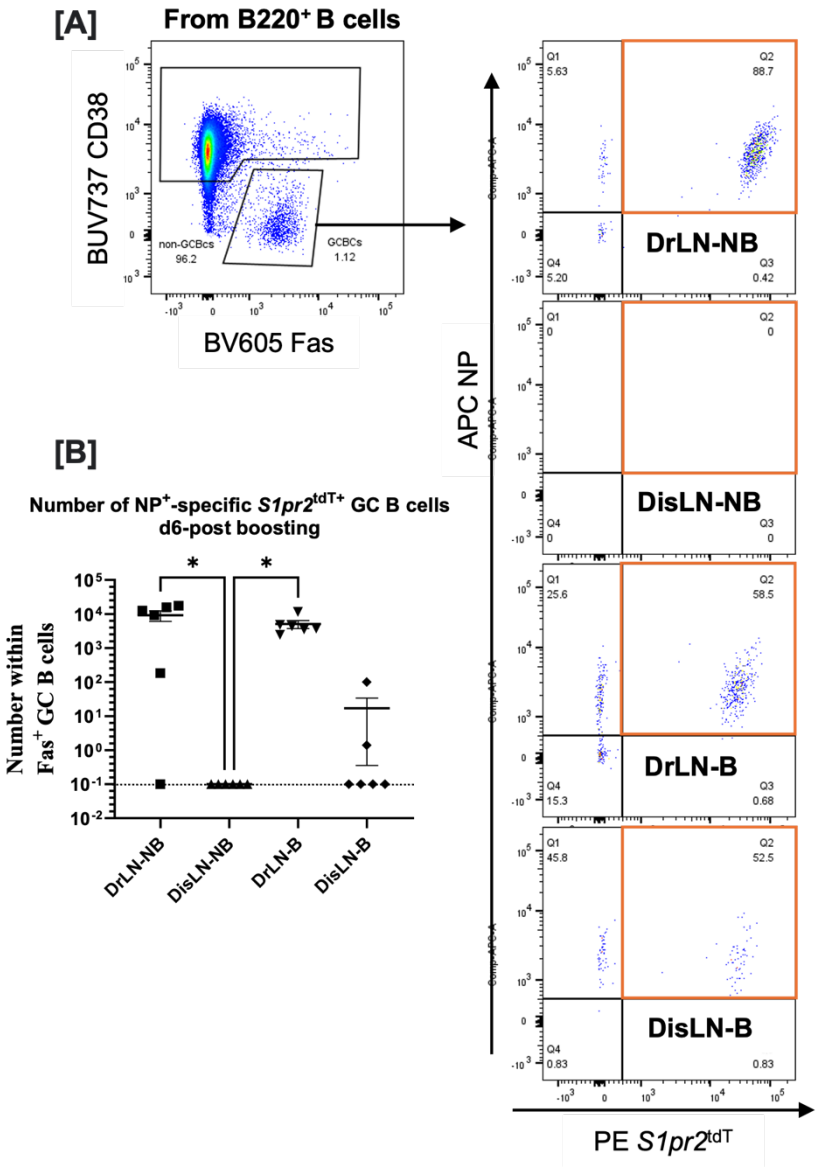


Figure 5.7. Analysis of NP^{+}-Specific *S1pr2*$^{tdT+}$ GC B cells after recall responses.

The experimental protocol is illustrated in Figure 5.1. **(A)** A typical flow cytometry example, showing gating on Fas^{+} GC B cells and further gating on NP^{+} and *S1pr2*$^{tdT+}$ positive cells (orange outlines). **(B)** The number of NP^{+} and *S1pr2*$^{tdT+}$ GC B cells within Fas^{+} GC B cells (mean ± SEM) on day 6 post-boosting. Data were obtained from a single experiment (6 mice for the boosted group and 6 mice for the non-boosted group). Each symbol represents one mouse. Data points with zero detectable were plotted at the lower limit of detection (10^{-1}) to allow visualisation on a logarithmic scale. Statistical tests were performed using a one-way ANOVA, a non-parametric test, and an analysis with the Kruskal-Wallis test, * $p < 0.05$.

5.2.3. Early increase in GC-matured PB-PCs response in the distal site after boosting.

Previous studies have indicated that local memory B cells can drive early PC responses upon secondary challenge. Tissue-resident memory B cell populations, such as those established in the lung after influenza infection, provide rapid and enhanced protection compared to circulating memory B cells [218]. However, lung-resident memory B cells do not recirculate compared to those in lymph nodes and splenic regions [153].

To investigate the PC response, we quantify the variation in $CD138^+$ PB-PC in local compared to distal sites (Figure 5.8A). Four days after boost, the number of $CD138^+$ PB-PCs in the DrLN-NB was comparable to those observed in DrLN-B (Figure 5.8B). As seen for memory and GC B cells, numbers were reduced by day 6, with the number of $CD138^+$ PB-PC decreasing by approximately a 10-fold reduction in DrLN-NB and a >10-fold reduction in DrLN-B compared to day 4 (Figure 5.8D). Notably, boosting did not increase the number of $CD138^+$ PB-PCs in the DrLN compared to the DrLN-NB. In contrast, the distal lymph nodes showed a clear boost-dependent response; $CD138^+$ PB-PC represented an approximately 27-fold (~96%) reduction from day 4 to day 6 after boosting (800 to 30 cells). Thus, while local draining lymph nodes did not exhibit an enhanced $CD138^+$ PB-PC response following re-exposure, the distal lymph nodes responded to boosting. This finding suggested that PB-PC expansion after boosting is more effectively supported at the distal site than at the primary draining lymph nodes. The absence of a detectable effect of boosting in the DrLN may reflect the unexpectedly high persistence of the primary response.

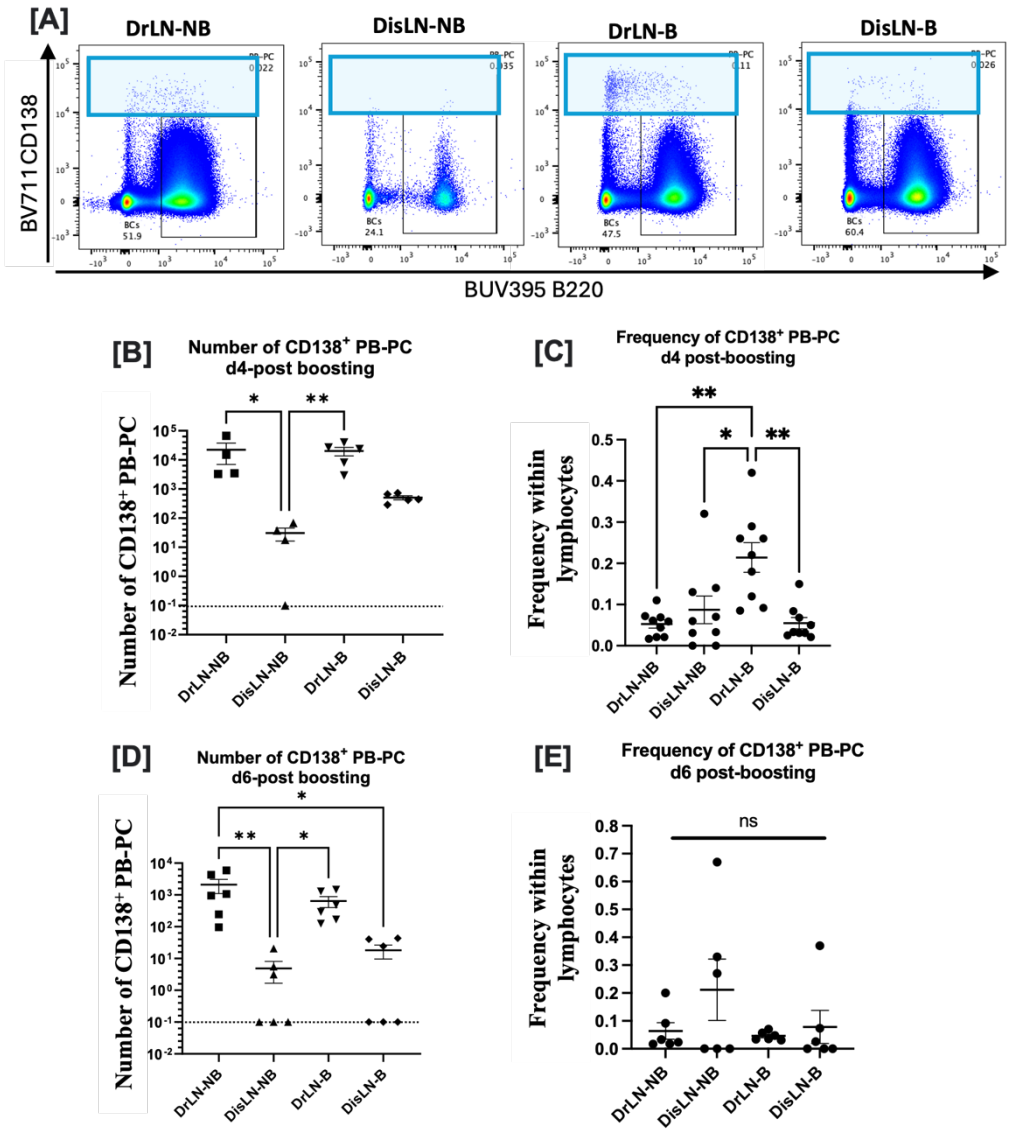


Figure 5.8. CD138⁺ PB-PC after recalling responses.

The experimental protocol is illustrated in Figure 5.1. **(A)** Representative flow cytometry plots were gated from live cells and further gated on CD138⁺ PB-PC. **(B-C)** The number and the frequency of CD138⁺ PB-PCs (mean ± SEM) on day 4 post-boosting. **(B)** Data obtained from a single experiment (5 mice for the boosted group and 4 mice for the non-boosted group). **(C)** Data were obtained from two individual experiments (9 mice for the boosted group and 9 mice for the non-boosted group). **(D-E)** The number and the frequency of CD138⁺ PB-PCs (mean ± SEM) on day 6 post-boosting. Data were obtained from a single experiment (6 mice for the boosted group and 6 mice for the non-boosted group). Each symbol represents one mouse. Samples with zero frequency were plotted at the lower limit of detection (10^{-1}) to allow visualisation on a logarithmic scale. Statistical tests were performed using a one-way ANOVA, a non-parametric test, and an analysis with the Kruskal-Wallis test. ns $p > 0.05$, * $p < 0.05$, ** $p < 0.01$.

Moreover, the range of CD138^{+} PB-PC numbers observed on day 4 partially overlapped with those detected on day 6 in the primed draining lymph nodes. Rather that showing two clearly separated populations, this overlap suggests variability in the time of the response between individual mice. Some animals may have already entered the contraction phase by day 4, whereas others may still have been near peak PB-PC expansion at day 6. The frequency of CD138^{+} PB-PCs was significantly increased in the DrLN-B (Figure 5.8C). But the frequency of CD138^{+} PB-PCs in the DisLN-NB showed high variability compared to day 4; three mice had no detectable PB-PC response, while one mouse exhibited a markedly elevated count (Figure 5.8E). The weaker responses observed in the DisLN reflect the relatively low numbers of memory B cells at these sites, in contrast to the higher memory B cell abundance and persistent GC responses observed in the DrLN.

PB-PCs are an independent cellular component crucial for maintaining long-term immunological memory by retaining antibody production against recently encountered pathogens while preventing the degradation of memory for pathogens encountered in the past [233]. Key to this mechanism is the competition for survival niches, including those found in lymph nodes, between newly generated PB and existing mature PC [233]. In the present study, the memory B cell-derived PB-PC response can be tested by *S1pr2*$^{tdT+}$ TACI^{+} CD138^{+} (Figure 5.9). Therefore, we investigated the proportion of CD138^{+} PB-PC that co-expressed *S1pr2*$^{tdT+}$ and TACI^{+}, to assess the proportion derived from the primary GC response (Figure 5.9A).

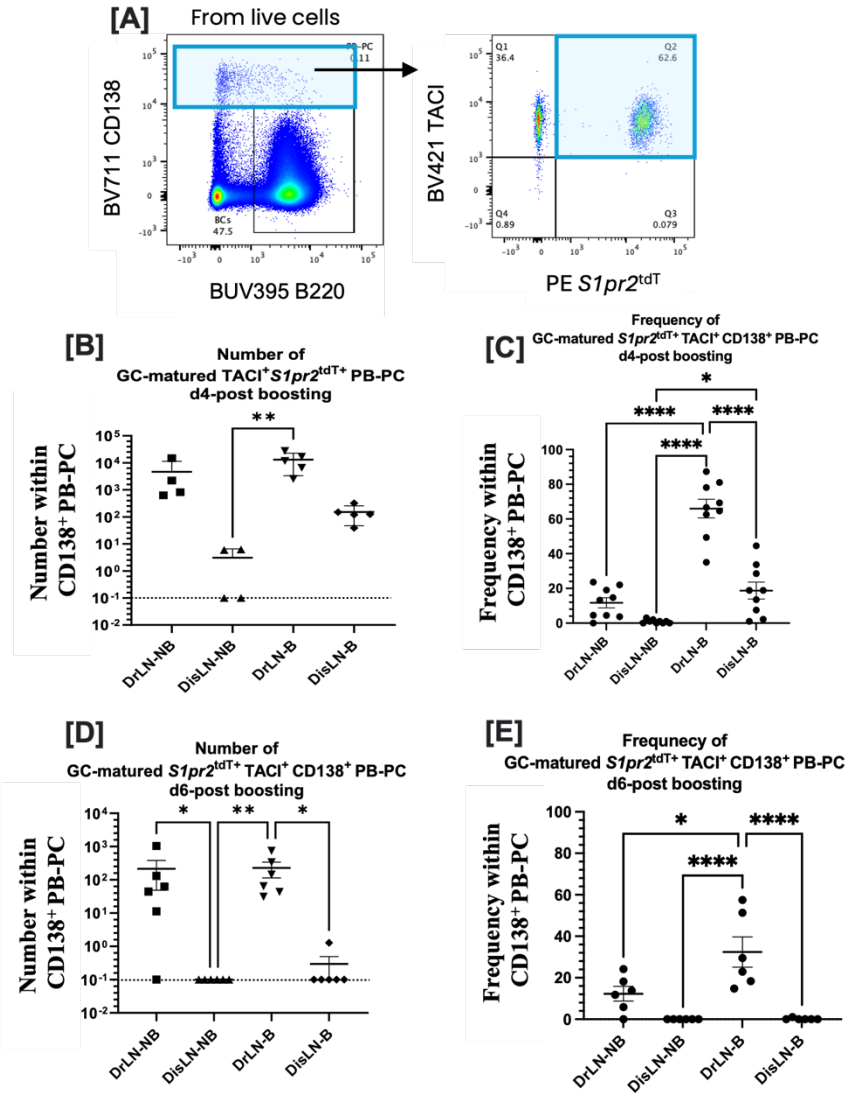


Figure 5.9. GC-matured *S1pr2*$^{tdT+}$ TACI^{+} CD138^{+} PB-PC after recalling responses.

The experimental protocol is illustrated in Figure 5.1. **(A)** Representative flow cytometry plots gated on CD138^{+} PB-PC then further gated on the dual expression of *S1pr2*$^{tdT+}$ and TACI^{+}. **(B-C)** The number and the frequency of GC-matured *S1pr2*$^{tdT+}$ TACI^{+} CD138^{+} PB-PCs (mean ± SEM) at day 4 post-boosting. **(B)** Data obtained from a single experiment (5 mice for the boosted group and 4 mice for the non-boosted group). **(C)** Data obtained from two individual experiments (9 mice for the boosted group and 9 mice for the non-boosted group). **(D-E)** The number and the frequency of GC-matured *S1pr2*$^{tdT+}$ TACI^{+} CD138^{+} PB-PCs (mean ± SEM) at day 6 post-boosting. Data obtained from a single experiment (6 mice for the boosted group and 6 mice for the non-boosted group). Each symbol represents one mouse. Samples with zero frequency were plotted at the lower limit of detection (10^{-1}) to allow visualisation on a logarithmic scale. Statistical tests were performed using a one-way ANOVA, a non-

parametric test, and an analysis with the Kruskal-Wallis test. * $p < 0.05$, ** $p < 0.01$, **** $p < 0.0001$.

At day 4 post-boost, the $CD138^+$ PB-PC in DrLN-NB (~40,000 cells) (Figure 5.8B), about 70% (~7,000 cells) were primary GC-derived *S1pr2*$^{tdT+}$ $TACI^+$ $CD138^+$ PB-PC (Figure 5.9B). In the non-boosted distal LN, 10% of $CD138^+$ PB-PCs (Figure 5.8B) were GC-matured *S1pr2*$^{tdT+}$ $TACI^+$ $CD138^+$ PB-PCs (Figure 5.9B). The high number of GC-matured *S1pr2*$^{tdT+}$ $TACI^+$ $CD138^+$ PB-PCs observed in the DrLN-NB reflects the propensity of GC-derived memory B cells to default to PC differentiation. Alternatively, this observation may reflect the early migration of GC-derived *S1pr2*$^{tdT+}$ $TACI^+$ $CD138^+$ PB-PCs to the BM or other secondary lymphoid niches, and they were no longer in the DrLN-NB at the time of analysis. In support of this possibility, Koike et al. (2022) demonstrated that both short-lived PC and long-lived PC can be detected in the BM around day 5 after immunisation [171, 188]. An additional explanation is that tamoxifen-induced labelling may have waned by the time additional naive FO B cells were activated and entered the GC response. These later-recruited cells would undergo GC maturation but remain *S1pr2*$^{tdT-}$, ultimately giving rise to PB-PC that lack the tdT label.

After boosting, the draining lymph node contained approximately 2×10^4 GC-derived *S1pr2*$^{tdT+}$ $TACI^+$ $CD138^+$ PB-PCs (Figure 5.9B), representing ~50% of the total $CD138^+$ PB-PC population (~4×10^4 cells) (Figure 5.8B), with a significant increase in their frequency (Figure 5.9C). Whilst lower, the boosted distal lymph node showed ~25% of $CD138^+$ PB-PCs were GC-derived *S1pr2*$^{tdT+}$ $TACI^+$ $CD138^+$ PB-PCs in the distal lymph node (~200 out of 800 cells). At day 6 post-boost, the GC-matured *S1pr2*$^{tdT+}$ $TACI^+$

CD138$^+$ PB-PC represented about 10% (~400 cells) of the CD138$^+$ PB-PC population (~40,000 cells) in the DrLN-NB (Figure 5.9D-E). Whereas 50% of CD138$^+$ PB-PC are GC-matured *S1pr2*$^{tdT+}$ TACI$^+$ CD138$^+$ cells in the DrLN-B (~400 cells out of 800 cells), with a 30% frequency within CD138$^+$ PB-PC (Figure 5.9E). However, the non-boosted distal lymph node did not exhibit any GC-experienced PB-PC, while the boosted counterpart showed a single mouse with detectable GC-experienced PB-PCs (Figure 5.9D). Overall, GC-matured *S1pr2*$^{tdT+}$ TACI$^+$ CD138$^+$ PB-PCs were increased in the boosted distal lymph node on day 4, compared to their level observed two days later.

The notable response on day 4 was that DrLN-B contained substantially fewer *S1pr2*$^{tdT+}$ TACI$^+$ cells within the Fas$^+$ GC B cell compartment (~3 x 10^3) (Figure 5.6B) compared with the CD138$^+$ PB-PC (~2 x 10^4) (Figure 5.9B). As *S1pr2*$^{tdT+}$ labelling marks GC-experienced cells, this indicates that a large fraction of GC-experienced B cells contributed to the PB-PC compartment early after boosting. The disappearance of this disparity by day 6 suggests dynamic fate decisions following boosting. However, while these data are consistent with rapid GC exit, they cannot exclude the possibility that GC-experienced cells differentiated directly into PB-PC without sustained participation in the recall GC. This disparity indicates early fate variability after boosting, suggesting that GC-derived cells were rapidly exiting the GC and preferentially differentiating into PB-PC rather than remaining in the GC. This aligns with the conception that secondary antigen exposure biases response toward antibody secretion rather than GC maintenance, while contracted by day 6.

The responses on day 6 showed waning responses compared to day 4. Here, another independent readout of the PB-PC response can be validated by NP-specific GC-

derived *S1pr2*$^{tdT+}$ CD138^{+} PB-PC, which represents GC-derived early PB rather than fully matured PC (Figure 5.10A). The number of these cells was comparable in the draining lymph nodes between the non-boosted and the boosted groups (Figure 5.10B). NP-specific GC-derived PB-PC were only detectable in a single mouse in the non-boosted distal site LN. After boosting, although the DisLN contained very few PB-PCs, ~10% of these cells were GC-derived and stained positive for NP (Figure 5.10B). Together, the distal lymph nodes showed a small but clear antigen-relevant response on day 6 after soluble antigen boosting.

5.2.4. Booster immunisation leads to a notable rise in NP_2-specific IgG1 titre by day 6.

B cells undergo somatic hypermutation, which induces random mutations into their BCR variable region genes. These mutations can increase, decrease or have no impact on the affinity of the BCR for the antigen [234, 235]. For quantifying the high-affinity titre of IgG1 and high-avidity titre of IgM antibodies in the sera, blood samples were collected by cardiac puncture (see section 2.9) on days 4 and 6 (see the experimental protocol in Figure 5.1) and then screened by ELISA (Figure 5.11A-D). The antibody titre in the non-boosted group reflects the primary response, whereas that in the boosted group represents the secondary response**.** The NP_2-specific IgG1 titre in the day 6 non-boosted group (d6NB) was significantly lower compared to d4NB, showing a nearly 10-fold reduction by day 6 (Figure 5.11E). This decrease is consistent with the reduced PC and GC responses observed between d4NB and d6NB. This finding was unexpected, as both groups underwent identical treatment—primary

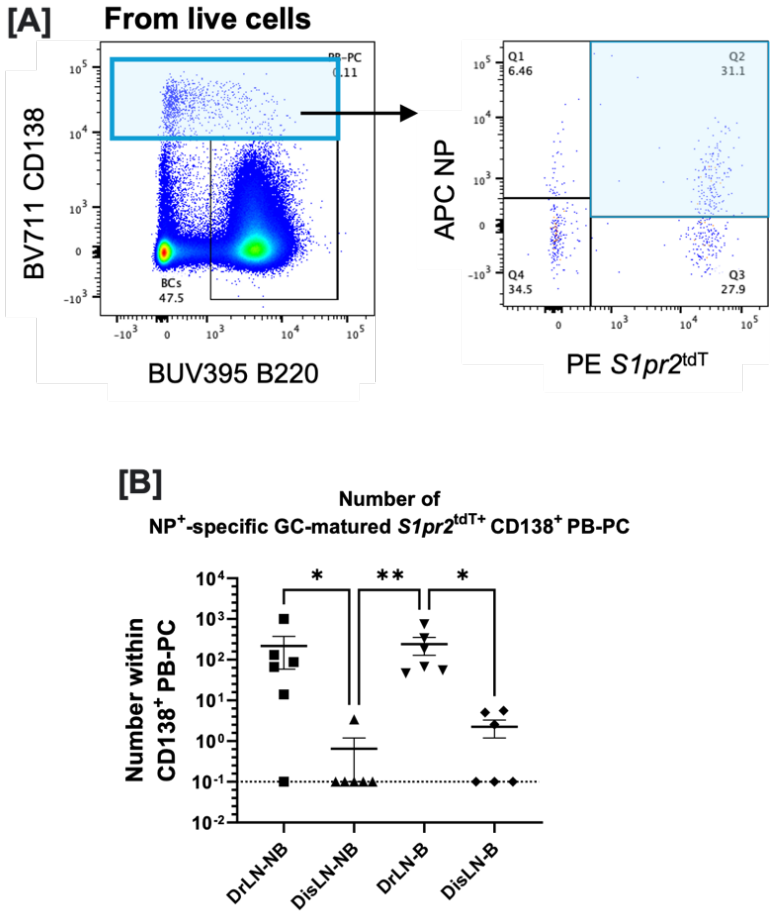


Figure 5.10. NP$^+$-specific GC-matured *S1pr2*$^{tdT+}$ CD138$^+$ PB-PC at day 6 after recalling responses.

The experimental protocol is illustrated in Figure 5.1. **(A)** Representative flow cytometry plots gated on CD138$^+$ PB-PC then further gated on the dual expression of *S1pr2*$^{tdT+}$ and NP$^+$. **(B)** The number of NP$^+$-specific GC-matured *S1pr2*$^{tdT+}$ CD138$^+$ PB-PCs (mean ± SEM) at day 6 post-boosting. Data obtained from a single experiment (6 mice for the boosted group and 6 mice for the non-boosted group).
Data points with zero detectable were plotted at the lower limit of detection (10^{-1}) to allow visualisation on a logarithmic scale.
Each symbol represents one mouse. Statistical tests were performed using a one-way ANOVA, a non-parametric test, and an analysis with the Kruskal-Wallis test. * $p < 0.05$, ** $p < 0.01$.

immunisation without boosting—and differed only in the timing of tissue collection (day 34 vs day 36). Therefore, no substantial difference between these groups was expected. The observed variability may reflect stochastic biological variation, technical variability, or potential cage effects that make the interpretation complicated. Furthermore, there was no clear increase in high-affinity IgG1 titre by day 6 (for d6NB vs d6B). Notably, high-affinity IgG1 titres on day 4 were comparable between primed and boosted groups, suggesting that the earliest secondary response phase had not differed from the residual primary-response dynamics.

The total titre of NP_2-specific IgM (Figure 5.11F) was about 10-fold lower compared to the NP_2-specific IgG1 titre. Although no statistically significant differences were observed among the groups, the single high response detected in the d6NB group suggests that additional biological variability may exist, which could be clarified by increasing the sample size. Furthermore, comparison of the relative titres of IgG1 and IgM indicates that antibody secretion in the d6NB group was comparable between these isotypes, with both reaching approximately 1.5×10^2. The present analysis captures only the titres of high-affinity IgG1 and high-avidity IgM NP-specific antibodies. Apart from repeating these data with a second cohort of animals, it would be recommended to assess titres to high valency NP-antigen (e.g., NP_{15} or NP_{27}) and analyse the NP_2/NP_{15} or NP_2/NP_{27} relative titre ratios to directly evaluate whether boosting enhanced antibody affinity compared to the primary response.

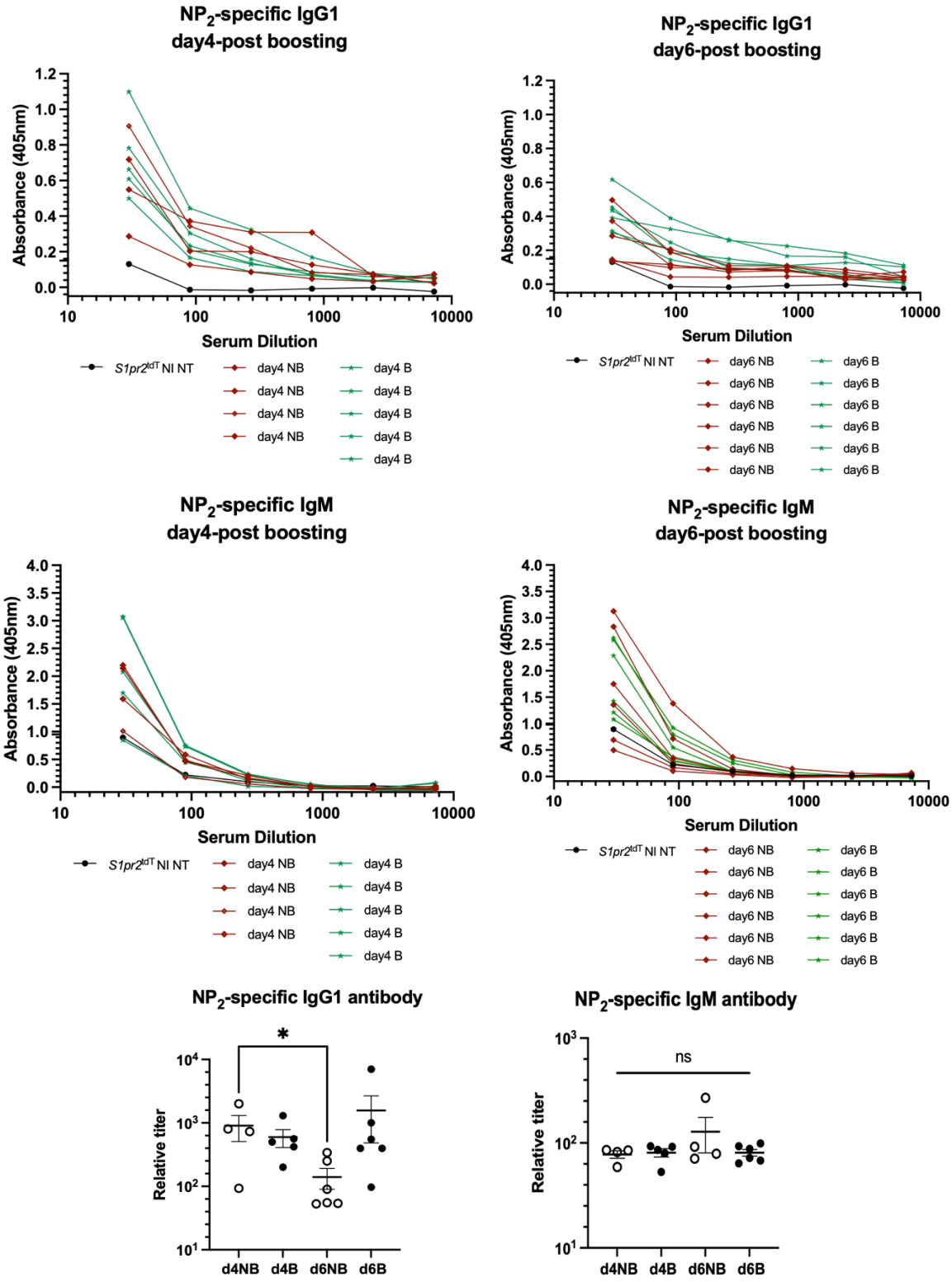


Figure 5.11. Affinity of IgG1 and IgM antibody response after recall responses to NP_{27}-KLH immunisation.

Mice were immunised as described in Figure 5.1. Sera samples were collected on day 4 and day 6 post-boosting. NP_2-specific IgM and IgG1 titres were determined by

ELISA. **(A)** Dilution curve for NP_2-specific IgG1 on day 4 post-boosting. **(B)** Dilution curve for NP_2-specific IgG1 on day 6 post-boosting. **(C)** Dilution curve for NP_2-specific IgM on day 4 post-boosting. **(D)** Dilution curve for NP_2-specific IgM on day 6 post-boosting. **(E)** Relative titre of NP_2-specific IgG1 levels at days 4 and 6 pre- and post-boosting with NP_{27}-KLH (mean ± SEM). **(F)** Relative titre of NP_2-specific IgM levels at days 4 and 6 pre- and post-boosting with NP_{27}-KLH (mean ± SEM).
Samples with absorbance values that did not exceed the threshold of detection were considered negative. Each symbol represents one mouse. Data were obtained from a single experiment, with n = 4 and 5 mice for non-boosted and boosted, respectively, on day 4, and n = 6 mice for both groups, non-boosted and boosted, on day 6. Statistical tests were performed by an unpaired parametric t-test. n.s. $p > 0.05$, * $p < 0.05$.

5.3 Discussion.

Recall B cell responses are studied because they determine how well humoral immunity improves after the first exposure. This study focused on antigen localisation rather than the fact that a boost is given at all, which allow to study how the location of the antigen delivery structures the recall response. Therefore, this study investigated an early time window to track memory response in the draining and distal lymph nodes at 4 and 6 days following a secondary NP_{27}-KLH challenge, delivered 30 days after the primary immunisation. During this timeframe, the local boosting more efficiently reactivates memory B cells than boosting at a distal site. The presence of some memory B cells and PCs in the distal lymph nodes—without direct antigen priming—indicates a degree of systemic memory dissemination. These observations agree with earlier studies that the strength of the local (ipsilateral) site is stronger than the distal (contralateral) site [219, 223], indicating that memory responses are not equally distributed across lymph nodes.

The GC response pattern in this study showed that local (ipsilateral) GC expansion differed significantly between after priming and after boosting, with GC responses remaining elevated after priming and failing to expand after boosting. This finding contrasts with the previous report by Kuraoka et al. (2022) [218], where GC responses expanded after boosting compared to priming at a similar time interval of 30 days. The potential explanation for this discrepancy lies in differences in antigen nature, including its form, persistence, and epitope accessibility. In the present study, priming was performed using NP-KLH; in contrast, Kuraoka et al. used hemagglutinin proteins (HA H1). NP-KLH derives broader epitope spreading due to its hapten-carrier nature, which

promotes antigen retention and prolonged availability on FDCs, whereas the epitope accessibility is restricted in HA H1. It has been reported that a longer time interval between initial and subsequent immunisations augmented recall responses [236]. However, GC responses consistently expanded after HA H1 across extended intervals up to 14 weeks post-priming [218], indicating the differences in GC kinetics are likely to account for antigen nature.

This study revealed the presence of ongoing GC B cells in the primed distal lymph node at day 34, which increased after boosting. This observation can be related to how the antigen distributes after immunisation. When antigens are linked to large protein carriers, any fraction that is not retained in the draining lymph node can enter the circulation via the thoracic duct. If the carrier persists in the blood for a longer time, it may accumulate in distal lymphoid organs such as the spleen and non-draining lymph nodes. This allows antigen to be presented at sites far from the injection point, potentially supporting GC responses in these distal locations [237, 238].

In addition to antigen distribution, memory B cell dynamics may also contribute to this response. A study by McHeyzer-Williams et al. showed that secondary GCs can form de novo from pre-existing class-switched memory B cells [214]. Based on this, it can be suggested that recirculating memory B cells can seed new GC responses in distal lymph nodes following priming. The disappearance of GC B cells in the distal lymph nodes by day 36 after priming likely reflects the lower antigen availability. While FDCs can retain antigen for extended periods, the amount of antigen reaching distal lymph nodes by day 36 eventually falls below the activation threshold required to sustain GC

B cell survival. Together, these findings suggest that the increased GC activity observed in primed distal lymph nodes may result from a combination of antigen availability in non-draining sites and the recruitment of circulating memory B cells that initiate secondary GC reaction.

Studying memory B cell dissemination to distal lymph nodes answers how immunity becomes systemic rather than local. Memory B cells are actively guided to distal sites—not just passively distributed—and depend on chemokine gradients such as CCR7/CCL19/21 [239]. A previous study showed that distal lymph nodes are capable of sustaining low-level memory responses for up to 16 weeks after priming in response to TNP-KLH [223]. When distal lymph nodes were directly boosted, these lymph nodes displayed an enhanced response; however, this did not alter the magnitude of the memory response within the site. Moreover, the responsiveness of the distal lymph nodes can be improved when mice are given an increasing dose of antigen or boosted with a heterologous antigen—hapten-carrier protein; however, it is not more robust than that observed in the draining lymph nodes [223]. In contrast, boosting with a heterologous antigen—as in antigenic drift—led to a significant reduction in memory B cell reactivation and weaker GC responses in the distal lymph nodes [218].

GC-derived $CD38^{+}$ $S1pr2^{tdT+}$ memory B cells exit from the GC as precursors supported by the expression of CCR6 [156]; however, memory B cells can be classified further depending on the expression of CD80 and PDL2 [151, 152] and CD73 [153]. GC-derived $CD80^{+}$ $PDL2^{+}$ memory B cells differentiate into $IgG1^{+}$ PBs [152], upregulating IRF4 and Blimp-1 [170]. The location of antigen-specific memory B cells after

immunisation has also been investigated. This study showed that NP-specific GC-derived memory B cells were predominantly retained in the original draining lymph node rather than disseminating to distal lymph nodes during the early recall response. Boosting did not substantially increase their numbers in the draining site by day 6. Distal recruitment of NP-specific memory B cells appeared very limited. However, the interpretation of these findings remains limited, as NP-specific memory B cells were not analysed at earlier time points following boosting, where transient expansion may have occurred. In Shenoy et al.'s study, they tracked the numbers and localisation of the immunising antigen-specific B cells to investigate whether memory B cells are retained in the initial antigen site or migrate to other tissues and how long they persist [219]. Regarding DrLNs and DisLNs, they found that large numbers of antigen-specific B cells were present in the DrLNs and were too low to be detected in DisLNs two weeks after immunisation. The number of antigen-specific memory B cells then dramatically declined ~10-fold by week 13 and ~50-fold by week 17 [219]. Other studies indicate that the retention of antigen-binding in the DrLNs for a long time can influence how memory B cells behave in the DrLNs, especially after a secondary response to the same antigen [218].

A study by Shenoy et al. explains why memory B cells do not effectively populate distal lymph nodes after priming, even if the antigen is reintroduced at those sites [219]. They demonstrated that most memory B cells adopt a $CD62L^{lo}$ phenotype, which limits their ability to enter resting lymph nodes under non-inflammatory conditions. Consequently, boosting needs inflammation to access distal lymph nodes, such as by co-administering LPS at the boost site [219]. However, distal lymph nodes fail to mount

an effective recall response when the spleen is removed or when TLR4 signalling is deficient, even in the presence of LPS [219]. These findings suggest that memory B cells do not efficiently access distal lymph nodes under steady-state conditions and that the spleen acts as a major reservoir supporting secondary responses [219, 223]. Consistent with this, stronger recall responses were observed when boosting was delivered i.p. compared with the plantar surface of the rear foot. Shenoy et al. (2012) further demonstrated that neither the BM nor the original draining lymph nodes contributed significantly to secondary antibody responses once the primary response had waned, with BM-resident memory B cells present at very low frequencies and contributing minimally to recall antibody production [219].

The participation of previously GC-experienced *S1pr2*$^{tdT+}$ B cells in recall GCs in the present study was very low at the DrLN-B but increased at the DisLN-B compared with DisLN-NB baseline, although their overall frequencies remain low relative to the draining sites (Figure 5.5). This suggests that boosting promotes at least partial recruitment of GC-experienced cells to distal recall sites. A similar participation interpretation was reported in the CGG model by Mesin et al. (2020), in which boosting was performed 30 days after priming, where primary GCs were still detectable [64]. Together, these findings support the interpretation that GC re-entry during recall remains limited even when residual primary GCs are still present at the time of boosting.

Moreover, this study revealed the persistence of CD138^{+} PB-PCs in DisLN-NB mice supports their role as an independent component of immunological memory,

contributing to long-term immune readiness against previously encountered antigens [233]. This finding suggests that DisLN-NB can function as a secondary survival niche, where a small population of PB-PCs migrates and persists over time. Following re-exposure to the same antigen, the survival dynamics of PB-PC may be influenced by competition between newly generated and pre-existing PB-PC for limited survival niches [233]. The marked population of GC-matured *S1pr2*$^{tdT+}$ TACI^{+} cells within the CD138^{+} PB-PC compartment, compared with the Fas^{+} GC B cell compartment at day 4, suggests that TACI-mediated signalling is accelerated early after boosting. TACI expression requires sustained BAFF/APRIL signalling to promotes Blimp-1 expression and suppresses Bcl6-biased GC-derived cells, thereby limiting GC retention. The supportive local BAFF/APRIL-rich microenvironment appears to be limited in distal lymph nodes or diminishes over time. Although an increase in GC-derived PB was observed on day 4 after boosting, it was not accompanied by a corresponding rise in serum NP_2-specific IgG1 titres as measured by ELISA. This suggests that early secondary responses are initially characterised by PB expansion, whereas detectable increases in systemic high-affinity antibody titres may lag behind or remain less apparent due to pre-existing circulating antibody generated during the primary response. Alternatively, the apparent lack of increase in NP_2-specific IgG1 may reflect the selective detection of high-affinity antibodies, as an increase in lower-affinity antibodies (e.g., NP15- NP27-binding IgG1) may have occurred but was not assessed in this study. This pattern may also indicate that newly generated PBs require migration and maturation within long-lived PC niches before substantially contributing to circulating antibody levels. Consistent with this interpretation, the mean relative NP_2-specific IgG1 titre showed an upward trend by day 6 (Figure 5.11), although this

increase did not reach statistical significance in this present study. Notably, PB numbers did not differ between primed and boosted groups at this time point.

Pre-existing antibodies generated during the primary response can strongly shape the nature of recall B cell responses following secondary antigen exposure [64, 236, 240]. High-affinity and high-titre antibodies directed against dominant epitopes may limit antigen accessibility through epitope masking and inhibitory FcγRIIb-mediated signalling, a mechanism referred to as negative antibody feedback [236, 240]. This process can restrict further engagement with the same antigenic determinants and alter the composition of recall GC responses. In contrast, broad-binding or lower-affinity antibodies may incompletely mask antigen epitopes, allowing continued antigen accessibility during recall responses [240]. Studies using SARS-CoV models demonstrated that low-affinity IgM antibodies did not efficiently block BCR engagement, thereby permitting ongoing diversification of the B cell response [240]. Together, these findings suggest that the affinity, specificity, and concentration of pre-existing antibodies are important factors that influence recall responses by regulating antigen availability and shaping the secondary B cell responses.

Boosting also alters the balance between GC B cells and memory B cells, with important consequences for affinity maturation. Previous studies demonstrated that GC B cells accumulate substantially more somatic mutation after multiple immunisations than after a single exposure (15.4 mutations after four immunisations vs. 9.3 after one; $p < 0.0001$). Whereas memory B cells show little change in mutation number (3.9 vs. 4.3; $p = 0.460$) and generally maintain low monovalent binding affinity, with some clones detectable only under polyvalent binding conditions [241]. Although

somatic hypermutation was not directly assessed in the present study, several experimental approaches could be used to investigate mutation accumulation in future work. Antigen-specific GC B cells and memory B cells could be isolated by flow cytometric sorting followed by immunoglobulin heavy-chain variable region sequencing to quantify mutation frequencies and clonal evolution. AIRR-seq or single-cell BCR sequencing approaches [22] could further determine whether boosting preferentially expands highly mutated GC-derived clones or recruits less-mutated memory populations. Sequence comparison with germline immunoglobulin genes would enable direct quantification of mutation burden within individual B cell clones and assessment of affinity maturation during recall responses.

The absence of NP-binding GC B cells in the DisLN-B indicates that naive B cells recruited following booster immunisation are unlikely to be specific for the immunodominant NP hapten, which elicited high-affinity antibodies during the primary response, and instead preferentially recognise alternative epitopes on the carrier protein. This observation is consistent with epitope-specific antibody-mediated feedback, whereby antibodies generated during the primary response mask dominant epitopes and limit their accessibility during subsequent antigen encounters. Recent experimental work by Barbulescu et al. demonstrates that antibodies produced during an ongoing immune response selectively suppress GC B cells recognising the same epitope, while sparing clones specific for non-overlapping epitopes, thereby reshaping interclonal competition without reducing overall GC size [184]. In parallel, conceptual frameworks synthesised by Liu et al. propose that such antibody feedback during recall responses biases recruitment towards naive B cells recognising new or previously

subdominant specificities epitopes, thereby promoting epitope spreading [185]. Furthermore, computational modelling by Garg et al. showed that when antibodies reduce the amount of antigen available to B cells, clones that dominated the primary response are more likely to be outcompeted, particularly under conditions of limited antigen access, such as distal lymph nodes [80]. Together, these studies provide a mechanistic explanation for the selective loss of NP-specific GC B cells in DisLN-B, supporting the interpretation that antibody feedback from the primary response redirects recall GC composition toward carrier-derived epitopes rather than reinforcing the original NP-dominant specificity.

Beyond the role of pre-existing antibodies, memory B cells expressing different antibody classes exhibit varying impacts on the recall outcome. Studies using adoptive transfer techniques reveal that memory B cells of varying antibody classes contribute differently to secondary GC formation [212, 213, 242]. IgM memory B cells tend to re-engage in GC reactions, while IgG memory B cells give rise to the PB-PC [212, 213, 242]. Shao et al. (2024) further revealed that this fate decision is not only isotype-dependent but also epigenetically primed—their DNA is already in a state that favours turning on PC genes rapidly during the recall response [213]. IgG^+ memory B cells often express higher levels of Blimp-1, a transcription factor driving PC fate, whereas IgM memory B cells maintain higher expression of GC-supporting factors like BACH2 [212, 213, 242]. Shao et al. (2024) identified IgM^+ memory B cells as $CD80^-PDL2^-$ cells and identified IgG^+ memory B cells as $CD80^+$ $PDL2^+$ cells. This phenotypic distinction reflects the underlying functional programming of memory B cells. Collectively, these studies provide the available background knowledge that highlights the complex mechanisms underlying recall immune responses.

One caveat of these analyses is to investigate the presence of memory B cells in the spleen as the main reservoir of long-lived memory B cells [219, 243]. It has been shown that memory B cells are largely spleen resident after the primary response, and they are long-lived memory B cells at later time points [219].

Expression of tdT driven by *S1pr2* remains permanently active in GC-derived B cells during the active window of tamoxifen following administration. Therefore, primary-activated *S1pr2*$^{tdT+}$ GC B cells observed after boosting are indistinguishable from newly reactivated memory B cells, specifically determining the re-entry primary memory B cells. A time-controlled fate mapping system would help resolve this distinction between primary and secondary memory B cells, as well as GC entrants. Such an approach could utilise the CD73 promoters to drive a fluorescent reporter such as GFP, combined with a Cre-inducible tdT under *S1pr2* control. After the primary immunisation, CD73-expressing cells would be GFP labelled. After secondary immunisation, tamoxifen administration would permanently label only those B cells active at the time by *S1pr2*^{Cre}. Subsequent identification of memory B cells could then be supported by the co-expression of CD80, PDL2 [153]. Such analyses may help to discriminate between functional heterogeneity of GC-derived memory B cell subsets and determine whether specific subsets preferentially contribute to recall responses in the distal site.

The longevity and memory capabilities of PCs play a central role in the maintenance of serological memory by sustaining stable antibody titres over time. By persisting within survival niches, such as lymph nodes, PCs contribute to long-term humoral protection independently of circulating memory B cell populations [233]. Consistent

with studies showing a lack of correlation between memory B cell numbers and serum antibody titres [244], this supports the concept that memory B cells and PCs represent independently regulated compartments of humoral immunity. Therefore, to strengthen the interpretation of recall antibody dynamics, future work should include NP_{15} ELISA to allow calculation of NP_2/NP_{15} affinity ratios and thereby directly assess affinity maturation. Additionally, quantifying antigen-specific Ig production within the draining and distal lymph nodes [218]—rather than relying on peripheral blood titres—would offer deeper insight into how anatomical location shapes the quality and magnitude of the humoral response.

5.4. Conclusion.

This study used homologous NP-KLH prime immunisation at the right site followed by boosting at the same and contralateral sites after a 30-day interval. This design allowed analysis of recall B cell responses within the original draining lymph nodes containing residual GCs and within distal draining lymph nodes likely seeded by circulating memory B cells. The findings support the concept of antibody feedback, suggesting that pre-existing high-titre antibodies and antigen nature shape the magnitude and localisation of the recall response. Together, these findings indicate that recall responses are strongly influenced by the primary immune environment established during the initial immunisation.

Chapter 6. General Discussion and Future Direction.

This thesis initially focused on the *S1pr2*^{CreERT2} *Rosa26*^{LSLtdTomato} *Prdm1*^{GFP} mouse model (HALO/triple mouse model). HALO mice were developed to enable simultaneous identification of GC experience and PC differentiation, allowing early GC-matured PB-PC to be distinguished from EF-derived PB-PC in vivo in response to a single antigen. B cell development in HALO mice was assessed to ensure that combining the *S1pr2*^{CreERT2} *Rosa26*^{LSLtdTomato} and *Prdm1*^{GFP} alleles did not have deleterious effects on overall B cell development in the BM [171]. The transitional and mature peripheral B cell populations in the spleen were also unaffected, indicating that B cell development proceeds normally in HALO mice [171]. Moreover, this model enables long-term tracking of memory B cells and PCs involved in a single immune response. Building on previous studies on HALO mice that used intravenous SRBC immunisation, this work employed further immunisation strategies. In this study, mice were subjected to a primary immunisation with SRBC, with response analysed on days 5, 6, and 8; a primary immunisation with NP_{27}-KLH, analysed on days 10 and 14; and a secondary (boost) immunisation with NP_{27}-KLH, analysed on days 5 and 8 following boosting.

Consistent with previous observations, HALO mice revealed that EF- and GC-derived PB-PCs responses coexist early after immunisation with SRBC, with their relative contributions changing rapidly over time. EF- and GC-matured *S1pr2*$^{tdT+}$ Blimp-1^{GFP+} PB-PC responses were both prominent at day 5; however, GC-derived *S1pr2*$^{tdT+}$ PB-PCs became dominant by day 6 (see section 3.2.1.1). Notably, GC-matured *S1pr2*$^{tdT+}$ Blimp-1^{GFP+} PB-PCs peaked at day 5 (see section 3.2.1.2), coinciding with a peak in

GC-derived CD38^{+} *S1pr2*$^{tdT+}$ Blimp-1^{GFP+} PC precursors (see section 3.2.1.3), while the overall GC response peaked at day 6 (see section 3.2.1.2)—accompanied by an increase in memory B cell output at day 6 (see section 3.2.1.2 Figure 3.8H). Furthermore, the accumulation of GC-matured CD138^{+} TACI^{+} *S1pr2*$^{tdT+}$ Blimp-1^{GFP+} PB-PCs was most evident at day 6, with fully differentiated cells, defined as B220^{lo} CD19^{lo}, emerging predominantly at this time point (see section 3.2.1.5). While the emergence of fully differentiated GC-matured PB-PCs was previously evident at days 6-8 following SRBC immunisation using *S1pr2*^{tdT} fate mapping mice [171], this study confirmed full differentiation in the HALO model at day 6. Analysis at day 8 was limited by the small number of animals available, preventing statistical assessment of this time point. In contrast, following secondary immunisation with NP-KLH, fully differentiated GC-matured PB-PC were detectable at day 8.

As TACI expression is primarily associated with PCs that have undergone class-switch recombination from producing IgM antibodies to other isotypes, such as IgG1 [245-247], these data suggest that both GC-derived B220^{hi} CD19^{hi} CD138^{+} TACI^{+} *S1pr2*$^{tdT+}$ Blimp-1^{GFP+} PB-PCs and GC-matured B220^{lo} CD19^{lo} CD138^{+} TACI^{+} *S1pr2*$^{tdT+}$ Blimp-1^{GFP+} PB-PCs are likely class-switched. However, phenotypic identification alone is insufficient to confirm GC maturation and affinity progression. Definitive validation will therefore require molecular analysis of hallmark somatic hypermutations – specifically the W33L and K59R mutations in the V186.2 heavy chain gene, at day 6 post-immunisation. Importantly, a recent study demonstrated that GCs output clonally diverse PC populations spanning a wide range of antibody affinities, including both high- and low-affinity clones, indicating that acquisition of somatic mutations does not necessarily equate to stringent affinity selection at the point of PC differentiation [105,

107, 108]. Future work arising from these studies should quantify the absolute number of high-versus low-affinity PC exiting GC over time, and the relative contribution of high-versus low-affinity PC to long-term serum antibody levels.

EF and GC responses are parallel but separate differentiation pathways. In this study, a proportion of Blimp-1^{GFP+} PB-PCs was identified within the GC gate (CD138^{-} B220^{+} Fas^{hi}). One possible explanation for this observation is incomplete GC fate mapping, as *S1pr2*^{ERT2Cre} *Rosa26*$^{LSL\text{-}tdT}$-mediated recombination in HALO mice labels approximately 80% of GC B cells. Another explanation is that the relationship between the two differentiation pathways is more dynamic, where EF PCs feed back into GCs. Early after immunisation, a wide range of affinities will similarly be distributed across GC and EF PC compartments [108]. Moreover, GCs are recognised as an open system, permitting the entry of naive or activated low-affinity B cells during ongoing response [248]. As high-affinity antibodies bind and limit antigen availability, they allow B cells with lower affinity to access antigen and Tfh help [248]. Although there is no direct evidence that PC-like features or EF PCs actively feedback into GC, these observations support the concept that EF and GC response are not linear or isolated processes but are instead shaped by cellular interaction and local environmental signals.

IL-21 has dual effects on B cell activation, with its outcome determined by the interaction between CD40 on B cells and CD40L on T cells [38]. When CD40 signalling is present, IL-21 promotes B cell proliferation; however, in the absence of CD40 stimulation, IL-21 instead induces growth arrest or apoptosis. In *Salmonella enterica typhimurium* (*S*Tm) infection, high IL-21 levels skew T cells toward a Th1 fate, which

limits Tfh development [57]. This leads B cells to mount an EF response and a delayed GC response. Whether GCs eventually recover through new Tfh development remains unclear [57]. The HALO mouse model can help fill this understanding by determining how GC and EF pathways contribute to PC output under conditions where Tfh development is disrupted.

The timing of SHM and CSR—whether they occur before or only after GC formation—remains controversial [38]. SHM during the EF response is either absent or occurs only at low levels, as observed in *Ehrlichia muris* and *S*Tm, where the GC response is delayed. SHM requires higher levels of AID than CSR, which explains why SHM is largely associated with GC B cells [249, 250]. In contrast, CSR raises the question of whether it follows two pathways: one associated with the EF response and another with the GC [38]. Liu et al. (1996) detected 5'Sγ-Sμ3' excision circles within GCs in human tonsils [251]. CSR can also occur during the EF response, emerging around 3 days after antigen exposure [40, 69]. Roco et al. (2019) further demonstrated the presence of GLTs as early as 1.5-2.5 days post-immunisation but they could not observe DNA circle in vivo within GC [174]. Within GCs, BACH2 promotes CSR by suppressing Blimp-1 expression [121]. Moreover, IL-4 supports B cell survival and, together with CD40 signalling, drives class switching toward the IgG1 isotype [252, 253]. Therefore, the HALO mouse model enables comparison of SHM frequencies and CSR events between these compartments, especially in response to pathogen infection.

The characterisation of a novel mouse model presents a set of methodological challenges for optimisation. Notably, the time and cost associated with breeding

genetically engineered mice with multiple reporter transgenes, like the HALO mice, restrict the feasibility of repeated optimisation experiments. First, surface immunoglobulin expression has not previously been characterised in the HALO mouse model. Therefore, in this study, IgD, IgM, and IgG1 were initially analysed; however, the resulting data showed inconsistent patterns that were difficult to interpret biologically, and these data were therefore excluded from further analysis. Second, a challenge associated with detecting intercellular IRF4, possibly due to the fixation and permeabilisation process used. After performing the surface staining protocol and applying the viability staining dye, BD Cytofix (4.2% formaldehyde; Cat: 554655 Lot: 2096593) was added at 100 µl for 30 minutes. A 10x permeabilisation buffer was used for washing after each step. Then, cells were incubated with rat serum for 10 minutes. Following this, the cells were stained with purified rat anti-IRF4 at 1/200 for 30 minutes, and after washing, they were incubated with Alexa 647 anti-rat IgG at 1/500. Flow cytometric analysis revealed an unexpectedly high proportion of $IRF4^{+}$ cells within $B220^{+}$ Fas^{hi} GC B cells. Given that IRF4 expression is generally considered low in GC B cells and upregulated during PC differentiation. Simultaneously, the fixation process quenched the fluorescence of GFP and tdTomato, affecting signal intensity. Further optimisation could explore alternative IRF4 staining and tissue fixation methods, including fixation buffer concentration, cross-linking agents, and investigation of antigen retrieval protocols to enhance epitope accessibility and signal detection.

Due to the challenges associated with the breeding of HALO mice, alternative projects were pursued using the $IgMg1AID^{Cre}$ mouse model and the *S1pr2*^{CreERT2} *Rosa26*^{LSLtdTomato} mouse model.

The IgMg1AID^{Cre} mouse model project originated from the potential to reduce IgM^{+} GC B cells and increase the dominance of IgG1^{+} GC B cells in the IgMg1 mouse model. By studying the GC response in IgMg1 mice in the context of AID deficiency, it can isolate the effects of BCR signalling on B cell activation and differentiation without the complicating factor of class switching. The IgMg1AID^{Cre} mouse model strongly supported the hypothesis that increased class-switched IgG1^{+} GC B cells are the primary cause of the reduction of IgM^{+} GC B cells in the original IgMg1 model. Moreover, using the IgMg1AID^{Cre} mouse model allowed us to find that surface IgG1 could still be detected by flow cytometry. However, it is important to note that these IgG1 cells may be incapable of secreting soluble IgG1; therefore, conducting an ELISA is necessary to provide additional evidence. Studies confirmed that IgG1 was present in the immune response to helminth infections using the AID^{CreERT2tdT} mouse model [254]. Similarly, IgG was confirmed using the AID^{CreERT2eYFP} mouse model in the secondary alloantibody response [255]. Therefore, this suggests that the ability to undergo a class switch depends on the functional presence of the AID enzyme itself, not just the AID^{Cre} construct.

The use of the IgMg1AID^{Cre} mouse model paves the way for additional research to explore the properties of the IgMg1 mouse model. For example, B cells lacking AID exhibited higher proliferation and reduced apoptosis upon stimulation, resulting in the formation of a larger GC structure compared to wild-type counterparts [81]. This is also observed in our study. On the other hand, the IgMg1 mouse model exhibited a higher level of apoptosis among GC B cells [200]. The IgMg1AID^{Cre} mouse model showed a reversal or reduction in the abnormal growth of GC with no significant difference from wild-type GC. This raised the question of whether the chimeric BCR in IgMg1 B cells

contributes to the reduced number of GC B cells. Furthermore, IgMg1 B cells exhibit upregulation of oxidative phosphorylation compared to wild-type B cells, which is a consequence of the presence of the IgG1 cytoplasmic tail [200]. To better understand the mechanisms underlying these observations, further studies should focus on investigating the signalling pathway involved in B cell activation and survival in the IgMg1AID^{Cre} mouse model.

The *S1pr2*^{CreERT2} *Rosa26*^{LSLtdTomato} mouse model was used to explore recall immune responses to the same antigen targeting two anatomical sites: the draining LN and the distal LN. This project demonstrated how immune protection established at the site of infection can be translated to a distal site. Sustaining memory responses in distal sites can be boosted through the activation of circulating memory B cells. However, the strength of that response depends on factors such as the availability of Tfh cell help, the memory B cell isotype and affinity, the antigen accessibility and presentation at the recall site, and circulating antibodies that can compete with memory B cells for antigen and modulate access to their BCRs by forming immune complexes [195]. The long-term presence of memory Tfh cells is assumed to correlate positively with the efficacy of draining lymph nodes in a recall response; however, it remains unclear whether this response is consistently stronger than at distal sites and whether memory Tfh cells are required for initiating such recall responses [195]. Future study could address this question using the *S1pr2*^{CreERT2} *Rosa26*^{LSLtdTomato} mouse model to trace and assess the role of memory Tfh cells in recall responses at both draining and distal sites. In parallel, further characterisation of memory B cells—especially those residing at the distal sites—could be achieved through detailed phenotypic analysis, such as CD62L^{lo}, CD80 and PDL2 [213, 219].

In more recent research, innate immune memory is understood as a dual phenomenon that occurs after an initial exposure to both pathogenic and nonpathogenic stimuli [256]. After the first exposure to a stimulus, innate immune cells undergo epigenomic changes that can bias their response towards tolerance or homeostasis, modifying how these cells react in future immune challenges. Research has shown that certain microbiota members or their metabolic byproducts can shape the phenotypic characteristics of innate immune cells. This leads to the development of memory-like states that contribute to responding to later infections and enabling a more proper response. This phenomenon is not absolute, as the same stimulus can give different memory outcomes depending on dose, duration, tissue, and the particular innate cell type involved [256]. Repeated exposure to LPS has been shown to induce endotoxin tolerance, a state in which innate immune cells exhibit reduced inflammatory responses to subsequent stimulation. The immune system's response to re-exposure is context-dependent and can vary in magnitude and quality depending on the pre-existing response established during priming.

Antigen binding is a survival gate. High-affinity NP-binding PCs are preferentially expanded more than low-affinity non-binding PCs [109]. Notably, this expansion continues even after GC depletion and reflects a history of selection in the light zone. This preferential expansion results in enrichment of high-affinity clones within the PC compartment [109]. NP-binding B cells in the GCLZ are protected from apoptosis through BCR signalling [257]. Inhibition of BCR signalling (e.g. via BTK inhibition) increases apoptosis in the LZ B cells, whereas NP-binding B cells exhibit reduced apoptotic levels [257]. Together, these findings indicate that antigen engagement is a critical survival checkpoint for PC and B cells.

Chapter 7. References

1. Deets, K.A. and R.E. Vance, *Inflammasomes and adaptive immune responses.* Nature immunology, 2021. **22**(4): p. 412-422.

2. Jain, A. and C. Pasare, *Innate control of adaptive immunity: beyond the three-signal paradigm.* The Journal of Immunology, 2017. **198**(10): p. 3791-3800.

3. Merad, M., et al., *The Dendritic Cell Lineage: Ontogeny and Function of Dendritic Cells and Their Subsets in the Steady State and the Inflamed Setting.* Annual Review of Immunology, Vol 31, 2013. **31**: p. 563-604.

4. Wang, R., et al., *The interaction of innate immune and adaptive immune system.* MedComm, 2024. **5**(10): p. e714.

5. Commins, S.P., L. Borish, and J.W. Steinke, *Immunologic messenger molecules: Cytokines, interferons, and chemokines.* Journal of Allergy and Clinical Immunology, 2010. **125**(2): p. S53-S72.

6. Soudja, S.M., et al., *Memory-T-Cell-Derived Interferon-γ Instructs Potent Innate Cell Activation for Protective Immunity.* Immunity, 2014. **40**(6): p. 974-988.

7. Ise, W., et al., *T follicular helper cell-germinal center B cell interaction strength regulates entry into plasma cell or recycling germinal center cell fate.* Immunity, 2018. **48**(4): p. 702-715. e4.

8. Zhang, Y., et al., *Plasma cell output from germinal centers is regulated by signals from Tfh and stromal cells.* Journal of Experimental Medicine, 2018. **215**(4): p. 1227-1243.

9. Bendelac, A., P.B. Savage, and L. Teyton, *The biology of NKT cells.* Annu Rev Immunol, 2007. **25**: p. 297-336.

10. Pistoia, V., et al., *Human gammadelta T-Cells: From Surface Receptors to the Therapy of High-Risk Leukemias.* Front Immunol, 2018. **9**: p. 984.

11. Montecino-Rodriguez, E. and K. Dorshkind, *B-1 B cell development in the fetus and adult.* Immunity, 2012. **36**(1): p. 13-21.

12. Pieper, K., B. Grimbacher, and H. Eibel, *B-cell biology and development.* J Allergy Clin Immunol, 2013. **131**(4): p. 959-71.

13. Pillai, S. and A. Cariappa, *The follicular versus marginal zone B lymphocyte cell fate decision.* Nature Reviews Immunology, 2009. **9**(11): p. 767-777.

14. Cariappa, A., et al., *The follicular versus marginal zone B lymphocyte cell fate decision is regulated by Aiolos, Btk, and CD21.* Immunity, 2001. **14**(5): p. 603-615.

15. Vale, A.M., et al., *Development and function of B cell subsets*, in *Molecular biology of B cells*. 2015, Elsevier. p. 99-119.

16. Cerutti, A., M. Cols, and I. Puga, *Marginal zone B cells: virtues of innate-like antibody-producing lymphocytes.* Nature Reviews Immunology, 2013. **13**(2): p. 118-132.

17. Attanavanich, K. and J.F. Kearney, *Marginal zone, but not follicular B cells, are potent activators of naive CD4 T cells.* J Immunol, 2004. **172**(2): p. 803-11.

18. Cyster, J.G. and C.D. Allen, *B cell responses: cell interaction dynamics and decisions.* Cell, 2019. **177**(3): p. 524-540.

19. Woof, J.M. and M.A. Kerr, *The function of immunoglobulin A in immunity.* J Pathol, 2006. **208**(2): p. 270-82.

20. Schroeder, H.W., Jr. and L. Cavacini, *Structure and function of immunoglobulins.* J Allergy Clin Immunol, 2010. **125**(2 Suppl 2): p. S41-52.

21. Collins, A.M., *IgG subclass co-expression brings harmony to the quartet model of murine IgG function.* Immunol Cell Biol, 2016. **94**(10): p. 949-954.

22. Watson, C.T., et al., *Looking to the future of antibody genetics: resolving the roles of immunoglobulin diversity in gene regulation, function, and immunity.* Genes Immun, 2024. **25**(1): p. 92-94.

23. Hasan, A., et al., *Cellular and humoral immune responses in covid-19 and immunotherapeutic approaches.* ImmunoTargets and Therapy, 2021: p. 63-85.

24. Teng, G. and F.N. Papavasiliou, *Immunoglobulin somatic hypermutation.* Annu. Rev. Genet., 2007. **41**(1): p. 107-120.

25. Liu, J.C., et al., *Immunoglobulin class-switch recombination: Mechanism, regulation, and related diseases.* MedComm (2020), 2024. **5**(8): p. e662.

26. Toellner, K.-M., et al., *Immunoglobulin switch transcript production in vivo related to the site and time of antigen-specific B cell activation.* The Journal of experimental medicine, 1996. **183**(5): p. 2303-2312.

27. Currie, E.G., et al., *Protection against Neisseria meningitidis nasopharyngeal colonization relies on antibody opsonization and phagocytosis by neutrophils.* bioRxiv, 2024: p. 2024.09. 11.612551.

28. Bahnan, W., et al., *Spike-dependent opsonization indicates both dose-dependent inhibition of phagocytosis and that non-neutralizing antibodies can confer protection to SARS-CoV-2.* Frontiers in immunology, 2022. **12**: p. 808932.

29. Noviski, M., et al., *IgM and IgD B cell receptors differentially respond to endogenous antigens and control B cell fate.* Elife, 2018. **7**: p. e35074.

30. Diaz, M. and P. Casali, *Somatic immunoglobulin hypermutation.* Current opinion in immunology, 2002. **14**(2): p. 235-240.

31. Hao, Q., et al., *DNA repair mechanisms that promote insertion-deletion events during immunoglobulin gene diversification.* Science immunology, 2023. **8**(81): p. eade1167.

32. Wilson, P.C., et al., *Somatic hypermutation introduces insertions and deletions into immunoglobulin V genes.* Journal of Experimental Medicine, 1998. **187**(1): p. 59-70.

33. Gatto, D. and R. Brink, *The germinal center reaction.* Journal of Allergy and Clinical Immunology, 2010. **126**(5): p. 898-907.

34. Toellner, K.-M., et al., *Low-level hypermutation in T cell–independent germinal centers compared with high mutation rates associated with T cell–dependent germinal centers.* The Journal of experimental medicine, 2002. **195**(3): p. 383-389.

35. Obukhanych, T.V. and M.C. Nussenzweig, *T-independent type II immune responses generate memory B cells.* Journal of Experimental Medicine, 2006. **203**(2): p. 305-310.

36. Garcia de Vinuesa, C., et al., *T-independent type 2 antigens induce B cell proliferation in multiple splenic sites, but exponential growth is confined to extrafollicular foci.* Eur J Immunol, 1999. **29**(4): p. 1314-23.

37. Zhang, J., et al., *B cell memory to thymus-independent antigens type 1 and type 2: the role of lipopolysaccharide in B memory induction.* Eur J Immunol, 1988. **18**(9): p. 1417-24.

38. Wishnie, A.J., et al., *BCR affinity influences TB interactions and B cell development in secondary lymphoid organs.* Frontiers in immunology, 2021. **12**: p. 703918.

39. Wicherska-Pawłowska, K., T. Wróbel, and J. Rybka, *Toll-like receptors (TLRs), NOD-like receptors (NLRs), and RIG-I-like receptors (RLRs) in innate immunity. TLRs, NLRs, and RLRs ligands as immunotherapeutic agents for hematopoietic diseases.* International journal of molecular sciences, 2021. **22**(24): p. 13397.

40. Pone, E.J., et al., *BCR-signalling synergizes with TLR-signalling for induction of AID and immunoglobulin class-switching through the non-canonical NF-κB pathway.* Nature communications, 2012. **3**(1): p. 767.

41. Castigli, E., et al., *Impaired IgA class switching in APRIL-deficient mice.* Proceedings of the National Academy of Sciences, 2004. **101**(11): p. 3903-3908.

42. Groom, J.R., et al., *BAFF and MyD88 signals promote a lupuslike disease independent of T cells.* The Journal of experimental medicine, 2007. **204**(8): p. 1959-1971.

43. Minguet, S., et al., *Enhanced B-cell activation mediated by TLR4 and BCR crosstalk.* European journal of immunology, 2008. **38**(9): p. 2475-2487.

44. Akhter, A., et al., *Concomitant high expression of Toll-like receptor (TLR) and B-cell receptor (BCR) signalling molecules has clinical implications in mantle cell lymphoma.* Hematological Oncology, 2017. **35**(1): p. 79-86.

45. Luo, W. and Q. Yin, *B cell response to vaccination.* Immunological investigations, 2021. **50**(7): p. 780-801.

46. Hong, Y. and K. Kwak, *Both sides now: evolutionary traits of antigens and B cells in tolerance and activation.* Frontiers in Immunology, 2024. **15**: p. 1456220.

47. Übelhart, R., et al., *Responsiveness of B cells is regulated by the hinge region of IgD.* Nature immunology, 2015. **16**(5): p. 534-543.

48. MacLennan, I.C., et al., *Extrafollicular antibody responses.* Immunological reviews, 2003. **194**(1): p. 8-18.

49. Callard, R.E. and M.W. Turner, *Cytokines and lg switching: evolutionary divergence between mice and humans.* Immunology Today, 1990. **11**: p. 200-203.

50. Dresser, D.W., H.H. Wortis, and H.R. Anderson, *The effect of pertussis vaccine on the immune response of mice to sheep red blood cells.* Clin Exp Immunol, 1970. **7**(6): p. 817-31.

51. Bouma, H.R., et al., *Hibernation is associated with depression of T-cell independent humoral immune responses in the 13-lined ground squirrel.* Developmental & Comparative Immunology, 2013. **39**(3): p. 154-160.

52. Lee, K.C., et al., *Requirement for accessory cells in the antibody response to T cell-independent antigens in vitro.* European journal of immunology, 1976. **6**(1): p. 63-68.

53. Elsner, R.A. and M.J. Shlomchik, *Germinal Center and Extrafollicular B Cell Responses in Vaccination, Immunity, and Autoimmunity.* Immunity, 2020. **53**(6): p. 1136-1150.

54. Elsner, R.A., et al., *Suppression of Long-Lived Humoral Immunity Following*

Infection. Plos Pathogens, 2015. **11**(7).

55. Hastey, C.J., et al., *Delays and diversions mark the development of B cell responses to Borrelia burgdorferi infection.* J Immunol, 2012. **188**(11): p. 5612-22.

56. Cunningham, A.F., et al., *Salmonella induces a switched antibody response without germinal centers that impedes the extracellular spread of infection.* The Journal of Immunology, 2007. **178**(10): p. 6200-6207.

57. Kim, Y., et al., *IL-21 shapes the B cell response in a context-dependent manner.* Cell Rep, 2025. **44**(1): p. 115190.

58. Li, C., et al., *Ion channel TRPV2 is critical in enhancing B cell activation and function.* Journal of Experimental Medicine, 2024. **221**(3): p. e20221042.

59. Kwak, K., et al., *B cell responses to membrane-presented antigens require the function of the mechanosensitive cation channel Piezo1.* Science signaling, 2023. **16**(804): p. eabq5096.

60. Sacquin, A., M. Gador, and N. Fazilleau, *The strength of BCR signaling shapes terminal development of follicular helper T cells in mice.* European Journal of Immunology, 2017. **47**(8): p. 1295-1304.

61. Chappell, C.P., et al., *Extrafollicular B cell activation by marginal zone dendritic cells drives T cell–dependent antibody responses.* Journal of Experimental Medicine, 2012. **209**(10): p. 1825-1840.

62. Lee, S.K., et al., *B cell priming for extrafollicular antibody responses requires Bcl-6 expression by T cells.* Journal of Experimental Medicine, 2011. **208**(7): p. 1377-1388.

63. Stebegg, M., et al., *Regulation of the Germinal Center Response.* Front Immunol, 2018. **9**: p. 2469.

64. Mesin, L., et al., *Restricted Clonality and Limited Germinal Center Reentry Characterize Memory B Cell Reactivation by Boosting.* Cell, 2020. **180**(1): p. 92-106 e11.

65. Arnon, T.I., et al., *Visualization of splenic marginal zone B-cell shuttling and follicular B-cell egress.* Nature, 2013. **493**(7434): p. 684-8.

66. Schroeder, K., M. Herrmann, and T.H. Winkler, *The role of somatic hypermutation in the generation of pathogenic antibodies in SLE.* Autoimmunity, 2013. **46**(2): p. 121-127.

67. Herlands, R.A., et al., *Anti-chromatin antibodies drive in vivo antigen-specific activation and somatic hypermutation of rheumatoid factor B cells at extrafollicular sites.* European journal of immunology, 2007. **37**(12): p. 3339-3351.

68. Warsame, A., et al., *Monocytoid B cells: an enigmatic B cell subset showing evidence of extrafollicular immunoglobulin gene somatic hypermutation.* Scandinavian journal of immunology, 2012. **75**(5): p. 500-509.

69. Marshall, J.L., et al., *Early B blasts acquire a capacity for Ig class switch recombination that is lost as they become plasmablasts.* European journal of immunology, 2011. **41**(12): p. 3506-3512.

70. Shlomchik, M.J. and F. Weisel, *Germinal center selection and the development of memory B and plasma cells.* Immunological reviews, 2012. **247**(1): p. 52-63.

71. Liu, X., Y. Zhao, and H. Qi, *T-independent antigen induces humoral memory through germinal centers.* Journal of Experimental Medicine, 2022. **219**(3): p. e20210527.

72. Bannard, O., et al., *Germinal center centroblasts transition to a centrocyte phenotype according to a timed program and depend on the dark zone for effective selection.* Immunity, 2013. **39**(5): p. 912-924.

73. Young, C. and R. Brink, *The unique biology of germinal center B cells.* Immunity, 2021. **54**(8): p. 1652-1664.

74. Liu, X., B. Liu, and H. Qi, *Germinal center reaction and output: recent advances.* Curr Opin Immunol, 2023. **82**: p. 102308.

75. Inoue, T., Y. Baba, and T. Kurosaki, *BCR signaling in germinal center B cell selection.* Trends Immunol, 2024. **45**(9): p. 693-704.

76. Song, H., et al., *Antibody feedback and somatic mutation in B cells: regulation of mutation by immune complexes with IgG antibody.* Immunological reviews, 1998. **162**(1): p. 211-218.

77. Zhang, Y., et al., *Germinal center B cells govern their own fate via antibody feedback.* Journal of Experimental Medicine, 2013. **210**(3): p. 457-464.

78. Fukuda, T., et al., *Disruption of the Bcl6 gene results in an impaired germinal center formation.* The Journal of experimental medicine, 1997. **186**(3): p. 439-448.

79. Tas, J.M., et al., *Visualizing antibody affinity maturation in germinal centers.* Science, 2016. **351**(6277): p. 1048-1054.

80. Garg, A.K., et al., *Amount of antigen, T follicular helper cells and affinity of founder cells shape the diversity of germinal center B cells: A computational study.* Frontiers in Immunology, 2023. **14**: p. 1080853.

81. Zaheen, A., et al., *AID constrains germinal center size by rendering B cells susceptible to apoptosis.* Blood, 2009. **114**(3): p. 547-54.

82. Liu, Y., et al., *Mechanism of antigen-driven selection in germinal centres.* Nature, 1989. **342**(6252): p. 929-931.

83. Boulianne, B., et al., *AID and caspase 8 shape the germinal center response through apoptosis.* The Journal of Immunology, 2013. **191**(12): p. 5840-5847.

84. Kräutler, N.J., et al., *Differentiation of germinal center B cells into plasma cells is initiated by high-affinity antigen and completed by Tfh cells.* Journal of Experimental Medicine, 2017. **214**(5): p. 1259-1267.

85. Lee, S.K., et al., *B cell priming for extrafollicular antibody responses requires Bcl-6 expression by T cells.* J Exp Med, 2011. **208**(7): p. 1377-88.

86. Kitano, M., et al., *Bcl6 protein expression shapes pre-germinal center B cell dynamics and follicular helper T cell heterogeneity.* Immunity, 2011. **34**(6): p. 961-72.

87. Moriyama, S., et al., *Sphingosine-1-phosphate receptor 2 is critical for follicular helper T cell retention in germinal centers.* Journal of Experimental Medicine, 2014. **211**(7): p. 1297-1305.

88. Choi, Y.S., et al., *ICOS receptor instructs T follicular helper cell versus effector cell differentiation via induction of the transcriptional repressor Bcl6.* Immunity, 2011. **34**(6): p. 932-946.

89. Xu, H., et al., *Follicular T-helper cell recruitment governed by bystander B cells and ICOS-driven motility.* Nature, 2013. **496**(7446): p. 523-7.

90. Merkenschlager, J., et al., *Dynamic regulation of TFH selection during the germinal centre reaction.* Nature, 2021. **591**(7850): p. 458-463.

91. Weinstein, J.S., et al., *TFH cells progressively differentiate to regulate the germinal center response.* Nature immunology, 2016. **17**(10): p. 1197-1205.

92. Yeh, C.-H., et al., *Primary germinal center-resident T follicular helper cells are a physiologically distinct subset of CXCR5hiPD-1hi T follicular helper cells.* Immunity, 2022. **55**(2): p. 272-289. e7.

93. Choi, J., S. Crotty, and Y.S. Choi, *Cytokines in Follicular Helper T Cell Biology in Physiologic and Pathologic Conditions.* Immune Netw, 2024. **24**(1): p. e8.

94. Zotos, D., et al., *IL-21 regulates germinal center B cell differentiation and proliferation through a B cell–intrinsic mechanism.* Journal of Experimental Medicine, 2010. **207**(2): p. 365-378.

95. Chen, Z., et al., *Heparan sulfate regulates IL-21 bioavailability and signal strength that control germinal center B cell selection and differentiation.* Science immunology, 2023. **8**(80): p. eadd1728.

96. Crotty, S., R.J. Johnston, and S.P. Schoenberger, *Effectors and memories: Bcl-6 and Blimp-1 in T and B lymphocyte differentiation.* Nature immunology, 2010. **11**(2): p. 114-120.

97. Johnston, R.J., et al., *Bcl6 and Blimp-1 are reciprocal and antagonistic regulators of T follicular helper cell differentiation.* Science, 2009. **325**(5943): p. 1006-1010.

98. Suan, D., C. Sundling, and R. Brink, *Plasma cell and memory B cell differentiation from the germinal center.* Current opinion in immunology, 2017. **45**: p. 97-102.

99. Turner, J.S., F. Ke, and I.L. Grigorova, *B cell receptor crosslinking augments germinal center B cell selection when T cell help is limiting.* Cell reports, 2018. **25**(6): p. 1395-1403. e4.

100. Victora, G.D., et al., *Germinal center dynamics revealed by multiphoton microscopy with a photoactivatable fluorescent reporter.* Cell, 2010. **143**(4): p. 592-605.

101. Schwickert, T.A., et al., *In vivo imaging of germinal centres reveals a dynamic open structure.* Nature, 2007. **446**(7131): p. 83-87.

102. Chen, S.T., et al., *B cell receptor signaling in germinal centers prolongs survival and primes B cells for selection.* Immunity, 2023. **56**(3): p. 547-561. e7.

103. Mayer, C.T., et al., *The microanatomic segregation of selection by apoptosis in the germinal center.* Science, 2017. **358**(6360).

104. He, C., et al., *The balance between conventional and unconventional T follicular helper cells influences autoreactive B cell responses.* Cell Reports, 2025. **44**(5).

105. Sprumont, A., et al., *Germinal centers output clonally diverse plasma cell populations expressing high- and low-affinity antibodies.* Cell, 2023. **186**(25): p. 5486-5499 e13.

106. Nakagawa, R., et al., *Permissive selection followed by affinity-based proliferation of GC light zone B cells dictates cell fate and ensures clonal breadth.* Proc Natl Acad Sci U S A, 2021. **118**(2).

107. Tachó-Piñot, R. and C.G. Vinuesa, *Affinity-independent plasma cell differentiation in germinal centers.* Trends in Immunology, 2024.

108. Sutton, H.J., et al., *Lack of affinity signature for germinal center cells that have initiated plasma cell differentiation.* Immunity, 2024. **57**(2): p. 245-255. e5.

109. MacLean, A.J., et al., *Affinity maturation of antibody responses is mediated by differential plasma cell proliferation.* Science, 2025. **387**(6732): p. 413-420.

110. Sundling, C., et al., *Positive selection of IgG(+) over IgM(+) B cells in the germinal center reaction.* Immunity, 2021. **54**(5): p. 988-1001 e5.

111. Shehata, L., et al., *Interleukin-4 downregulates transcription factor BCL6 to promote memory B cell selection in germinal centers.* Immunity, 2024. **57**(4): p. 843-858. e5.

112. Yam-Puc, J.C., et al., *Enhanced BCR signaling inflicts early plasmablast and germinal center B cell death.* Iscience, 2021. **24**(2).

113. Binet, L., et al., *Specific pre-plasma cell states and local proliferation at the dark zone–medulla interface characterize germinal center-derived plasma cell differentiation in lymph node.* bioRxiv, 2024: p. 2024.07. 26.605240.

114. Laidlaw, B.J. and J.G. Cyster, *Transcriptional regulation of memory B cell differentiation.* Nat Rev Immunol, 2021. **21**(4): p. 209-220.

115. Nutt, S.L., et al., *The genetic network controlling plasma cell differentiation.* Semin Immunol, 2011. **23**(5): p. 341-9.

116. Nutt, S.L., et al., *Pax5 determines the identity of B cells from the beginning to the end of B-lymphopoiesis.* Int Rev Immunol, 2001. **20**(1): p. 65-82.

117. Shi, W., et al., *Transcriptional profiling of mouse B cell terminal differentiation defines a signature for antibody-secreting plasma cells.* Nat Immunol, 2015. **16**(6): p. 663-73.

118. Ye, B.H., et al., *The BCL-6 proto-oncogene controls germinal-centre formation and Th2-type inflammation.* Nat Genet, 1997. **16**(2): p. 161-70.

119. Muto, A., et al., *The transcriptional programme of antibody class switching involves the repressor Bach2.* Nature, 2004. **429**(6991): p. 566-71.

120. Recaldin, T. and D.J. Fear, *Transcription factors regulating B cell fate in the germinal centre.* Clin Exp Immunol, 2016. **183**(1): p. 65-75.

121. Muto, A., et al., *Bach2 represses plasma cell gene regulatory network in B cells to promote antibody class switch.* EMBO J, 2010. **29**(23): p. 4048-61.

122. Cattoretti, G., et al., *BCL-6 protein is expressed in germinal-center B cells.* 1995.

123. Basso, K., et al., *Integrated biochemical and computational approach identifies BCL6 direct target genes controlling multiple pathways in normal germinal center B cells.* Blood, The Journal of the American Society of Hematology, 2010. **115**(5): p. 975-984.

124. Tunyaplin, C., et al., *Direct repression of prdm1 by Bcl-6 inhibits plasmacytic differentiation.* The Journal of Immunology, 2004. **173**(2): p. 1158-1165.

125. Bollig, N., et al., *Transcription factor IRF4 determines germinal center formation through follicular T-helper cell differentiation.* Proceedings of the National Academy of Sciences, 2012. **109**(22): p. 8664-8669.

126. Ochiai, K., et al., *Transcriptional regulation of germinal center B and plasma cell fates by dynamical control of IRF4.* Immunity, 2013. **38**(5): p. 918-929.

127. Song, S. and P.D. Matthias, *The transcriptional regulation of germinal center formation.* Frontiers in immunology, 2018. **9**: p. 2026.

128. Klein, U., et al., *Transcription factor IRF4 controls plasma cell differentiation and class-switch recombination.* Nat Immunol, 2006. **7**(7): p. 773-82.

129. Sciammas, R., et al., *Graded expression of interferon regulatory factor-4 coordinates isotype switching with plasma cell differentiation.* Immunity, 2006. **25**(2): p. 225-236.

130. Manakkat Vijay, G.K. and H. Singh, *Cell fate dynamics and genomic programming of plasma cell precursors.* Immunological reviews, 2021. **303**(1): p. 62-71.

131. Kallies, A., et al., *Initiation of plasma-cell differentiation is independent of the transcription factor Blimp-1.* Immunity, 2007. **26**(5): p. 555-566.

132. Tellier, J., et al., *Blimp-1 controls plasma cell function through the regulation of immunoglobulin secretion and the unfolded protein response.* Nature immunology, 2016. **17**(3): p. 323-330.

133. Shinnakasu, R., et al., *Regulated selection of germinal-center cells into the memory B cell compartment.* Nature immunology, 2016. **17**(7): p. 861-869.

134. Chiu, Y.K., et al., *Transcription factor ABF-1 suppresses plasma cell differentiation but facilitates memory B cell formation.* J Immunol, 2014. **193**(5): p. 2207-17.

135. Wang, Y., et al., *Germinal-center development of memory B cells driven by IL-9 from follicular helper T cells.* Nature immunology, 2017. **18**(8): p. 921-930.

136. Jash, A., et al., *ZBTB32 Restricts the Duration of Memory B Cell Recall Responses.* J Immunol, 2016. **197**(4): p. 1159-68.

137. Huang, C., et al., *Cooperative transcriptional repression by BCL6 and BACH2 in germinal center B-cell differentiation.* Blood, 2014. **123**(7): p. 1012-20.

138. Miura, Y., et al., *Bach2 Promotes B Cell Receptor-Induced Proliferation of B Lymphocytes and Represses Cyclin-Dependent Kinase Inhibitors.* J Immunol, 2018. **200**(8): p. 2882-2893.

139. Tangye, S.G., *Staying alive: regulation of plasma cell survival.* Trends Immunol, 2011. **32**(12): p. 595-602.

140. Eslami, M., et al., *Unique and redundant roles of mouse BCMA, TACI, BAFF, APRIL, and IL-6 in supporting antibody-producing cells in different tissues.* Proc Natl Acad Sci U S A, 2024. **121**(29): p. e2404309121.

141. Cassese, G., et al., *Plasma cell survival is mediated by synergistic effects of cytokines and adhesion-dependent signals.* The Journal of Immunology, 2003. **171**(4): p. 1684-1690.

142. Hauser, A.E., et al., *Chemotactic responsiveness toward ligands for CXCR3 and CXCR4 is regulated on plasma blasts during the time course of a memory immune response.* The Journal of Immunology, 2002. **169**(3): p. 1277-1282.

143. Jelínek, T., et al., *Current applications of multiparameter flow cytometry in plasma cell disorders.* Blood cancer journal, 2017. **7**(10): p. e617-e617.

144. Sanz, I., et al., *Challenges and opportunities for consistent classification of human B cell and plasma cell populations.* Frontiers in immunology, 2019. **10**: p. 2458.

145. Liu, L., K. Takeda, and M. Akkoyunlu, *Disease stage-specific pathogenicity of CD138 (Syndecan 1)-expressing T cells in systemic lupus erythematosus.* Frontiers in Immunology, 2020. **11**: p. 1569.

146. McCarron, M.J., P.W. Park, and D.R. Fooksman, *CD138 mediates selection of mature plasma cells by regulating their survival.* Blood, The Journal of the American Society of Hematology, 2017. **129**(20): p. 2749-2759.

147. Meyer-Hermann, M., et al., *A theory of germinal center B cell selection, division, and exit.* Cell reports, 2012. **2**(1): p. 162-174.

148. Pracht, K., et al., *A new staining protocol for detection of murine antibody-secreting plasma cell subsets by flow cytometry.* European journal of immunology, 2017. **47**(8): p. 1389-1392.

149. Gagro, A., et al., *Naive and memory B cells respond differentially to T-dependent signaling but display an equal potential for differentiation toward the centroblast-restricted CD77/globotriaosylceramide phenotype.* European journal of immunology, 2003. **33**(7): p. 1889-1898.

150. Agematsu, K., et al., *CD27: a memory B-cell marker.* Immunology today, 2000. **21**(5): p. 204-206.

151. Zuccarino-Catania, G.V., et al., *CD80 and PD-L2 define functionally distinct memory B cell subsets that are independent of antibody isotype.* Nature immunology, 2014. **15**(7): p. 631-637.

152. Callahan, D., et al., *Memory B cell subsets have divergent developmental origins that are coupled to distinct imprinted epigenetic states.* Nature immunology, 2024. **25**(3): p. 562-575.

153. Cancro, M.P. and M.M. Tomayko, *Memory B cells and plasma cells: The differentiative continuum of humoral immunity.* Immunological reviews, 2021. **303**(1): p. 72-82.

154. Tomayko, M.M., et al., *Roles of bone morphogenetic protein receptor 1a in germinal centers and long-lived humoral immunity.* Immunohorizons, 2021. **5**(5): p. 284-297.

155. Weisel, F. and M. Shlomchik, *Memory B Cells of Mice and Humans.* Annu Rev Immunol, 2017. **35**: p. 255-284.

156. Suan, D., et al., *CCR6 Defines Memory B Cell Precursors in Mouse and Human Germinal Centers, Revealing Light-Zone Location and Predominant Low Antigen Affinity.* Immunity, 2017. **47**(6): p. 1142-1153 e4.

157. Takatsuka, S., et al., *IL-9 receptor signaling in memory B cells regulates humoral recall responses.* Nat Immunol, 2018. **19**(9): p. 1025-1034.

158. Madisen, L., et al., *A robust and high-throughput Cre reporting and characterization system for the whole mouse brain.* Nature neuroscience, 2010. **13**(1): p. 133-140.

159. Kallies, A., et al., *Plasma cell ontogeny defined by quantitative changes in blimp-1 expression.* The Journal of experimental medicine, 2004. **200**(8): p. 967-977.

160. Ramiro, A.R., et al., *AID is required for c-myc/IgH chromosome translocations in vivo.* Cell, 2004. **118**(4): p. 431-438.

161. Zhang, L., *Characterisation of anergic B cells in a new mouse model with altered B cell receptor signalling.*, in *Immunology and Immunotherapy*. 2019, University of Birmingham.

162. Titford, M., *Progress in the development of microscopical techniques for diagnostic pathology.* Journal of histotechnology, 2009. **32**(1): p. 9-19.

163. Kusser, K.L. and T.D. Randall, *Simultaneous detection of EGFP and cell surface markers by fluorescence microscopy in lymphoid tissues.* Journal of Histochemistry & Cytochemistry, 2003. **51**(1): p. 5-14.

164. Iyiola, S. and G. Avwioro, *A new haematoxylin stain for the demonstration of nuclear and extra nuclear substances.* Journal of Pharmacy and Clinical Sciences, 2011. **1**: p. 20-3.

165. Cai, H., J. Caswell, and J. Prescott, *Nonculture molecular techniques for diagnosis of bacterial disease in animals: a diagnostic laboratory perspective.* Veterinary pathology, 2014. **51**(2): p. 341-350.

166. Wilmore, J.R., D.D. Jones, and D. Allman, *Protocol for improved resolution of plasma cell subpopulations by flow cytometry.* Eur J Immunol, 2017. **47**(8): p. 1386-1388.

167. McAllister, E.J., et al., *New methods to analyze B cell immune responses to thymus-dependent antigen sheep red blood cells.* The Journal of Immunology, 2017. **199**(8): p. 2998-3003.

168. Sze, D.M., et al., *Intrinsic constraint on plasmablast growth and extrinsic limits of plasma cell survival.* J Exp Med, 2000. **192**(6): p. 813-21.

169. Haberman, A.M., et al., *Germinal center B cell initiation, GC maturation, and the coevolution of its stromal cell niches.* Immunological reviews, 2019. **288**(1): p. 10-27.

170. Laidlaw, B.J., et al., *The Eph-related tyrosine kinase ligand Ephrin-B1 marks germinal center and memory precursor B cells.* Journal of Experimental Medicine, 2017. **214**(3): p. 639-649.

171. Price, M.J., *MUrine tools to catch high-affinity plasma cells (MUTCHAP)*. 2021, University of Birmingham.

172. Stoler-Barak, L., et al., *B cell dissemination patterns during the germinal center reaction revealed by whole-organ imaging.* Journal of Experimental Medicine, 2019. **216**(11): p. 2515-2530.

173. Calame, K.L., *Plasma cells: finding new light at the end of B cell development.* Nature immunology, 2001. **2**(12): p. 1103-1108.

174. Roco Alegre, J.E., et al., *Class-Switch Recombination Occurs Infrequently in Germinal Centers.* 2019.

175. Wolniak, K.L., R.J. Noelle, and T.J. Waldschmidt, *Characterization of (4-hydroxy-3-nitrophenyl) acetyl (NP)-specific germinal center B cells and antigen-binding B220− cells after primary NP challenge in mice.* The Journal of Immunology, 2006. **177**(4): p. 2072-2079.

176. O'Connor, B.P., M. Cascalho, and R.J. Noelle, *Short-lived and long-lived bone marrow plasma cells are derived from a novel precursor population.* J Exp Med, 2002. **195**(6): p. 737-45.

177. Sander, S., et al., *PI3 kinase and FOXO1 transcription factor activity differentially control B cells in the germinal center light and dark zones.* Immunity, 2015. **43**(6): p. 1075-1086.

178. Ademokun, A.A. and D. Dunn-Walters, *Immune responses: primary and secondary.* eLS, 2010.

179. Martins, G.A., et al., *Transcriptional repressor Blimp-1 regulates T cell homeostasis and function.* Nature immunology, 2006. **7**(5): p. 457-465.

180. Wilmore, J.R., D.D. Jones, and D. Allman, *Improved resolution of plasma cell subpopulations by flow cytometry.* European journal of immunology, 2017. **47**(8): p. 1386.

181. Liu, Y.J., et al., *Sites of specific B cell activation in primary and secondary responses to T cell-dependent and T cell-independent antigens.* European journal of immunology, 1991. **21**(12): p. 2951-2962.

182. Jacob, J., R. Kassir, and G. Kelsoe, *In situ studies of the primary immune response to (4-hydroxy-3-nitrophenyl) acetyl. I. The architecture and dynamics of responding cell populations.* Journal of Experimental Medicine, 1991. **173**(5): p. 1165-1175.

183. Donocoff, R.S., et al., *Optimization of tamoxifen-induced Cre activity and its effect on immune cell populations.* Scientific reports, 2020. **10**(1): p. 15244.

184. Barbulescu, A., et al., *Antibody-mediated feedback modulates interclonal competition in the germinal center.* bioRxiv, 2025: p. 2025.11. 06.686519.

185. Liu, S., Y. Zhang, and K.M. Toellner, *Mastering Immunity: Antibody Feedback as a Driver of Germinal Center Fate and Vaccine Responses.* European Journal of Immunology, 2025. **55**(12): p. e70108.

186. Wu, A. and B.Y. Kim, *Affinity-dependent local antibody feedback shapes germinal centre dynamics: Preprint watch.* Nature Reviews Immunology, 2026: p. 1-1.

187. Mao, X., et al., *Activation of EGFP expression by Cre-mediated excision in a new ROSA26 reporter mouse strain.* Blood, The Journal of the American Society of Hematology, 2001. **97**(1): p. 324-326.

188. Koike, T., et al., *Progressive differentiation toward the long-lived plasma cell compartment in the bone marrow.* Journal of Experimental Medicine, 2022. **220**(2): p. e20221717.

189. Manakkat Vijay, G.K., et al., *Temporal dynamics and genomic programming of plasma cell fates.* Nat Immunol, 2024. **25**(6): p. 1097-1109.

190. Furukawa, K., et al., *Junctional amino acids determine the maturation pathway of an antibody.* Immunity, 1999. **11**(3): p. 329-338.

191. Allen, D., et al., *Antibody engineering for the analysis of affinity maturation of an anti-hapten response.* The EMBO journal, 1988. **7**(7): p. 1995-2001.

192. Arce, S., et al., *CD38 low IgG-secreting cells are precursors of various CD38 high-expressing plasma cell populations.* Journal of Leucocyte Biology, 2004. **75**(6): p. 1022-1028.

193. Benkisser-Petersen, M., et al., *Spleen tyrosine kinase is involved in the CD38 signal transduction pathway in chronic lymphocytic leukemia.* PLoS One, 2016. **11**(12): p. e0169159.

194. Wong, R., et al., *Affinity-restricted memory B cells dominate recall responses to heterologous flaviviruses.* Immunity, 2020. **53**(5): p. 1078-1094. e7.

195. Syeda, M.Z., et al., *B cell memory: from generation to reactivation: a multipronged defense wall against pathogens.* Cell Death Discovery, 2024. **10**(1): p. 117.

196. Frölich, D., et al., *Secondary immunization generates clonally related antigen-specific plasma cells and memory B cells.* The Journal of Immunology, 2010. **185**(5): p. 3103-3110.

197. Huang, H.-Y., et al., *Identification of a new subset of lymph node stromal cells involved in regulating plasma cell homeostasis.* Proceedings of the National Academy of Sciences, 2018. **115**(29): p. E6826-E6835.

198. Sun, W., et al., *BCR Composition and Structure*, in *B Cell Activation in Biology and in Disease*. 2025, Springer. p. 5-10.

199. Zhang, L., *Characterisation of anergic B cells in a new mouse model with altered B cell receptor signalling*. 2019, University of Birmingham.

200. Hudson, A.R., *B cell development, activation, and autoimmunity in mice with altered B cell receptor signalling*. 2023, University of Birmingham.

201. Muramatsu, M., et al., *Class switch recombination and hypermutation require activation-induced cytidine deaminase (AID), a potential RNA editing enzyme.* Cell, 2000. **102**(5): p. 553-563.

202. Zaheen, A. and A. Martin, *Activation-induced cytidine deaminase and aberrant germinal center selection in the development of humoral autoimmunities.* The American journal of pathology, 2011. **178**(2): p. 462-471.

203. Yamada, A., et al., *Dual Role of Fas/FasL-Mediated Signal in Peripheral Immune Tolerance.* Front Immunol, 2017. **8**: p. 403.

204. Fagarasan, S., et al., *Critical roles of activation-induced cytidine deaminase in the homeostasis of gut flora.* Science, 2002. **298**(5597): p. 1424-7.

205. Elliot, T.A.E., et al., *Nur77-Tempo mice reveal T cell steady state antigen recognition.* Discov Immunol, 2022. **1**(1): p. kyac009.

206. Xie, W., K. Wucherpfennig, and D.J. Patel, *A structural platform for B cell receptor signaling.* Cell Research, 2023. **33**(2): p. 95-96.

207. Harzschel, A., et al., *Kindlin-3 maintains marginal zone B cells but confines follicular B cell activation and differentiation.* J Leukoc Biol, 2022. **111**(4): p. 745-758.

208. Wen, L., et al., *Evidence of marginal-zone B cell-positive selection in spleen.* Immunity, 2005. **23**(3): p. 297-308.

209. Kanayama, N., M. Cascalho, and H. Ohmori, *Analysis of marginal zone B cell development in the mouse with limited B cell diversity: role of the antigen receptor signals in the recruitment of B cells to the marginal zone.* J Immunol, 2005. **174**(3): p. 1438-45.

210. Ottens, K. and A.B. Satterthwaite, *IRF4 has a unique role in early B cell development and acts prior to CD21 expression to control marginal zone B cell numbers.* Frontiers in immunology, 2021. **12**: p. 779085.

211. Tsiantoulas, D., et al., *Secreted IgM deficiency leads to increased BCR signaling that results in abnormal splenic B cell development.* Scientific reports, 2017. **7**(1): p. 3540.

212. Kitamura, D., *Mechanisms for the regulation of memory B-cell recall responses in mice.* International immunology, 2021. **33**(12): p. 791-796.

213. Shao, W., et al., *Epigenetic recording of stimulation history reveals BLIMP1–BACH2 balance in determining memory B cell fate upon recall challenge.* Nature Immunology, 2024. **25**(8): p. 1432-1444.

214. McHeyzer-Williams, L.J., et al., *Class-switched memory B cells remodel BCRs within secondary germinal centers.* Nature immunology, 2015. **16**(3): p. 296-305.

215. Turner, J.S., et al., *Human germinal centres engage memory and naive B cells after influenza vaccination.* Nature, 2020. **586**(7827): p. 127-132.

216. Shlomchik, M.J., *Do memory B cells form secondary germinal centers? Yes and no.* Cold Spring Harbor perspectives in biology, 2018. **10**(1): p. a029405.

217. Pape, K.A. and M.K. Jenkins, *Do memory B cells form secondary germinal centers? It depends.* Cold Spring Harbor Perspectives in Biology, 2018. **10**(1): p. a029116.

218. Kuraoka, M., et al., *Recall of B cell memory depends on relative locations of prime and boost immunization.* Sci Immunol, 2022. **7**(71): p. eabn5311.

219. Shenoy, G.N., et al., *Recruitment of memory B cells to lymph nodes remote from the site of immunization requires an inflammatory stimulus.* J Immunol, 2012. **189**(2): p. 521-8.

220. Joo, H.M., Y. He, and M.Y. Sangster, *Broad dispersion and lung localization of virus-specific memory B cells induced by influenza pneumonia.* Proceedings of the National Academy of Sciences, 2008. **105**(9): p. 3485-3490.

221. Allie, S.R., et al., *The establishment of resident memory B cells in the lung requires local antigen encounter.* Nat Immunol, 2019. **20**(1): p. 97-108.

222. Tangye, S.G., et al., *Intrinsic differences in the proliferation of naive and memory human B cells as a mechanism for enhanced secondary immune responses.* The Journal of Immunology, 2003. **170**(2): p. 686-694.

223. Baine, Y. and G.J. Thorbecke, *Induction and persistence of local B cell memory in mice.* Journal of immunology (Baltimore, Md.: 1950), 1982. **128**(2): p. 639-643.

224. Reusch, L. and D. Angeletti, *Memory B-cell diversity: From early generation to tissue residency and reactivation.* Eur J Immunol, 2023. **53**(4): p. e2250085.

225. Toellner, K.M., et al., *T helper 1 (Th1) and Th2 characteristics start to develop during T cell priming and are associated with an immediate ability to induce immunoglobulin class switching.* J Exp Med, 1998. **187**(8): p. 1193-204.

226. Valny, M., et al., *Tamoxifen in the mouse brain: implications for fate-mapping studies using the tamoxifen-inducible Cre-loxP system.* Frontiers in cellular neuroscience, 2016. **10**: p. 243.

227. Zhang, Y., et al., *Recycling of memory B cells between germinal center and lymph node subcapsular sinus supports affinity maturation to antigenic drift.* Nature Communications, 2022. **13**(1): p. 2460.

228. Lee, J.H., et al., *Long-primed germinal centres with enduring affinity maturation and clonal migration.* Nature, 2022. **609**(7929): p. 998-1004.

229. Aiba, Y., et al., *Preferential localization of IgG memory B cells adjacent to contracted germinal centers.* Proceedings of the National Academy of Sciences, 2010. **107**(27): p. 12192-12197.

230. Bachmann, M.F., et al., *Induction of long-lived germinal centers associated with persisting antigen after viral infection.* J Exp Med, 1996. **183**(5): p. 2259-69.

231. Zhang, Y., et al., *Effect of TACI signaling on humoral immunity and autoimmune diseases.* Journal of immunology research, 2015. **2015**(1): p. 247426.

232. Toellner, K.-M., D.M.-Y. Sze, and Y. Zhang, *What are the primary limitations in B-cell affinity maturation, and how much affinity maturation can we drive with vaccination? A role for antibody feedback.* Cold Spring Harbor perspectives in biology, 2018. **10**(5): p. a028795.

233. Radbruch, A., et al., *Competence and competition: the challenge of becoming a long-lived plasma cell.* Nature Reviews Immunology, 2006. **6**(10): p. 741-750.

234. Chen, C., V.A. Roberts, and M.B. Rittenberg, *Generation and analysis of random point mutations in an antibody CDR2 sequence: many mutated antibodies lose their ability to bind antigen.* The Journal of experimental medicine, 1992. **176**(3): p. 855-866.

235. Akiba, H. and K. Tsumoto, *Thermodynamics of antibody–antigen interaction revealed by mutation analysis of antibody variable regions.* The journal of biochemistry, 2015. **158**(1): p. 1-13.

236. Cyster, J.G. and P.C. Wilson, *Antibody modulation of B cell responses—Incorporating positive and negative feedback.* Immunity, 2024. **57**(7): p. 1466-1481.

237. Irvine, D.J., A. Aung, and M. Silva, *Controlling timing and location in vaccines.* Advanced Drug Delivery Reviews, 2020. **158**: p. 91-115.

238. Mehta, N.K., et al., *Pharmacokinetic tuning of protein–antigen fusions enhances the immunogenicity of T-cell vaccines.* Nature biomedical engineering, 2020. **4**(6): p. 636-648.

239. Burnett, C.J.M., *Generation of emigrating memory B cells and their migratory behaviours*. 2024, University of Birmingham.

240. Tas, J.M., et al., *Antibodies from primary humoral responses modulate the recruitment of naive B cells during secondary responses.* Immunity, 2022. **55**(10): p. 1856-1871. e6.

241. Viant, C., et al., *Antibody affinity shapes the choice between memory and germinal center B cell fates.* Cell, 2020. **183**(5): p. 1298-1311. e11.

242. McHeyzer-Williams, L.J., C. Dufaud, and M.G. McHeyzer-Williams, *Do memory B cells form secondary germinal centers? Impact of antibody class and quality of memory T-cell help at recall.* Cold Spring Harbor perspectives in biology, 2018. **10**(1): p. a028878.

243. Mamani-Matsuda, M., et al., *The human spleen is a major reservoir for long-lived vaccinia virus–specific memory B cells.* Blood, The Journal of the American Society of Hematology, 2008. **111**(9): p. 4653-4659.

244. Amanna, I.J., N.E. Carlson, and M.K. Slifka, *Duration of humoral immunity to common viral and vaccine antigens.* N Engl J Med, 2007. **357**(19): p. 1903-15.

245. Wan, Z., et al., *The activation of IgM- or isotype-switched IgG- and IgE-BCR exhibits distinct mechanical force sensitivity and threshold.* Elife, 2015. **4**.

246. Salzer, U., S. Jennings, and B. Grimbacher, *To switch or not to switch–the opposing roles of TACI in terminal B cell differentiation.* European journal of immunology, 2007. **37**(1): p. 17-20.

247. Xu, S. and K.-P. Lam, *Transmembrane activator and CAML interactor (TACI): another potential target for immunotherapy of multiple myeloma?* Cancers, 2020. **12**(4): p. 1045.

248. Hagglof, T., et al., *Continuous germinal center invasion contributes to the diversity of the immune response.* Cell, 2023. **186**(1): p. 147-161 e15.

249. Muramatsu, M., et al., *Specific expression of activation-induced cytidine deaminase (AID), a novel member of the RNA-editing deaminase family in germinal center B cells.* Journal of Biological Chemistry, 1999. **274**(26): p. 18470-18476.

250. Yeap, L.-S., et al., *Sequence-intrinsic mechanisms that target AID mutational outcomes on antibody genes.* Cell, 2015. **163**(5): p. 1124-1137.

251. Liu, Y.J., et al., *Within germinal centers, isotype switching of immunoglobulin genes occurs after the onset of somatic mutation.* Immunity, 1996. **4**(3): p. 241-250.

252. Song, W. and J. Craft, *T follicular helper cell heterogeneity: Time, space, and function.* Immunol Rev, 2019. **288**(1): p. 85-96.

253. Gong, F., T. Zheng, and P. Zhou, *T Follicular Helper Cell Subsets and the Associated Cytokine IL-21 in the Pathogenesis and Therapy of Asthma.* Front Immunol, 2019. **10**: p. 2918.

254. Haase, P., et al., *B cell fate mapping reveals their contribution to the memory immune response against helminths.* Front Immunol, 2022. **13**: p. 1016142.

255. Fribourg, M., et al., *Allospecific Memory B Cell Responses Are Dependent on Autophagy.* Am J Transplant, 2018. **18**(1): p. 102-112.

256. Pellon, A., et al., *Friends to remember: innate immune memory regulation by the microbiota.* Trends in Microbiology, 2025. **33**(5): p. 510-520.

257. Chen, S.T., et al., *B cell receptor signaling in germinal centers prolongs survival and primes B cells for selection.* Immunity, 2023. **56**(3): p. 547-561 e7.